THÈSE

Université Pierre et Maire Curie

Spécialité
Chimie et Physico-Chimie des Polymères
(École Doctorale 397, Physique et Chimie des Matériaux)

Présentée Par
Peiluo SHI

Pour obtenir le grade de
DOCTEUR DE L'UNIVERSITÉ PIERRE ET MARIE CURIE

Sujet de la thèse :

Mécanique linéaire et non linéaire des mélanges de polymères miscibles autour de la transition vitreuse

Soutenue le : 13 décembre 2013
Devant la commission d'examen formée de :

M. Jörg BASCHNAGEL	Professeur, Université de Strasbourg	Rapporteur
M. Leon E. GOVAERT	Professeur, Eindhoven University of Technology	Examinateur
M. Jean-François JOANNY	Professeur, UPMC - Institut Curie	Président
M. François LEQUEUX	Directeur de recherche, ESPCI	Directeur de thèse
Mme. Hélène MONTES	Maître de conférence, ESPCI	Directrice de thèse
M. Paul SOTTA	Directeur de recherche CNRS	Rapporteur

Invité :

M. Régis SCHACH	Docteur ingénieur à MFP Michelin	

Remerciements

CONTENTS

General introduction

Understanding quantitatively the nature of the glass transition remains one of the most challenging problems in the condensed matter physics. The phenomenon of the glass transition is directly associated to the segmental relaxation dynamics. Blending has an important effect on the segmental relaxation dynamics and is thus an interesting system to help getting a fundamental understanding of the physical principles of the glass transition. In addition, blending has many industrial applications, since it is a powerful and convenient way to tune mechanical properties of materials without the expense of new synthesis. For example, in the tire industry, a great variety of natural rubber and synthetic rubbers are blended, where polybutadiene (PB) and styrene butadiene rubber (SBR) are two synthetic rubbers that are mostly used in the tire industry. However a limited knowledge of the blending restricts the advance in the pursuit of tailor-made materials. A deep molecular level understanding of the effect of blending on the local dynamics in polymers is thus crucial.

We study miscible PB and SBR polymer blends in this PhD work. All the physical properties, especially the mechanical properties in the linear and non linear regimes will be investigated separately, and related to the heterogeneous nature of the polymer blends. The objectives of this work is to measure the length scale ξ associated to segmental relaxations and the distribution of relaxation times $P(\tau)$ in different blends, and to quantitatively relate this distribution to its observed linear and non linear mechanical properties.

Firstly, we give detailed introductions on glasses, the glass transition in general and its specificities in polymer materials, as well as some typical characteristics of miscible polymer blends in chapter 1.

Then we present experimental procedures and results of miscible polymer blends of polybutadiene (PB) and styrene butadiene rubber (SBR), and show the effect of broad glass transition on dynamical properties by different techniques: calorimetry, rheology, and dielectric measurements (chapter 2 and 3). The dynamic heterogeneity in the blend system will be quantitatively characterized in chapter 4 through a distribution of glass transition temperature T_g measured in calorimetry. We propose and test a mechanical approximation that accounts for a 3D average of the viscoelastic modulus. We show that this averaging method of the linear viscoelastic modulus, based on the self-consistent approach of the Olroyd-Palierne model gives excellent quantitative results even in the case of a wide distribution of viscoelastic moduli. This quantitative prediction confirms that mechanically, a blend can be considered as an ensemble of domains each of which having a different glass transition temperature.

We will also evaluate the length scale of segmental movement associated to the segmental relaxation. This will help us to understand the effect of blending on the linear properties and its relation with the microstructures.

Finally, the mechanical properties in the non linear regime will be studied with large deformation uniaxial extension test and cyclic shear test. We find that the non linearity of polymer blends in the glass transition zone is strongly related to its microstructures. As the

system approaches glass transition, the entanglement slipping initially observed in the rubber elasticity regime is greatly reduced due to appearance of glassy domains that immobilize the chains. Plasticity begins to be dominant as the system goes deeper into the glass transition zone, and corresponds to a percolation of glassy domains (chapter 5).

1. Introduction

Glasses are among the most ancient materials in human history since thousands of years ago, and they have various applications in modern life: lighting, decoration, construction, transportation, etc. However our knowledge of their structure remains incomplete.

Glass-forming materials are commonly obtained by cooling viscous liquids fast enough to avoid crystallization. They are essentially amorphous solids i.e. materials without crystalline order. These materials include silica glasses, metallic glasses, and polymers.

In the study of polymer materials and their applications, it is important to understand the features associated to the concept of glass transition temperature, T_g. As the temperature drops below T_g, a polymer behaves like a solid with a modulus of typically 1GPa, and is increasingly brittle. In addition it shows some specific time evolution called aging. As the temperature increases above T_g, the polymer behaves like a liquid without any significant change of its structure, it becomes either molten or rubber-like depending on its molecular architecture.

Nowadays, understanding quantitatively the nature of the glass transition remains one of the most challenging problems in the condensed matter physics.

In this chapter, we describe several basic features of the thermodynamics and dynamics of glasses. Then we present the specificity of the glass transition in polymers and its consequence on their mechanical properties.

1.1. *What is a glass?*

A glass is a disordered system for which the time scale of molecular motions is longer than the experimental observation time scale. It can be obtained by cooling a viscous liquid fast enough to avoid crystallization. Such a liquid at temperature below its melting point is called a supercooled liquid. Cooling a supercooled liquid decreases its molecular mobility. When the relaxation time becomes larger than the experimental time window, i.e. temperature is below its glass transition temperature T_g the system becomes a glass.

Glasses are thus slow and non equilibrium solids with a liquid-like structure. The simplest feature is to observe the volume variation with temperature. When decreasing the temperature, the density and viscosity of a supercooled liquid increases, and the molecular motions become slower and slower. As a consequence, the molecules do not have enough time to rearrange to find the equilibrium volume before the temperature is further lowered. The system becomes an out of equilibrium system and its thermodynamical properties are no longer the one they would be at equilibrium. Hence, for instance, the observed specific volume begins to deviate from the value at equilibrium, and indeed decreases slower than its

equilibrium value. This frozen structure is a glass. One usual definition of the glass temperature T_g is the temperature where the volume with temperature deviates from equilibrium and thus exhibits a sudden change of slope [1].
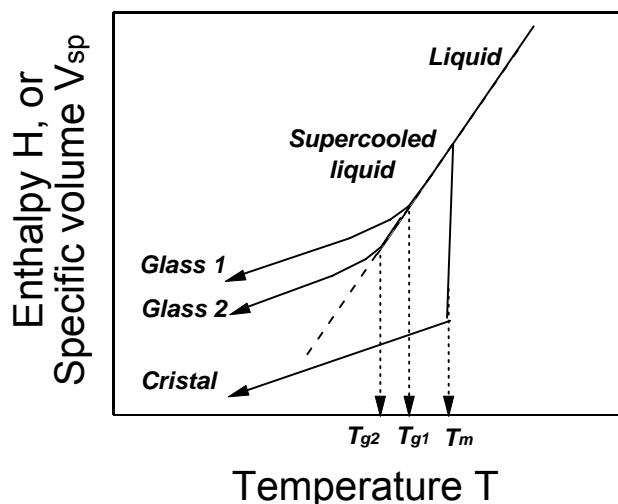
Figure 1.1. Enthalpy or specific volume as a function of temperature for a liquid which can form a crystal or glass. Glass 2 is formed with a smaller cooling rate.

The glass transition temperature T_g can be rigorously defined as the intersection of the specific volume V_{sp} versus temperature curve in the glassy state and supercooled liquid (see **Figure 1.1**). However, one must keeps in mind that the determination of T_g depends on cooling rate. If the cooling rate is smaller, it will allow the material to stay in equilibrium state until lower temperature, the value of T_g is consequently lower. In **Figure 1.1**, glass 2 has a lower T_g because the cooling rate is smaller. However, an order of magnitude change in cooling rate can change T_g by only about 3-5 K, and cooling rate in laboratory experiments are in a limited range in practice, so T_g obtained by volumetry or calorimetry whatever the cooling rate is in practice a material characteristic [2,3].

1.1.1. Non equilibrium aspects of the glass transition

Glass transition is not a phase transition, which means the change in thermodynamic quantities like enthalpy, specific volume, etc…, is gradual through the transition interval. But the derivatives of these parameters, even if they do not exhibit any singularities, change rapidly in the glass transition zone. For instance, the specific heat capacity (i.e. the temperature derivative of enthalpy) has a rapid change ΔC_p in the glass transition zone (**Figure 1.2**). This change can be observed by Differential Scanning Calorimetry (DSC) technique, which is widely used to determine the glass transition temperature T_g. A glass is a structure far from equilibrium and has the tendency to go towards its equilibrium but extremely slowly. This phenomenon is called aging. Let us just decrease the temperature at constant rate and then stop the cooling ant maintain the temperature below T_g. The frozen system will evolve slowly towards (but may no reach) equilibrium (from state-A to state-B in **Figure 1.2**). This evolution is called physical aging.
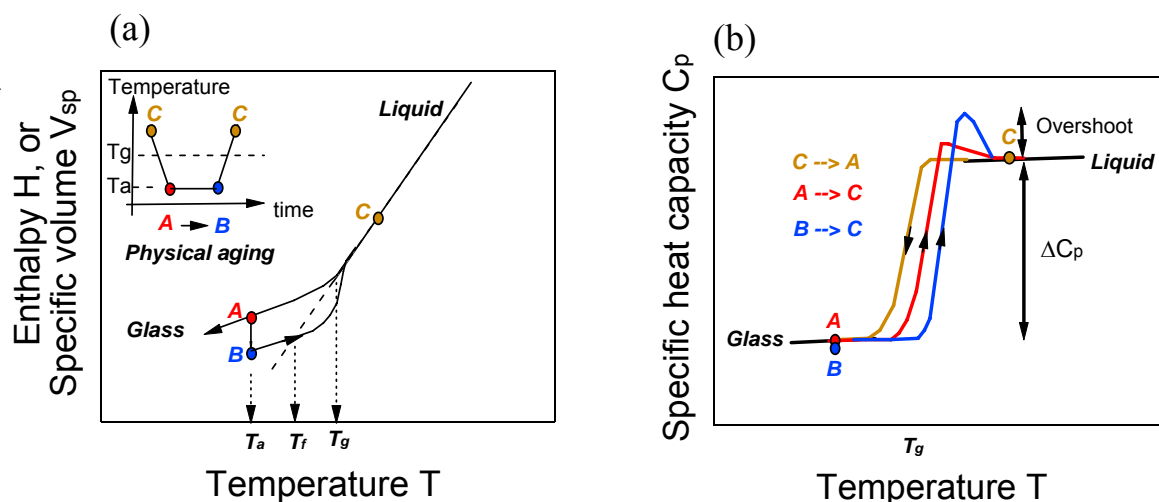
Figure 1.2. Schematic illustration of physical aging in glasses (a) enthalpy or specific volume vs. temperature plot. Inset figure is the temperature evolution: state-A is reached by cooling at constant rate from equilibrium state-C and state-B is reached from state-A after annealing at an temperature T_a for time t. The intersection of B-C and supercooled liquid line is called the fictive temperature T_f. (b) DSC curves of specific heat capacity vs. temperature.

At a constant aging temperature $T_a<T_g$, as time is allowed for the previously frozen molecules to rearrange, the system becomes more and more compact, manifesting as a drift towards smaller and smaller volume and enthalpy. This drift will continue until the equilibrium state is established at the aging temperature T_a [4].

As a consequence, the DSC curves present history dependence. A hysteretic behavior can be observed comparing the cooling-heating loop curve (C→A→C) without physical aging and (C→A→B→C) with physical aging [5,6]. Enthalpy changes can be found by integrating DSC curves. The difference in enthalpy between A and B by physical aging can thus be calculated as the difference in the integrations of the areas under DSC curves, that we will use in chapter 3 to characterize the aging behavior of our polymer blends.

1.1.2. Dynamic aspects of the glass transition

As temperature approaches T_g, molecular motions become very slow. Indeed, another definition of T_g – widely used in the covalent glass former community – is the temperature at which the shear viscosity reaches 10^{12} Pa•s, or at which the molecular relaxation time τ_a becomes larger than a macroscopic time scale, e.g. $\tau_g \approx$ 1s or 100s.

The relaxation time distribution could be measured by various techniques: mechanical spectroscopy, dielectric spectroscopy, light scattering, NMR, etc. In fact, different dynamic measurement techniques reveal similar features for the temperature dependencies for the relaxation time distribution [7]. Among these techniques, a popular one is the dielectric spectroscopy, which measures the dielectric susceptibility due to dipolar relaxations. As an example for introducing the time relaxation distribution of glass, we will just have a look on the temperature and frequency dependence of the imaginary part of the dielectric

susceptibility, $\varepsilon''(\omega)$, is shown in **Figure 1.3** for the glass-former benzophenone over a wide temperature and frequency range. However the features obtained from the dielectric relaxation are the same as those one could obtain from other techniques like rheology for instance.
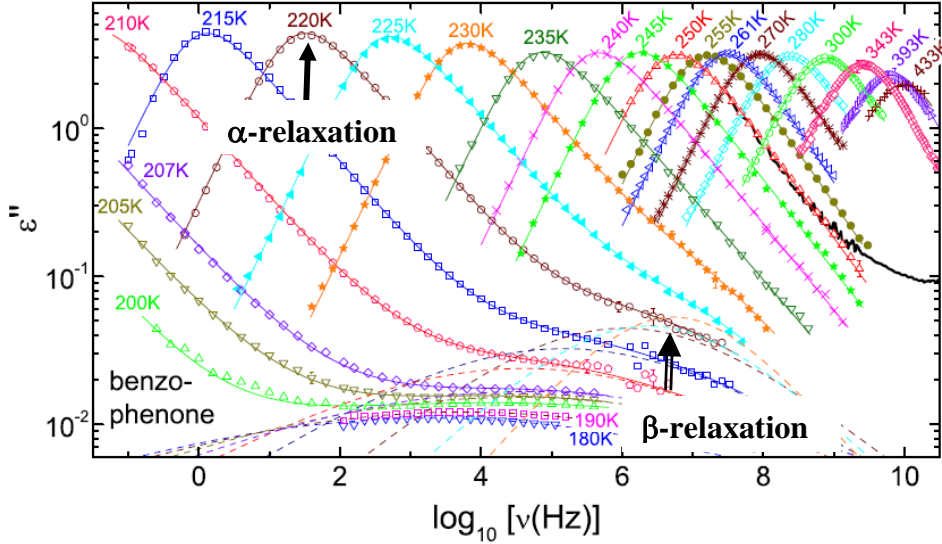
Figure 1.3. Temperature and frequency dependence of the imaginary part of the dielectric susceptibility $\varepsilon''(\omega)$ for the glass-former benzophenone. Figure from Pardo *et al.* [8]. α-relaxation and β-relaxation are indicated by arrows in the figure.

Two relaxation processes indicated by peaks in dielectric loss ε'' can be seen.

     α-relaxation. The main relaxation peaks at lower frequencies are due to the segmental relaxation or α-relaxation which corresponds to the dynamic glass transition. Except for covalent glass former that we will not consider here, the temperature dependence of the average α-relaxation time is described by the Vogel-Tammann-Fulcher (VTF) equation:

$$\tau = \tau_0 \exp(\frac{B}{T - T_0}) \qquad \text{(eq 1.1)}$$

where τ_0 and B are temperature independent constants. It suggests a divergence of the relaxation time at a finite, so-called Vogel temperature T_0, usually 30-70 K below T_g, but in practice the divergence can never be observed and is no relevant. It is suggested that this equilibrium state below T_g has a weaker divergence at finite temperature as predicted by VTF [6,9].

     An analog equation that is often used to describe relaxation times in polymer is the Williams-Landel-Ferry (WLF) equation:

$$\log_{10} \frac{\tau}{\tau_0} = -\frac{C_1 \times (T - T_0)}{C_2 + (T - T_0)} \qquad \text{(eq 1.2)}$$

where T_0 is a reference temperature (usually taken as T_g); C_1 and C_2 are characteristic constants of the polymer. This equation is mathematically equivalent to the VTF equation [10] and is very popular in the polymer literature. In this manuscript we will use the WLF equation and measure the coefficients C_1 and C_2 of our samples.

β-relaxation. The additional broad peaks, of indeed lower amplitude, at low temperature reveal the existence of a secondary relaxation or β-relaxation. The temperature dependence of the β-relaxation time is described by an Arrhenius equation:

$$\tau = \tau_0 \exp(\frac{B}{T}) \qquad \text{(eq 1.3)}$$

The β-relaxation arises from localized rotational fluctuations of the dipole vector. In practice the β-relaxation has a small contribution to the viscoelastic modulus, because it corresponds to limited strain amplitude, and we will not focus on it in our manuscript – except in the dielectric chapter of this manuscript.
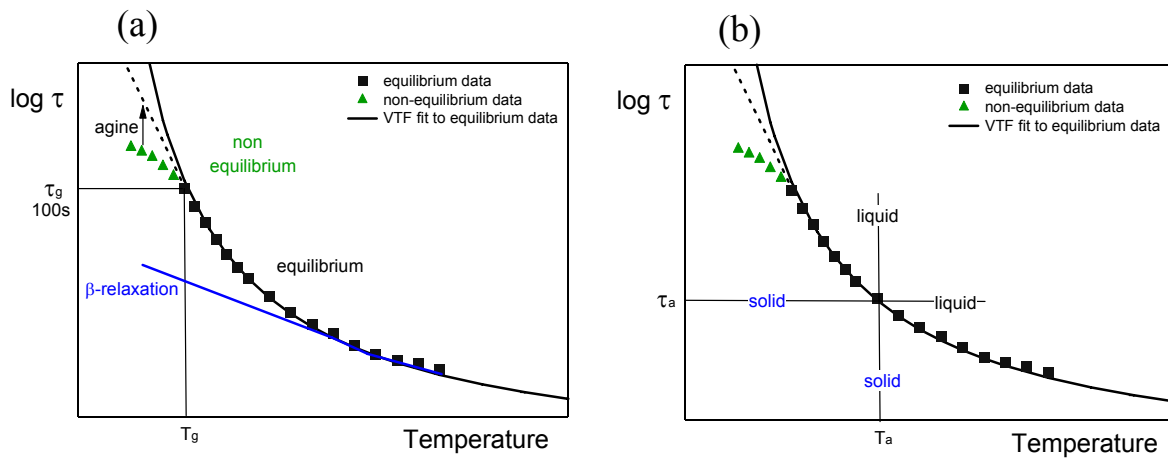
Figure 1.4. Schematic of temperature dependence of the relaxation times determined by peak dielectric relaxation frequency. At high enough temperature there is a single relaxation mechanism. At lower temperature in the supercooled regime the peak splits into α-relaxation and β-relaxation. α-relaxation exhibits non-Arrhenius (VTF or WLF) temperature dependence. Dashed line represents the equilibrium state below T_g.

Temperature dependence of the relaxation times. Most of the trends of the glass transition can be summarized in **Figure 1.4**(a) that illustrates the behavior of temperature dependence of the α-relaxation and the β-relaxation. The β-relaxation exhibits an Arrhenius temperature dependence, while the data of α-relaxation at equilibrium is well described by VTF equation. The out of equilibrium regime ($T < T_g$) derivates from this VTF form. A glass cooled below T_g as explained before, is out of equilibrium. The non-equilibrium behavior seems to be an Arrhenius low. This time relaxation, faster than the equilibrium one drifts towards its equilibrium value with physical aging.

Solid-liquid transition. One have to keep in mind that a glass is the system for which the relaxation time is larger than the time of observation. Thus at a given temperature $T = T_\alpha$, if the timescale of experimental observation τ_{exp} is longer than the corresponding relaxation time τ_α, the material can flow and it behaves liquid-like; otherwise it is solid-like. At a given experimental observation time $\tau_{exp} = \tau_\alpha$, if $T > T_\alpha$ it is liquid-like; otherwise it is solid-like (see **Figure 1.4** (b)).

1.2.   Glass transition: specificities in polymer materials

Polymers are flexible long-chain molecules. Many of these systems easily form glasses even at very slow cooling rate, since their molecular structure may be extremely complex and irregular and the arrangement for a well defined crystalline state may be highly improbable. We describe in this section the structure and the dynamics of polymers that do not crystallize. We will describe how the glass-rubber transition is associated with different length scales and different mechanical properties.

1.2.1. Structure of a polymer

A polymer chain is composed of repeating structured units (monomers) linked with covalent bonds. A single chain may consist of more than thousands of monomers and may have a linear, branched, or network structure.

In a polymer sample, there are additional interactions (Van der Waals, H bonds) between 2 polymer chains. For long chain molecules, a three-dimensional network can be formed by a certain number of junction points either by crosslinks or by entanglements.
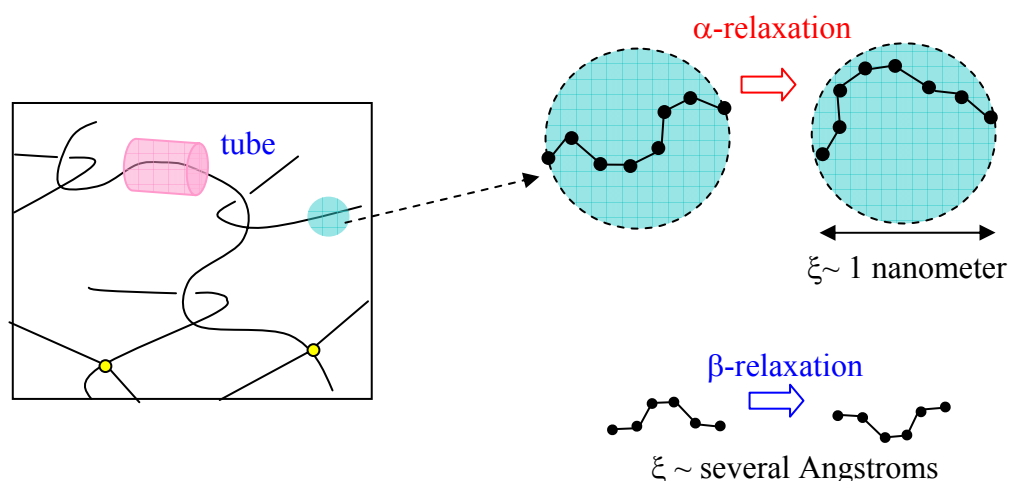
Figure 1.5. Schematic of the structure of a polymer: entanglements (topological constrains between chains), confining tube, cross-links (bridges marked as yellow points), and size scale ξ of segmental α-relaxation and localized β-relaxation.

Crosslinks. A three-dimensional polymer network can be obtained by crosslinks between individual polymer chains. For instance, sulphur bridges can be formed between polymer chains with double C-C bonds through a chemical process called vulcanization – that we will describe in chapter 2. This network controls the rubber-like elasticity of polymers at high temperature, i.e. above T_g. In fact, at high temperature, forces between molecules are weak and the dynamics are the one of a liquid. However, the molecules are linked together by the network and they cannot move independently on long distances as in a liquid. This phenomenon is responsible for the rubber-like elasticity. It has an entropic origin, which is due to the variety of statistical conformations of polymer chains. As a result from Gaussian statistics, i.e. in simple models where the crosslinks are assumed to follow the

macroscopic deformation and the entanglements are neglected, the shear modulus G_c at the high temperature rubbery plateau of a crosslinked polymer writes:

$$G_c = \frac{\rho RT}{M_c} \qquad \text{(eq 1.4)}$$

where ρ is the material density($\rho = 950\,kg \cdot m^{-3}$ for our polymers), $R=8.31\text{JK}^{-1}\text{mol}^{-1}$ is the gas constant, M_c is the number average molar mass of a network strand. It can be seen that the modulus increases with temperature. However in practice, for low crosslink density - as in our systems, see chapter 3- entanglement has predominant roles. By **entanglement**, we mean the topological constrains imposed by neighboring chains on a given chain. Entanglements restrict the molecular motion to a tube-like region called the confining tube (see **Figure 1.5**). The motions of the chain along the tube are free while the perpendicular ones are restricted. The tube diameter a is determined as [11]:

$$a \approx b\sqrt{N_e} \qquad \text{(eq 1.5)}$$

where b is the length of a Kuhn monomer and N_e is the number of Kuhn monomers in an entanglement strand. We give an example of a 1,4-Polybutadiene polymer at 25°C where $b = 1nm$ and $N_e = 18$, giving $a \approx 4.1nm$.

Indeed Gaussian statistics –that again assumes that the entanglements follow the macroscopic deformation of the sample – leads to the following expression for the modulus of weakly crosslinked rubber, but also for polymers of long chain $(N>>N_e)$:

$$G_e = \frac{\rho RT}{M_e} \qquad \text{(eq 1.6)}$$

where M_e is the number average molar mass of an entanglement strand with N_e monomers.
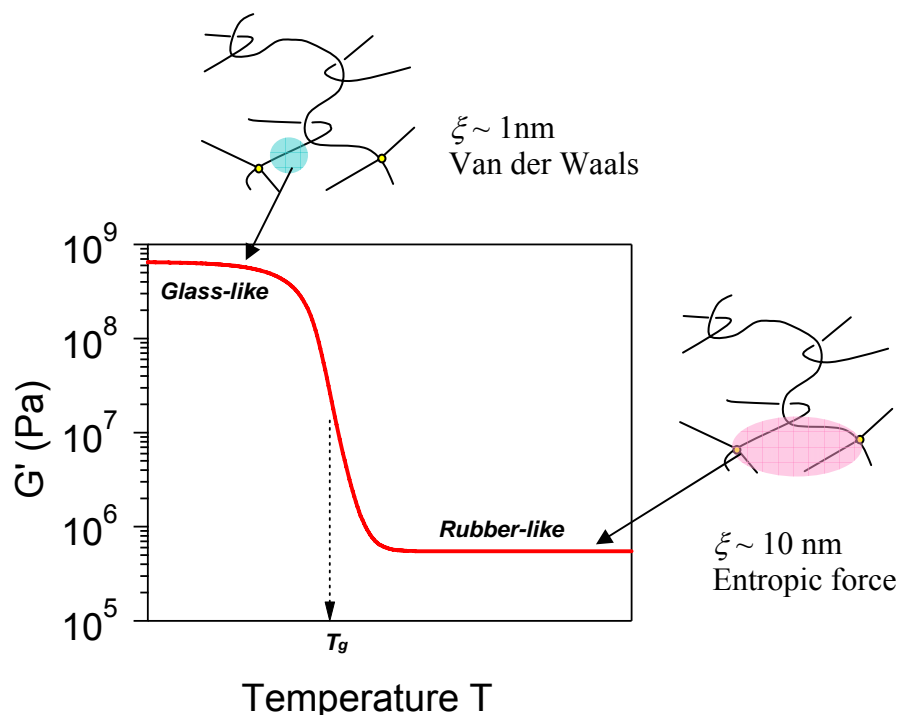
Figure 1.6. Modulus as a function of temperature. Different length scales for rubbery state and glassy state.

To conclude, above T_g, the dynamics of the polymer chains are the one of a liquid. However molecules diffusion is restricted due to the topological constrains. The elastic modulus is determined by the mass between entanglements and between crosslinks. In the chapter 5 we will discuss in more details the linear and nonlinear mechanics of rubbers, in term of entanglement slips.

Glass-rubber transition. As temperature is lowered, the thermal energy of the rotating groups of polymer chains becomes insufficient to surmount the potential barrier imposed by the neighboring groups [12]. Molecules are no longer able to explore their environment in a reasonable time. The rubber-like behavior evolves towards a glassy-like one (see **Figure 1.6**). In this manuscript we will focus on this progressive shorting of the range of fluctuations, and its consequences on the nonlinear mechanics of polymers.

Length scale. In the rubbery state, the typical length scale of fluctuation is at the scale either of the crosslinks or of the entanglements. In the glass transition domains the relevant fluctuations occur at a shorter range, the one of the α-relaxation. α-relaxation is a cooperative phenomenon where a selected segment moves together with its environment. The extent of cooperativity could be described by a length scale ξ, which is estimated to be comparable to the Kuhn length $\xi \sim 1nm$ [13]. An important issue is to know whether ξ increases with decreasing temperature or not [14]. It is also noted that ξ is directly related to the activation volume V in the Eyring model. However, the measurement and the physical origin of the α-relaxation is still an open question. We will indeed give in chapter 4 an experimental method that provides a determination of ξ.

<u>**Conclusion.**</u> The mechanical behavior of amorphous polymers depends on temperature and time-scale. At high temperature and long time-scale, the material behaves rubber-like, with low initial modulus and long-range reversible elasticity. At low temperature and short time scale, the material behaves glass-like, with high initial modulus and plastic deformation at higher strain. We will discuss in the following sections the mechanical properties of rubber-like and glass-like regimes separately.

1.2.2. Rubber elasticity
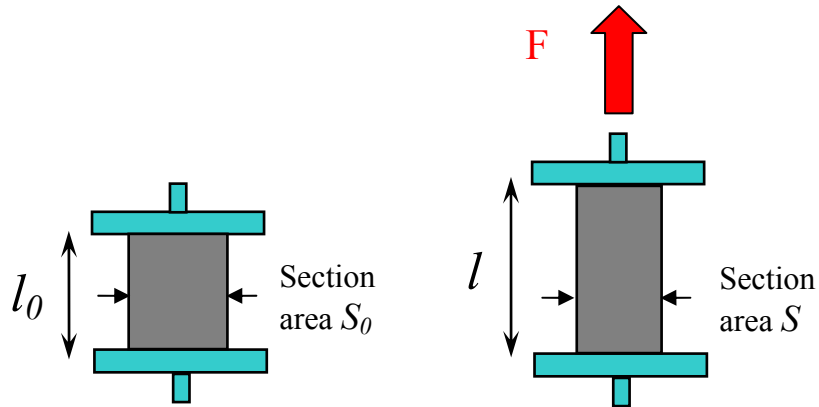
Figure 1.7. The force, means a stress σ, causes a deformation that is measured as the strain ε. The length l_0 is the initial displacement and S_0 is the initial section area; l and S are respectively those under load.

The mechanical behavior of a conventional solid is usually described by its elastic behavior. As long as the deformations are not too large Hooke's Law applies:

$$\sigma = E\varepsilon \qquad (eq\ 1.7)$$

where $\sigma = F/S$ is the stress, E is the Young's modulus, $\varepsilon = (l - l_0)/l_0 = \lambda - 1$ is the strain and λ is the elongation. Longitudinal deformation usually comes with changes of the cross section (see **Figure 1.7**). It is thus important to distinguish between true stress (force per strained area F/S) and engineering stress (force per unstrained area F/S_0, also called nominal stress). Using the constant volume approximation, the following equation applies:

$$\sigma_{true} = \lambda \sigma_{eng} \qquad (eq\ 1.8)$$

A true strain can also be defined as:

$$\varepsilon_{true} = \int_{l_0}^{l} dl/l = \ln(l/l_0) = \ln(\lambda) = \ln(1 + \varepsilon_{eng}) \qquad (eq\ 1.9)$$

Affine deformation Gaussian elasticity. According to the classical Gaussian rubber elasticity theory, the rubber elasticity has an entropic origin, which is due to the variety of statistical conformations of polymer chains. The affine deformation Gaussian elasticity theory assumes that the networks junctions are fixed in a strained background and the material deforms affinely. The engineering and true stresses are:

$$\sigma_{eng} = \frac{E}{3}\left(\lambda - \frac{1}{\lambda^2}\right) \qquad (eq\ 1.10)$$

and

$$\sigma_{true} = \frac{E}{3}\left(\lambda^2 - \frac{1}{\lambda}\right) \qquad (eq\ 1.11)$$

where E is the Young modulus. In the case where crosslinks are dominant its value is given by $E = 3\rho RT / M_c$. It should be noted that for rubbers that are in first approximation incompressible, the Poisson ratio $\nu \approx 0.5$, and the relation between shear modulus G and Young's modulus E is:

$$E = 2G(1+\nu) = 3G \qquad \text{(eq 1.12)}$$

According to eq 1.10, the linear Hooke's law $\sigma = E\varepsilon$ still applies at small strains. At larger deformations, the mechanical behavior of the classical Gaussian theory is already non linear. We can plot a stress-elongation curve of the classical Gaussian theory and compare it to experiments, as is presented in **Figure 1.8**. We noted that at very beginning of elongation, this behavior is well described by the affine Gaussian rubber elasticity theory. But at larger elongations, this model does not agree with experiments. The discrepancy between the Gaussian model and the experimental results originates from two different phenomena:

- Stress is smaller than predicted by the Gaussian approximation at small strains. This can be interpreted by the fact that entanglements between chains slip.
- Stress is larger at large strains, with a strain hardening behavior not predicted by Gaussian approximation. Indeed, this can be interpreted by facts that chains are stretched to their limit of extensibility at very large elongations, and we observe thus a strain hardening.
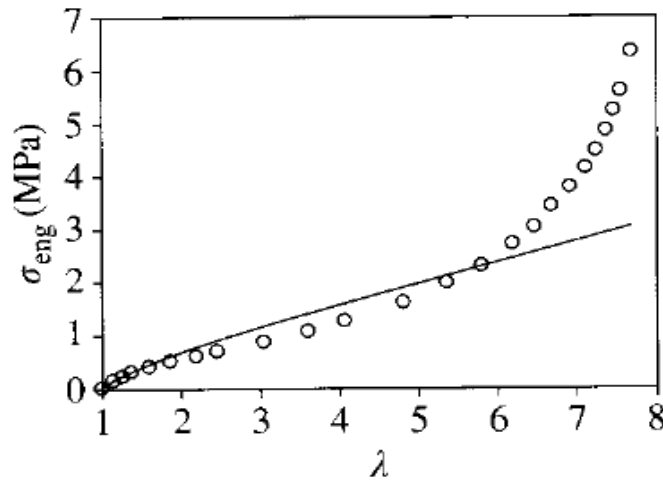
Figure 1.8. Engineering stress-elongation behavior of a cross-linked rubber. Circles are data from experiments and the solid line is a fit of the classical Gaussian theory. Figure from the book of Colby and Rubinstein [11].

The strain softening at intermediate strain and strain hardening at large strain are further described by various approaches.

Strain softening of rubbers. A phenomenological description of the strain softening has been proposed by Mooney-Rivlin. Based on a first order series expansion and on the symmetry of the stress tensor, it introduces 2 parameters C_1 and C_2 to describe the strain softening with increasing elongation. The free energy writes [12]:

$$F = C_1(\lambda_1^2 + \lambda_2^2 + \lambda_3^2 - 3) + C_2(1/\lambda_1^2 + 1/\lambda_2^2 + 1/\lambda_3^2 - 3) \qquad \text{(eq 1.13)}$$

where C_1 and C_2 are two elastic constants. λ_1, λ_2 and λ_3 are three principal extension ratios along three mutually perpendicular axes. Considering incompressibility condition, we

have $\lambda_1\lambda_2\lambda_3 = 1$ and $\lambda_2^2 = \lambda_3^2 = 1/\lambda_1 = 1/\lambda$. The stress is $\sigma = dF/d\lambda$, which leads to the general equation:

$$\sigma_{eng}^{MR} = (2C_1 + \frac{2C_2}{\lambda})(\lambda - \frac{1}{\lambda^2}) \qquad \text{(eq 1.14)}$$

It is often assumed in literature [11] that the parameter $2C_1$ corresponds to the contribution of chemical cross-links, and the parameter $2C_2$ corresponds to that of entanglements. The eq 1.10 derived from the statistical Gaussian elasticity theory corresponds to the particular case of $C_2 = 0$. In addition, writing eq 1.13 in the form of "**reduced stress**" $f = \sigma_{eng}/(\lambda - \lambda^{-2})$ against $1/\lambda$ should yield a straight line (see red line of **Figure 1.9**).

(Note: To avoid misunderstanding of the coefficients C_1 and C_2 of Mooney-Rivlin equation (eq1.14) with that of WLF equation (eq 1.2), we will use C_1^g and C_2^g to design WLF coefficients since we will always use T_g as the reference temperature in WLF equation.)

Indeed, there exist also several molecular models of rubber elasticity. The phantom network model assumes that the network junctions are fluctuating in space, instead of deforming affinely in a non fluctuating background with macroscopic deformation. The constrained junction model and Edwards tube model assume a confining potential, due to the effect of topological interactions, which evolves with network deformation. As explained by Rubinstein and Panyukov, none of these models are able to describe precisely the nonlinear behavior at small strains. The same authors propose a non-affine slip tube model which takes into account the redistribution of all the chain length in 3 directions during deformation and give expression for the free energy [15]:

$$F_{st}(\lambda) = F_c(\lambda) + \frac{vkTL}{2}\sum_\alpha (\frac{\lambda_a}{g_a^{1/2}} + \frac{g_a^{1/2}}{\lambda_a}) - vTS\{g_a\} \qquad \text{(eq 1.15)}$$

where $F_c(\lambda)$ is the contribution of the crosslinks, v is the chain number density, L is the total number of slip-links per network chain, λ_a (a=1, 2, 3) are three principal extension ratios along three mutually perpendicular axes, g_a is the redistribution parameters of chain length along the axis (a=1, 2, 3) and $g_1 + g_2 + g_3 = 3$. $S\{g_a\}$ is the entropy of slip-links in the slip-tube model.

Slip-tube model accounts for the redistribution of stored length along the confining tube and predicts for the stress the following expression:

$$\sigma_{eng}^{RP} = (G_r + \frac{G_e}{0.74\lambda - 0.61\lambda^{-1/2} - 0.35})(\lambda - \frac{1}{\lambda^2}) \qquad \text{(eq 1.16)}$$
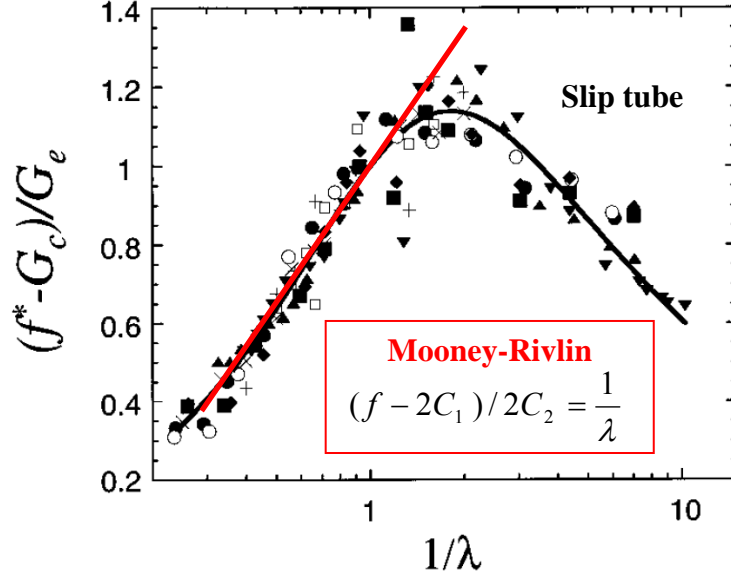
Figure 1.9. A series of experimental and simulation data of PDMS and natural rubber samples. Black solid line is the non-affine slip tube plot; red solid line is the fit of Mooney-Rivlin equation. Figure by Rubinstein and Panyukov [15]. In this figure, parameter f is called reduced stress and is defined as $f = \sigma_{eng} / (\lambda - \lambda^{-2})$.

The non-affine slip tube model is in excellent agreements with experiments and simulations in a wide range of deformation. It is also be described satisfactorily by the Mooney-Rivlin equation in the range of $0.2 < 1/\lambda < 1$, i.e. $1 < \lambda < 5$.

Strain hardening of rubbers. At large elongations, because polymer chains reach their extensibility limit, the Gaussian approximation that approximates the polymer by an harmonic spring fails. The experimental stress is much higher than that predicted by the Gaussian theory. For a freely jointed chain with N segments of length b, the theoretical extensibility limit is:

$$\lambda_{max} = \frac{R_{max}}{\left\langle R_0^2 \right\rangle^{1/2}} = \frac{bN}{bN^{1/2}} = N^{1/2} \qquad \text{(eq 1.17)}$$

Gaussian chain statistics suppose that the elongation of the chain is not very large and the end-to-end distance of the chain is much shorter than the fully stretched one:

$$R \approx \left\langle R_0^2 \right\rangle^{1/2} \ll R_{max} \qquad \text{(eq 1.18)}$$

If these conditions are not satisfied, a more suitable model of non-Gaussian chain statistics will apply. For instance, the widely used Langevin chain statistics predicts – in the case of a phantom network- the force f needed to maintain such a chain at a length R. This force f writes:

$$f = \frac{kT}{b} L^{-1}(\frac{R}{Nb}) \qquad \text{(eq 1.19)}$$

where L is the Langevin function : $L(\beta) = \coth(\beta) - 1/\beta$; L^{-1} is the inverse Langevin function and $L^{-1}(s) = 3x + \frac{9}{5}x^3 + \frac{297}{175}x^5 + ...$
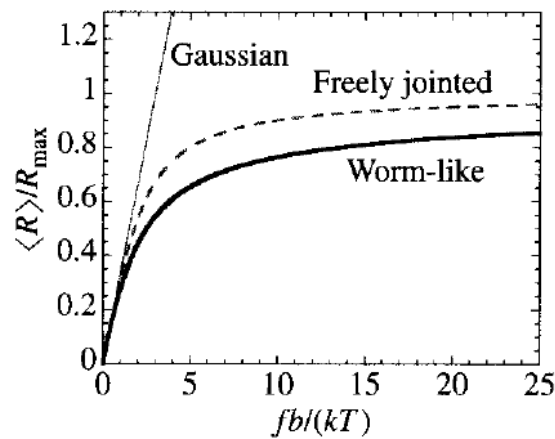
Figure 1.10. End-to-end distance as a function of stretching force for different models. Figure from the book of Colby and Rubinstein [11].

As shown in **Figure 1.10**, the freely jointed inverse Langevin function gives a linear dependence at small elongation as predicted by the Gaussian statistics, and deviates from it at larger elongation. It diverges at $R=R_{max}$. However, up to now there is no quantitative expression –such as the Rubinstein Panyukov model for smaller strains – that are able to give any satisfactory results in this domain of strain hardening.

Conclusions on rubber elasticity: rubber elasticity has an entropic origin and its mechanical property is non linear due to Gaussian affine deformation, entanglement slipping and extensibility limit of chains. The non linearity in glassy polymers has different origins as will be presented below.

1.2.3. Linear properties in glassy polymers

In addition to the WLF (VFT) law for the evolution of the relaxation time, polymer glasses exhibit a huge broadness in the relaxation time spectrum. We will now discuss the origin of this broadness. We will in particular introduce the notation of dynamical heterogeneities, that if of importance for the polymer glass mechanics.

As glassy transition temperature T_g is approached, supercooled liquid flow very slowly and the viscosity could increase rapidly to typically 10^{12} Pa•s at T_g. In comparison, liquids such as water and ethanol have viscosities about 10^{-3} Pa•s at room temperature.

The Stokes-Einstein equation, that predicts the translational diffusion coefficient, D_t, for a sphere in a hydrodynamic continuum, writes:

$$D_t = \frac{kT}{6\pi\eta r}$$

(eq 1.20)

where η is the viscosity of the liquid at the considered temperature and r is the radius of the sphere. This equation is valid in principle only for particles that are much larger than the molecules of the liquid in which they diffuse. For most of the simple liquids this expression gives an excellent prediction. On the contrary, this equation fails for supercooled liquids as we will explain now.

Several experimental studies [16–19] have shown that the quantity $D_t\eta/T$ is a roughly constant value at high temperature ($T>1.2T_g$) , which is consistent with the Stokes-Einstein equation. But at lower temperature ($T<1.2T_g$), the quantity $D_t\eta/T$ significantly increases. It was found that $D_t \propto \eta^{-0.75}$ at low temperature. Otherwise, the rotational diffusion coefficient is inversely proportional to the viscosity, $D_r \propto \eta^{-1}$, for all temperatures [16]. Indeed as compared to the Stokes Einstein law, the translational diffusion coefficient is larger than the one predicted using the macroscopic viscosity. This remark has led the community to the following conclusion: the macroscopic viscosity is larger than the average one that drives the motion of individual molecules. These differences which originate in the way the dynamical properties are averaged suggest that the dynamics are spatially extremely heterogeneous.
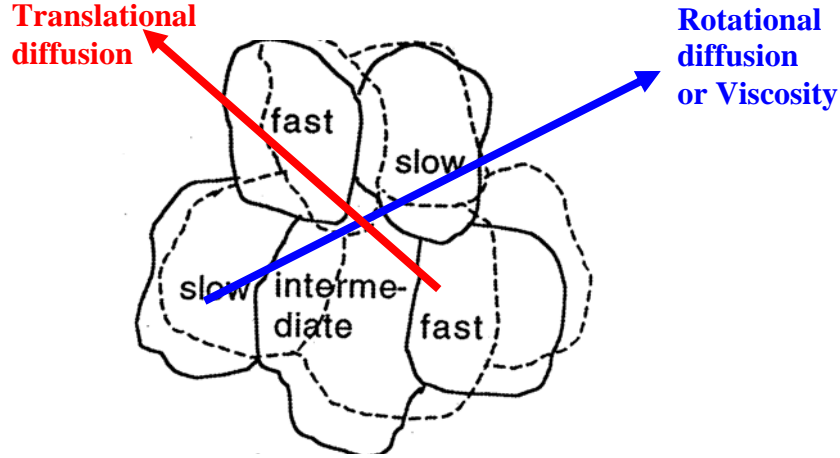
Figure 1.11. Schematic illustration of the spatially heterogeneous dynamics when approaching T_g. Solid lines represent the dynamic heterogeneity at a certain time t_1, and dashed lines represent that of time t_2. Figure by Ediger [1].

Spatially heterogeneous dynamics. The physical interpretation of these results is that the system presents spatially heterogeneous dynamics when approaching T_g. The macroscopic viscosity or rotational diffusion is dominated by the slow dynamics aggregates and increases rapidly, while the translational diffusion is dominated by the fast dynamics regions [1,19] as shown in **Figure 1.11**.

In this point of view, the heterogeneity can be represented by a distribution of relaxation times $P(\tau)$ and each region has a special relaxation time, which could be orders of magnitude faster or slower than that of the neighbor regions located only a few nanometers away. This distribution evolves with time as illustrated by **Figure 1.11**. It is suggested that the length scale of these heterogeneous domains is about 3nm, the dynamics between the fastest and slowest regions vary between 1-5 orders of magnitude at T_g [1].

Another consequence of the spatial heterogeneity is the non-exponential relaxation. If we suppose that the relaxation in a given domain is exponential, and the macroscopic relaxation response is an integral of all the domains, we have

$$R(t) = \int_0^\infty \exp(-t/\tau)P(\tau)d\tau \qquad \text{(eq 1.21)}$$

where $P(\tau)$ is the relaxation time distribution function.

The macroscopic time relaxation function thus becomes increasingly non-exponential for broader and broader time distribution. This function $R(t)$ is often approximated by the well known Kohlrausch-Williams-Watts (KWW) function, or "stretched exponential" function:

$$R(t) = \exp[-(t/\tau_{KWW})^{\beta_{KWW}}] \qquad \text{(eq 1.22)}$$

where τ_{KWW} is a characteristic relaxation time and β_{KWW} is a parameter ranging between 0 and 1.

In the frequency-domain, the Fourier transform of $R(t)$ can also be approximated by empirical relaxation functions such as Havriliak-Negami law [20]. In this manuscript, we will always use Havriliak-Negami approximation, which is widely used in literature and gives satisfactory results. This function writes:

$$R^*(\omega) = \frac{1}{\left(1 + \left(j\omega\tau_{HN}\right)^\alpha\right)^\gamma} \qquad \text{(eq 1.23)}$$

where τ_{HN} is a characteristic relaxation time and α and γ are parameters ranging between 0 and 1. This relaxation function is widely used to describe dielectric data. For $\alpha=1$ and $\gamma=1$, this function corresponds to a simple Maxwell model.

The time domain KWW parameters could be directly measured by stress relaxation test. They can also be related to the frequency domain Havriliak-Negami parameters (they are not exactly Fourier transforms of each other), through a method developed by Alvarez et al. [21]:

$$\ln(\frac{\tau_{HN}}{\tau_{KWW}}) = 2.6(1-\beta)^{0.5}\exp(-3\beta) \qquad \text{(eq 1.24)}$$

for the characteristic relaxation times and

$$\alpha\gamma = \beta^{1.23} \qquad \text{(eq 1.25)}$$

for the β parameter.

H-N function could be applied to dielectric spectra as well as viscoelastic spectra, which reads:

$$\frac{G_{glass} - G^*(\omega)}{G_{glass} - G_{rub}} = \frac{1}{\left(1 + \left(j\omega\tau_{HN}\right)^\alpha\right)^\gamma} \qquad \text{(eq 1.26)}$$

where G_{glass} is the glassy modulus, G_{rub} is the rubbery modulus and $G^* = G'+jG''$. G' is the elastic modulus and G'' is the loss modulus. In fact, the parameter τ_{HN} gives approximately the average value of all the relaxation times: $\tau_{HN} \approx \langle\tau\rangle$.
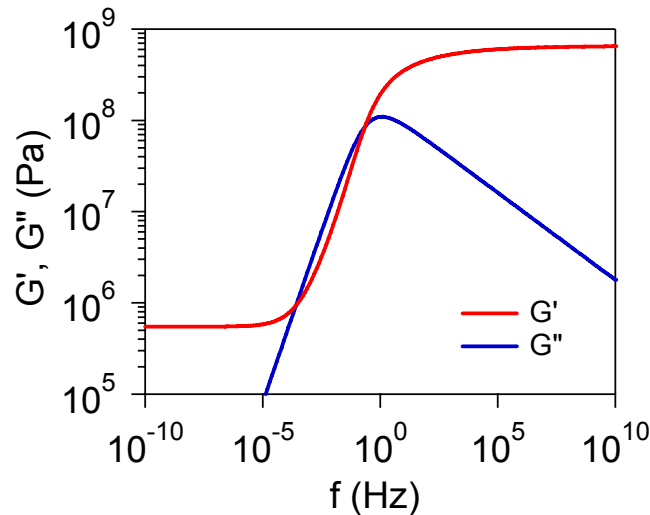
Figure 1.12. Complex shear modulus as a function of frequency

Back to the α-relaxation of polymers, where the distribution of relaxation time exhibits typically more than 4 decades' broad, and its average $\tau_{HN} \approx \langle\tau_\alpha\rangle$ varies following a

WLF law. In addition the broadness of the spectrum does not vary significantly with temperature. Hence, the effect of temperature is nearly to simply shift the relaxation time distribution. It implies that time-temperature superposition (TTS) is in practice a very good approximation.
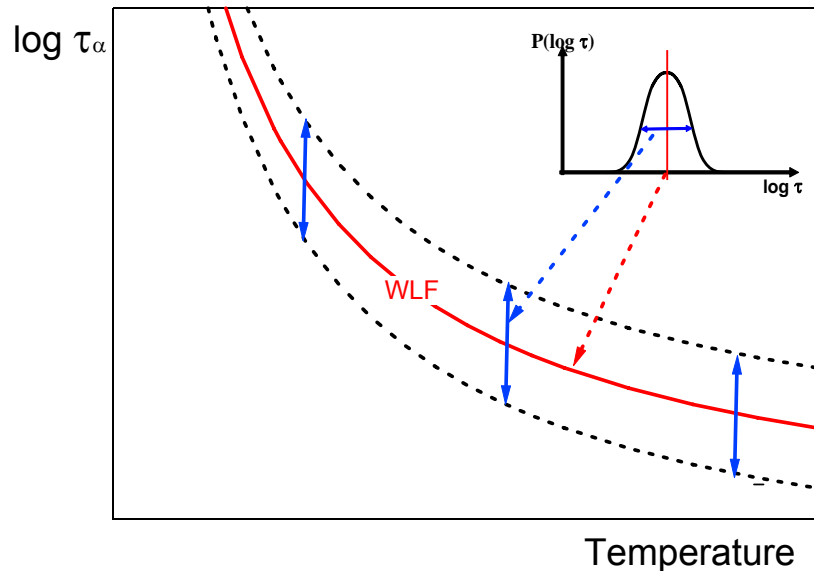
Figure 1.13. The evolution of relaxation times as a function of temperature - the WLF equation.

Time-temperature superposition (TTS) in polymers. We will now shortly explain what the time temperature superposition is. The linear viscoelastic behavior of a polymer depends on time (or frequency), and depends on temperature. This dependence is most spectacular in the transition zone, where the modulus could drop as much as a thousand times, from glass-like (1GPa) to rubber-like (1MPa).
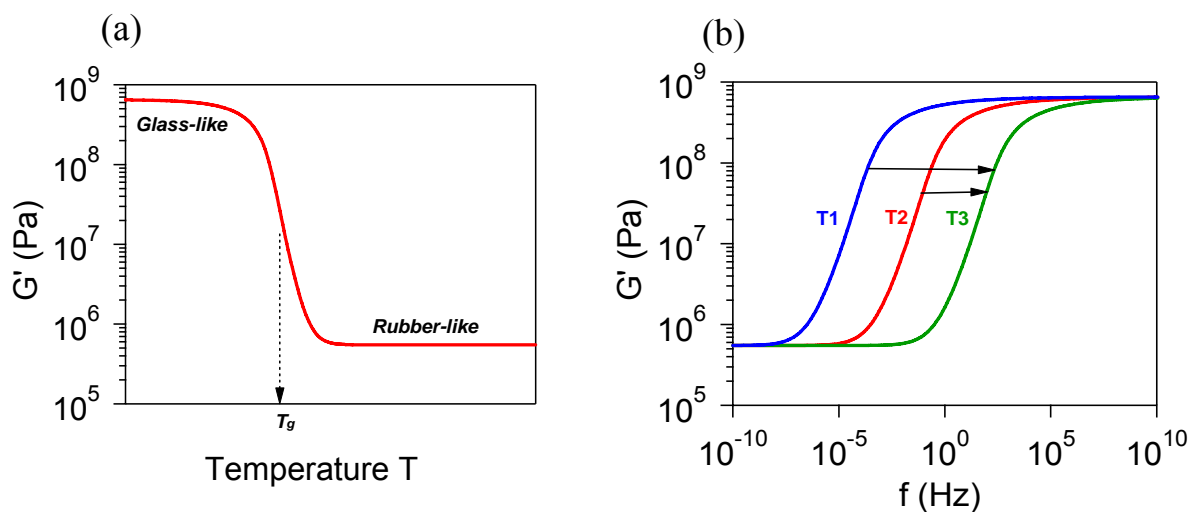
Figure 1.14. (a) Elastic modulus as a function of temperature. (b) Time-temperature superposition, $T_1<T_2<T_3$

The principle of time-temperature superposition (tTS) is the following: decreasing the temperature is equivalent to increasing the frequency. More precisely, for instance for the viscoelastic modulus G*, this writes:

$$G^*(T, \frac{\omega}{a_T}) = G^*(T_0, \omega) \qquad \text{(eq 1.27)}$$

The shift factor a_T can be well described by WLF equation in the temperature range from T_g to T_g +100K:

$$\log_{10} \frac{\tau}{\tau_0} = -\frac{C_1^g \times (T - T_g)}{C_2^g + (T - T_g)} \qquad \text{(eq 1.28)}$$

where the reference temperature is taken as T_g; C_1^g and C_2^g are characteristic constants of the polymer that can be easily measured and also found in literature.

tTS procedure is commonly used to extrapolate the polymer properties over many orders of magnitude of frequencies, at a reference temperature, by measuring its properties in a small window of frequency, while sweeping the temperature. For a given reference temperature, a fully overlapped curve could be formed, which is called the master curve.

In this manuscript, we will describe the linear dielectric and viscoelastic properties of all polymers and blends, versus frequency by H-N equation, and assume that the WLF-law is valid to describe the α-relaxation time (by default but with some exceptions).

1.2.4. Nonlinear properties in glassy polymers

There is an abundant literature on the nonlinear mechanics of polymer in their glassy state. While there is nearly no report on the nonlinear mechanics with the glass transition domain. We will thus describe the state of the art on nonlinear mechanics of polymers in their glassy state.

A typical stress-strain curve of a glassy polymer is plotted in **Figure 1.15**. For increasing strain, it exhibits an initial elastic region, followed by an anelastic one (nonlinear but recoverable deformation), a yielding, strain softening, and finally strain hardening at large strains before fracture.
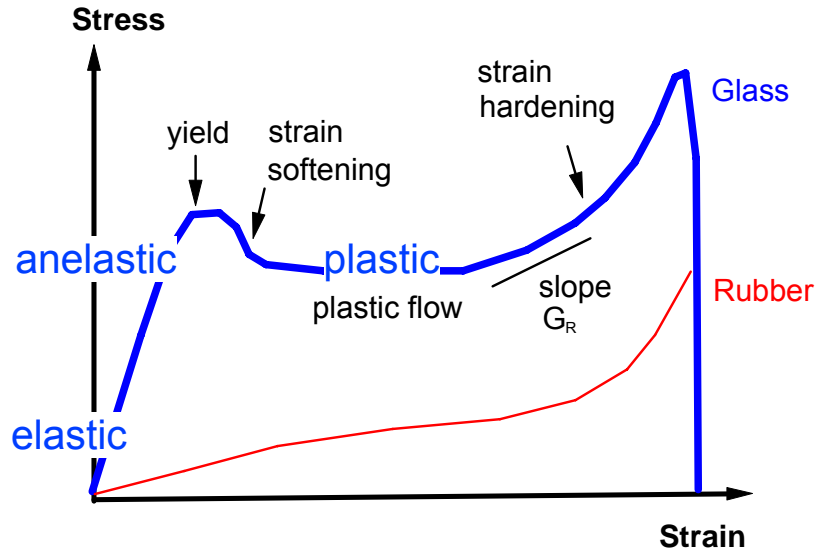
Figure 1.15. Schematic of a typical stress-strain curve of an amorphous glassy polymer.

Strain decomposition. Quinson and Perez [22] have suggested for glassy polymer the following strain decomposition:

$$\varepsilon = \varepsilon_{el} + \varepsilon_{an} + \varepsilon_{pl} \qquad \text{(eq 1.29)}$$

where the three terms of the right hand side represent respectively the elastic, anelastic and plastic contributions. In a point of view of the recovery time, the elastic strain recovers instantaneously, the anelastic one recovers in a certain time and the plastic one is nearly permanent at temperature far below T_g and can recover in a short time at T_g or above [23].

The evolution of these components as a function of strain is illustrated in **Figure 1.16**. It can be observed that ε_{an} and ε_{an} appear from the very beginning of the test and keeps growing until the yielding point and become stable. The plastic contribution ε_{pl} begins after the yielding point and grows continuously [22].
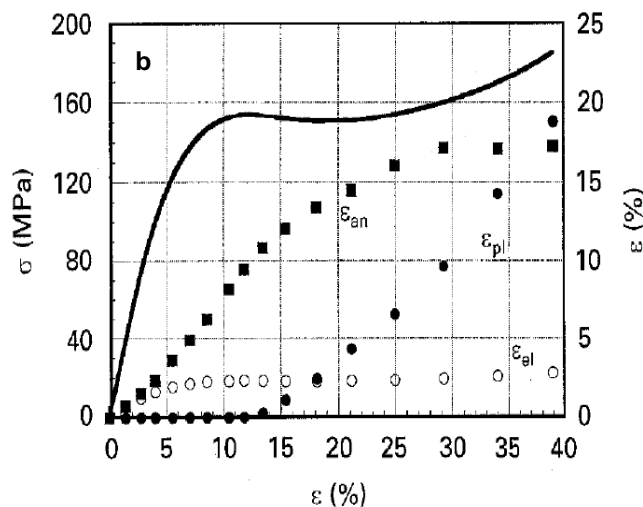
Figure 1.16. Decomposition of the strains into elastic, anelastic and plastic contributions. Figure by Quinson and Perez [22] illustrating a PMMA sample in compression at glassy state.

Energy changes during nonlinear deformation. Hasan and Boyce use differential scanning calorimetric measurements to study the microstructural evolution of different glassy polymers during non-elastic deformations [14]. They found that during yielding and strain softening there is a change of the thermodynamical state of the glass. This is obvious on DSC graph, where an enthalpy gain is observed for stretched samples. This energy gain erases the physical aging of the sample. The enthalpic overshoot that is characteristic to the physical aging disappears for stretched annealed samples.

Steady-state flow behaviors of annealed and quenched samples are identical, indicating that the effect of annealing can be totally erased after yielding and strain-softening. The yield stress is thus a signature of the structure of the glass at rest.
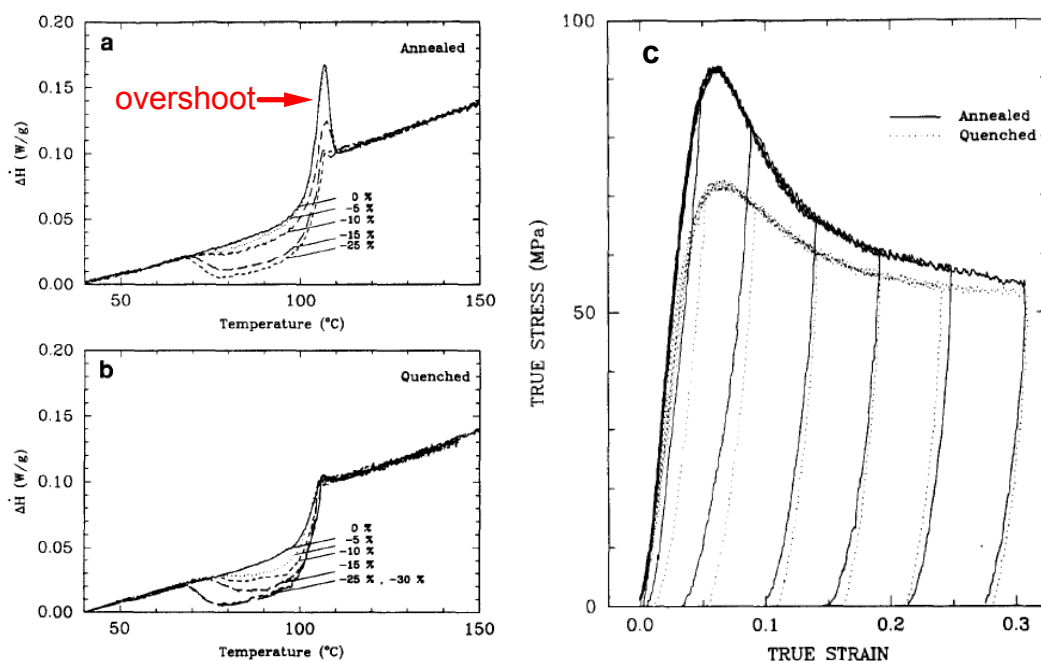
Figure 1.17. DSC scans at 10K/min of (a) annealed and (b) quenched PS sample at different strains in compression. (c) Stress-strain curves of annealed and quenched PS sample in compression at 296K and strain rate 0.001s^{-1}. Figure by Hasan and Boyce [23].

Plastic flow generates internal stress that stores a lot of energy. Using constant temperature deformation calorimetry technique [24–26], it is possible to follow the evolution of mechanical work, the heat of deformation and the internal energy storage during the deformation of the sample. It shows that a large amount of energy, up to about 50% of mechanical work, is irreversibly stored during cold-drawing. This energy can be recovered into heat only while heating the sample at temperatures above the plastic deformation temperature and T_g. This energy is likely due to internal stress, thus reveals also the strong heterogeneity of mechanical properties of glassy polymers in their nonlinear regime.

Strain hardening is commonly assumed to originate in the limit of extensibility of the chains in a glassy regime. Indeed the relation between stress and strain in this domain is

similar – up to a very different prefactor – to the Gaussian behavior of rubbers. It has resulted in many confusion in the literature that have been recently clarified by Robbins and collaborators [27–29]. In compression, and if localization phenomena like necking and crazing are absent, in extension, the strain hardening regime can be fit to a Gaussian strain hardening model derived from affine deformation entropic network models:

$$\sigma_{true} = \sigma_{flow} + G_R(\lambda^2 - \lambda^{-1})$$ (eq 1.30)

where σ_{flow} is the plastic flow stress, G_R is the strain hardening modulus, and $\lambda^2 - \lambda^{-1}$ is the same expression as the on describing the entropy reduction for ideal Gaussian chains (see section 1.2.2).

It is found that this expression fit well with experimental results and G_R is linearly proportional to the entanglement density ρ_e [30]. However, strain hardening of glassy polymers can not be attributed to entropic. In fact, simulations of Hoy and Robbins [27,28] and other experiments show that the hardening modules G_R of a glassy polymer is about 100 times larger than the corresponding rubbery modules. Moreover, instead of increasing linearly with T(K), as that is for entropic rubber elasticity, G_R decreases with T(K) [27,28,31,32]. All these evidences show that the origin of strain hardening in glassy polymer is enthalpy and not entropy. Indeed the strain hardening domain is still nowadays not described by any physical model.

Evolution of molecular mobility during deformation. Lee et al. [33], use an optical photo-bleaching technique and demonstrate that, during an uniaxial tensile creep test, in the strain softening regime until stable plastic flow, segmental mobility speeds up by a factor of 1000, and the distribution of relaxation times becomes narrower. In the strain hardening regime, segmental mobility decreases with strain. A strong correlation between molecular mobility and strain rate is found (see **Figure 1.18**).
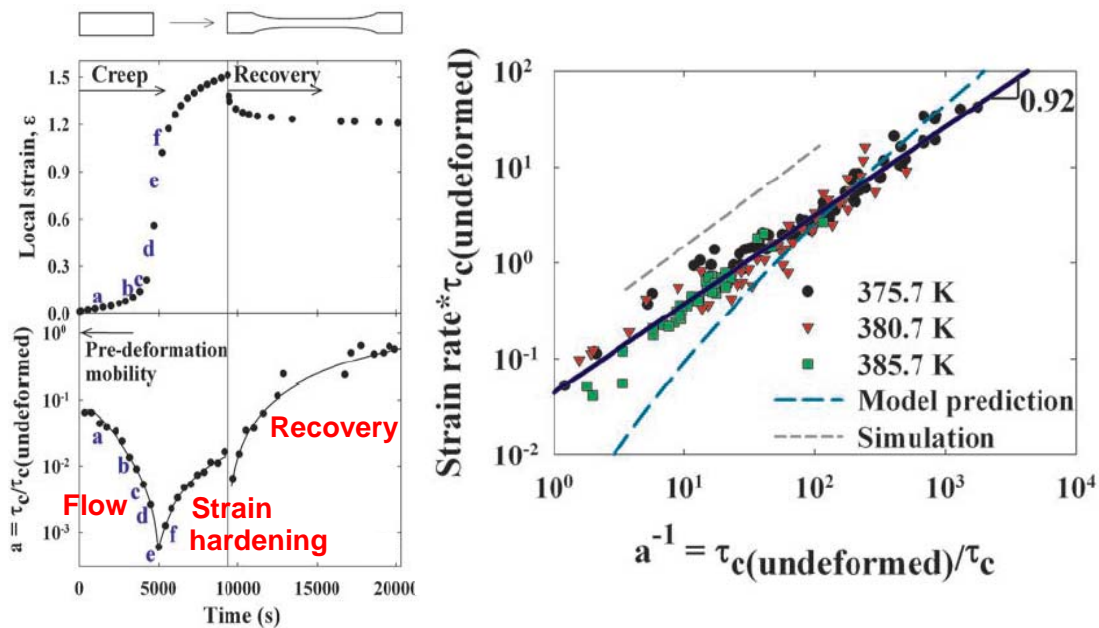
Figure 1.18. (a) Measurements of molecular mobility during deformation and recovery. (b) Relationship between strain rate and mobility. Figure by Lee et al. [33].

Molecular mobility seems to be proportional to strain rate. We will give theoretical interpretations of the plasticity in the following section.

1.2.5. Theoretical interpretations of plasticity

Eyring model. The phenomenological Eyring model is widely used to describe the yielding in glassy polymers. This model assumes that the activation energy for a particle to hop in the direction of the applied stress reduces linearly with the stress. The hopping time thus writes:

$$\tau_+ = \tau_0 \exp(\frac{E - \sigma V}{k_B T}) \qquad \text{(eq 1.31)}$$

where τ_+ is hopping time in the direction of applied stress, τ_0 is a constant time, E is the activation energy, V is an empirical activation volume. Similarly, the hopping time in the reverse direction is:

$$\tau_- = \tau_0 \exp(\frac{E + \sigma V}{k_B T}) \qquad \text{(eq 1.32)}$$
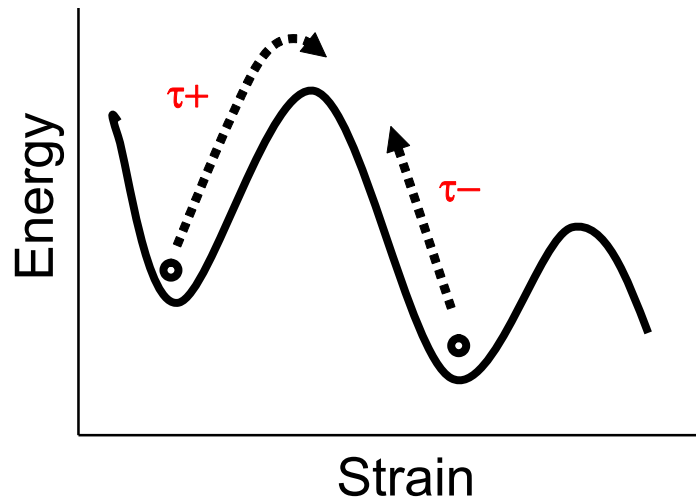
Figure 1.19. Schematic of the Eyring model, where the energy barrier is modified by the applied stress.

The strain rate can be expressed as:

$$\dot{\varepsilon} = \frac{1}{\tau_+} - \frac{1}{\tau_-} = \frac{1}{\tau_0} \exp(-\frac{E}{k_B T})[\exp(\frac{\sigma V}{k_B T}) - \exp(-\frac{\sigma V}{k_B T})] \qquad \text{(eq 1.33)}$$

The general form of Eyring model can thus be written as:

$$\dot{\varepsilon} = \frac{2}{\tau_0} \exp(-\frac{E}{k_B T}) \sinh(\frac{\sigma V}{k_B T}) \qquad \text{(eq 1.34)}$$

In the linear regime, we have $\tau_+ \approx \tau_- \approx \tau_0 \exp(\frac{E}{k_B T})$, the behavior is liquid-like. Since $sinhx \approx x$ in the linear regime, the strain rate is proportional to stress:

$$\dot{\varepsilon} = \sigma[\frac{2}{\tau_0}\exp(-\frac{E}{k_B T})\frac{V}{k_B T}]$$ (eq 1.35)

The viscosity is:

$$\eta = \frac{\tau_0}{2}\exp(\frac{E}{k_B T})\frac{k_B T}{V}$$ (eq 1.36)

we get the behavior of a viscous liquid where the viscosity follows an Arrhenius temperature dependence.

In the nonlinear regime, we have $\tau_+ << \tau_-$, hopping rate in the reverse direction of applied stress (τ_-) is negligible, and it gives:

$$\dot{\varepsilon} = \frac{1}{\tau_0}\exp(-\frac{E}{k_B T})\exp(\frac{\sigma V}{k_B T})$$ (eq 1.37)

The yield stress can be given by:

$$\sigma_y = \frac{E}{V} + \frac{k_B T}{V}\ln(\dot{\varepsilon}\tau_0)$$ (eq 1.38)

This model that predicts a linear dependence of yield stress on logarithmic strain rate is in practice used to estimate the activation volume V.

Conclusion of Eyring model: if the applied strain rate is smaller than the thermal hopping rate, the behavior is liquid-like. Otherwise, it is a plastic behavior.
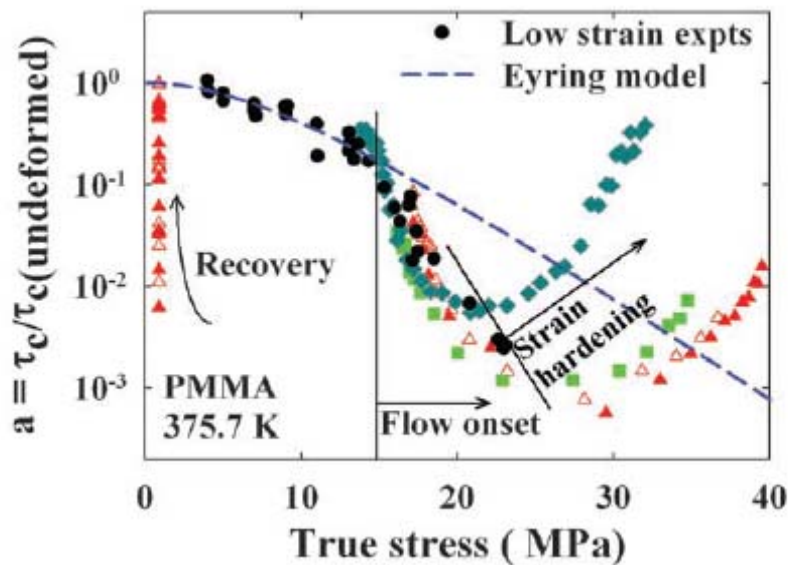
Figure 1.20. Molecular mobility vs. true stress and comparison with Eyring model. Figure by Lee et al. [33].

The Eyring model predicts that the segmental relaxation time τ is decreased by the applied stress σ according to:

$$\tau \propto \sigma / \sinh(\frac{\sigma V}{k_B T})$$ (eq 1.39)

Ediger et al. compared the molecular mobility with the prediction of Eyring model and found that the Eyring model works only in the low stress regime before yielding (see **Figure 1.20**). It works neither in the plastic flow regime nor in the strain hardening regime. These disagreements could be explained by the fact that spatially heterogeneous dynamics and polymer structure are not considered in the Eyring model. Indeed, it was found that the shape of the relaxation time distribution (correlated to β_{KWW} parameter) narrows significantly as the mobility increases in the plastic flow regime. Indicating that stresses are concentrated in slow dynamic regions and the dynamics in these slow regions are much more accelerated than in the fast regions [33].

Limitations of Eyring model

Indeed Eyring model is one of the rare models that provides physical description of the transition between liquid and plastic behavior. However, the Eyring model has these 3 main limitations:

1. Eyring model does not incorporate spatially heterogeneous dynamics. It would be more realistic to consider a distribution of activation energy $P(E)$ rather than a single value for E common to all regions. It should be noted that it's equivalent to consider the distribution of activation energy $P(E)$, or of activation volume $P(V)$ or of relaxation times $P(\tau)$. The importance of this structural disorder is for example discussed by the Soft Glassy Rheology (SGR) model of Sollich et al. [34].

2. It does not take into account the mechanical couplings of different domains. If one domain undergoes a plastic hop, it modifies the elastic field in the whole sample. Indeed, it is likely for instance that the local stresses are concentrated in slow dynamic domains. As a consequence one may expect that for instance the broadness of relaxation times distribution $P(\tau)$ changes during the deformation. Plasticity at glassy state has to be regarded as local structure rearrangements with a lot of internal stresses and internal energy storage. After cold-drawing, the internal stress is revealed by an exothermal as explained by Hasan and Boyce [23].

3. Lastly, the polymer structure, i.e. topological entanglements, should be considered, especially at large strain where strain hardening effect occurs. Indeed, for instance experiments and simulations [27,28,31]show that the hardening modules G_R of a glassy polymer is linearly proportional to the entanglement density ρ_e.
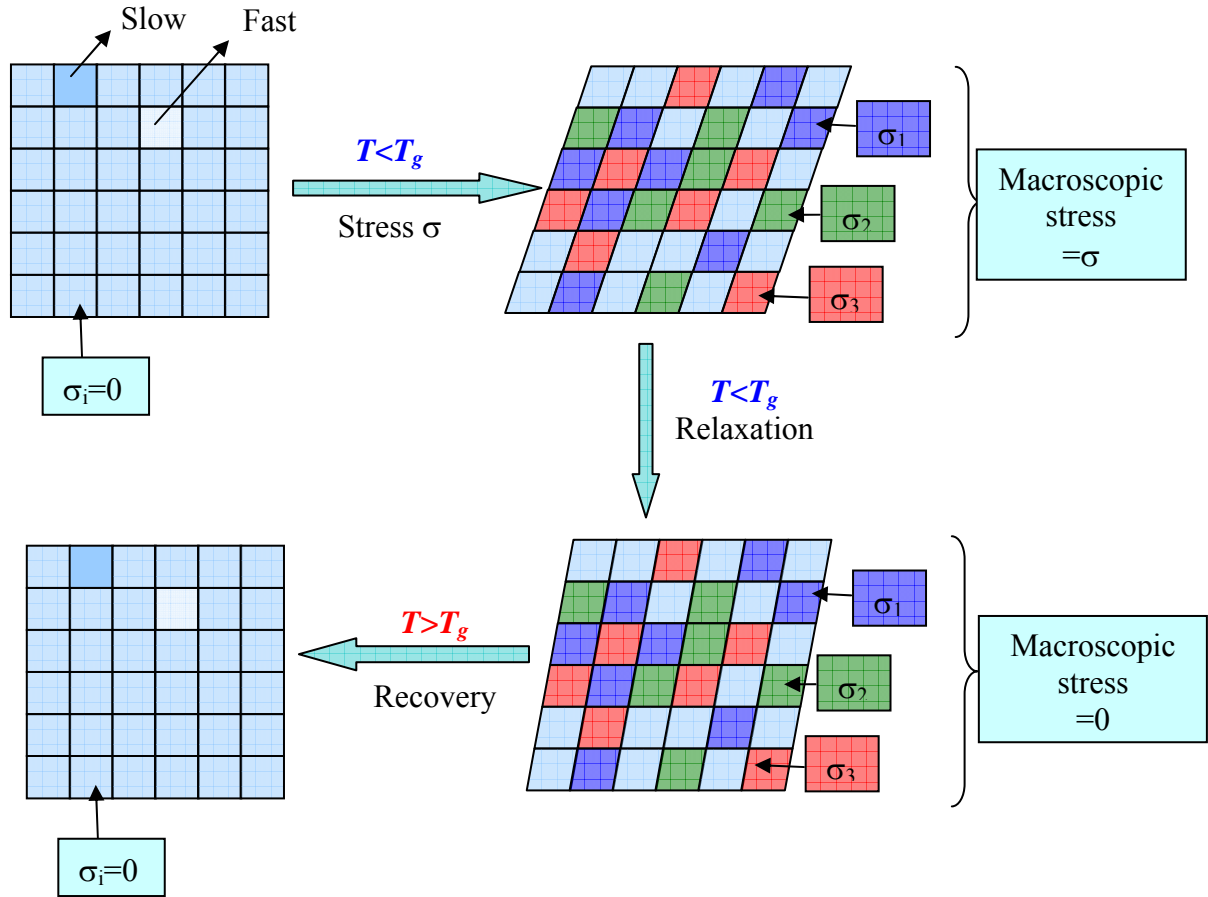
Figure 1.21. Schematic of local structure rearrangement and local energy storage: (a) the system is unstrained at glassy state with no internal stress but the dynamics are highly heterogeneous; (b) the system is strained with plastic deformations, (c) the system is relaxed at glassy state, with residual plastic deformation, with internal stresses and the macroscopic stress is zero, (d) the system is heated to T_g or above, internal stresses are released and the residual plastic deformation is recovered.

One qualitative description already incorporates ideas of the first two limitations, i.e. spatial heterogeneity and mechanical couplings, and give a qualitative description of the plasticity of polymer glasses is the Plastic Shear Transformation (PST) theory [35,36]. It claims that a glassy polymer is considered to have a distribution of activation energy barrier and the internal energy is stored through localized PST events. During the deformation, energy storage grows gradually through PST events, the locations of which are related to their local activation energies. Meanwhile, there are PST relaxation through conformationally excited coils (CEC), where the local strain is conserved, and local internal energy decreases, allowing creation of new PST sites. In the steady-state flow regime, the PST creation rate is equal to PST relaxation rate and the total internal energy storage is constant.

It is already stated that the distribution of activation energy barrier $P(E)$ is equivalent to the distribution of relaxation times $P(\tau)$. In order to further understand the non linear mechanical properties in the transition zone, it is very useful to study systems where $P(\tau)$ could be controlled and measured. Miscible polymer blends with great difference of T_g of each component are such systems that allow the control of the distribution of relaxation times $P(\tau)$.

1.3. Miscible polymer blends

Polymers are long chains with very small mixing entropy, and chemically different polymers are in general energetically immiscible. There exist, however, some polymer pairs that exhibit miscibility in a certain ranges of temperature and composition.

Blending is a powerful and convenient way to tune mechanical properties of materials. A great amount of effort has been made during the past 15 years in order to understand the effect of blending on the local dynamics in polymers. In fact, it has been shown that the local dynamics are extremely heterogeneous because the local composition of the blends exhibits spatial fluctuations. This dynamical heterogeneity provides to the miscible polymer blends a variety of interesting features including **broadening of glass transition**(see **Figure 1.22**) in all cases and in some cases a failure of time-temperature superposition (thermo-rheological complexity).
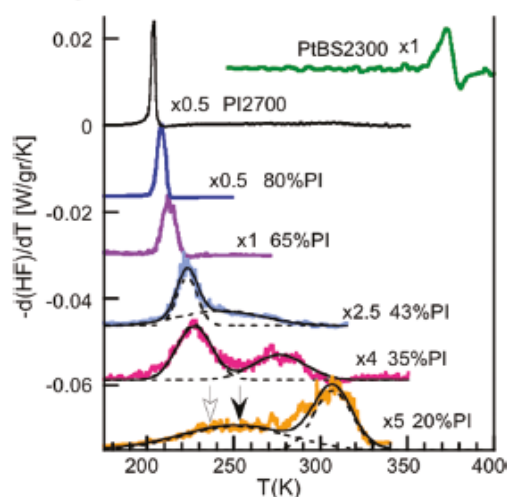
Figure 1.22. Temperature derivatives of heat flow for PI/PtBS blends [37] showing broadening of glass transition.

Some models have been developed to describe the broadening of the time relaxation spectrum from the microscopic structure. For this description, the chain connectivity has to be taken into account (self-concentration effect) [38], as well as thermally driven concentration fluctuations [39]. In these approaches, at the nanometric scale, a mixture of miscible polymers is considered as a random distribution of polymer domains exhibiting a wide distribution of relaxation times. In this frame, dielectric or DSC data measured on various miscible blends have been quantitatively described through detailed analysis of the dynamical heterogeneity [13,39–47].
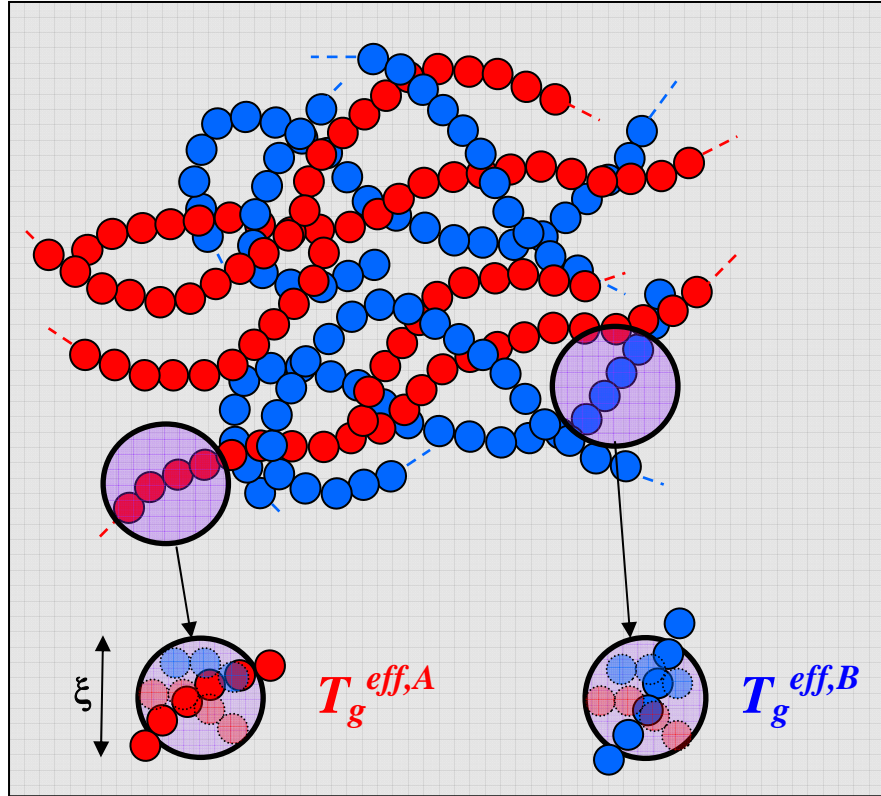
Figure 1.23. Schematic illustration of chain connectivity effect in miscible polymer blends composed of polymer chain A(red) and B(blue).

We will now give a brief review of these models that describe quantitatively the broadening of the glass transition in miscible polymer blends.

Self-concentration model

Since a monomer of component A (the same for component B) is connected to other monomers A of the same chain, the local concentration around the considered segment is richer in A. This effect is called "self-concentration", as illustrated in **Figure 1.23**. Lodge and McLeish [38] is accounted in a simple theoretical model assuming that the local effective concentration ϕ_{eff} is a contribution of both the self-concentration ϕ_{self} and the environment composition - the macroscopic one Φ:

$$\phi_{eff} = \phi_{self} + (1 - \phi_{self}) \times \Phi \qquad \text{(eq 1.40)}$$

where ϕ_{self} is the volume fraction of a Kuhn segment of polymer A in a volume $V \approx l_k^3$ and l_k is the Kuhn length. Accordingly, the effective glass transition temperature T_g^{eff} in a blend depends on ϕ_{eff} and is fixed by the empirical Fox equation:

$$\frac{1}{T_g^{eff,A}} = \frac{\phi_{eff,A}}{T_g^A} + \frac{1 - \phi_{eff,A}}{T_g^B} \qquad \text{(eq 1.41)}$$

Lodge-McLeish model accounts for the existence of two different mean relaxation times observed in some experiments, and each of them corresponds to the dynamics of one component modified by blending (see the DSC derivative curves of **Figure 1.22**).

This model is based on two assumptions: first, the relevant length scale is of the order of the Kuhn length $\xi=l_k$; secondly, the environment composition is equal to the macroscopic one, thus neglecting the thermodynamical concentration fluctuations.

Concentration fluctuations model

A few years later, another model, based on the thermally driven concentration fluctuations [13,39] was introduced. The idea is that life times of the local concentration fluctuations are much longer than the segmental relaxation time of the blend near in the glass transition zone. Consequently, the sample can be divided into a number of subcells of volume V, and each of them has a local composition ϕ_i and a corresponding local glass transition temperature T_g^i. The relaxation function of a given subcell is equal to a corresponding pure component. A distribution of local composition $P(\phi)$ or local relaxation times $P(\tau)$ or local glass transition temperature $P(T_g)$ is introduced. For instance, Shenogin et al. assume a standard Gaussian form of $P(\phi)$ (for component A):

$$P(\phi_{eff}^A) = \frac{1}{\sqrt{2\pi\left\langle \delta\phi_{eff,A}^{\;2}\right\rangle}} \exp\left\{ -\frac{(\phi_{eff}^A - \overline{\phi_{eff}^A})^2}{2\left\langle \delta\phi_{eff,A}^{\;2}\right\rangle} \right\}$$ (eq 1.42)

The relaxation function of the blend is a superposition of simple relaxation functions with different relaxation times [42], and can be expressed as:

$$f_{blend}(\omega) = \int f_{pure}(\omega,\tau)P(\tau)d\tau$$ (eq 1.43)

This can describe the broadening of the relaxation function as temperature approaches T_g. This describes well the dielectric signal for instance. But we will see that the linear superposition clearly fails in the case of viscoelastic properties.

Confinement effects

However, other neutron scattering studies evidence that the simple assumption of the Fox law fails when applied at the nanometric scale. Colmenero and coworkers [42] found that for miscible polymer blends of components with very different T_g, the dynamics of the fast component seems to be confined within the frozen chains of the slow component. Consequently, the motion of the fast component becomes localized with low degree of cooperatives, and exhibits Arrhenius-like temperature dependence at low temperature. However this effect seems not drastic as the Fox law approximation is able to account for the dielectric properties of miscible blends and also as we will show in chapter 4, to the viscoelastic properties, at least in first approximation.

Length scale ξ in miscible polymer blends

Plastic events, like the one introduced by Eyring model have to occur at a given length scale. The relevant volume V corresponds to a cooperative volume of the glass transition of the order of the activation volume. In the concentration fluctuation model, the distribution function $P(\phi)$ is usually assumed to be Gaussian with a variance $<(\delta\phi)^2>$, which is inversely proportional to the volume V, through the static structure factor $S(Q)$ and the mean field random phase approximation (RPA) method. Some studies use the radius R_c of a spherical volume V as a fitting parameter [39,45]. In this frame, the length scale $\xi=2R_c$ is found comparable to the Kuhn length b as assumed in the self-concentration model, i.e. ~1 nm. It should also be noted that for components with very different structures or flexibilities, it is possible to observe two different length scales for each of the component considered [48].

A list of blend systems in literature

Segmental dynamics or α-relaxation is the most relevant property for studying blend dynamics. In order to study it in a broad dynamic range, different techniques are combined, including: dielectric spectroscopy (DS), differential scanning calorimetry (DSC), mechanical spectroscopy (MS), nuclear magnetic resonance (NMR), quasielastic neutron scattering (QENS)…**Table 1.1** presents a selection of miscible blend systems studied by different techniques, with corresponding references.

Table 1.1. Blend systems studied by different techniques in literature.

Polymer A	Polymer B	Reference				
		DS	DSC	MS	NMR	QENS
PI	PVE	[39,48,49]	[50,51]	[46,52]	[51]	[53]
PI	PtBS	[37]	[54]			
PVME	PS	[39,55]			[55]	[55,56]
PVME	PoCS	[13]				
PMPS	PS	[57]				
PBO	PVE	[39]				
PMMA	SAN		[58]	[43]		
PMMA	PEO	[57]				

It should be noted that dielectric data of various miscible blends have been quantitatively described through detailed analysis of the dynamical heterogeneity. On the contrary, there are in the literature only few results that quantitatively related the structure and the dynamic of the system at the scale of dynamic fluctuations to the macroscopic viscoelastic properties of miscible polymer blends, which are in general purely descriptive.

Plasticity of polymer blends

Despite all these studies on different polymer blends and with different techniques, there are scarce results in literature not only about the linear and non linear mechanical properties, but also about the nonlinear mechanical properties of polymer blends in the glass transition zone, in-between rubbery state and glassy state.

One example is the study on plasticity of PS/PPO polymer blends [59]. At low temperature, PS behaves brittle and PPO behaves ductile. It shows that the yield stress is significantly changed by blending. By investigating the strain rate dependence and comparing with Eyring model, it is claimed that, the activation volume increases by increasing PPO content, indicating a more cooperative nature of the plastic deformation, and a brittle to ductile transition.

1.4. Problematics

As it is already stated above, the Eyring model leave three questions that are essentially related to the viscoelasticity and the plasticity of glassy polymers and needed to be further studied:
- the distribution of relaxation times $P(\tau)$,
- the mechanical couplings of different domains,
- the effect of polymer topological structure on large deformation.

This thesis tries to answer the first two questions, by using systems of miscible polymer blends that allow us controlling the distribution of relaxation times $P(\tau)$. Detailed investigations of the dynamic behavior of miscible polymer blends, especially their mechanical properties are presented.
- Firstly we measure the length scale ξ and the distribution of relaxation times $P(\tau)$ in different blends. We give quantitative relations between $P(\tau)$ and experimental data of calorimetry, rheology, and dielectric measurements (chapter 2, 3, 4).
- Then we study the nonlinear mechanical properties in the glass transition zone by both simple extension test and cyclic shear test (chapter 5).

This thesis reports our work on two regimes:

Linear regime

According to different models of miscible polymer blend presented in the previous section and the physical interpretation of the glasses by Ediger, miscible polymer blend can be regarded as a highly heterogeneous system, with a very broad glass transition zone. This broadening effect can be characterized by a broad distribution of relaxation times. How to characterize this distribution? Is there a time-temperature superposition for linear mechanical properties? How to predict the linear mechanical properties of a polymer blend from that of pure polymers?

In chapter 2 and 3, we present experimental procedures and results of miscible polymer blends of polybutadiene (PB) and styrene butadiene rubber (SBR), and show the effect of broad glass transition on dynamical properties by different techniques: calorimetry, rheology, and dielectric measurements.

In chapter 4, we probe the distribution of glass transition temperature (T_g) of miscible polymer blends with calorimetric data, with or without aging. Using the self-consistent averaging method inspired by the Olroyd−Palierne model, we predict quantitatively, with no adjustable parameter, the viscoelastic spectrum of our blends from the T_g distribution obtained by calorimetry. This quantitative prediction confirms thus the assumption that mechanically a blend can be considered as an ensemble of domains, each of which have a different glass transition temperature.

Non linear regime

Is there a time-temperature superposition for nonlinear mechanical properties? What controls the transition from rubber elasticity to polymer glass plasticity? With the coexistence

of glassy zones and rubbery zones in polymer blends, what is the behavior of the macroscopic strain softening and strain hardening and the relationship with their microstructures?

In chapter 5, we will analyze the mechanical properties of polymer blends at large deformation and find that the appearance of plasticity correlates to the percolation of glassy domains.
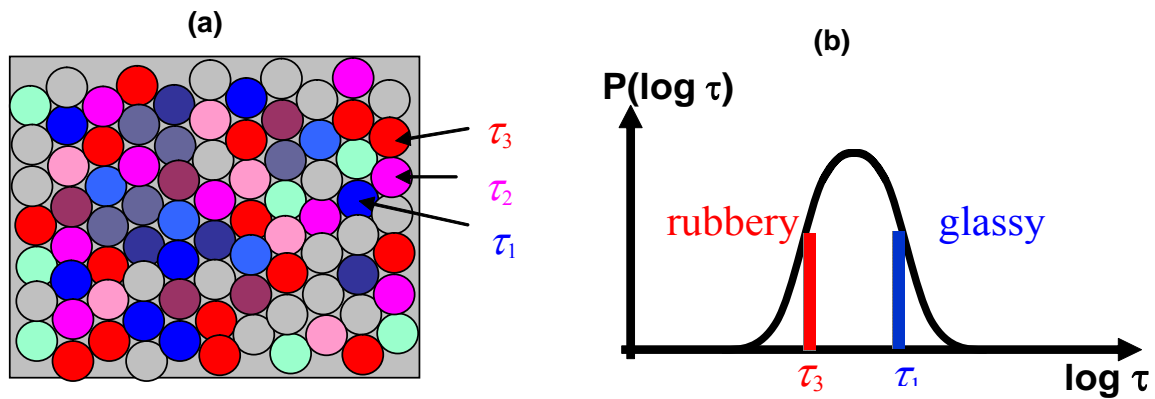
Figure 1.24. Schematic of a polymer blend: heterogeneous systems with a broad distribution of relaxation times. Glassy zones and rubbery zones can coexist. We will in this manuscript try to answer what are the consequences of this coexistence.

2.   Materials and methods
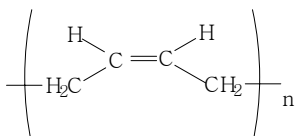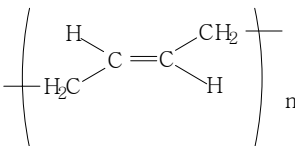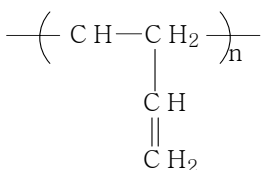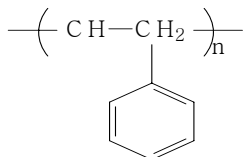
2.1. PB/SBR sample preparation

We study blends of polybutadiene (PB) and styrene-butadiene random copolymer chains (SBR) provided by Michelin. The PB chains contain 93% *cis*-1,4-PB, 3% *trans*-1,4-PB, and 4% 1,2-PB, with $T_g^{PB} \approx -100°C$. The SBR chains are composed of 16% *cis*-1,4-PB, 16% *trans*-1,4-PB, 43% 1,2-PB, and 25% of styrene, with $T_g^{SBR} \approx -20°C$. These two polymers are miscible in all proportions for temperature below 160°C. .

2.1.1. Structure

The chemical structures of different components and their corresponding T_g are presented in the following **Table 2.1**. It should be noted that *cis*-1,4-PB chains have a very regular structure and crystallizes easily. This is also the case of the PB chains used in this study due to their large content of *cis*-1,4-PB. However, their crystallization can be avoided by cross-linking. In this work, we have carefully checked that the cross-linking changes neither DSC nor rheological measurements in the glass transition domain, except a shift of T_g position of few degrees.

Table 2.1. Chemical structures of different components and their corresponding T_g

	Chemical Structures	T_g (°C)
cis-**1,4-PB**		-108
trans-**1,4-PB**		-92
1,2-PB		10
PS		100

2.1.2. Blend preparation

Blends with various concentrations and an appropriate concentration of crosslinkers were prepared either by solvent mixing or by mechanical mixing processes.

Solvent mixing. Blends of PB and SBR chains are prepared by dissolving the polymers in a mutual solvent, i.e. chloroform solution. Crosslinking agents were added directly in the polymer blend solution. Their concentration was fixed to 1.2 per hundred rubbers (PCR) of sulfur and 1.9 PCR of *N-cyclohexyl-2-benzothiazyl sulfenamide* (CBS) accelerators. The solvent is first evaporated and the polymer blends are then dried under vacuum at 60°C during 24 hours. The crosslinking reaction is done at 150°C during 3 hours. The advantage of solvent mixing is that there is an intimate mixing of both polymer chains in the blend.

Mechanical melt mixing. The PB and SBR polymers are pre-mixed and fed into an internal mixer Thermo Haake. The blending process was carried out for 5 minutes with a mixing speed of 50 rotations per minute at an initial temperature of 50°C (far above the T_g of both components). During the blending process, large amplitude shear deformation is applied to the blends in order to have an intimate mixing. Temperature of the polymer melt could increase up to 80°C due to conversion of a part of the mechanical work into heat. Raw polymer materials were added in the internal mixer just when the machine started. Then 1.5 PCR of zinc oxide (ZnO), 2 PCR of stearic acid and 3 PCR of rubber antioxidant *N(1,3-dimethyl-butyl)-N'-phenyl-P-phenylenediamine* (6PPD) were added in the internal mixer 1 minute after the blending process started. These ingredients were allowed to mix for another 3 minutes before crosslinking agents of 1.2 PCR of sulfur, 1.9 PCR of accelerator CBS were added into the internal mixer. The machine continue running for 1 minute. Next, the mixture was removed from the internal mixer and subsequently rolled using a hot roll mill at 50°C to assure an intimate mixing. Curing and crosslinking reaction are done at 150°C during 20 minutes for PB, 30 minutes for PB50%/SBR50%, and 80 minutes for SBR. Polymers have different cure times because their vulcanization rates are different. The optimum cure times are determined from rheological measurements showing the evolution of the torque during the vulcanization process [60]. The advantage of mechanical mixing is that it is easier to produce a large quantity and the crosslinking agents are homogeneously dispersed into the polymer blend.

2.1.3. Gluing to metal holders

All the mechanical measurements presented in this word are done with samples glued to metallic holders. The gluing could be done from pre-cured samples using the "Cyberbond 2240" adhesive, or for non pre-cured sample using the "Chemosil" adhesive.

"Cyberbond 2240" adhesive is used to bond cured elastomer compounds to metal substrates. The metal surfaces are cleaned first by grinding sandpaper, and then by ethanol solvent. Then the sample is glued onto the metal surfaces applying a force (~10N) during 1 minute. The glued sample is then dried at room temperature during 24 hours. The glued samples are in fact larger than the desired final size, and the additional parts are carefully cut off along the metal borders using a sharp cutter blade. The final "cut-off" process avoids the

additional adhesive that could have been flowed to the sample borders. A good rubber-metal bond is thus obtained for mechanical measurements in the nonlinear regime performed over a large temperature range.

"Chemosil" adhesive is used to bond elastomer compounds to metal substrates during the sample vulcanization. After a thorough cleaning of metal surfaces (first by grinding sandpaper, and then by ethanol solvent), the adhesive is applied by two steps: first a primer adhesive (Chemosil 211) is applied to the metal surfaces. After 20 minutes of drying at room temperature, a second coat (bonding agent Chemosil 411) is applied to the metal surfaces, followed by another 20 minutes' drying at room temperature. Afterwards, the metal holders and uncured samples are placed in a mold that determines the geometry of samples. Metal – polymer bonding occurs during the vulcanization process of the rubber at 150°C.

2.2. *Experimental techniques and sample geometries*

DSC measurements were conducted with a TA Instruments Co. 2920 DSC, with sample weights of 10 mg or less. Calorimetric properties were measured between -140°C and 40°C with or without aging process.
- *DSC measurements on un-aged samples.* For all experiments, the samples are kept at 40°C during 15 minutes in order to erase their thermal histories. Then the sample is cooled towards -140°C applying a temperature rate of 10K/min. After isotherm of 15 minutes, the sample is heated at 10K/min up to 40°C (see process S2 of **Figure 2.1**).
- *DSC measurements on aged samples.* We applied the same procedure used for un-aged samples. But we introduce in the cooling step an isotherm of duration t_a at temperature T_a. We compare then the response of the aged sample (S1) to the one immediately measured on the same sample without applying an aging step (S2). This procedure eliminates errors due to sample-to-sample variation, differences in instrumental calibration and differences in location of the sample in the DSC cell. We get a good superposition of the baselines of two curves S1 and S2 in below and above the glass transition domain.
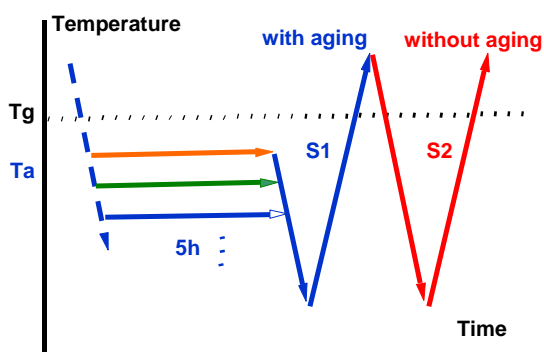

Figure 2.1. DSC measurement procedures with aging: cooling at 10 K/min from equilibrium, annealing of 5 h at different T_a, and heating scans at 10 K/min (S1), followed by a second cooling-heating scan without annealing (S2).

Dielectric measurements are performed over a broad frequency range (10^{-2} Hz$<f<10^7$ Hz) in a temperature range of about -150°C$<T<$30°C using BDS-NOVOCONTROL system. The temperature is controlled by a nitrogen jet and a temperature controller. Samples are thin films of about 0.3mm thick and 40mm in diameter.

Rheology. The linear viscoelastic properties are measured with an Anton Paar Physica MCR 501 rheometer using plate-plate geometry as illustrated in Figure 2.2(a). The samples are cylinders of 8mm in diameter and 2mm thick. The complex shear modulus have been measured in the 10^{-2} to 50 Hz frequency range, for various temperature from T_g-20°C to T_g+60°C.

Simple extension measurements are done with MTS 830 Material Test System. Sample geometry is illustrated in Figure 2.2(b). The samples are cylinders of 10mm in diameter and 10mm in thickness. The gluing is done using the "Chemosil" adhesive. Measurements are done in a temperature range from T_g-10°C to T_g+60°C, and with 4 different true strain rates: $\dot{\varepsilon}_1$=0.0083/s, $\dot{\varepsilon}_2$=0.083/s, $\dot{\varepsilon}_3$=0.83/s and $\dot{\varepsilon}_4$=8.3/s.

For measurements performed in the glass transition domain, the sample is kept at room temperature during 15 minutes, then temperature is decreased at 10K/min and an isotherm of 20 minutes duration is applied at the temperature of the mechanical test.

The extension ratio $\lambda = l / l_0$ goes up to 2. Prior to the extension measurement, the sample is slightly compressed to a ratio of $\lambda = l / l_0$ of 0.97. This experimental procedure was taken as a precaution in order to have no transient regime from the extension machine disturbing the data measured at the very early beginning of the extension. Forces and displacements are measured by the MTS system. The temperature evolution during the test is also simultaneously measured by an infrared camera.

Nonlinear cyclic shear measurements are done with MTS 830 and 831 Material Test System. The sample geometry is illustrated in Figure 2.2(c). The samples are cylinders of 10mm in diameter and 2mm in thickness. The gluing is done with "Cyberbond 2240" adhesive. Measurements are done over a temperature range from T_g-10°C to T_g+60°C. We apply a sinusoidal strain $\gamma = \gamma_0 \sin(\omega t)$ of different amplitudes (γ_0=1%, 2%, 5%, 10%, 20%) and different frequencies ($f = \omega / 2\pi$ =0.01Hz, 0.1Hz, 1Hz, 10Hz). The temperature evolution during the test is measured by an infrared camera.

For measurements performed in the glass transition domain, the sample is kept at room temperature during 15 minutes, then temperature is decreased at 10K/min and an isotherm of 20 minutes duration is applied at the temperature of the mechanical test.

For a given temperature and a given frequency, measurements are performed at various strain amplitude on the same sample. We started from the lowest amplitude (1%) towards the highest (around 20%). For each strain amplitude, 5 cycles are applied for 0.01Hz, and 10 cycles for other frequencies. Between two consecutive strain amplitude series, the sample is maintained at zero shear strain during a time around 5 minutes if self-heating $\Delta T<$1°C and 20 minutes if $\Delta T>$1°C.
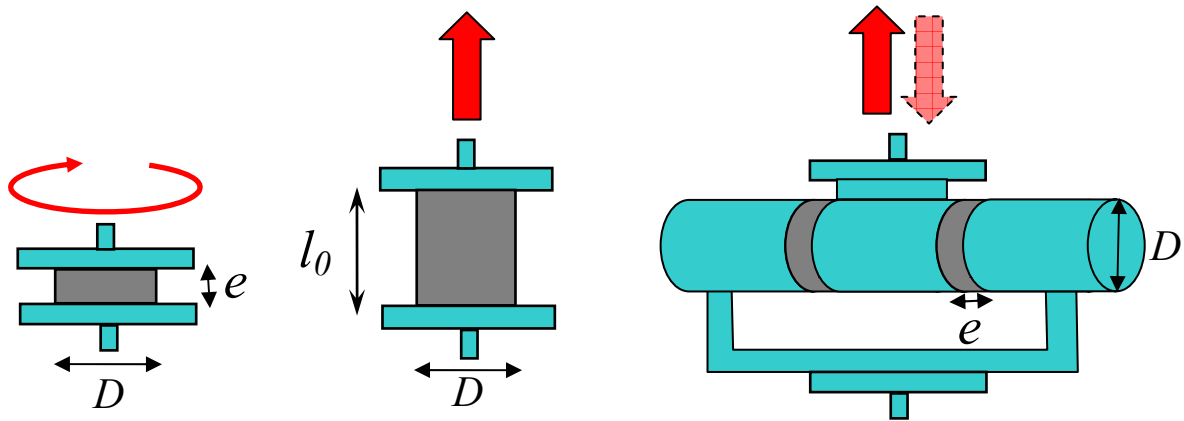
Figure 2.2. Sample geometries for: (a) rheology, D=8mm, e=2mm; (b) simple extension, D=10mm, l0=10mm, (c) cyclic shear, D=10mm, e=2mm.

Infrared camera. We measure the temperature evolution in nonlinear simple extension and cyclic shear mechanical tests with a FLIR SC7300L infrared camera. The focal length of the optical lens is 100mm. The main specifications of the camera we used are: temperature accuracy ±0.02K, thermal resolution 0.01K, frame rate of 256 images/second, spectral response of 7.7-9.3μm, pitch 30μm×30μm and pixels of 320×256. The principle of thermo-graphic measurement and the calibration of our infrared camera are presented in Annex A.

3. Measurements of linear properties of the PB/SBR blends in the glass transition zone

3.1. Introduction

In a polymer blend system, local dynamics are highly heterogeneous. This dynamic heterogeneity strongly modifies physical properties of the system, compared to that of the pure polymers.

The broadening of the glass transition region is one of the most spectacular aspects of dynamic heterogeneity of polymer blends. This broadening can be observed by different techniques: DSC, rheology, most notably dielectric spectroscopy. Meanwhile, the effect of the dynamic heterogeneity on the width of the glass transition depends on the length scale of the motions involved. Moreover, the macroscopic behavior is the result of the average of local responses in the blend that varies according to the physical properties observed. Indeed, by comparing results obtained from different techniques, we will observe that they are strongly related one to another.

The first step of this work is to characterize the dynamic heterogeneities existing in the PB/SBR blend system. This is the object of this chapter. We therefore measured different physical properties: calorimetric properties from DSC, physical aging properties from DSC, rheological and dielectric spectroscopy. All the experimental data are reported in this chapter 3. All the properties presented here are measured in the linear regime. The non linear mechanical properties will be presented and discussed in chapter 5.

Once the linear response is well characterized by various techniques, the next step will be to identify the relaxation time distribution in our PB/SBR blend system associated to each of these measurements. We will thus compare these distributions, each of them being related to certain length scales. This will be done in the chapter 4.

3.2. Overview of the samples and experimental techniques

Table 3.1 is a list of all the measurements that we have done. Depending on the techniques, we did have to use either crosslinked or non crosslinked samples.

Table 3.1. A list of measurements done with different techniques and different sample types.

PB/SBR	DSC (no aging)	DSC (aging)	Rheology	MTS	Dielectric
Type A	√		√		√
Type B	√	√	√		
Type C			√	√	

A=solvent mixing, non cross-linked
B=solvent mixing, cross-linked
C=mechanical mixing, cross-linked

We have already mentioned in chapter 2 that the PB chains we used in this work can crystallize due to their high content of *cis*-1,4-PB. For this reason, most of characterizations were performed on crosslinked samples – that avoid crystallization, except for dielectric measurements. Indeed, in this case, crosslinking agents introduce additional dielectric signals of large amplitude, which strongly modify the dielectric data measured on our polymer systems, and which is very difficult to subtract. In order to get the precise dielectric response of our polymer blends, we choose to perform it only with non-crosslinked polymer samples.

We did DSC and rheological measurements on both crosslinked and non-crosslinked blends – both of them prepared by solvent mixing procedure. We have thus identified the effect of crosslinking on the structural properties in the PB/SBR blends. We verify first that crosslinking avoids crystallization of PB chains. Crosslinking induces also a slight shift of the glass transition temperature towards higher ones.

Lastly, the nonlinear mechanical properties of the PB/SBR blends will be performed on crosslinked samples prepared with a mechanical mixing procedure, which allows obtaining easily large amounts of samples. Obviously we have also characterized these samples in the linear regime.

3.3. *Calorimetric properties of PB/SBR blends*

We first present the characterization of the glass transition of our PB/SBR blends by traditional DSC measurement, i.e. simple temperature ramp. Then we will investigate the physical aging property, using more complex temperature history.

3.3.1. Position and width of the glass transition

Figure 3.1(a) presents the differential calorimetric scanning response measured with a TA Instruments Co. 2920 DSC setup at a heating rate of 10 K/min for blends having different macroscopic PB volume fraction Φ. All the DSC curves have been shifted vertically for a better visualization of the results. We also plotted the temperature derivative of the heat flow dHF/dT as a function of temperature (see **Figure 3.1**(b)).

Figure 3.1. (a) Experimental DSC curves for different crosslinked blends at dT/dt=10K/min. (b) Temperature derivatives of the heat flow as a function of temperature. All the curves are shifted vertically for clarity.

In agreement with the observations reported in literature from other polymer blends, the glass transition of our PB/SBR blends is significantly broader than the one of the two homopolymers. We observe a single peak in Figure 3.1(b), indicating that our systems have good miscibility. We observe in addition two kinds of asymmetries of the broadening as mentioned in below.
- Asymmetry on concentration: the width of the glass transition of the blend containing 25% of PB is larger than the one measured on the PB75% blend.
- Asymmetry on temperature: for a given blend, the broadening is more obvious on one side than the other side. For example, the derivative curve of PB25% has a long tail in the low temperature side, while that of PB75 is in the high temperature side.

The DSC macroscopic T_g of a polymer is usually defined as the maximum position of $\left| dHF/dT \right|$, i.e. the inflection point where heat flow change most rapidly. This is a simple and reliable method for homopolymers. However, due to the dissymmetric form of the $\left| dHF/dT \right|$ curves, especially for blends, a more proper value is in fact an average one.

Indeed, an approximation of T_g distribution $P(T_g)$ can be simply extracted from the temperature derivative of the heat flow curve, using:

$$P(T_g) \cong P_{deriv}(T_g) = \frac{dHF(T)}{dT}$$ (eq 3.1)

And the DSC macroscopic T_g of a polymer can be deduced from the following average:

$$\langle T_g \rangle = \int T_g P_{deriv}(T_g) dT_g$$ (eq 3.2)
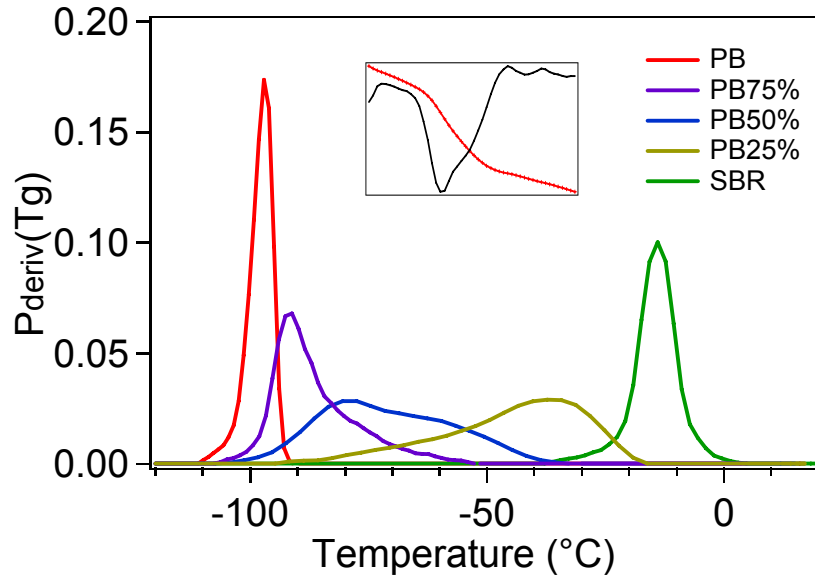
Figure 3.2. T_g distributions $P(T_g)$ by derivative method. The inset is an example of the temperature derivative of the heat flow curve of PB50%.

Figure 3.2 shows the T_g distributions $P(T_g)$ by derivative method. **Table 3.2** gives the macroscopic T_g values determined by the above equation, and the width of glass transition region determined at the half-height of $P_{deriv}(T_g)$. The widths of T_g in blends are indeed more than two times broader than that of homopolymers.

Table 3.2. Macroscopic T_g values and the width of glass transition region for different PB/SBR blends in crosslinked samples.

	$<T_g>$ (°C)	ΔT_g(°C)
PB	-98	5
PB75%	-86	12
PB50%	-71	36
PB25%	-47	30
SBR	-14	10

3.3.2. Influences of the crosslinking

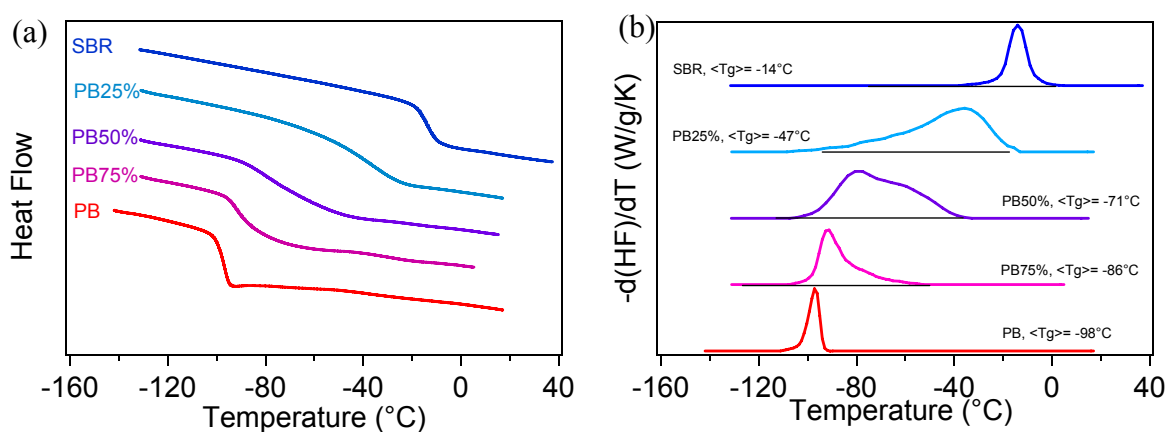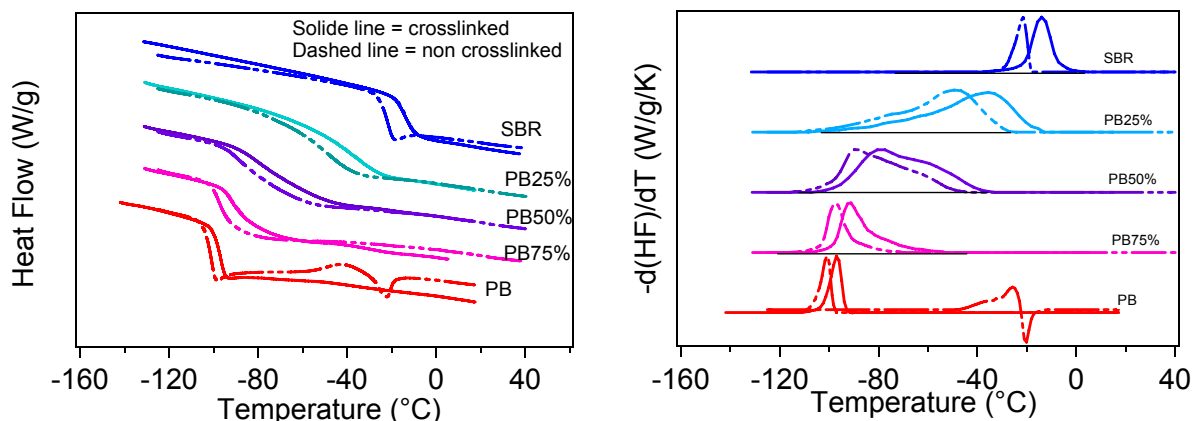**Figure 3.3**. Comparison of DSC measurements of the blends with or without cross-linking. (a) Experimental DSC curves for different crosslinked blends at dT/dt=10K/min. (b) Temperature derivatives of the heat flow as a function of temperature. All the curves are shifted vertically for clarity. Solid lines are crosslinked samples, and dashed lines are non-crosslinked samples.

The crystallization of PB chains is visible from the endothermic peak of non crosslinked PB from about -40°C to -20°C, and is avoided in crosslinked samples (see **Figure 3.3**). In addition, crosslinking induces a slight shift of the glass transition temperature towards higher ones. But the form and the width of T_g distribution are not changed by crosslinking (see **Table 3.3**).

Table 3.3. Comparison of macroscopic T_g values and the width of glass transition region for different PB/SBR blends in crosslinked and non-crosslinked samples.

DSC	Non-crosslinked		Crosslinked	
	$<Tg>$ (°C)	ΔTg(°C)	$<Tg>$°C)	ΔTg(°C)
PB	-102	5	-98	5
PB75%	-95	10	-86	12
PB50%	-80	35	-71	36
PB25%	-58	30	-47	30
SBR	-23	7	-14	10

3.3.3. Physical aging

Physical aging is known to be strongly controlled by the distribution of relaxation times in a glassy system. It appears fruitful to measure the structural evolution of our PB/SBR blends due to physical aging. This could be a new way to probe the relaxation time distribution in polymer blends.

The origin of the physical aging is already described in chapter 1.1.1 and illustrated schematically in **Figure 1.2**, where the initial enthalpy at state A is achieved reproducibly by cooling at a controlled rate from equilibrium state C at temperature far above T_g. On aging at temperature T_a, the enthalpy reduces to a lower value after an annealing time t_a. The difference in enthalpy between A and B, i.e. the enthalpy lost during aging, can be found from the DSC curves as the difference in the areas under these curves, see **Figure 3.4**(b).

Here we choose to anneal the sample at various temperatures. The procedure is illustrated in **Figure 3.4**(a). The first scan S1 includes an annealing step of 5 h at different annealing temperature T_a.
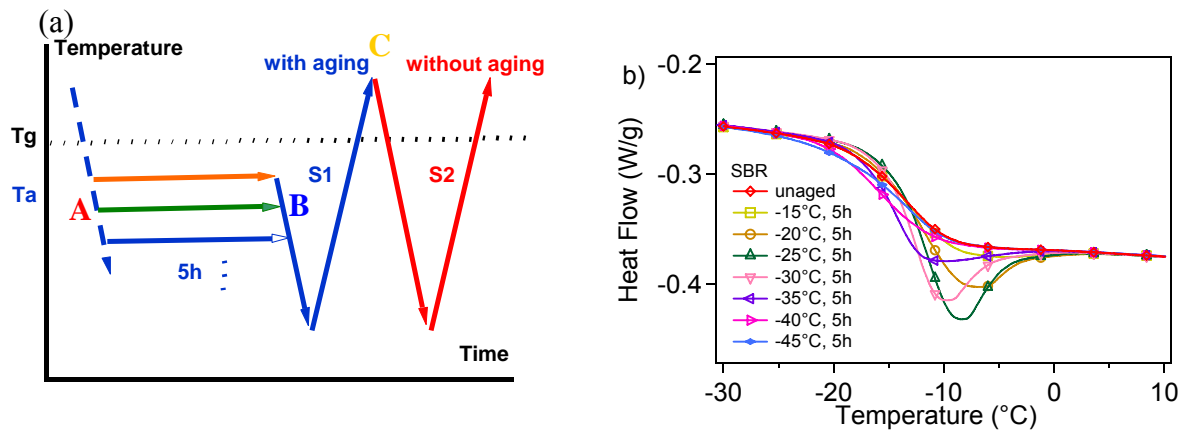
Figure 3.4. (a) The main characteristics of the physical aging procedure are: cooling rate at 10K/min from 40°C, annealing during a time t_a (=5 hours in this case) at different temperature T_a, and further cooling at 10K/min towards -140°C. After isotherm of 15 minutes, the sample is heated (S1) at 10K/min up to 40°C. This procedure is followed by a second cooling-heating scan without annealing (S2). (b) Heat flow curves measured on aged and unaged pure SBR (type B: crosslinked) sample (T_g=-14°C). Samples were aged during 5h at various annealing temperature T_a ranged from -15°C to -45°C.

To put into evidence the effect of annealing, we calculate the difference of heat flow between unaged (S2 curve) and aged (S1 curve) sample. The differences, so-called "overshot", are presented in Figure 3.5 for pure SBR sample, as well as pure PB sample and other blends.
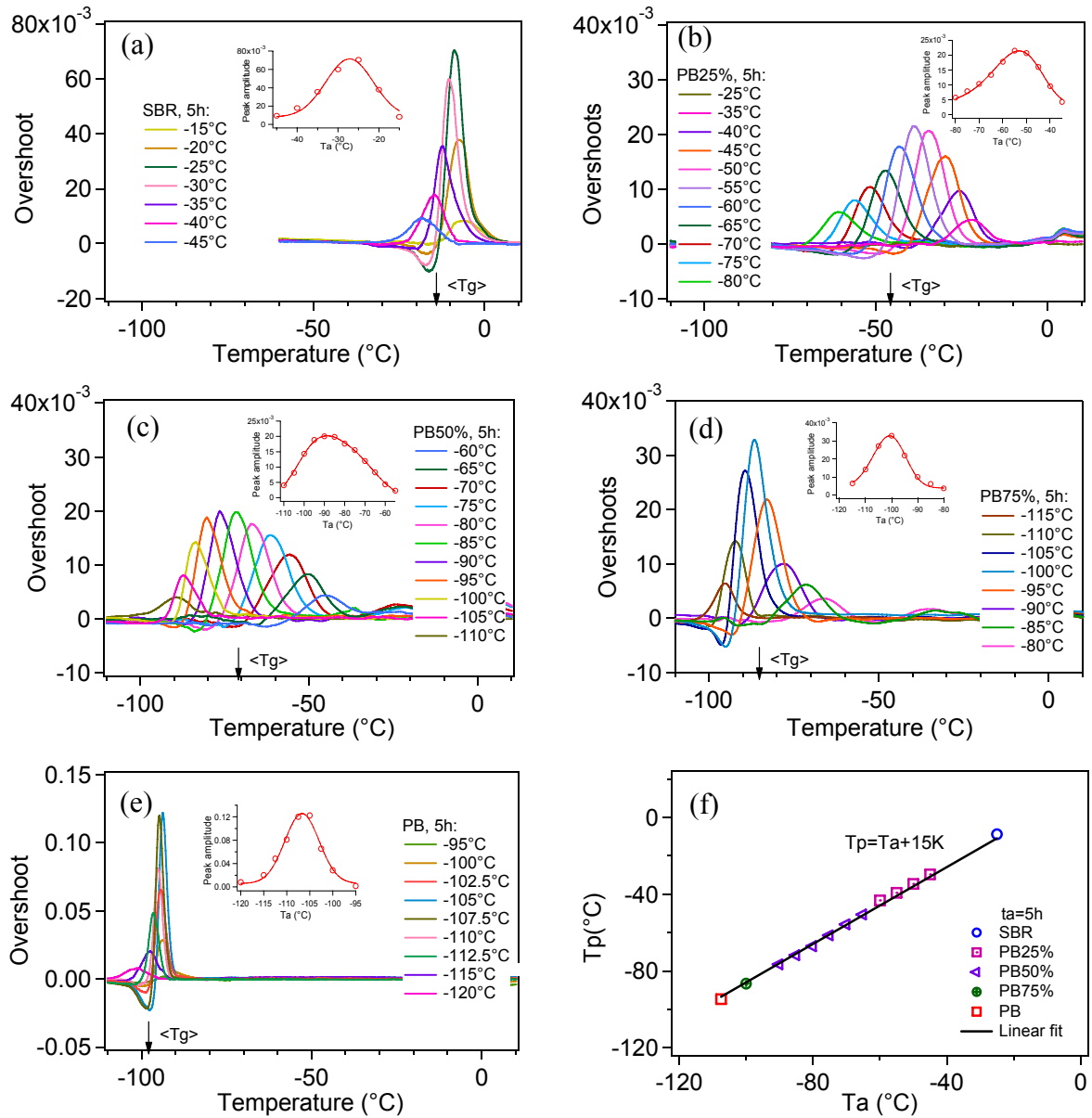
Figure 3.5. Curves of calorimetric overshoots (S2−S1) at various T_a measured on crosslinked pure polymers: (a) pure SBR (T_g=-14°C), (e) pure PB (T_g=-98°C). PB/SBR blends: (b) Φ = 0.25, (c) Φ = 0.5 and (d) Φ = 0.75. In each inset of figure a to e, the amplitudes of peaks are plotted as a function of aging temperature. (e) Temperature at the overshot maximum as a function of the aging temperature.

Physical aging induces an overshoot of the heat flow curves. **Figure 3.5** (a) to (e) show the differences of heat flow between unaged and aged samples (S2-S1). The position of the overshoot depends on the annealing temperature: it is shifted towards higher temperature as T_a increases (see **Figure 3.5** (f)). More precisely, the temperature at the overshot maximum T_p varies linearly with T_a.

The overshoot is located in the glass transition domain. In **Figure 3.6** we compared the curve representing envelop of various overshoots to the one corresponding to $|dHF/dT|$. We found that the two curves are in good agreement. Both of them give a good approximation of $P(T_g)$.
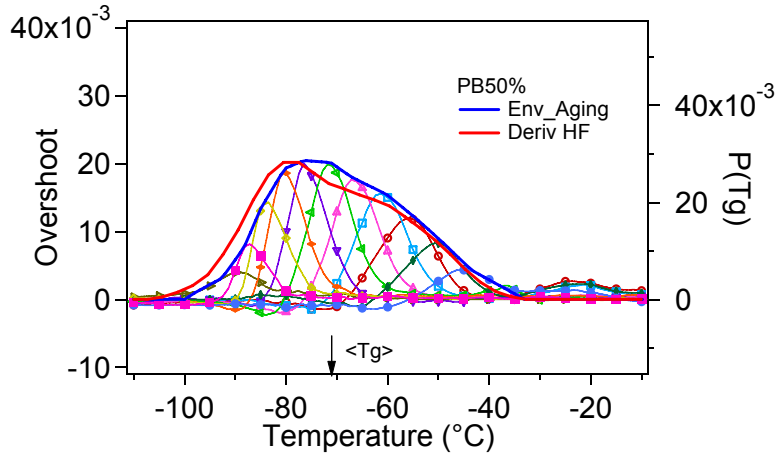
Figure 3.6. Comparison of the curve representing envelop of various overshoots to the one corresponding to $|dHF/dT|$.

The physical aging measurements in annealed DSC curves give us a direct and intuitive insight of the broad distribution of T_g in polymer blends. Thus we can approximate $P(T_g)$ by the normalized envelope of these aging peaks that we will call $P_{aging}(T_g)$.
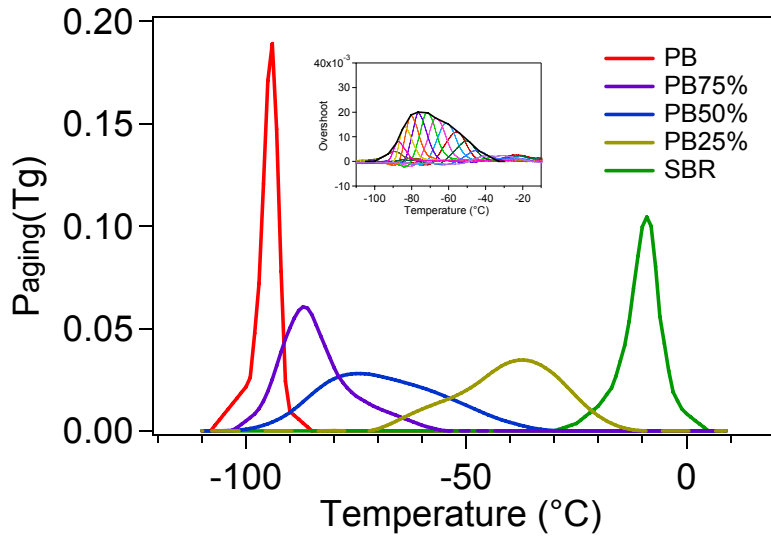
Figure 3.7. $P(T_g)$ by envelop of physical aging DSC measurements for 2 pure polymers and 3 blends. The inset is an example of envelop of blend PB50%.

Moreover there is a linear response for physical aging in PB/SBR blends. If we apply two consecutive annealing steps at T_{a1} and T_{a2}, we observe two overshoots. Each of them superpose well with the overshot peak obtained by a simple annealing (see **Figure 3.8**).

All these results show that there is a selectivity of the annealing process. More precisely, an annealing at a given T_a induces structural rearrangements of domains having a local T_g about T_a +15K. Moreover, domains of different local T_g physically age nearly independently each other.

This selectivity effect is difficult to show for pure polymers with narrow T_g distribution, since only the narrow domain around the maximum of $P(T_g)$ that can be selected.
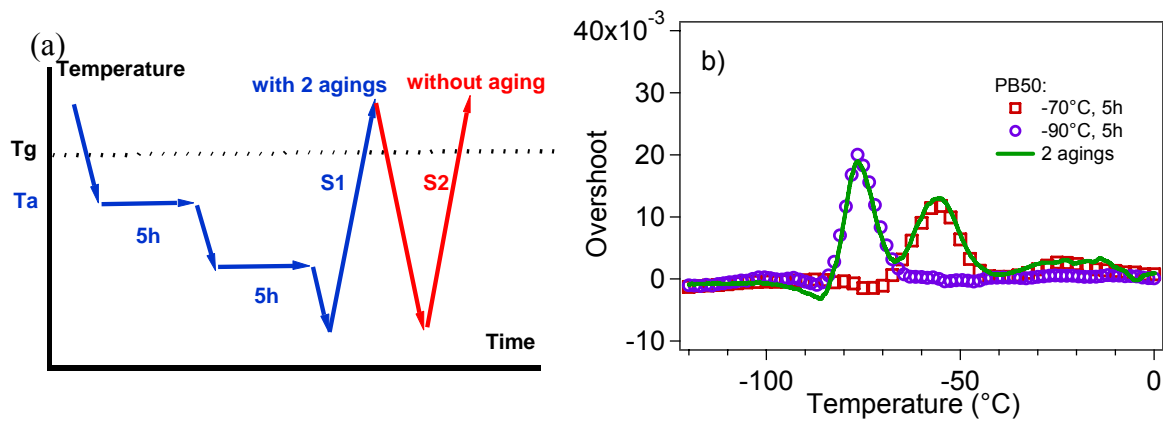
Figure 3.8. (a) Physical aging procedure for two consecutive annealings. (b) Comparison of two consecutive annealings and two separate annealings at T_{a1}=-70°C and T_{a2}=-90°C.

This selectivity can also be influenced by the annealing duration. During the annealing step of duration t_a=12 minutes, structure rearrangements occur in domains with a T_g about T_a +10K. The amplitude of the overshoot varies also with the duration of the annealing, see **Figure 3.9**.

However it seems that time-temperature superposition exists for physical aging. Even if the amplitude of t_a=12 minutes is smaller than that of t_a=5 hours, their normalized overshoot peaks could superpose very well for a certain time-temperature combinations. For example, in a PB25% blend, (t_a=12 minutes and T_a=-50°C) has the same form as (t_a=5 hours and T_a=-55°C), see **Figure 3.9**(d). There seems to be a time-temperature superposition in physical aging.
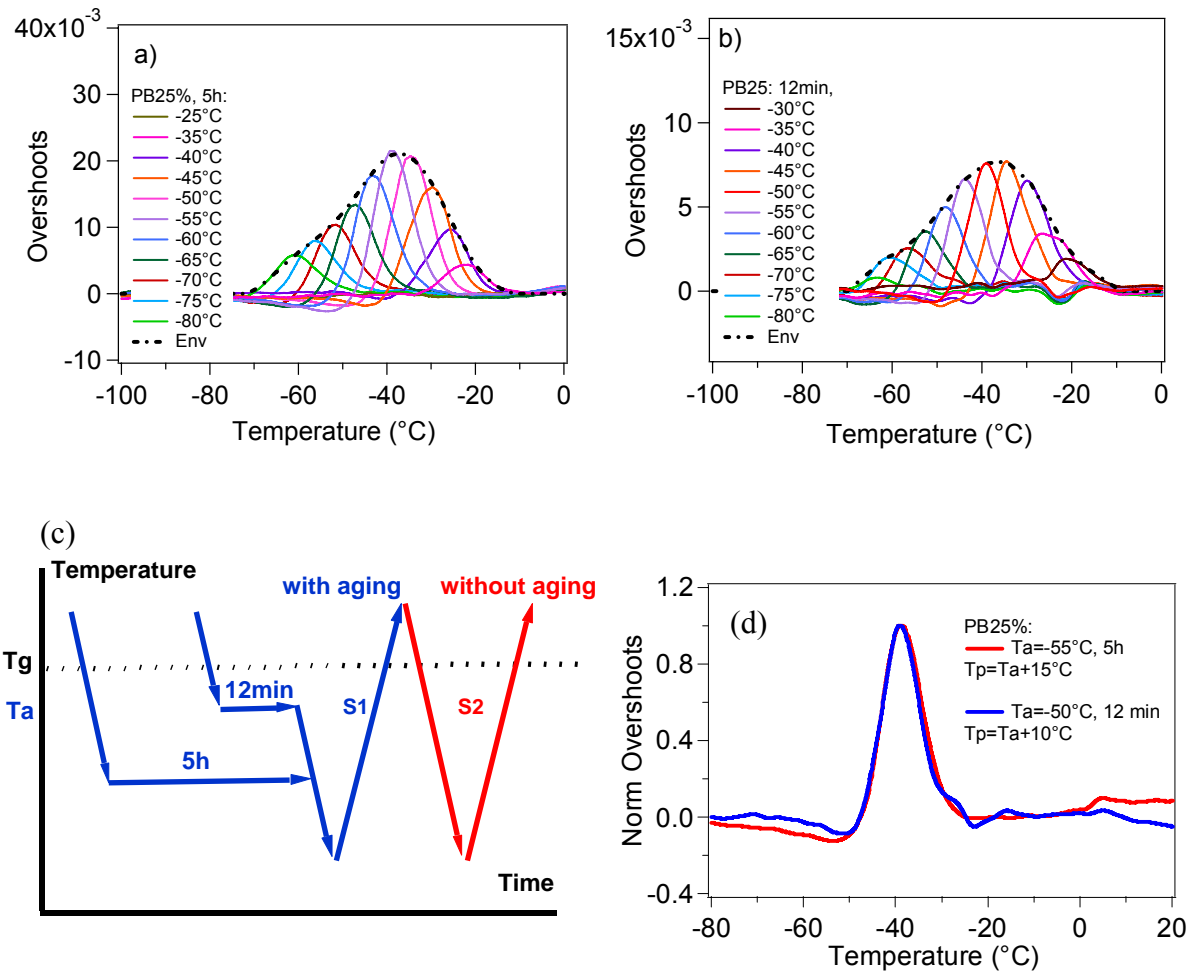
Figure 3.9. Physical aging overshoot peaks for PB25% with different duration (a) t_a=5 hours, (b) t_a=12 minutes, (c) schematic of measurement procedure for annealings with different duration t_a (=5 hours or 12 minutes) and different temperature T_a. (d) Comparison of two overshoots – their amplitudes are normalized.

On **Figure 3.10** we plot the aging time versus aging temperature t_a-T_a giving similar overshoot. We compare it to the temperature dependence of the relaxation time determined from rheological master curves (that we will present immediately in the next section). We find that two curves have the same slope, indicating that time-temperature superposition law is similar in rheology and in physical aging of calorimetry. This confirms the statement that the domain being selected by annealing is the one that has a relaxation time about the annealing time (with a shift factor) at the temperature of annealing.
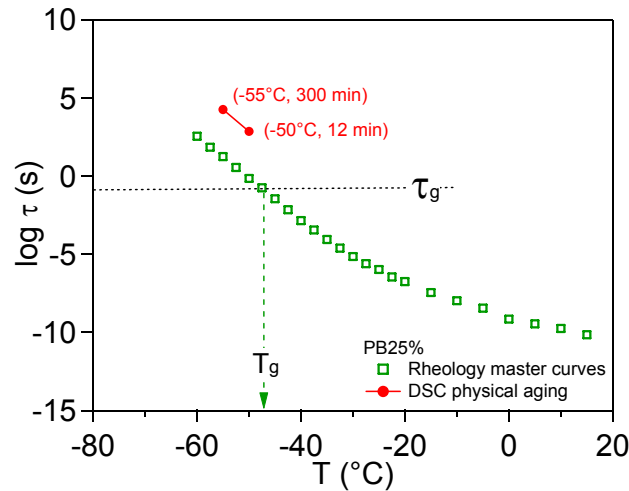
Figure 3.10. Comparison of temperature dependent relaxation time evolution from rheology master curves with t_a-T_a from DSC physical aging measurements.

Conclusions on physical aging measurements:

- DSC measurement with physical aging at different T_a exhibits a peak that reveals the independent contribution of different domain of T_g.

- There is an annealing time-temperature superposition for physical aging.

- The T_g distribution obtained by aging $P_{aging}(T_g)$ is in good agreement with the on obtained simply by the heat flux derivative $P_{deriv}(T_g)$.

Conclusions on calorimetry measurements

The calorimetry is a simple and efficient tool to observe the broadening of the glass transition. We show here that the whole signal of blends can be interpreted as the sum of contributions originating from independent domains, each one having its own glass transition temperature. We will interpret these results in the Chapter 4.

3.4. *Linear viscoelastic measurements*

We present here the characterization of the linear viscoelastic properties of our PB/SBR blends in the glass transition region. Similarly to calorimetry, we observe a broadening of the glass transition zone for polymer blends.

We will check that the time temperature superposition is then reasonably verified for the pure polymers and for the blends. This will allow us to built master curves that we will discuss in the Chapter 4.

3.4.1. Rheological data

Examples of some rheological data of pure SBR sample and blend 50% are presented in **Figure 3.10**. Storage modulus G' and loss modulus G'' depend on both temperature and frequency. G' decreases about 3 decades from glassy state to rubbery state.
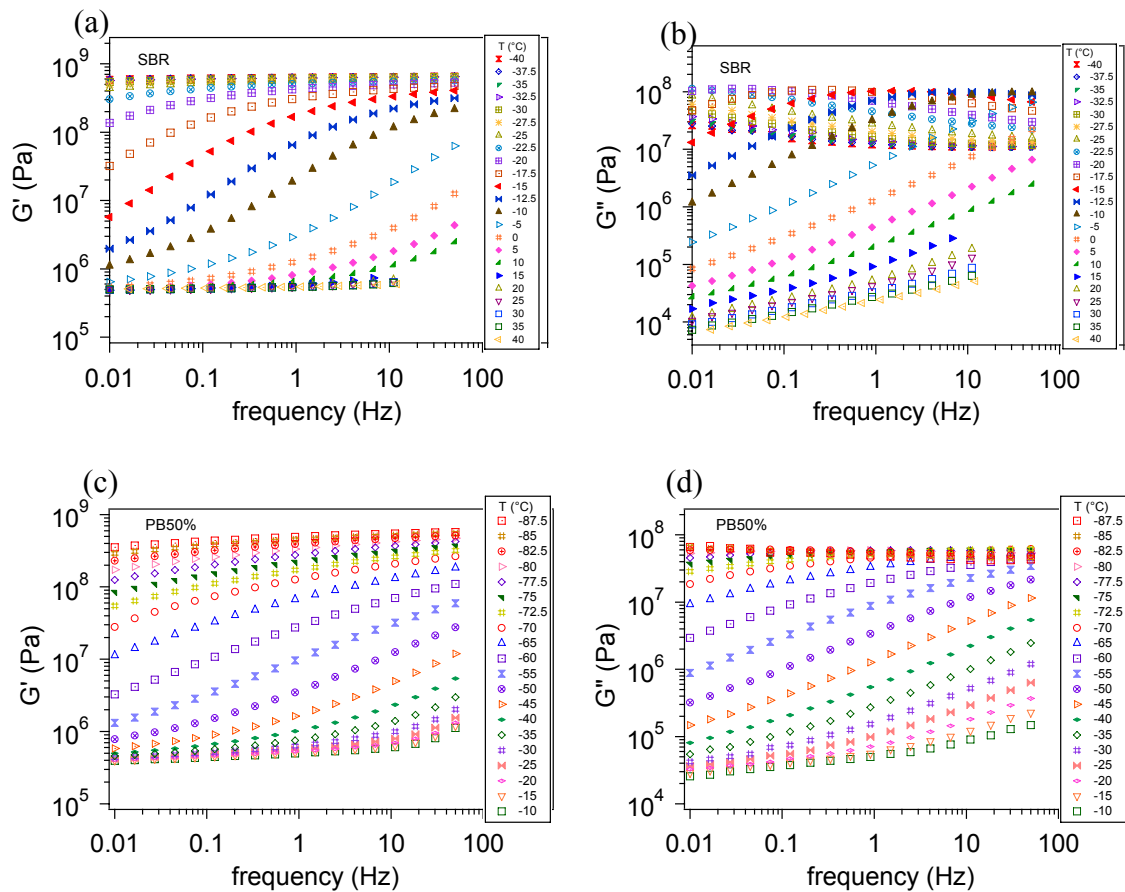
Figure 3.10. Rheological data of (a) storage shear modulus G' of SBR, (b) loss shear modulus G'' of SBR, (c) storage shear modulus G' of blend PB50%, (b) loss shear modulus G'' of blend PB50%. Samples are crosslinked (type B).

G' value at high temperature and low frequency corresponds to the shear modulus at the rubbery plateau G_r, and is related to the average molar mass of an apparent network strand M_c by:

$$M_c = \frac{\rho RT}{G_r}$$ (eq 3.3)

Table 3.4 gives the rubbery plateau modulus G_r and calculated apparent M_c for different pure polymers and blends PB/SBR. Apparent M_c is about 5000g/mol for all the compositions. This is in fact fixed by the crosslinking density and the quantity of crosslinkers used in each sample, but also induced by the present of entanglements. The precise discussion on the origin of the rubber elasticity will be done in Chapter 5, where non linear elastic response will allow discussing precisely the role of entanglements and crosslinks.

Table 3.4. Shear modulus at the rubbery plateau G_r, the corresponding temperature and the calculated average molar mass of a network strand M_c for different pure polymers and blends PB/SBR. Samples are solvent mixed and cross-linked.

Rheology	G_r (Pa)	T (K)	M_c (g/mol)
PB	500000	283	4703
PB75%	450000	273	5041
PB50%	394000	263	5270
PB25%	500000	313	5202
SBR	549000	313	4738

The macroscopic glass transition temperature T_g is determined as the temperature at which the maximum of loss modulus G'' is found at about $f = 1Hz$, i.e. the relaxation time is $\tau = 1/2\pi f \approx 0.16s$ and $\log \tau$=-0.798. Results for different blends are presented in **Table 3.5**.

Table 3.5. Macroscopic glass transition temperature T_g deduced from mechanical measurement and the corresponding relaxation time for different pure polymers and blends PB/SBR. Samples are solvent mixed and cross-linked. T_g determined by DSC measurements on the same samples are added for comparison (dT/dt=10°C/minute)

Rheology	T_g(°C) rheo	$\log(\tau_g)$(s)	T_g(°C) DSC
PB	-100.5	-0.798	-98
PB75%	-93	-0.798	-86
PB50%	-77.5	-0.798	-71
PB25%	-47.5	-0.798	-47
SBR	-15.5	-0.798	-14

3.4.2. Time-temperature superposition

All the curves at different temperatures could be shifted and form a master curve for pure polymers and polymer blends PB/SBR. **Figure 3.11** gives some examples of G' and G'' for pure SBR and blend PB50%.
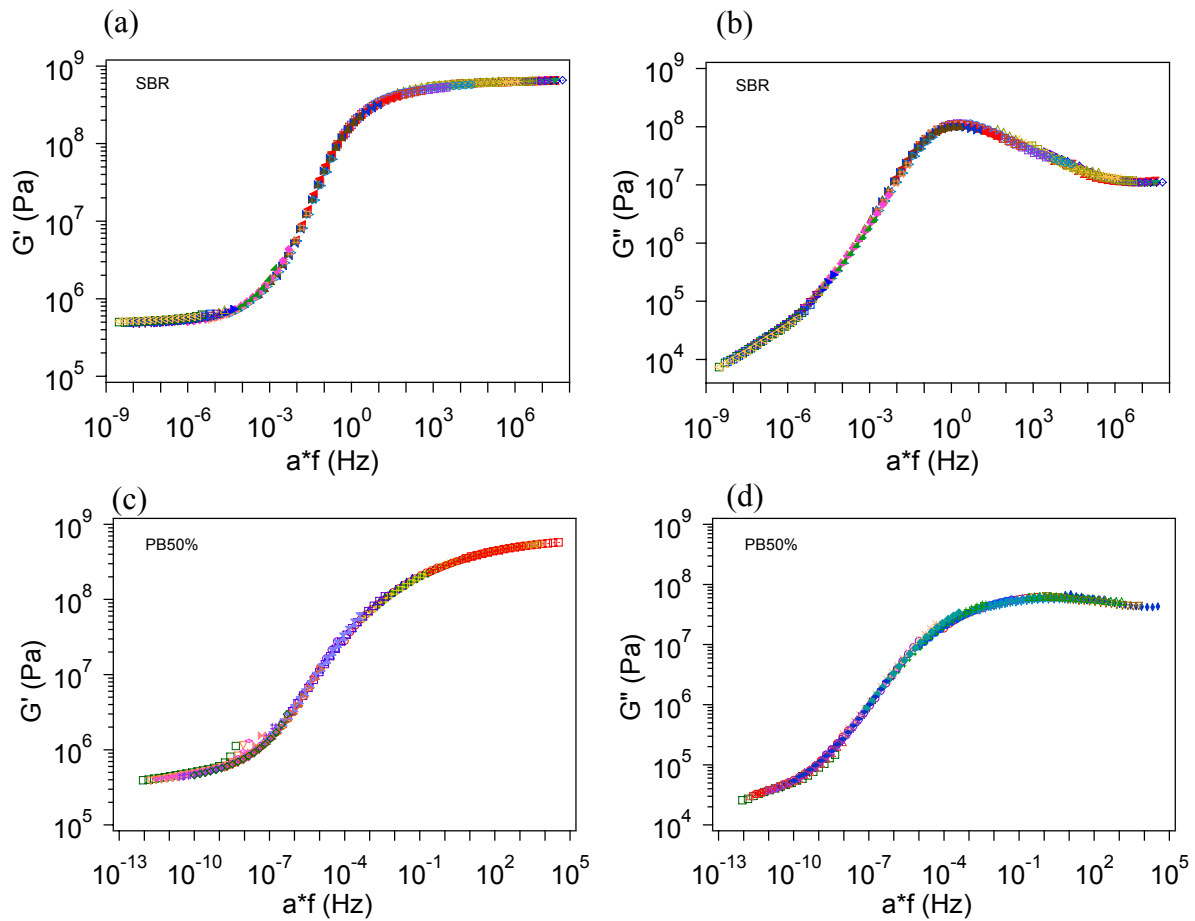
Figure 3.11. Master curves of (a) storage shear modulus G' of SBR, (b) loss shear modulus G" of SBR, (c) storage shear modulus G' of blend PB50%, (b) loss shear modulus G" of blend PB50%. Samples are crosslinked (type B). References temperatures are the glass transition temperature of each polymer: $T_{ref}=T_g$, presented in **Table 3.5**.

From the above master curves of G' and G", time-temperature superposition quality is good in our PB/SBR blend system. However, some slight differences can be observed in the maximum of tanδ=G"/G' master curves.
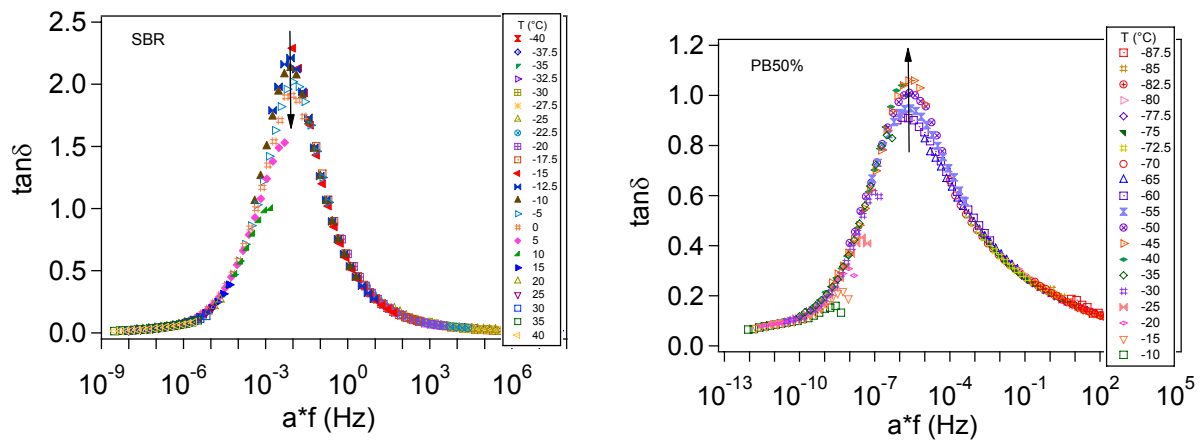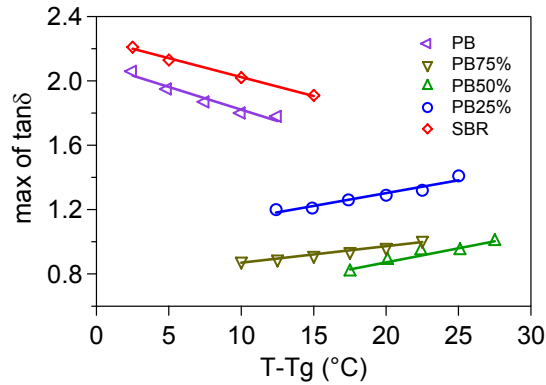
Figure 3.12. Master curves of tanδ for (a) SBR and (b) PB50%. (c) Evolution of the maximum of tanδ as a function of temperature for pure polymers and blends PB/SBR. Samples are crosslinked (type B).

The quality of the time temperature superposition can be estimated by plotting the maximum of tanδ versus temperature. If it is a constant, it means the time temperature superposition is very good. If it depends on temperature, the quality is less good. **Figure 3.12** shows that the maximum of tanδ changes with temperature. The tendencies of the evolution are different:

- For pure polymers, maximum of tanδ decreases with temperature.
- For polymer blends, maximum of tanδ increases with temperature.

However, the absolute value of the slope of the change of maximum of tanδ is not significantly larger for polymer blends than for pure polymer. We do not have any physical interpretation of this effect. In this study, we assume that time-temperature superposition is a good approximation for all PB/SBR rheological measurements and will use master curves for further analysis.
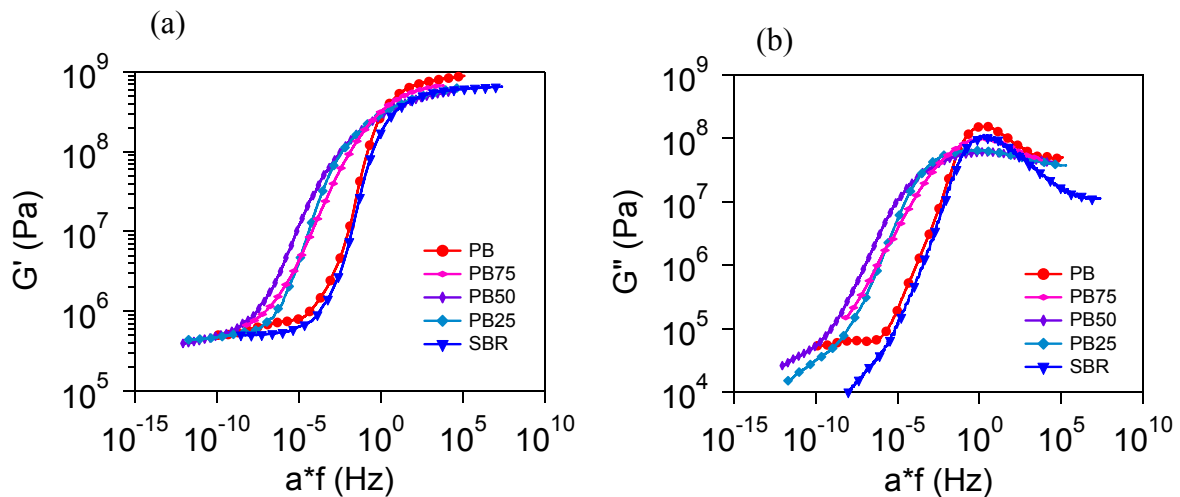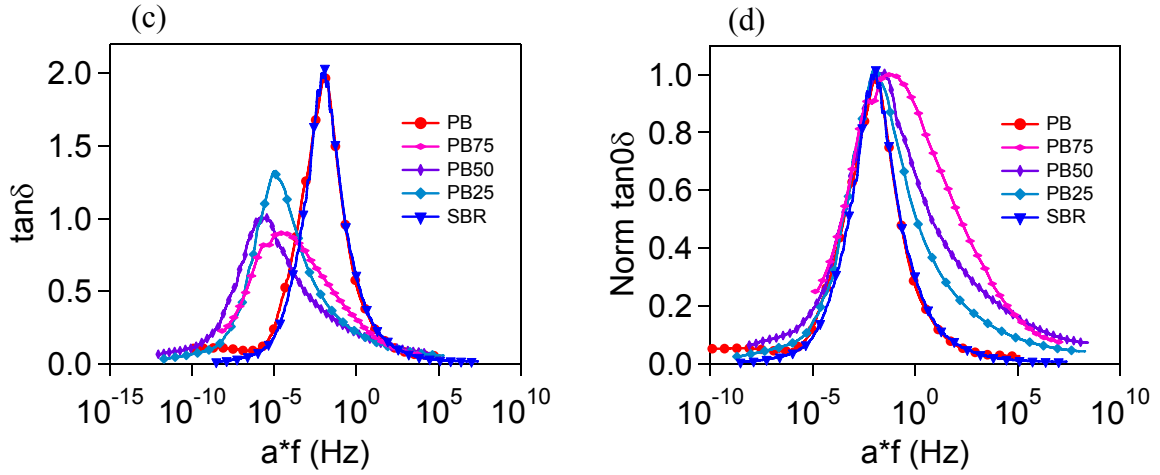
Figure 3.13. Master curves for (a) storage modulus *G'*, (b) loss modulus *G''*, (c) *tanδ* and (d) normalized and superposed *tanδ* as a function of frequency. Samples are blends of solvent mixing and cross-linked ones (type B). References temperatures are the glass transition temperature of each polymer: $T_{ref}=T_g$, presented in **Table 3.5**.

Rheological master curves in **Figure 3.13** show also a broadening for polymer blends, similar to DSC measurements. This is most evident when we normalize and superpose the curves of *tanδ*(=*G''*/*G'*) for various blends (see **Figure 3.13**(d)).

It is worth noticing that the broadening exists especially in the right side, i.e. the glassy domain, and the curves in the rubbery domain are practically unchanged. The effect of blending will be also slightly discussed in chapter 4. We will show in this chapter that if the broadening due to blending can be quantitatively described, the description of the effect of blending in the Rouse regime is still an open question. The discussion of Rouse mode is likely very interesting but is out of the scope of this work.

The shift factors a_T of the master curves can be used to calculate the evolution of relaxation times using:

$$\log_{10}(\frac{\tau}{\tau_g}) = \log_{10}(a_T) = -\frac{C_1^g(T-T_g)}{C_2^g+T-T_g}$$

(eq 3.4)

This evolution is controlled by a WLF law as shown in **Figure 3.14**, and fitting parameters of all the crosslinked samples are presented in **Table 3.6**.

Table 3.6. WLF law fitting parameters for cross-linked samples (type B)

Rheology	C_1^g	C_2^g	T_g(°C)	log(τ_g)(s)
PB	12.0	36.7	-100	-0.97
PB75%	18.9	56.8	-92.5	-0.97
PB50%	22.4	76.9	-77.5	-1.41
PB25%	18.1	55.3	-47.5	-0.76
SBR	11.6	37.8	-15	-0.97
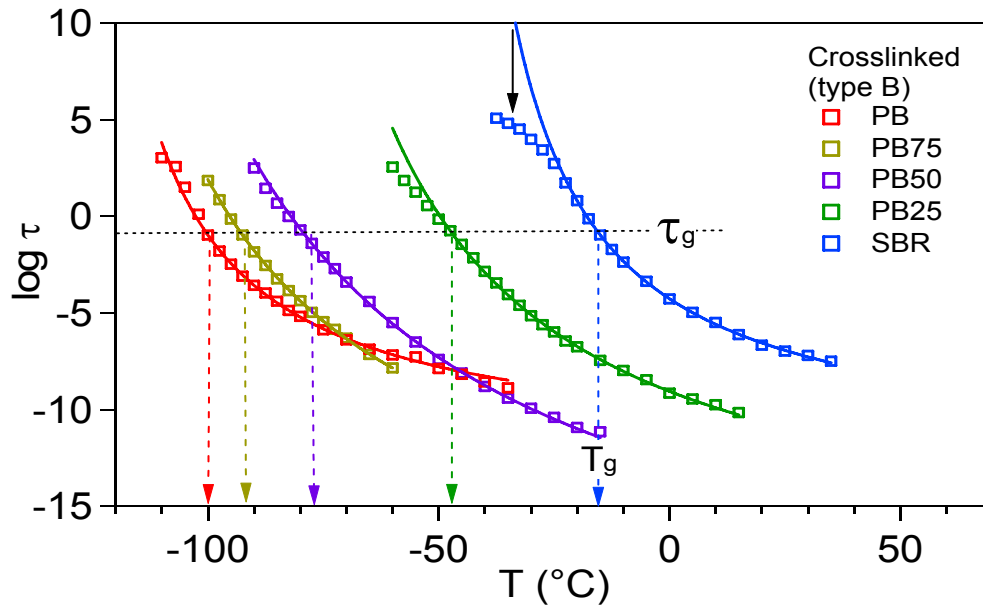
Figure 3.14. Evolution of the relaxation time as a function of temperature. Squares are data from master curves and lines are fits to WLF laws. Dashed line indicates the relaxation time at T_g, and dashed arrows indicate the value of T_g of each sample. Solid arrow indicates the non equilibrium regime.

The data derivate from the WLF law at lower temperatures, typically $T < T_g - 10K$, because the system is in the non equilibrium glass regime. For this reason, the determination of the C_1 and C_2 WLF coefficients was performed by fitting only with data in the equilibrium from T_g to $T_g + 50K$.

3.4.3. Influence of crosslinking and sample preparations

Other samples (non-crosslinked and mechanical mixing ones) show also good time temperature superposition and their master curves are shown in **Figure 3.15**. It is found that the glass transition temperature T_g of non-crosslinked samples are a few degrees lower than crosslinked samples, but the shapes of the curves are not changed at all in the glass transition zone. Slight differences can be found in the low frequency zone, where non cross-linked samples flow, storage modulus decreases and loss modulus increases.
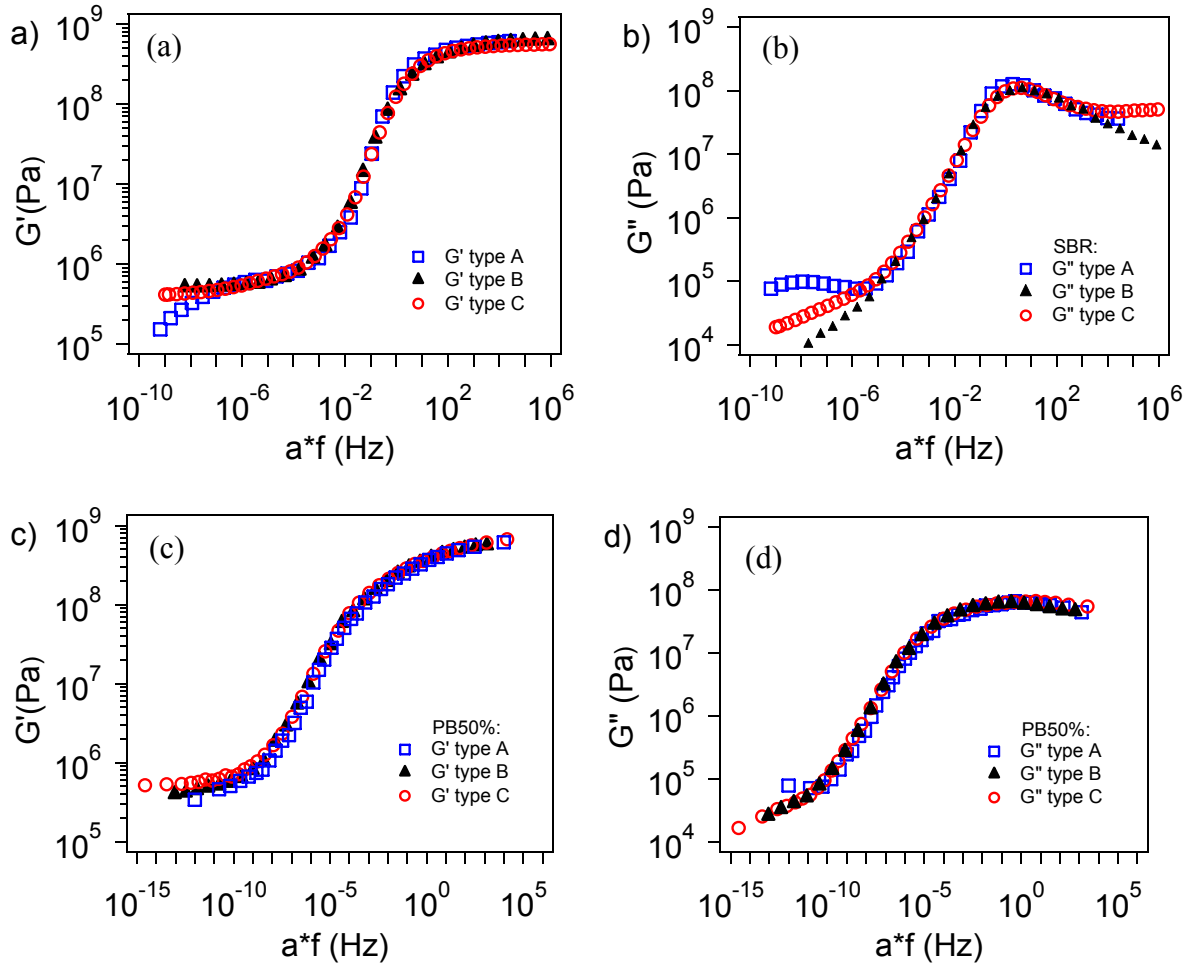
Figure 3.15. Master curves for (a) SBR storage modulus *G'*, (b) SBR loss modulus *G''*, (c) PB50% storage modulus *G'* and (d) PB50% loss modulus *G''* as a function of frequency, with 3 types of preparations. References temperatures are the glass transition temperature of each polymer: $T_{ref}=T_g$, the values of which are shown in **Table 3.8**.

The shear modulus at the rubbery plateau G_r for non-crosslinked samples is determined at the position of the minima of G''at $f=f_0$, see **Figure 3.16**. The corresponding value of rubbery plateau modulus is $G_r=G'(f_0)$. The average molar mass of an entanglement strand M_e is:

$$M_e = \frac{\rho RT}{G_r}$$
(eq 3.5)

Table 3.7 gives the rubbery plateau modulus G_r and calculated M_c or M_e for different samples. M_e value for non-crosslinked PB is absent due to crystallization of chains.
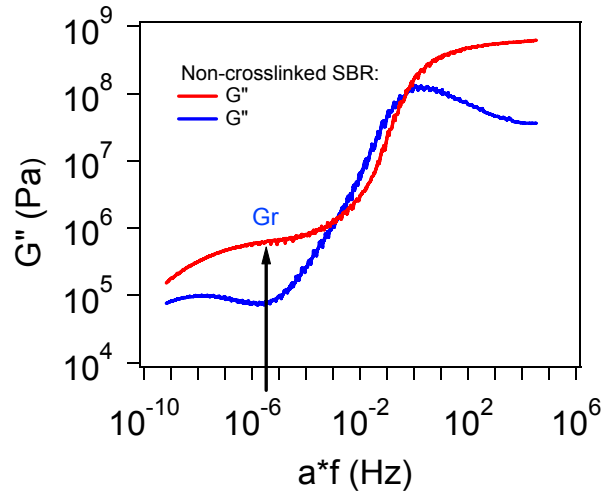
Figure 3.16. Master curves for non-crosslinked SBR sample. Arrow indicates the position of the minima of G''at $f=f_0$, and the corresponding value of rubbery plateau modulus $G_r=G'(f_0)$.

Table 3.7. Shear modulus at the rubbery plateau G_r, the corresponding temperature and the calculated average molar mass of an apparent network strand M_c for crosslinked type B and C samples, or entanglement strand M_e for non-crosslinked type A samples.

		G_r (Pa)	T (K)	M_c/M_e (g/mol)
Type A	PB	/	/	/
	PB75%	385000	208	4265
	PB50%	474000	243	4047
	PB25%	504000	243	3806
	SBR	624000	308	3897
Type B	PB	500000	283	4703
	PB75%	450000	273	5041
	PB50%	394000	263	5270
	PB25%	500000	313	5202
	SBR	549000	313	4738
Type C	PB50%	510000	323	5000
	SBR	408000	318	6153

A=solvent mixing, non cross-linked
B=solvent mixing, cross-linked
C=mechanical mixing, cross-linked

The glass transition temperature T_g of non-crosslinked samples are a few degrees lower than crosslinked samples, but the WLF coefficient C1 and C2 are similar (see **Figure 3.17** and **Table 3.8**).
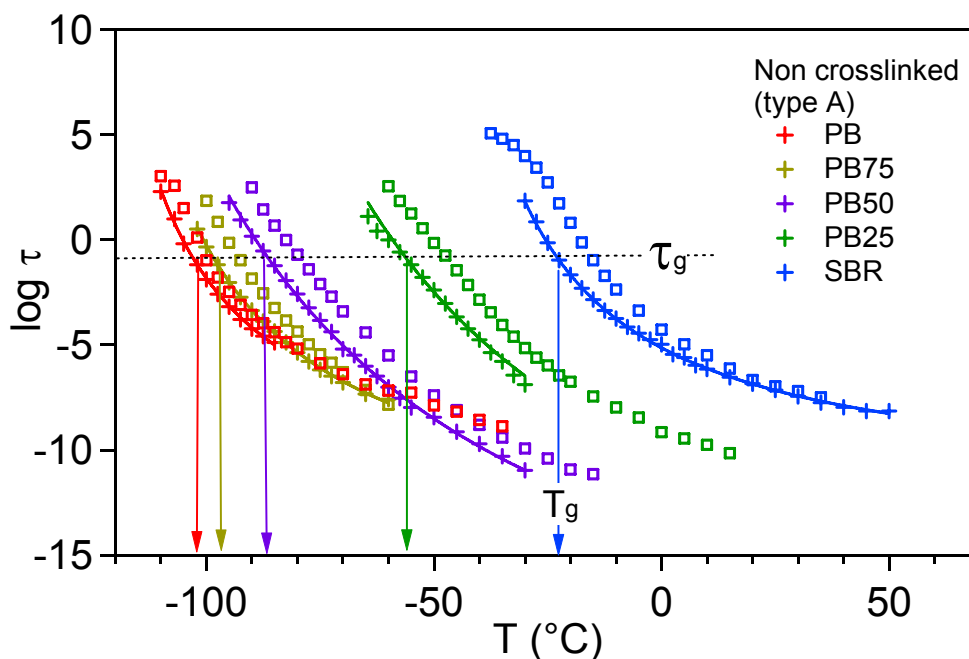
Figure 3.17. Evolution of the relaxation time as a function of temperature. Curves with + symbols are data of non-crosslinked samples, and lines are fits to WLF laws. Dotted line indicates the relaxation time at T_g, and arrows indicate the value of T_g of each sample. Squares are data of crosslinked samples for comparison.

Table 3.8. WLF law fitting parameters from rheological data for different samples.

		$C_1{}^g$	$C_2{}^g$	T_g(°C)	$\log(\tau_g)$(s)
	PB	11.3	33.3	-102	-1.19
	PB75%	13.4	39.0	-97.5	-1.19
Type A	PB50%	24.7	78.6	-87.5	-0.54
	PB25%	22.7	82.1	-55	-1.19
	SBR	11.0	36.9	-22.5	-0.97
	PB	12.0	36.7	-100	-0.97
	PB75%	18.9	56.8	-92.5	-0.97
Type B	PB50%	22.4	76.9	-77.5	-1.41
	PB25%	18.1	55.3	-47.5	-0.76
	SBR	11.6	37.8	-15	-0.97
Type C	PB50%	25.8	83.4	-80	-0.97
	SBR	11.4	35.3	-20	-0.97

A=solvent mixing, non cross-linked
B=solvent mixing, cross-linked
C=mechanical mixing, cross-linked

All these comparisons confirm that the cross-linking doesn't change the glass transition distribution in the blends.

3.4.4. Broadening of the glass transition zone

Master curves in chapter 3.4.2 show that the glass transition zone in polymer blends are broader than that in the pure polymers. The viscoelastic master curves can be described by the Havriliak-Negami function [42,61]:

$$\frac{G_{glass} - G^*(\omega)}{G_{glass} - G_{rub}} = \frac{1}{\left(1 + (j\omega\tau_{HN})^\alpha\right)^\gamma}$$

$$\tau_{HN} = \tau\left[\tan\left(\frac{\pi}{2(\beta+1)}\right)\right]^{1/\alpha}$$

(eq 3.6)

where parameters α and γ describe the dynamic heterogeneity and broadness of the distribution of the relaxation times, i.e. the broadness of the glass transition zone. $\alpha = 1$ and $\gamma = 1$ correspond to a single relaxation time; $0 < \alpha < 1$ and $0 < \gamma < 1$ correspond to a distribution of relaxation times. Smaller values of these two parameters correspond to a broader distribution. The parameter τ corresponds to the relaxation time given by the WLF relation:

$$\log_{10}\left(\frac{\tau}{\tau_g}\right) = \log_{10}(a_T) = -\frac{C_1^g(T - T_g)}{C_2^g + T - T_g}$$

(eq 3.7)

H-N fitting results are presented in **Figure 3.18** and **Table 3.9**. The glass transition zones in the polymer blends are so broad that the slopes of G'' in the high frequency side is nearly horizontal, and the flexion point at the maximum of G'' is not as clearly defined as that in pure polymers. The fittings are thus less reliable for polymer blends. Nevertheless, the broadening results in small values of α and γ parameters in **Table 3.9**.
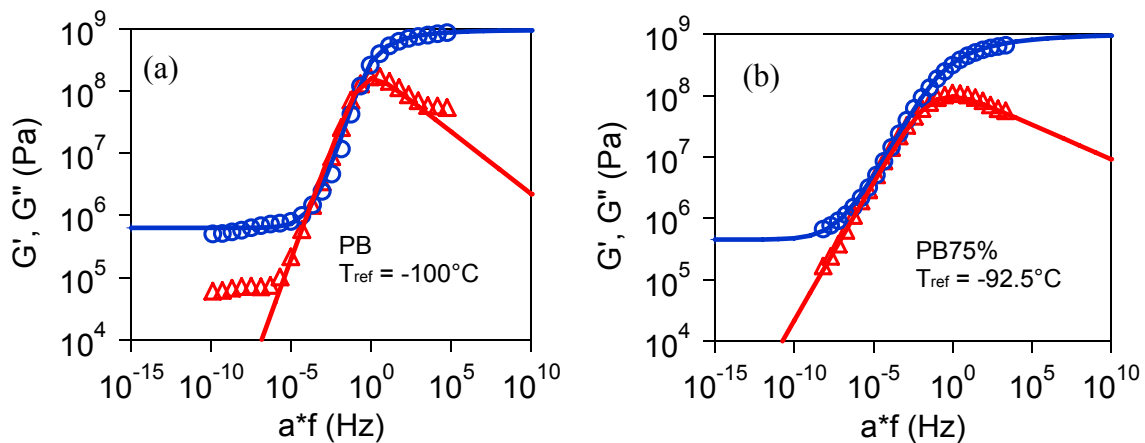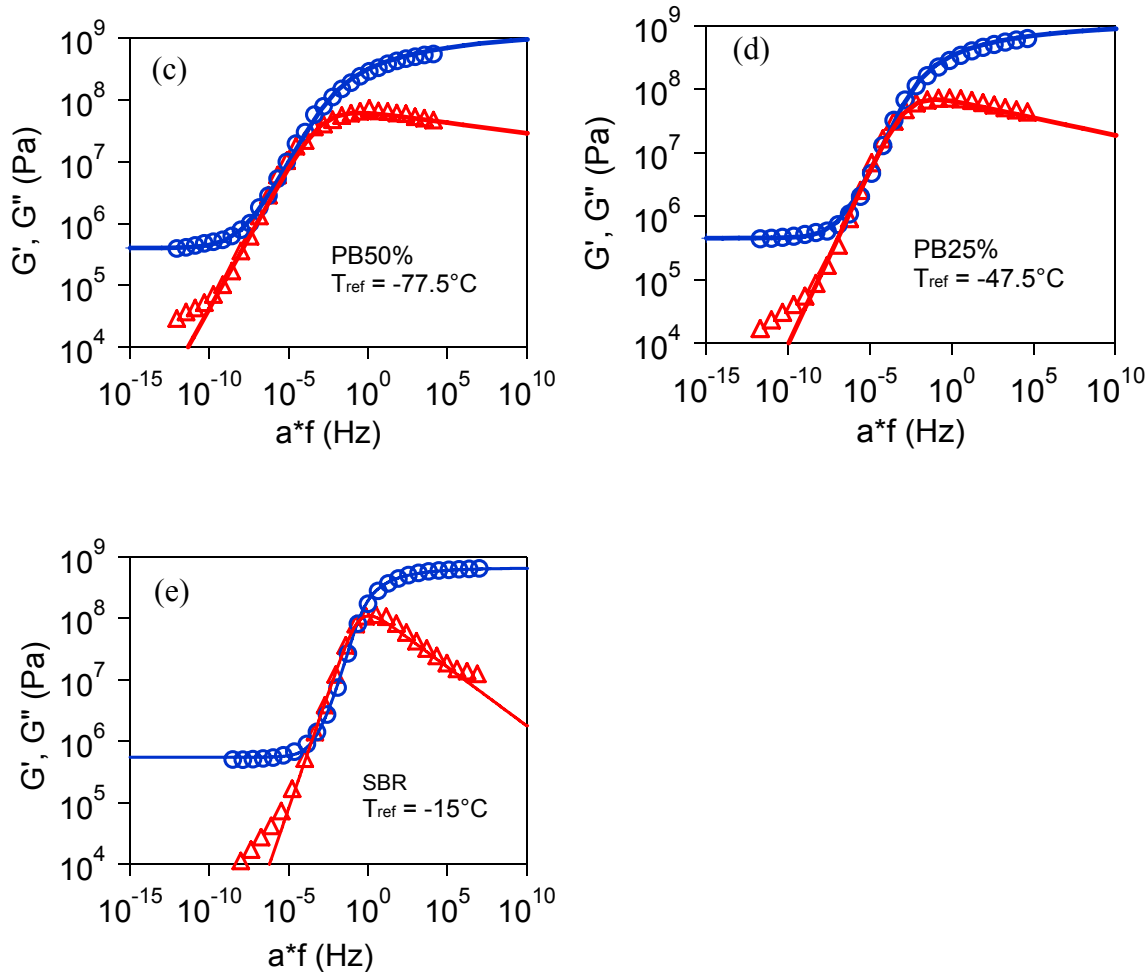
Figure 3.18. Master curves for storage modulus (circles) and loss modulus (triangles) as a function of frequency and their H-N function fittings (solid lines). (a) PB, (b) PB75%, (c) PB50%, (d) PB25%, and (e) SBR. Samples are blends of solvent mixing and cross-linked ones (type B). References temperatures are the glass transition temperature of each polymer: $T_{ref}=T_g$.

Table 3.9. Best chi-square fitting Havriliak-Negami parameters for pure polymers and polymer blends at $T_{ref}=T_g$.

	PB	PB75%	PB50%	PB25%	SBR
α	0.71	0.45	0.46	0.55	0.75
γ	0.28	0.25	0.07	0.10	0.25
$\log(\tau_g)$	-0.95	-0.50	0.11	0.50	-0.87
$T_g(°C)$	-100	-92.5	-77.5	-47.5	-15
G_{glass} (Pa)	9.5E+08	1.0E+09	1.5E+09	1.1E+09	6.5E+08
G_{rub} (Pa)	6.3E+05	4.5E+05	4.0E+05	4.5E+05	7.4E+05

The viscoelastic behavior of a polymer blend could be considered as a sum of various components, each of which has a distinct glass transition temperature T_g. We will develop a more detail analysis in chapter 4 assuming that the polymer blend is a composite material with domains of varying T_g.

We observed that there are two intersection points between G' and G'' in pure polymers. While for blends where the glass transition zone is broad, there is no intersection (see P50%and PB75%). As a consequence, and tanδ ≈1 or <1 for polymer blends and can be higher than 1 in pure polymers, see **Figure 3.13**(c).

The most obvious broadening in the high frequency side in the polymer blends (in **Figure 3.13**(d)) indicates that there are strong dynamic heterogeneities at the length scale associated to the segmental movement of the α-relaxation.

On the contrary, in the low frequency side, viscoelastic behaviors are similar for polymer blends and pure polymers. The mechanical property at the length scale related to the rubber elasticity seems to be less controlled by the dynamic heterogeneity in our polymer blends. It is possible that for the Rouse modes, the relaxation times are more homogeneous. In this work, however, our focus is on the glass transition α-relaxation domain.

At this step if we know that the rheological properties are strongly controlled in the glass transition domain by the dynamical heterogeneities existing in our polymer blends, we did not determine the relaxation times distribution function associated to rheological behavior.

In chapter 4, we will then give detailed analysis based on these questions of mechanical properties. Our aim is to compare the T_g distribution functions associated to rheological and calorimetric measurements. We want also identify the length scale associated to each of these T_g distributions.

3.5. *Linear dielectric measurements*

Dielectric measurements are performed only with non cross-linked blends, because cross-linkers introduce additional loss peaks that are even stronger than the α-relaxation peak and make the data analysis impossible.

3.5.1. **Main characteristics of the dielectric responses**

Origin of the dielectric response. The dielectric response for both SBR and PB originates in the motions of the dipolar groups of the chains. The origin of the dipole moment is the positive and negative charge concentrations in the material under investigation. It depends on the chemical structures (see **Table 3.10** for the dipole moments in PB and SBR).

Table 3.10. Chemical structures of different components and schematics of their dipole components (see red arrows).

Chemical Structures
cis-**1,4-PB**
1,2-PB
PS
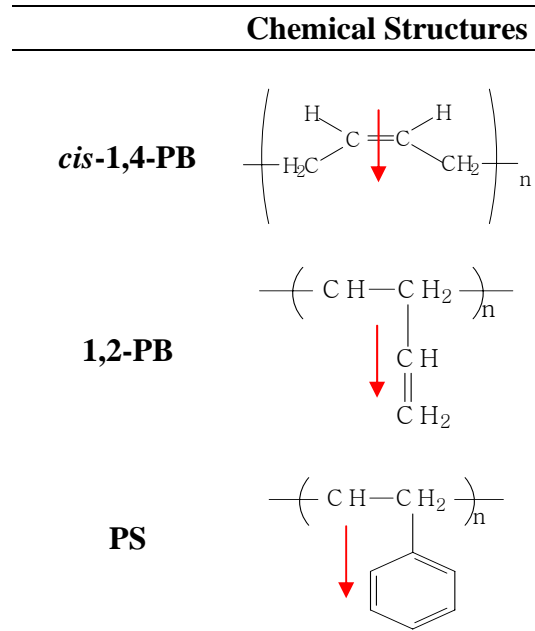
Pure SBR. It is observed from **Figure 3.19**(a) that SBR sample presents a clear α-relaxation peak, whose position is dependent on temperature. The amplitude of the α peak seems constant. We deduce the evolution of α relaxation time $\tau=1/(2\pi f_{max})$ with temperature shown on **Figure 3.19**(b). The evolution measured with dielectric spectroscopy agrees well with the one determined from rheological properties. We found the WLF coefficients: $C_1^g=$ 11,2, C_2^g =45,5 for the reference temperature T_g= -18,4°C and e reference relaxation time $\log(\tau^g)$=-0.798.

SBR samples show a slight difference in T_g: -18.4°C in dielectric vs. -22.5 in rheology. However, the WLF fitting parameters C_1 and C_2 are very similar in both measurements.
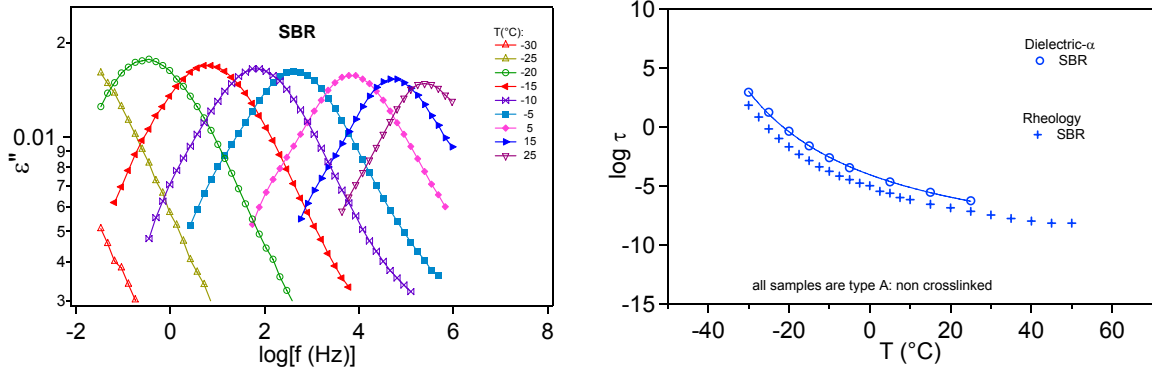
Figure 3.19. (a) Temperature and frequency dependence of the dielectric loss ε" for non cross-linked pure polymers SBR. (b) Temperature dependence of the relaxation time τ versus temperature.

Time temperature superposition of the α-relaxation peaks of pure polymers SBR seems valid (see **Figure 3.20**). We observe in addition that the maximum of the peaks of SBR decreases as temperature increases, which is in agreement with previous observations on rheological tanδ data of pure polymers.
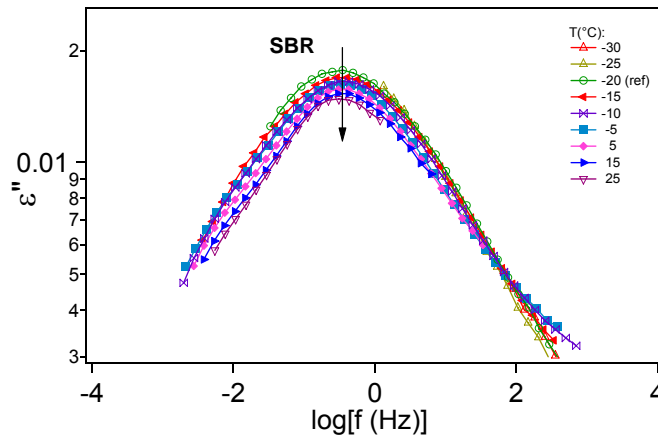
Figure 3.20. Superposition of dielectric α-relaxation loss peaks of different temperatures for SBR with T_{ref}= -20°C.

Pure PB. In addition to an α-relaxation peak, the PB sample shows in addition a β-relaxation peak at low temperature and high frequency (see **Figure 3.21**(a)). As temperature increases, these two peaks overlap, indicating that α and β-relaxation times have the same temperature dependence at high temperatures.

From the measurements performed at the lowest temperatures, we can deduce the characteristics of the β relaxation of the PB chains. **Figure 3.21**(b) shows that the β relaxation time $log(\tau)$ for pure PB varies linearly with $1/T$(K), i.e. it follows an Arrhenius law:

$$\tau = \tau_0 \exp(\frac{E_a}{RT}) \qquad (eq\ 3.8)$$

with: $\tau_0 = 10^{-16}s$ and $E_a = 38.7 kJ \cdot mol^{-1}$

65
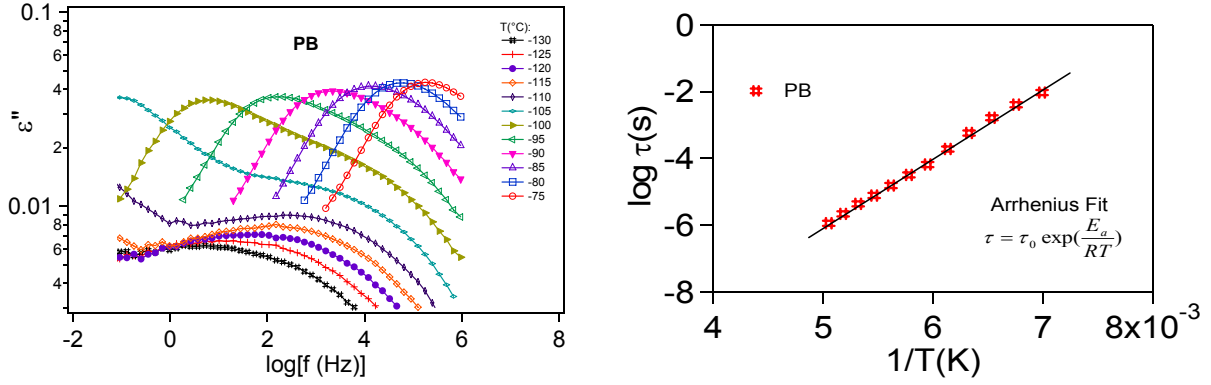
Figure 3.21. (a) Temperature and frequency dependence of the dielectric loss ε'' for non cross-linked pure polymers PB. (b) Evolution of β-relaxation times $log(\tau)$ for PB sample as a function of 1/T(K). Solid line is a fit to Arrhenius equation with $\tau_0 = 10^{-16}\,s$ and $E_a = 38.7 kJ \cdot mol^{-1}$.

The analysis of the α-relaxation peak is more difficult than for the pure PB due to the partial overlap with the β-relaxation process. We have to separate these two peaks. Before that, that, we will first present data of polymer blends which exhibit the same feature concerning the proximity between α and β relaxations.
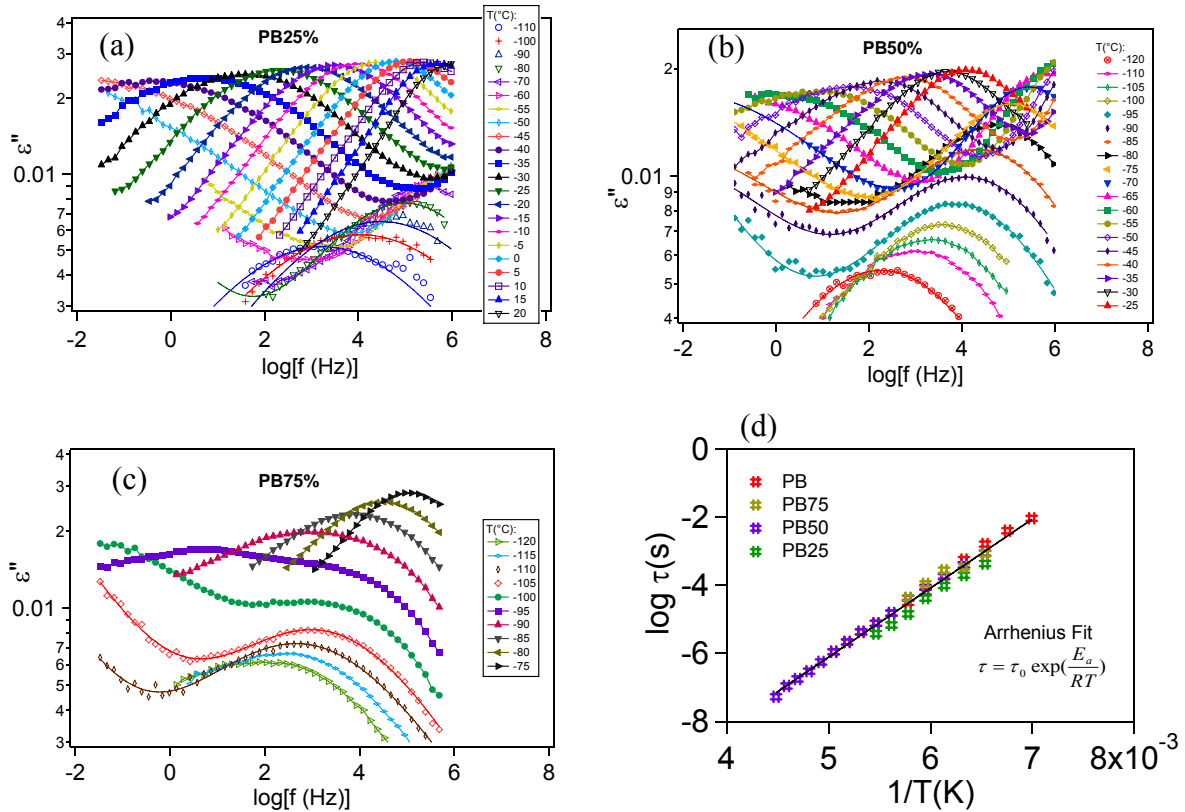
Figure 3.22. Temperature and frequency dependence of the dielectric loss for (non cross-linked) polymer blend (a) PB25%, (b) PB50% and (c) PB75%. (d) Evolution of β-relaxation times $log(\tau)$ for PB sample and 3 polymer blends as a function of 1/T(K). Solid line is a fit to Arrhenius equation with $\tau_0 = 10^{-16}\,s$ and $E_a = 38.7 kJ \cdot mol^{-1}$.

66

SBR/PB Blends. The dielectric data of a polymer blends show a broadening of the α-relaxation peaks. In addition, two distinct relaxation peaks that do not converge even at high temperatures for PB25% and PB50% blends, see **Figure 3.22**(a-b).

The β relaxation in SBR/PB blends. The first observation of β-relaxation is surprising: it does not overlap with the α-relaxation at high temperatures for PB25% and PB50% blends. The two relaxations are always far away. However, β-relaxation overlaps with α-relaxation at high temperature for pure PB polymer and PB75% blend, which is in agreement with common observations.

We can determine the characteristics of the β relaxation of the PB/SBR mixtures. The maxima of β-relaxation peaks could be easily identified for PB75% blends at low temperatures, as well as for PB50% and PB25 blends for all temperatures. **Figure 3.22**(d) shows the temperature dependence of the β relaxation time observed in blends. Data of the different blends superpose very well with the one measured on the PB sample showing the same linear dependence of $log(\tau)$ with $1/T$(K). We found again $\tau_0 = 10^{-16} s$ and $E_a = 38.7 kJ \cdot mol^{-1}$. It seems that as temperature increases, the amplitude of β-relaxation increases, we will try to quantify this evolution later.

We conclude that the β-relaxation of polymer blends remains exactly the one of pure polymer PB, indicating that β-relaxation is associated to localized motion accruing at a very small length scale. The β-relaxation measured by dielectric measurements is then hardy affected by blending.

The α relaxation in SBR/PB blends. There are overlaps of the α and β relaxation processes at high temperatures, preventing a direct analysis of the α process. In order to analyze the dielectric properties in the glass transition domain (α-relaxation), it is necessary to separate α-relaxation and β-relaxation and to study their respective evolutions.

3.5.2. α-relaxation and β-relaxation separation

For pure polymer PB and polymer blends, α-relaxation and β-relaxation have to be separated in order to test the time temperature superposition of the α-relaxation peaks. We have observed that the position of β-relaxation is independent on blend composition. However, the position of α-relaxation is dependent on blend composition and temperature. We will extract α-relaxation from our data.

The separation can be done by fitting the experimental data to the sum of two individual Havriliak-Negami functions:

$$\varepsilon^* - \varepsilon_\infty = \frac{\Delta\varepsilon_1}{\left(1 + \left(j\omega\tau_{HN}^1\right)^{\alpha 1}\right)^{\gamma 1}} + \frac{\Delta\varepsilon_2}{\left(1 + \left(j\omega\tau_{HN}^2\right)^{\alpha 2}\right)^{\gamma 2}} \qquad \text{(eq 3.9)}$$

where $\Delta\varepsilon_1$, α_1, γ_1 and τ^1_{HN} are the parameters for the α-relaxation and $\Delta\varepsilon_2$, α_2, γ_2 and τ^2_{HN} are the parameters for the β-relaxation. Since the loss peaks of β-relaxation are symmetric, γ_2 is usually fixed as γ_2=1, i.e. a Cole-Cole function [62].

Fitting the experimental data with the above equation requires knowing the temperature evolution of the amplitude of the two peaks $\Delta\varepsilon_1$ and $\Delta\varepsilon_2$, which numerically equal to the area of the calculated dielectric loss peak in log(f) coordinates [39].

The evolution of the amplitude of β-relaxation $\Delta\varepsilon_2$ at is easy to determine at low temperatures since α-relaxation does not overlap with the β-relaxation. **Figure 3.23** shows that $\Delta\varepsilon_2$ increases with temperature. At higher temperatures where two relaxations begin to overlap we do not know how $\Delta\varepsilon_2$ evolves. There are two hypotheses:
-   Hypothesis 1: the amplitude of β-relaxation is a constant one, as assumed by Colmenero et al. [55]. As a consequence, the α_2 parameter increases with temperature.
-   Hypothesis 2: the amplitude of β-relaxation increases. We can extrapolate from the data measured at low temperatures the ones at higher temperatures. As a consequence, the α_2 parameter varies slightly with temperature.
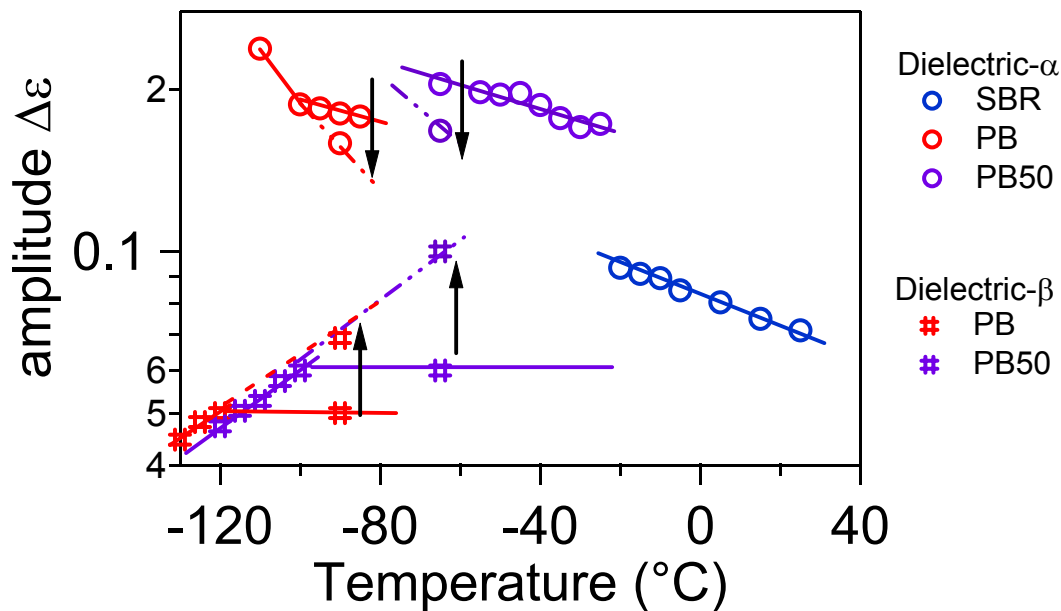
Figure 3.23. Evolution of the amplitude $\Delta\varepsilon$ of α and β relaxations for polymer blends PB/SBR as a function of temperature. Solid lines are fits with lower β-relaxation amplitude value (hypothesis 1) and dotted lines are fits with higher β-relaxation amplitude value (hypothesis 2).

We will test these two hypotheses separately. We observed that the assumption 2 induced a larger decrease of the amplitude of the α-relaxation peak. From **Figure 3.23** and **Figure 3.24**, we can observe that the form of the α-relaxation is changed at the high frequency side according to the assumption chosen for the temperature dependence of $\Delta\varepsilon_2$(T). The low frequency side is unchanged. Moreover, the position (i.e. maximum) of the α-relaxation does not depend on the assumption made for $\Delta\varepsilon_2$ (T) (see **Figure 3.24**).
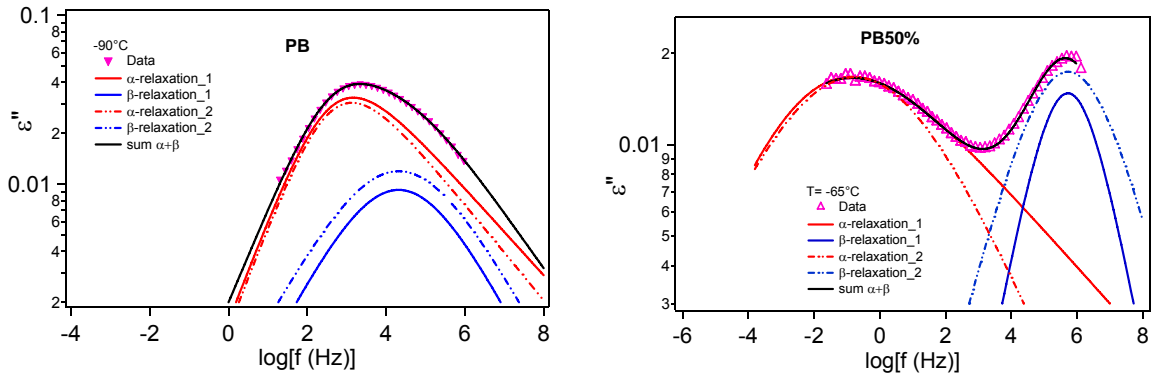
Figure 3.24. Separation of α-relaxation and β-relaxation by two individual Havriliak-Negami functions; (a) PB sample at -90°C, (b) PB50% samples at -65°C. Solid lines are fits with lower β-relaxation amplitude value (hypothesis 1) and dotted lines are fits with higher β-relaxation amplitude value (hypothesis 2).

In the following, we will present only the α relaxation peak extracted from experimental data using the assumption 1 for $\Delta\varepsilon_2(T)$. As a consequence, we will only analyze the temperature dependence of the α-relaxation peak position, which is not affected by the value chosen for $\Delta\varepsilon_2$ at high temperature.

With eq 3.8 and hypothesis 1, the α-relaxation and β-relaxation are thus separated for all temperatures. **Figure 3.25** shows all the curves of α-relaxation and β-relaxation after separation.
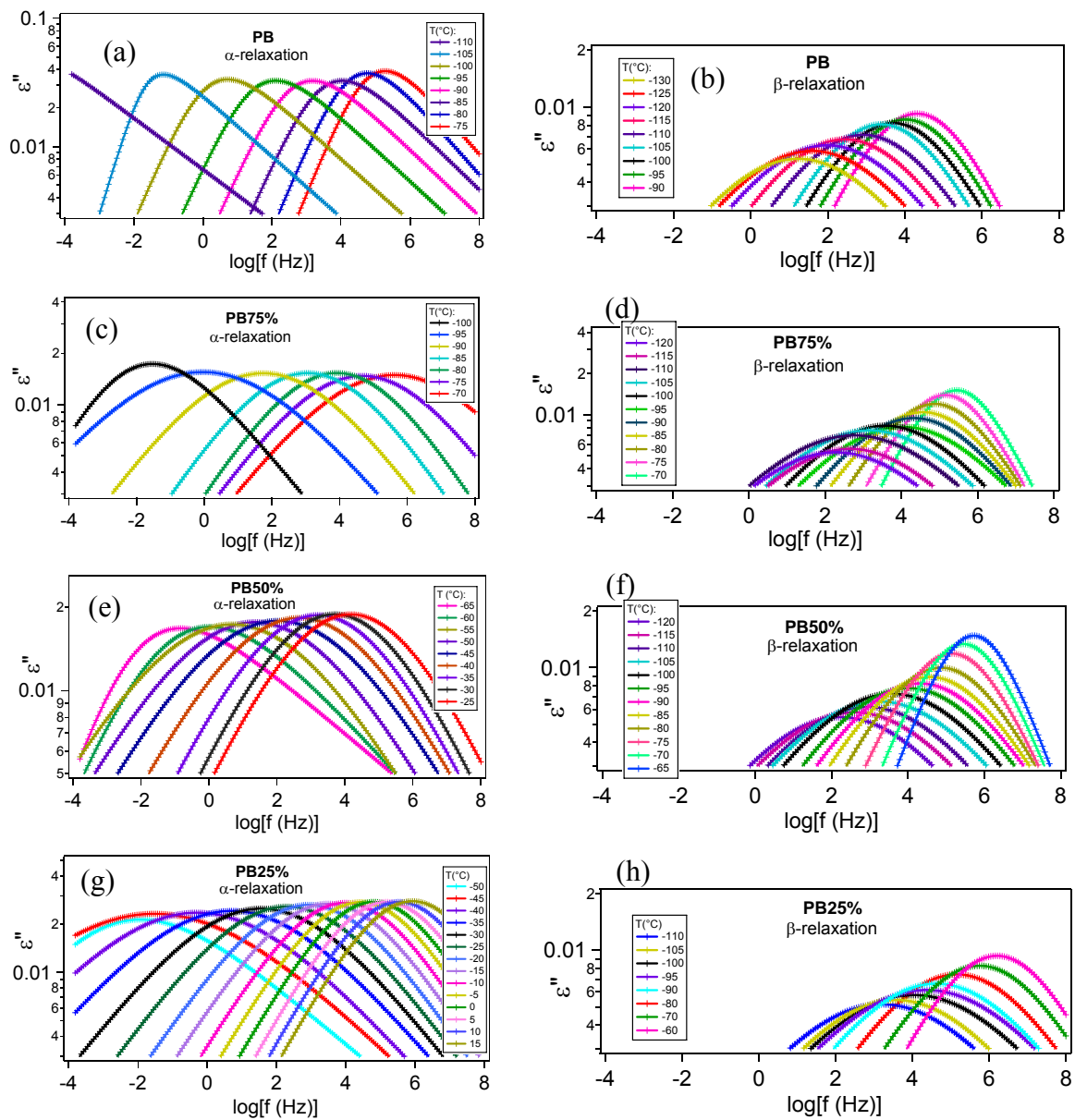
Figure 3.25. Separation of α-relaxation and β-relaxation by two individual Havriliak-Negami functions; (a) PB sample α-relaxation, (b) PB sample β-relaxation, (c) PB75% sample α-relaxation, (d) PB75% sample β-relaxation, (e) PB50% sample α-relaxation, (f) PB50% sample β-relaxation, (g) PB25% sample α-relaxation and (h) PB25% sample β-relaxation.

We will analyze the evolution of α-relaxation times versus temperature in the next section.

3.5.3. **Evolution of the position of α-relaxation in PB/SBR blends**

Pure PB. We first deduce the temperature dependence of the α-relaxation time. The evolution of the α-relaxation times $\tau = 1/(2\pi f_{max})$ of pure polymers PB is plotted as a function of temperature in **Figure 3.26**. They are compared to the one measured from rheological data. There is a good agreement between both set of α relaxation time values. They are fitted to the WLF law (see **Table 3.11**)
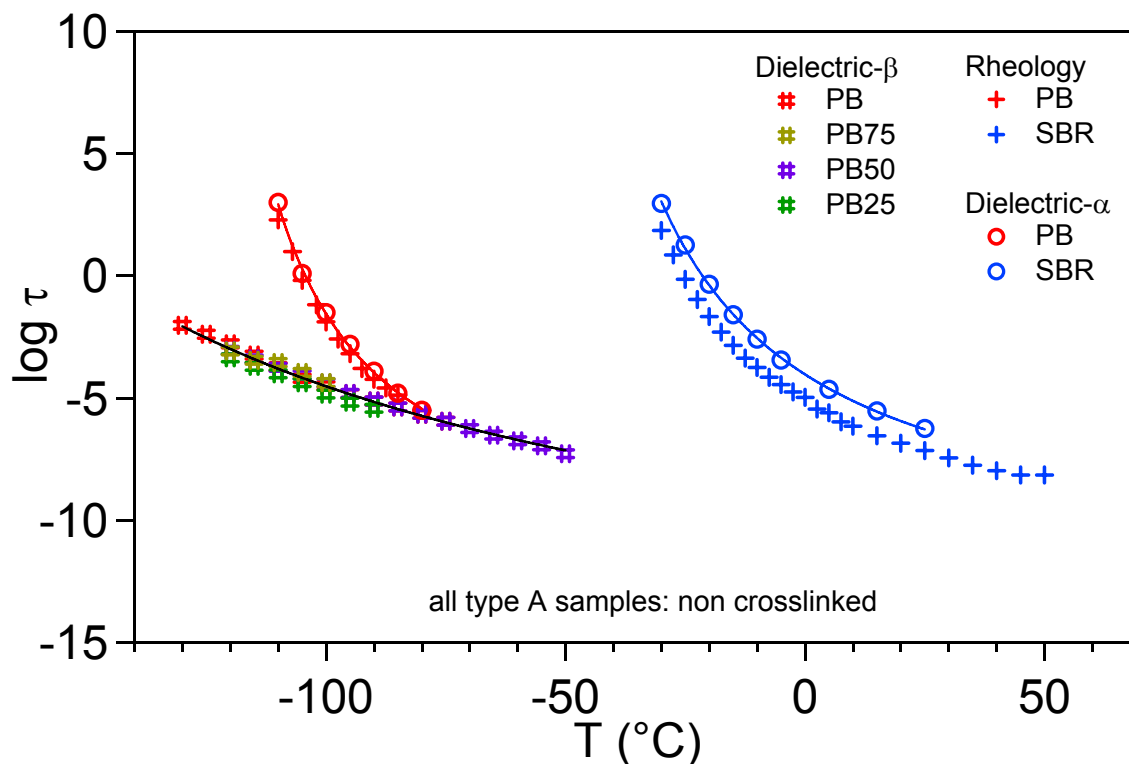
Figure 3.26. Evolution of the relaxation time as a function of temperature of non-crosslinked samples. Curves in (+) are rheological data, circles correspond to α-relaxation dielectric data, symbols (#) are β-relaxation dielectric data, and lines between circles are fits to WLF laws.

PB samples show a good agreement between rheological and dielectric α-relaxation data: the glass transition temperature T_g, and WLF fitting parameters C_1 and C_2 are all very similar.

Moreover the α-relaxation peaks of pure polymer PB superpose very well (see **Figure 3.27**). We observed a slight disagreement in the high frequency domain that can be explained by the influence of β-relaxation amplitude chosen for the α process extraction. Curves superpose well in the low frequency domains.
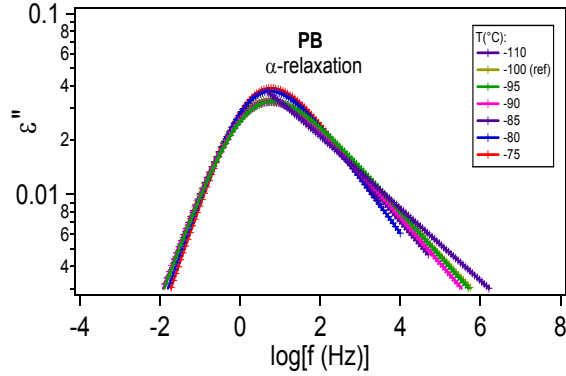
Figure 3.27. Superposition of dielectric α-relaxation loss peaks of different temperatures for PB with T_{ref}= -100°C.

PB/SBR blends. The evolution of the α-relaxation times is plotted as a function of temperature for each polymer blend (see **Figure 3.28**). From these curves, we determine a set of WLF coefficients giving the shift factors to apply to superpose the maximum of the dielectric loss (see **Figure 3.30**). We compared it to the one deduced from the rheological data.

Table 3.11. WLF law fitting parameters from dielectric data for non-crosslinked samples.

Dielectric		C_1^g	C_2^g	T_g (°C)	$\log(\tau_g)$ (s)
	PB	11.1	30.7	-102.3	-0.798
	PB75%	15	45.5	-95.6	-0.798
Type A	PB50%	15.4	99.5	-59.9	-0.798
	PB25%	13.1	72	-38.9	-0.798
	SBR	11.2	45.5	-18.4	-0.798

A=solvent mixing, non cross-linked

For PB75% samples, there is a good agreement between the results deduced from the two experimental techniques. However, for PB50% and PB25% samples, i.e. for blends showing the broadest T_g distribution by DSC, we observe a large difference between the mechanical and dielectric data on the value of τ_g but also on C_1 and C_2; This can be seen in the **Figure 3.28**.We will try to interpret these results in chapter 4.

The great difference between two experimental techniques is highlighted in **Figure 3.29**. The difference in temperature is about 30°C and in frequency is about 6 decades.
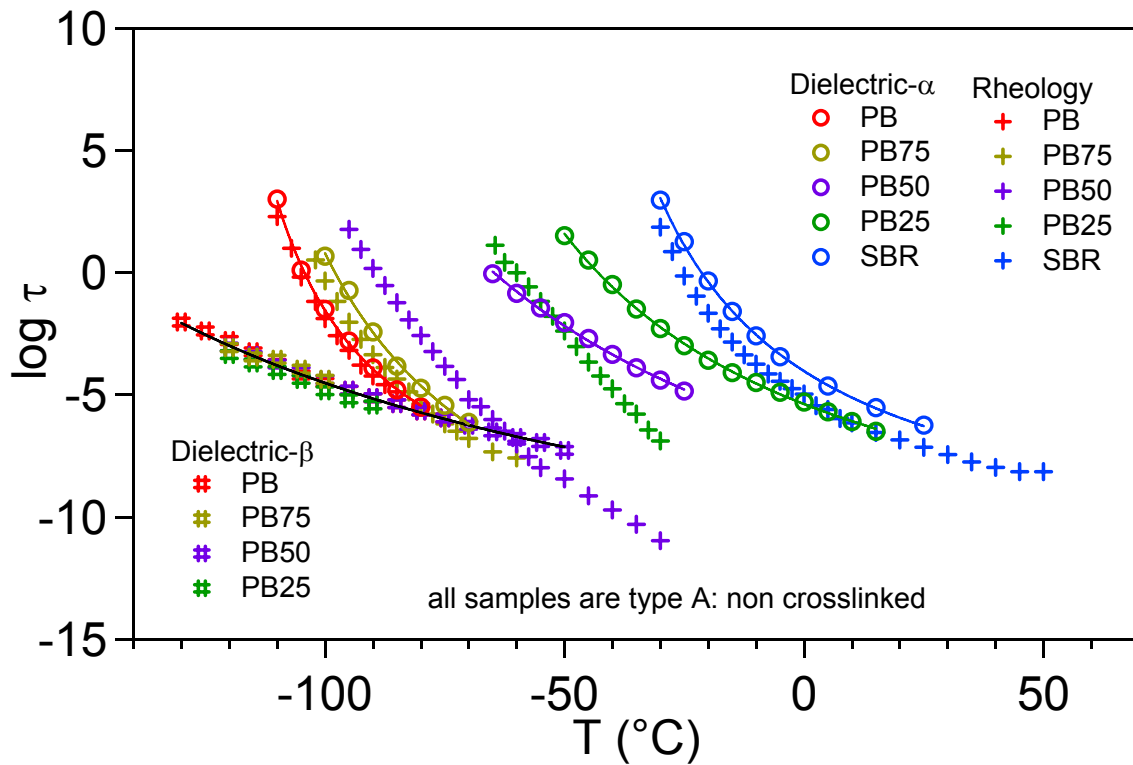
Figure 3.28. Evolution of the relaxation time as a function of temperature of non-crosslinked samples. Pluses are rheological data, circles are α-relaxation dielectric data, and symbols (#) are β-relaxation dielectric data. The line between (#) is a fit to the Arrhenius law, and lines between circles are fits to WLF laws.
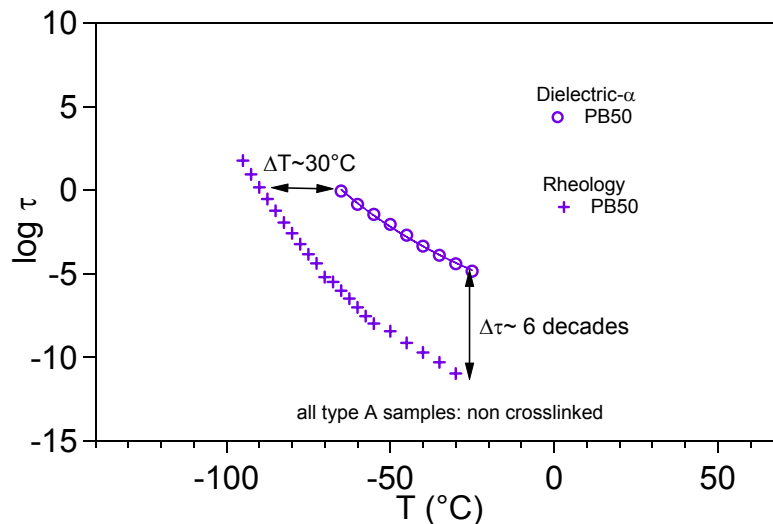
Figure 3.29. Evolution of the relaxation time as a function of temperature of non-crosslinked samples. Pluses are rheological data, circles are α-relaxation dielectric data, and lines between circles are fits to WLF laws.

Due to the influence of the β-relaxation subtraction on the α-relaxation shape, we can not really comment on the time-temperature evolution of the α-relaxation peak shape.

However, if we superimpose the maximum of the α-relaxation peaks, we do not observe a superposition of the low frequency side of the relaxation peaks for SBR/PB blends. It indicates that there would be a failure of the time-temperature superposition for the dielectric responses of our PB/SBR blends.
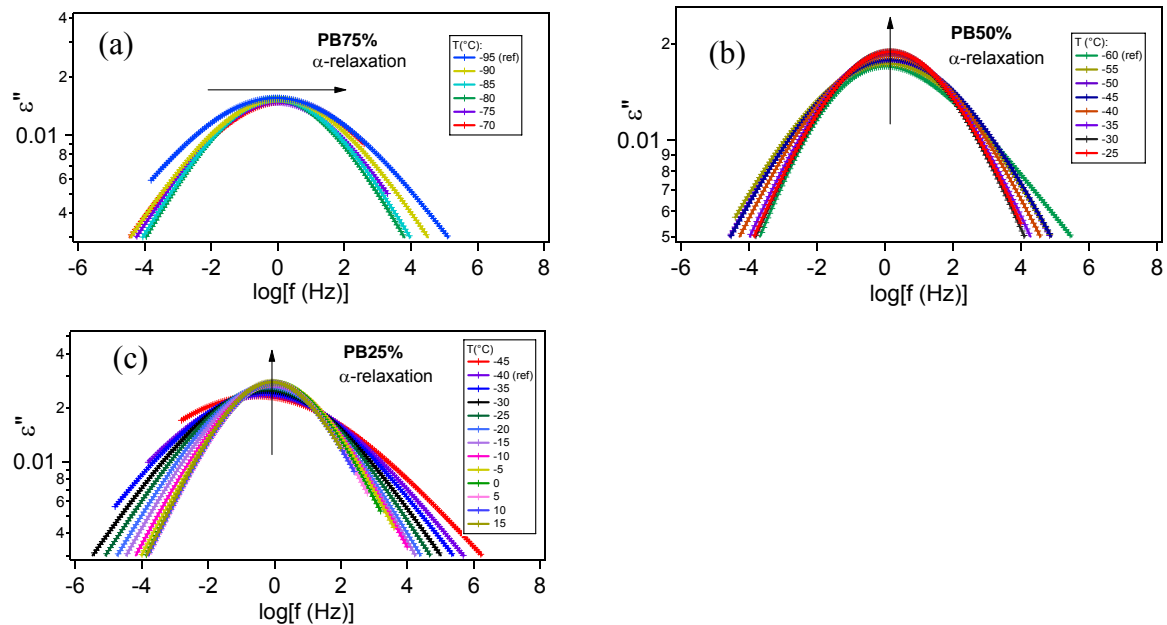
Figure 3.30. Superposition of dielectric α-relaxation loss peaks of different temperatures for (a) PB75% with T_{ref}= -95°C, (b) PB50% with T_{ref}= -60°C and (c) PB25% with T_{ref}= -40°C.

In conclusion, we observed that the dynamic heterogeneities have no effect on the secondary β dielectric relaxation in PB/SBR blends. At this length scale, there is no influence of blending on the local motions. However, heterogeneities induce changes of the dielectric properties in the glass transition domain. First, the characteristic relaxation time is significantly affected by mixing. However we observe a large deviation from the values determined from rheological measurements for mixtures in which the dynamical heterogeneities are the widest.

We will try to identify the origin of these differences between the rheological and dielectric response in chapter 4.

3.6. Conclusions on linear measurements

Experimental data of DSC, rheology and dielectric measurements have been presented in this chapter. In all cases, we observe a broadening of the glass transition zone (or the corresponding α-relaxation peaks), confirming that large dynamic heterogeneity exists in our PB/SBR blend.

These heterogeneities are particularly strong at the length scale of the segmental movement associated to the α-relaxation. However, their influence is not obvious on our blend systems at the longer length scales involved in rubber elasticity, nor in smaller length scale of localized motions controlling the β-relaxation. Indeed we do not observe any modification of the β relaxation of PB due to blending.

We observed in general a good time-temperature superposition for pure polymers and polymer blends for rheological data, but not for dielectric measurements

In the following chapter 4, we will focus on the distribution of relaxation times in our blend system and its relation with the different physical properties we measured.

We will first identify the distributions of relaxation times that control each physical response measured in chapter 3, and compare them with each other. We will then try to determine the length scale associated to each time relaxation distribution deduced from our experimental results.

4. Interpretation of the linear properties of PB/SBR blends in the glass transition zone

In chapter 3, we have observed the dynamic heterogeneity in our PB/SBR blends by different experiments, revealing a huge broadening of the glass transition zone.

The local dynamics are heterogeneous because of variability of the local arrangements of the two types of monomers in space. Some models have been developed to describe these effects, where the chain connectivity is taken into account (self-concentration effect) [38], and later the thermally driven concentration fluctuations [39]. In these approaches, at the nanometric scale, a mixture of miscible polymers is considered as a random distribution of domains, each one with a given composition, and thus exhibiting its own glass transition temperature. The concentration fluctuation is thus responsible for the width of glass transition temperatures (or relaxation times) distribution. In this frame, dielectric or DSC data measured on various miscible blends have been quantitatively described through detailed analysis of the dynamical heterogeneity [13,39–47]. On the contrary, there are in literature only few results that related the macroscopic viscoelastic properties of miscible blends to the dynamic heterogeneities. It is partly due to the difficulty to average properly the local mechanical properties of a heterogeneous system. It is thus difficult to clearly identify from a given macroscopic mechanical behavior the real relaxation time distribution associated. We will show in this chapter how to overcome this difficulty. We will show that it is the same relaxation time distribution that controls the calorimetric properties of our blends and their rheological properties in the glass transition domain. We will then identify the length scale of the concentration fluctuation that controls the linear mechanical behavior of our PB/SBR blends.

In this chapter, we will first estimate the length scale of the dynamic heterogeneities controlling the calorimetric response in our PB/SBR blends. To do this, we will start from the T_g distribution directly measured by DSC (chapter 4.1). We will then apply the approach developed by Shenogin et al.[39] to describe concentration fluctuation in miscible polymer blends (chapter 4.2).

Secondly we will discuss the consequences of the dynamic heterogeneity on the linear dielectric properties of blends (chapter 4.3) and we will interpret the great discrepancy between dielectric data and calorimetric data observed in chapter 3.

Finally, we will discuss the consequences of the dynamic heterogeneity on the linear viscoelastic properties of blends. We will prove experimentally for the first time that the assumption of a distribution of glass transition temperature gives quantitative relation between calorimetry and rheology (chapter 4.4). Chapter 4.1 and 4.4 are indeed part of our publication on 2013: Peiluo SHI, Hélène MONTES, Régis SCHACH, Etienne MUNCH, and François LEQUEUX. "Glass Transition Distribution in Miscible Polymer Blends: from Calorimetry to Rheology". *Macromolecules*, 2013, 46 (9), pp 3611–3620 [63].

4.1. T_g distribution $P(T_g)$ from calorimetry

In chapter 3.3, we already showed that we can deduce the T_g distribution function that controls the calorimetric response by derivation of the heat flow versus temperature $P(T_g) \cong P_{deriv}(T_g) = dHF(T)/dT$ (see **Figure 3.2**). This method is already used in literature [37,54]. We also showed in chapter 3.3 that $P(T_g)$ can be determine from the calorimetry response measured after physical aging. The envelop of all the heat flow differences measured between aged and unaged blends- called as $P_{aging}(T_g)$ in this work -gives a good approximation for $P(T_g)$ (see **Figure 3.7**).

In physical aging measurements, we choose to anneal the sample at a given temperature, to "print" by a memory effect the response of the domains at this given temperature. More precisely, annealing leads to a modification of a tiny domain's relaxation spectrum, the domain being the one of a relaxation time about the annealing time at the temperature of annealing. When heating back the sample, this relaxation spectrum modification printed by annealing can be read. This effect is well known as the memory effect previously studied on dielectric measurements [64,65] and mechanical measurements [66].
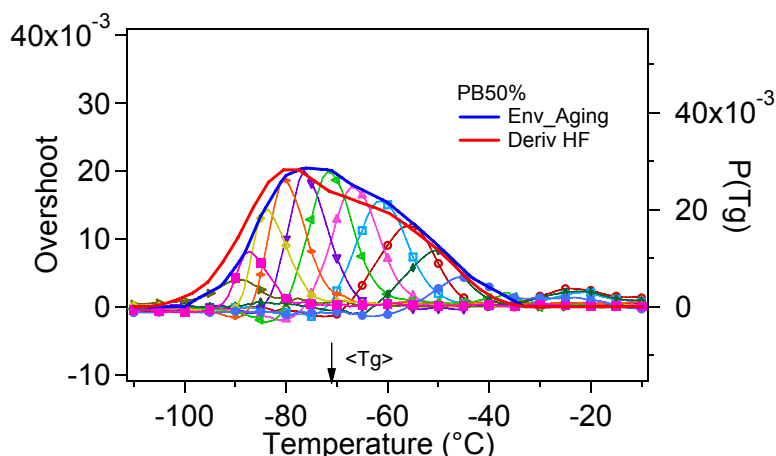
Figure 4.1. Comparison of the curve representing envelop of various overshoots to the one corresponding to $|dHF/dT|$.

The "fit" method and $P_{fit}(T_g)$. In order to describe the $P(T_g)$ distribution with the intrinsic parameters of our systems (for instance macroscopic composition of the blend, length scale of the T_g fluctuations, Kuhn length, …), we need to develop an analytical approach. In this frame, we will deduce the $P(T_g)$ by fitting the raw calorimetric response of the blends. We assume that a polymer blend is composed of independent domains of different local T_g, with a distribution $P(T_g)$. As a consequence, the calorimetric spectrum of a blend is expected to be a linear superposition of all the contributions of domains of various local T_g.

However, one of the difficulties of this extrapolation is that the SBR copolymer chains exhibit a width of its calorimetric response different from the one of PB. For each domain of composition T_g, we assume that the calorimetric response corresponding to such a domain that

78

we call $f(T-T_g)$ can be linearly extrapolated from the ones of the pure PB $f_{PB}(T-T_g)$ and SBR $f_{SBR}(T-T_g)$ polymers:

$$f(T - T_g) = k_{PB} f_{PB}(T - T_g) + k_{SBR} f_{SBR}(T - T_g) \qquad \text{(eq 4.1)}$$

with:

$$k_{PB} = (T_g - T_g^{SBR})/(T_g^{PB} - T_g^{SBR})$$
$$k_{SBR} = (T_g^{PB} - T_g)/(T_g^{PB} - T_g^{SBR}) = 1 - k_{PB}$$

where k_{PB} and k_{SBR} are the linear extrapolation coefficients. T_g^{PB} and T_g^{SBR} are the glass transition temperatures of respectively pure PB and SBR polymers. $f_{PB}(T-T_g)$ and $f_{SBR}(T-T_g)$ are the calorimetric response of respectively pure PB and SBR. Eq 4.1 assumes that the width of the glass transition, that is slightly broader for SBR than for PB varies linearly with the glass transition of the domains. We will see later that this approximation does not modify in practice the obtained T_g distribution.

Hence, the response of heat flow of a blend, $HF(T)$, can be calculated by summing over all the domains of T_g varying from T_g^{PB} to T_g^{SBR}.

$$HF(T) = \int_{T_g^{PB}}^{T_g^{SBR}} f(T - T_g) P_{fit}(T_g) dT_g \qquad \text{(eq 4.2)}$$

where $P_{fit}(T_g)$ is the distribution of glass transition temperature we are seeking for.
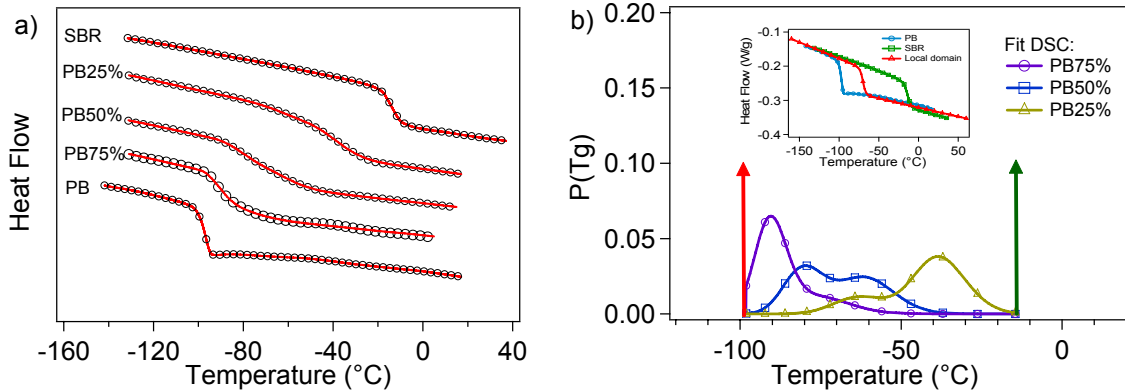
Figure 4.2. (a) DSC curves for different blends with experimental data (circles) and curve fitting (solid lines), curves are shifted vertically for clarity; **(b)** T_g distributions $P(T_g)$ for macroscopic blends Φ=0.25, 0.5 and 0.75. The inset is the calorimetric spectrum of pure PB (left), pure SBR (right) and a local domain of T_g=-77°C (middle).

For the sake of simplicity for the determination of $P_{fit}(T_g)$, we take for the T_g distribution $P_{fit}(T_g)$ a sum of two Gaussian distributions, corresponding to respectively the contribution of PB or SBR. It appears that it is similar to the method of Shenogin et al. [39]. The amplitude of each is thus fixed by the macroscopic composition Φ or $(1-\Phi)$. These conditions impose to consider only 4 free parameters that are the position $\overline{T_g}$ and the width w of the two Gaussian-like contributions. This writes indeed:

$$P_{fit}(T_g) = \Phi \frac{1}{\sqrt{2\pi w_{PB}}} \exp\left\{-\frac{(T_g - \overline{T_g^{PB}})^2}{2w_{PB}}\right\} + (1-\Phi) \frac{1}{\sqrt{2\pi w_{SBR}}} \exp\left\{-\frac{(T_g - \overline{T_g^{SBR}})^2}{2w_{SBR}}\right\} \qquad \text{(eq 4.3)}$$

We vary the four free parameters - by best chi-square fitting method - such that we obtain a good description of the experimental DSC curves (see **Figure 4.2**(a)). As we can see in **Figure 4.2** (b), our procedure allows to extract $P_{fit}(T_g)$ properly from the DSC data, and the $P_{fit}(T_g)$ has two peaks, this is in fact required by the self-concentration model.

$P_{fit}(T_g)$ is in principle similar to $P_{deriv}(T_g)$ only if $f(T\text{-}T_g)$ in eq 4.2 can be approximated by an Heaviside step function $H(T\text{-}T_g)$. In fact the main difference between the derivative method and the fit one, is that we include the natural broadness of the pure component glass transition with the derivative method, while the other not. This difference is thus given by the broadness of the homopolymer's T_g width observed by calorimetry. We will compare these methods in the following paragraph.

Discussion of the calorimetric response technique used to extract $P(T_g)$

We have shown that it is possible to obtain by three different ways, an approximated distribution of the glass transition temperature in polymer blends. However, the three methods differ also by the fact that they may exhibit or not an intrinsic broadness for the glass transition of the pure components themselves. Indeed $P_{fit}(T_g)$ has by definition a zero width for the glass transition of each of the pure components, which is not the case for $P_{deriv}(T_g)$ and $P_{aging}(T_g)$.

One of the difficulties of our blend is that the width of the glass transition as measured by calorimetry is different for the two components – because they are different copolymers. Our objective is to relate the width of the glass transition of the blends to its viscoelastic spectrum. But it is clearly out of the scope of this study to discuss the relation between the width of the calorimetric response and the viscoelastic one for the pure components. So in the next sections we will assign a single value of T_g to the viscoelastic response of a pure component PB or SBR.

However, to compare quantitatively the three methods, one have to take into account the broadness of the single constituent's glass transition. More precisely, we expect that the convolution between $P_{fit}(T_g)$ by the response of the single components ($f_{PB}(T\text{-}T_g)$ and $f_{SBR}(T\text{-}T_g)$) would approach $P_{deriv}(T_g)$ and $P_{aging}(T_g)$.

In **Figure 4.3**, on the left column (a), (b) and (c) we have plotted the raw value of $P_{deriv}(T_g)$, $P_{aging}(T_g)$ and $P_{fit}(T_g)$ for three PB/SBR mixtures, 25/75, 50/50 and 75/25 respectively. On the right column (d), (e) and (f) are plotted the same $P_{deriv}(T_g)$ and $P_{aging}(T_g)$, while $P_{fit}(T_g)$ is convoluted response of the pure components obtained with the aging techniques.

We see that there is a very good agreement between the aging and the convoluted "fit" in (d), (e) and (f), at least better than that in the (a), (b) and (c). On the contrary the amplitude of the maximum of the derivative technique, compared to other techniques, is respectively smaller and higher for PB25% and PB75%. We observe in addition that the agreement between $P_{aging}(T_g)$ and the convoluted $P_{fit}(T_g)$ is excellent, while the value of $P_{deriv}(T_g)$ seems slightly different from the two previous.
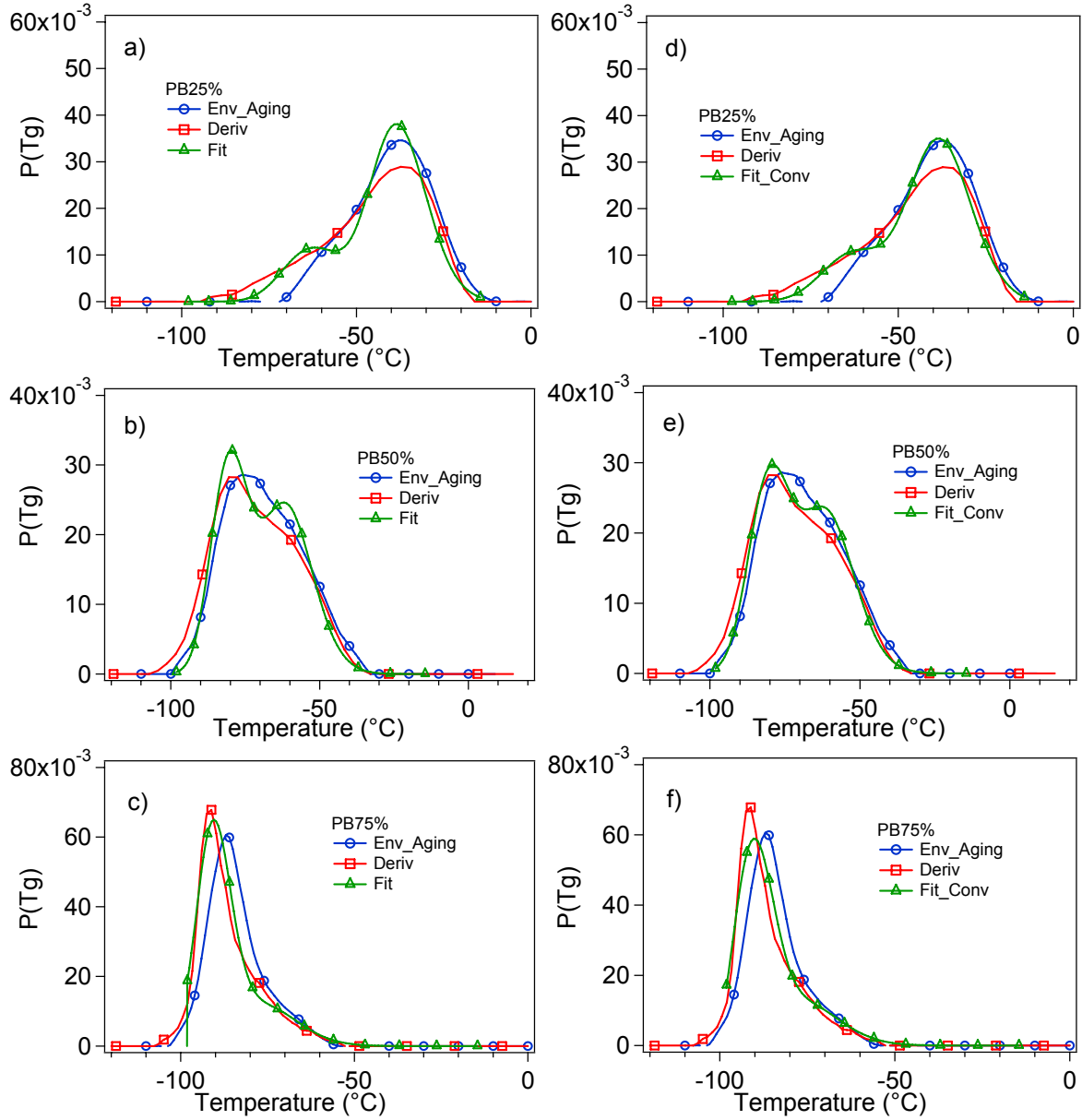
Figure 4.3. (a-c) Comparison of $P_{aging}(T_g)$, $P_{deriv}(T_g)$, and $P_{fit}(T_g)$ for Φ=0.25, 0.5 and 0.75. (d-f) Convolution of these 3 blends' $P_{fit}(T_g)$ with pure polymers' $P_{aging}(T_g)$ and comparison.

To sum up, the aging technique is the more accurate one, but it's time consuming and has to be deconvoluted from the intrinsic broadness of the homopolymers to get the blend information. The fit technique is extremely powerful, since it doesn't require deconvoluting the data. Finally, the derivative technique gives a fast result, but is less precise than the others. Therefore, in the next sections of this manuscript, we will use either aging or fit techniques, taking care of the convolution by the natural shape of the glass transition of each of the components of the blend.

4.2. Microscopic organization: what length scale for glass transition?

In this part, we will use the theoretical advances for miscible polymer, and extract the characteristic length scale of the concentration fluctuations that controls the glass transition measured by calorimetry in our blends. In practice we will use a method nearly equivalent to the one of Shenogin et al. [39], but applied to the calorimetric response.

4.2.1. Model description

The classical theoretical idea consists of considering that the segmental dynamics are controlled by the local effective concentration within a sphere of radius R_c centered on a certain component chain (A or B) (see **Figure 4.4**). Local effective concentration ϕ_{eff} in this sphere is a contribution of both the self-concentration ϕ_{self} and the environment composition ϕ :

$$\phi_{eff} = \phi_{self} + (1 - \phi_{self}) \times \phi \qquad \text{(eq 4.4)}$$

For small length scale $R_C < b$, the self-concentration ϕ_{self} is given by:

$$\phi_{self} = \frac{2vR_c/b}{4/3(\pi R_c^3)} = \frac{3}{2\pi} \frac{v}{bR_C^2}, \qquad R_C < b \qquad \text{(eq 4.5)}$$

where b is the Kuhn segment length and v is the volume occupied by a Kuhn segment.
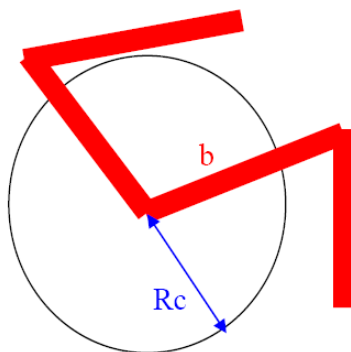
Figure 4.4. Schematic of the length scale in a polymer chain determining the self-concentration.

In the self-concentration model of Lodge and McLeish [38], the environment composition is the macroscopic blend composition, i.e. $\phi \equiv \Phi$. In the concentration fluctuation model [39], the environment composition is described by a distribution function $P(\phi)$, which is usually assumed to be Gaussian with a variance $\langle \delta\phi^2 \rangle$, and is inversely proportional to the volume V, through the static structure factor $S(Q)$ and the mean field random phase approximation (RPA) method. It gives:

$$\langle \delta\phi^2 \rangle = \frac{3\sqrt{v_A v_B}}{2\pi R_c} \left[\frac{b_A^2}{\Phi_A} + \frac{b_B^2}{\Phi_B} \right]^{-1} \tag{eq 4.6}$$

and the effective concentration variance (for component A) is:

$$\langle \delta\phi_{eff,A}^2 \rangle = (1 - \phi_{self}^A)^2 \langle \delta\phi^2 \rangle \tag{eq 4.7}$$

The local effective concentration ϕ_{eff}^A is thus also a Gaussian distribution:

$$p(\phi_{eff}^A) = \frac{1}{\sqrt{2\pi\langle \delta\phi_{eff,A}^2 \rangle}} \exp\left\{ -\frac{(\phi_{eff}^A - \overline{\phi_{eff}^A})^2}{2\langle \delta\phi_{eff,A}^2 \rangle} \right\} \tag{eq 4.8}$$

where the mean effective concentration $\overline{\phi_{eff}^A}$ is :

$$\overline{\phi_{eff}^A} = \phi_{self}^A + (1 - \phi_{self}^A) \times \Phi_A \tag{eq 4.9}$$

There are similar expressions for component B.

In this study, we consider by default that component A is PB and component B is SBR for simplicity in expressions. So ϕ_{eff}^A is the effective PB concentration in a volume centered on a PB chain, and ϕ_{eff}^B is the effective SBR concentration in a volume centered on a SBR chain. We define in addition that ϕ_{eff} is the effective PB concentration in a given volume, and $\phi_{eff} = \phi_{eff}^A = 1 - \phi_{eff}^B$.

The total distribution of the effective concentration in PB can be considered as a sum of the two distributions of each component, and the amplitude of each is determined as the macroscopic blend composition:

$$p(\phi_{eff}) = \frac{\Phi_A}{\sqrt{2\pi\langle \delta\phi_{eff,A}^2 \rangle}} \exp\left\{ -\frac{(\phi_{eff} - \overline{\phi_{eff}^A})^2}{2\langle \delta\phi_{eff,A}^2 \rangle} \right\} + \frac{\Phi_B}{\sqrt{2\pi\langle \delta\phi_{eff,B}^2 \rangle}} \exp\left\{ -\frac{(\phi_{eff} - (1 - \overline{\phi_{eff}^B}))^2}{2\langle \delta\phi_{eff,B}^2 \rangle} \right\}$$
$$\tag{eq 4.10}$$

An example is given in **Figure 4.5**. The macroscopic blend composition is $\Phi_A = \Phi_B = 0.5$. We observe two separate broad distributions, corresponding to two component dynamics A and B. Their positions are shifted from the macroscopic blend composition towards the pure ones of each, due to self-concentration effect. The broadness is due to concentration fluctuations.
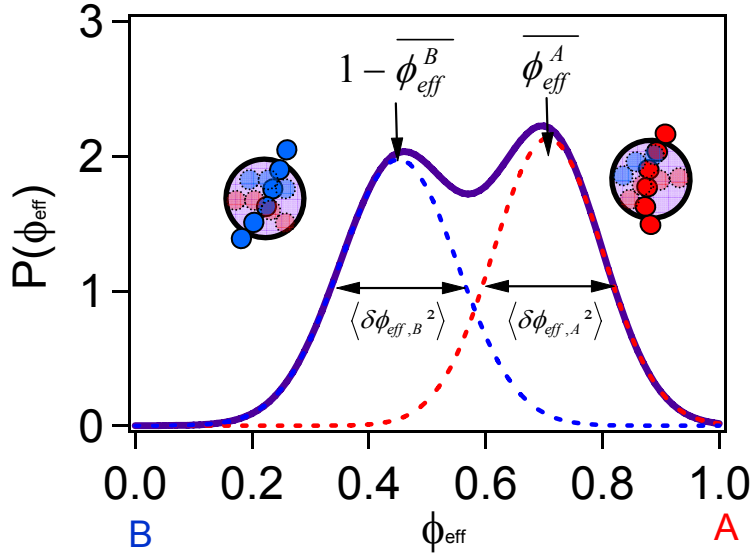
Figure 4.5. Effective concentration distributions of two component dynamics and the total bimodal distribution. The macroscopic blend composition is $\Phi_A = \Phi_B = 0.5$.

4.2.2. Evolution of $P(\phi_{eff})$ with the length scale

The structural parameters like Kuhn length b, volume v of a Kuhn segment for pure polymers PB and SBR are presented in **Table 4.1**. These parameters are calculated as an average of the parameters of the components 1,4-PB, 1,2-PB and PS, and details are given in **Annex B**.

Table 4.1. Kuhn length b, volume v of a Kuhn segment and the low limit of the length scale R_{c0} for pure polymers PB and SBR.

	b (Å)	v (Å^3)	R_{c0} (Å)
PB	9.9	147	2.7
SBR	11.8	266	3.4

Kuhn length of PB and SBR are similar and are about 1nm. **Table 4.1** shows in addition a parameter R_{c0} that is the low limit of R_c given by:

$$\phi_{self} = \frac{3}{2\pi} \frac{v}{bR_{C0}^2} = 1 \qquad \text{(eq 4.11)}$$

where R_{c0} corresponds to a domain entirely filled with the considered monomer. $R_c > R_{c0}$ simply appears because ϕ_{self} has to be smaller than 1.

The evolution of the mean effective concentration $\overline{\phi_{eff}^A}$ as a function of R_c can be calculated from **(eq 4.5)** and **(eq 4.9)**, and it gives:

$$\overline{\phi_{eff}^A} = \phi_{self} + (1 - \phi_{self}) \times \Phi_A = \frac{3v_A}{2\pi b_A R_c^2}(1 - \Phi_A) + \Phi_A \qquad \text{(eq 4.12)}$$

We can plot it in **Figure 4.6**(a). As R_c increases, ϕ_{self} decreases from 1 to 0, and $\overline{\phi_{eff}^A}$ decreases from 1 to the macroscopic blend composition Φ_A.

The effective concentration variance $\langle \delta\phi_{eff,A}^2 \rangle$ a function of R_c can be calculated from (eq 4.7) and it gives:

$$\langle \delta\phi_{eff,A}^2 \rangle = (1 - \phi_{self}^A)^2 \langle \delta\phi^2 \rangle = (1 - \frac{3v_A}{2\pi b_A R_c^2})^2 \frac{3\sqrt{v_A v_B}}{2\pi R_c} \left[\frac{b_A^2}{\phi_A} + \frac{b_B^2}{\phi_B} \right]^{-1} \qquad \text{(eq 4.13)}$$

The value is about 0 at R_{c0}, and it experiences a maximum value at a certain R_c before it goes down, see **Figure 4.6**(b)
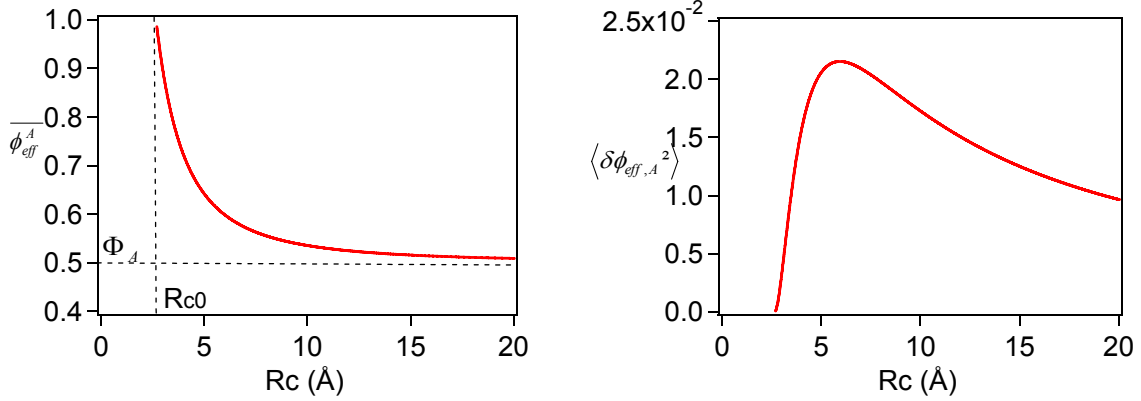
Figure 4.6. Evolution of (a) the mean effective concentration $\overline{\phi_{eff}^A}$ and (b) the effective concentration variance $\langle \delta\phi_{eff,A}^2 \rangle$ as a function of length scale R_c with parameters of pure PB: b=9.9Å and v = 147 Å^3, R_{c0} =2.7Å.

These evolutions can be illustrated in **Figure 4.7**. At very small length scale, the self-concentration effect is so strong that each of the two components is almost the same to its pure component, and we observe two narrow and distinct distributions, see **Figure 4.7**(b). At intermediate length scale, concentration fluctuation dominates, and we observe two broad distributions, see **Figure 4.7**(c). At very large length scale, concentration fluctuation is 0 and the effective concentration equals to the macroscopic one, see **Figure 4.7**(d).
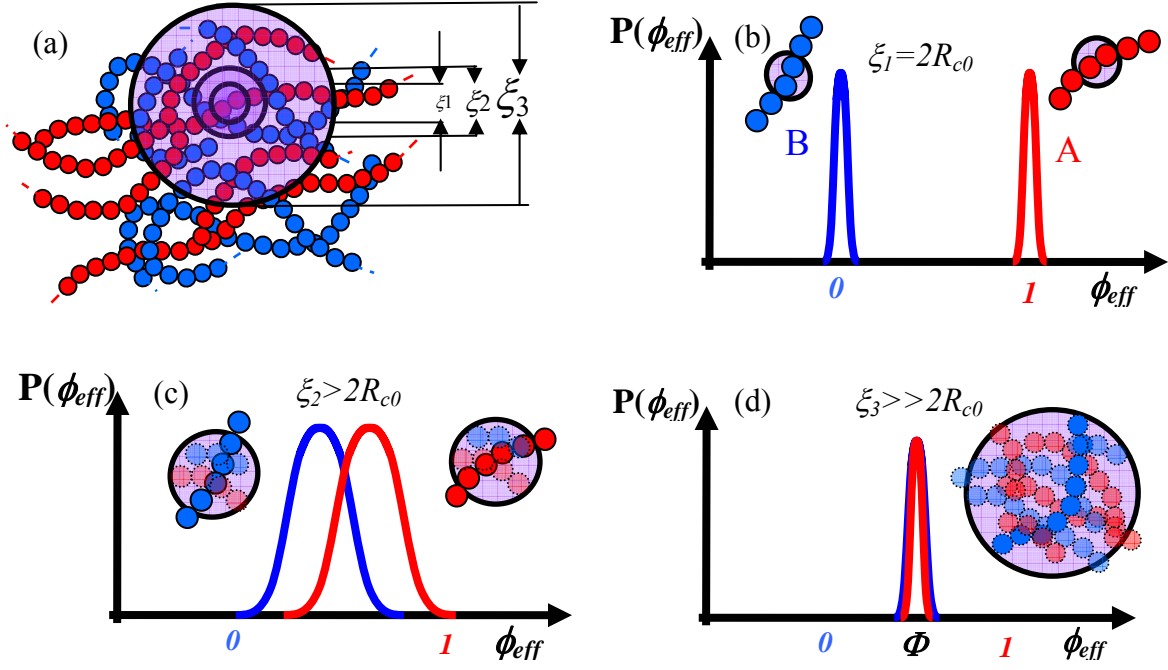
Figure 4.7. Illustration of the evolution of the position (mean effective concentration $\overline{\phi_{eff}^{A}}$) and the width (effective concentration variance $\left\langle \delta\phi_{eff,A}{}^{2} \right\rangle$) at different length scales. (a) Domains of a blend system with different length scales, (b) concentration distributions at very small length scale, (c) concentration distributions at intermediate length scale, and (d) concentration distributions at very length scale.

As a consequence, it is possible to estimate the length scale of a system, once the position and the width of the effective concentration distribution are quantified.

4.2.3. Length scale of PB/SBR blends

In this study, we first estimate the total effective concentration distribution $P(\phi_{eff})$ from $P_{fit}(T_g)$ in calorimetric fit method. We decide to fit $P(\phi_{eff})$ applying (**eq 4.10**) and varying the four parameters $\overline{\phi_{eff}^{PB}}$, $\overline{\phi_{eff}^{SBR}}$, $\left\langle \delta\phi_{eff,PB}{}^{2} \right\rangle$ and $\left\langle \delta\phi_{eff,SBR}{}^{2} \right\rangle$, in order to have a good description of the experimental data. Then we relate each of the four parameters to a length R_c in agreement with the approach developed by Shenogin [39]. We compare then the four R_c values we obtained. This method gives a good description of $P(\phi_{eff})$ that is not possible assuming only 2 lengths R_c, one for the PB chains and the second for the SBR component.

Then we have to assume that the local T_g of a blend follows the macroscopic and phenomenological Fox mixing law. This assumption is indeed very strong and some authors claim that it is not correct [37]. However, other authors have shown that it gives good results in practice, and it is the only available one up to now. Hence, in this Fox law approximation, the effective concentration ϕ_{eff} (of PB) is directly related to the local T_g through:

$$\frac{1}{T_g(\phi_{eff})} = \frac{\phi_{eff}}{T_g^{PB}} + \frac{1-\phi_{eff}}{T_{gB}^{SBR}} \qquad \text{(eq 4.14)}$$

and the effective concentration distribution $P(\phi_{eff})$ is related to the $P(T_g)$ by:

$$P(\phi_{eff}) = P(T_g)\frac{dT_g}{d\phi_{eff}}$$

(eq 4.15)

$P(T_g)$ is already obtained from calorimetric $P_{fit}(T_g)$. We can thus calculate the $P(\phi_{eff})$ in our polymer blends PB/SBR from DSC curves, see **Figure 4.8**. They are fitted to two Gaussian distributions by **(eq 4.10)** with four adjustable parameters: $\overline{\phi_{eff}^{PB}}$, $\overline{\phi_{eff}^{SBR}}$, $\left\langle \delta\phi_{eff,PB}{}^2 \right\rangle$ and $\left\langle \delta\phi_{eff,SBR}{}^2 \right\rangle$. They correspond respectively to the position and width of the two effective concentration distributions.
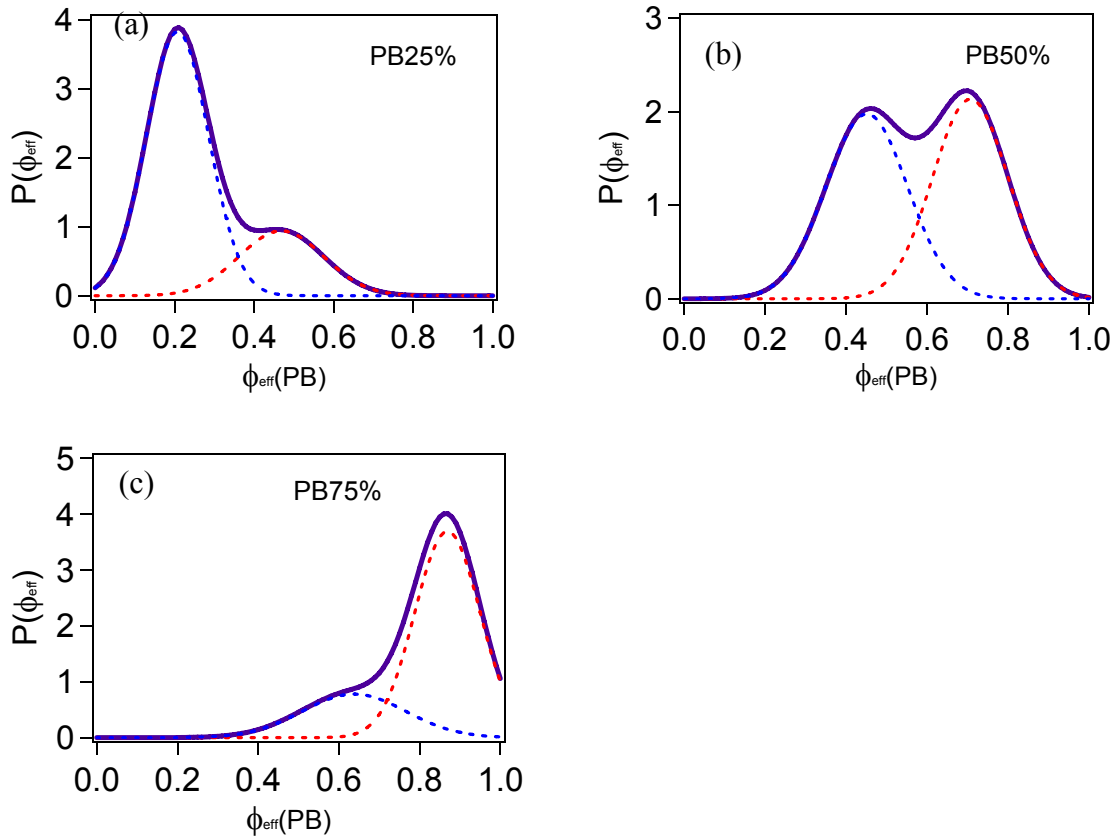
Figure 4.8. Effective concentration distribution $P(\phi_{eff})$ calculated from fitting method of DSC curves in polymer blends (a) PB25%, (b) PB50% and (c) PB75%.

Table 4.2. Fit parameters of the effective concentration distributions for PB/SBR blends.

	PB25%	PB50%	PB75%
Width of PB $\left\langle \delta\phi_{eff,PB}{}^2 \right\rangle$	0.11	0.09	0.08
Width of SBR $\left\langle \delta\phi_{eff,SBR}{}^2 \right\rangle$	0.08	0.1	0.12
Position of PB $\overline{\phi_{eff}^{PB}}$	0.47	0.71	0.87
Position of SBR $\overline{\phi_{eff}^{SBR}}$	0.21	0.45	0.64

Each of these four parameters can be associated to a certain value of R_c through **(eq 4.12)** and **(eq 4.13)**. For example, for a polymer blend PB50%, we can relate the position $\overline{\phi_{eff}^{PB}}$ =0.71 to a value of R_c=4.1Å, see **Figure 4.9**(a). The width of the effective concentration distribution of PB $\left\langle \delta\phi_{eff,PB}{}^2 \right\rangle$=0.09 can give two values of R_c=3.4Å or 21.5Å. The smaller one is in agreement with the one obtained from $\overline{\phi_{eff}^{PB}}$. We have verified in all cases that the smaller value of R_c is a reliable one. All the value of R_c with different blends and different parameters are presented in **Figure 4.10**.
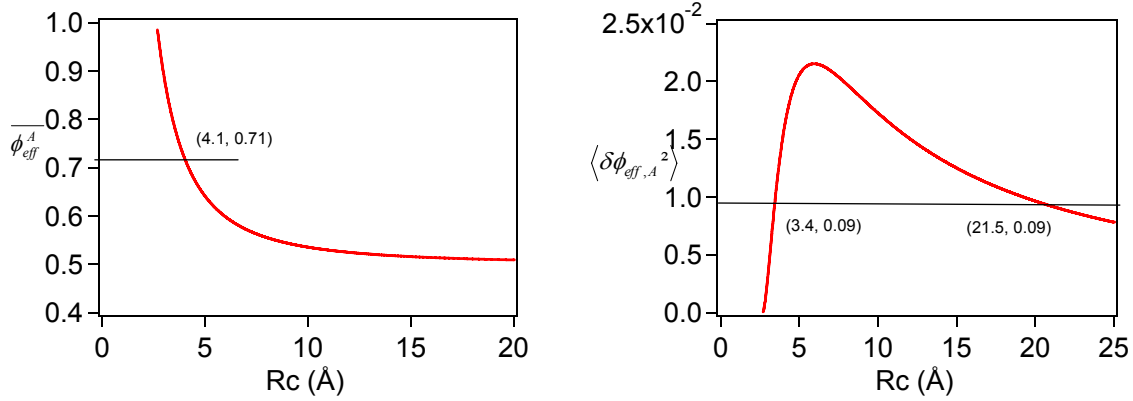
Figure 4.9. Determination of the length scale R_c from (a) the mean effective concentration $\overline{\phi_{eff}^{A}}$ and (b) the effective concentration variance $\left\langle \delta\phi_{eff,A}{}^2 \right\rangle$, with parameters of pure PB: b=9.9Å and v = 147 Å^3, R_{c0} =2.7Å, and Φ_{PB}= 0.5.

The value of R_c obtained from the position of SBR component is bigger than others, but they are of the same order. The average value of R_c is about 5Å for both PB and SBR. The self-concentration ϕ_{self} for PB is bout 0.4 and for SBR is about 0.2.
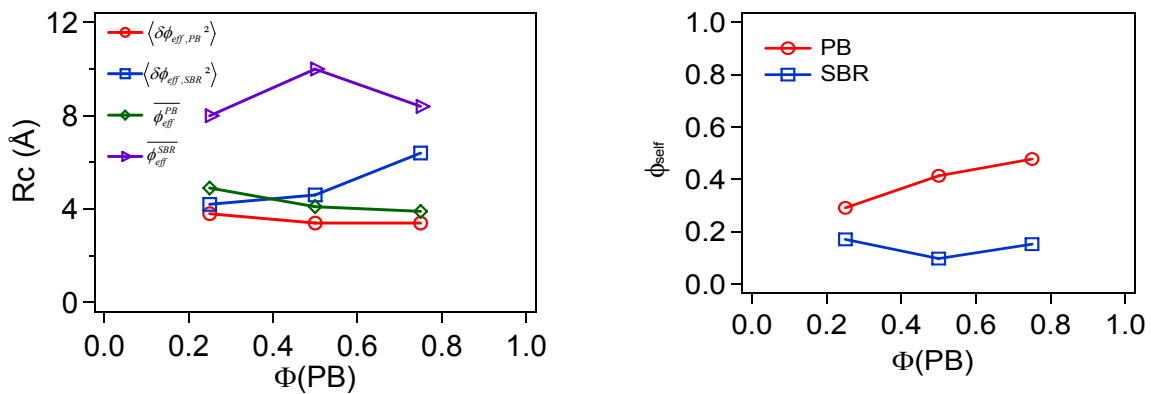
Figure 4.10. Values of (a) R_c and (b) ϕ_{self} for different blends.

In fact there are two weak points in our derivation of the length scale. First we assume a Fox law, and secondly we did not take in account explicitly the fact that our pure polymers are indeed copolymers, with an intrinsic composition fluctuation along the chains. Despite these two approximations, we obtain that the length scale which controls segmental dynamics

of blends PB/SBR at glass transition in calorimetric measurements is distributed at an average value of R_c=5Å, i.e. ξ=2R_c=1nm. The results are similar to the ones obtained by dielectric measurements on other miscible polymer blends [39], and is of the order of the corresponding Kuhn length assumed in literature [38,45].

4.3. T_g distribution and linear dielectric properties

In chapter 3, we have observed that calorimetric and rheological measurements give similar macroscopic T_g for our blends PB/SBR. However, dielectric measurements present a strong difference: the macroscopic T_g is about 30°C higher in PB50% blend.

In this section, we will analyze this discrepancy based on the self-concentration concept. We will show that the macroscopic T_g observed by dielectric measurements in the blend PB50% originate indeed mostly in the contribution of SBR chains. We will also discuss on the T_g distribution deduced from dielectric measurements.

Firstly, we will explain how to relate $P(T_g)$ to the macroscopic dielectric measurements. We will show that for a given $P(T_g)$, the intrinsic parameters fixing the broadness and the intensity of each local dielectric contributions can strongly influence the macroscopic response of the blend. We will then show in which way the dielectric response measured in the glass transition domain is related to the T_g distribution $P(T_g)$ determined from calorimetry measurements.

4.3.1. How to relate $P(T_g)$ to the macroscopic dielectric measurements?

The dielectric property of a pure polymer is usually described by a Havriliak-Negami function:

$$\varepsilon^* = \varepsilon' - j\varepsilon'' = \varepsilon_\infty + \frac{\Delta\varepsilon}{\left(1 + \left(j\omega\tau_{HN}\right)^\alpha\right)^\gamma}$$

$$\tau_{HN} = \tau\left[\tan\left(\frac{\pi}{2(\gamma+1)}\right)\right]^{1/\alpha} \qquad \text{(eq 4.16)}$$

where the relaxation time τ is determined by a WLF law **(eq 3.4)** as a function of temperature T, through C_1, C_2, T_g and τ_g parameters. We can thus describe the dielectric loss as a function of various parameters through HN function and WLF law:

$$\varepsilon'' = \varepsilon_{HN}''(\Delta\varepsilon, \alpha, \gamma, \tau_g, C_1, C_2, T_g, T, \omega)$$

$$= \varepsilon_{HN}''(i, T_g, T, \omega) \qquad \text{(eq 4.17)}$$

where i represents various characteristic component parameters: $\Delta\varepsilon, \alpha, \gamma, \tau_g, C_1, C_2$. For pure polymer A, we have a set of parameters i_A: $\Delta\varepsilon_A, \alpha_A, \gamma_A, \tau_g^A, C_1^A, C_2^A$, and

$$\varepsilon_A'' = \varepsilon_{HN}''(i_A, T_g^A, T, \omega) \qquad \text{(eq 4.18)}$$

Similar for pure polymer B, with parameters i_B: $\Delta\varepsilon_B, \alpha_B, \gamma_B, \tau_g^B, C_1^B, C_2^B$ and

$$\varepsilon_B'' = \varepsilon_{HN}''(i_B, T_g^B, T, \omega) \qquad \text{(eq 4.19)}$$

If the system has a strong dynamic heterogeneity, described for example by a broad distribution of $P(\phi_{eff})$, or $P(log\tau)$, or $P(T_g)$, the macroscopic property can be calculated by a sum of various local components in two methods.
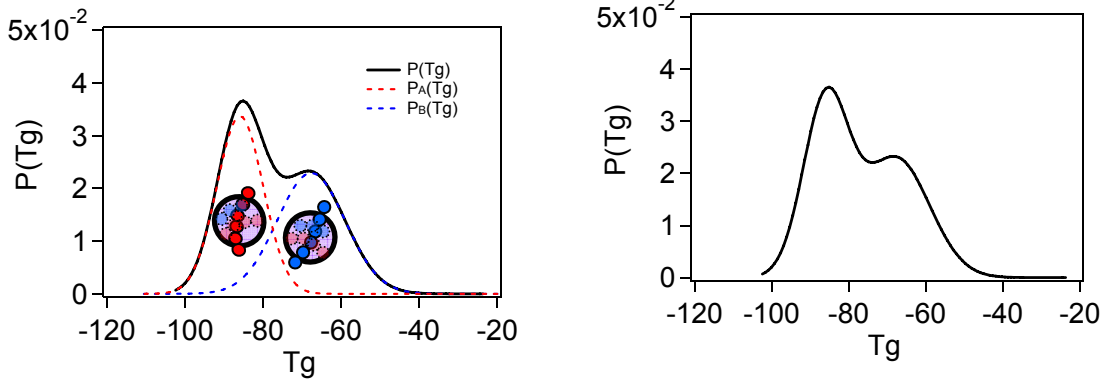
Figure 4.11. From $P(T_g)$ to macroscopic properties by two methods: (a) with separation of the distribution $P(T_g)$ in to two contributions : $P(T_g) = P_A(T_g) + P_B(T_g)$. (b) Without separation.

Method 1. The first method consist of separating the distribution $P(T_g)$ in to the contributions of the two types of polymer: $P(T_g) = P_A(T_g) + P_B(T_g)$, see **Figure 4.11**(a). The dynamical property is highly dependent on local structures. Even if two domains, one around polymer A and the second around polymer B, have the same effective concentration and thus local T_g, the local dynamics may be different for two domains. The response of each domain centered on a given polymer is thus described by the parameters of the pure polymer chain in the center of the domain, but with a glass transition shifted to the one of the domain average concentration according to the Fox law.

In the case of dielectric properties, domain A is described by $\varepsilon_A'' = \varepsilon_{HN}''(i_A, T_g, T, \omega)$, and domain B by $\varepsilon_B'' = \varepsilon_{HN}''(i_B, T_g, T, \omega)$. Two domains with same local T_g have different dynamics described by different i_A and i_B parameters. The macroscopic response is the total contribution of all the local T_g domains A and B:

$$\varepsilon'' = \varepsilon_A'' + \varepsilon_B'' = \int \varepsilon_{HN}''(i_A, T_g, T, \omega) P_A(T_g) dT_g + \int \varepsilon_{HN}''(i_B, T_g, T, \omega) P_B(T_g) dT_g$$

(eq 4.20)

In this method, i_A and i_B are calculated from the fits to the experimental relaxation data for pure components and are fixed values (except for $\Delta\varepsilon_A$ and $\Delta\varepsilon_B$ parameters that are adjusted by fits for each composition and for each temperature). This method is recently widely used by many authors [39,54,55].

Method 2. The second method does not distinguish two contributions of domains A or B. It assumes that the local dynamic is controlled by the effective concentration or local T_g. The dynamical parameters i_{AB} are assumed to have a linear composition dependence on i_A and i_B :

$$i_{AB} = i_A \phi_{eff} + i_B (1 - \phi_{eff})$$

(eq 4.21)

The macroscopic property is thus the total contribution of all the local domains:

$$\varepsilon'' = \int \varepsilon_{HN}''(i_{AB}, T_g, T, \omega) P(T_g) dT_g$$

(eq 4.22)

This idea has been suggested more than 10 years ago [67]. It is a simpler one without investigating the local structures. Indeed, if $i_A \approx i_B$ for all parameters, **(eq 4.22)** is equivalent to **(eq 4.20)**.

We will see in the following chapters that local dynamics in dielectric measurements are very different and we will use method 1 (chapter 4.3.2).

4.3.2. Prediction of dielectric properties of PB/SBR blends

In order to decide whether we use method 1 or 2, we will investigate all the parameters i_A and i_B of pure polymers PB and SBR.
The parameters i for pure polymers PB and SBR were calculated from the fits to the experimental relaxation data and are shown in **Table 4.3**. $i_A \approx i_B$ is valid for all parameters and we will thus use method 1 for dielectric predictions.

Table 4.3. Havriliak-Negami parameters and WLF parameters for pure PB and SBR polymers used for calculation of dielectric loss spectra. T_g determined by rheological and DSC (dT/dt=10°C/minute) measurements on the same samples are added for comparison.

Dielectric	PB	SBR
$\Delta\varepsilon$	0.18	0.08
α	0.62	0.46
γ	0.42	0.99
$\log(\tau_g)$	-0.798	-0.798
C_1^g	11.1	11.2
C_2^g	30.7	45.5
T_g(°C) Dielctric	-102.3	-18.4
T_g(°C) DSC	-102	-23
T_g(°C) rheology	-102	-22.5

We apply **(eq 4.10)** to predict the dielectric response of the SBR/PB blends. As already assumed by Shenogin et al. [39], the values of dielectric amplitude $\Delta\varepsilon$ are adjustable parameters in our fitting procedure. This choice is based first on the fact that the dielectric intensity $\Delta\varepsilon$ deduced from pure component dielectric data (**Table 4.3**) are not very reliable due to measurement error of the dielectric sample thickness (~0.3mm). In addition, the temperature dependence of dielectric amplitude is difficult to quantify as is shown in chapter 3.3.

Our prediction begins with the $P_{fit}^{DSC}(T_g) = P_{PB}^{DSC}(T_g) + P_{SBR}^{DSC}(T_g)$ from DSC method described in chapter 4.1. We assume that two Gaussian-like distributions correspond to domains centered on PB and SBR chains respectively.

We note from **Figure 3.26** and **Table 4.3** that rheology, DSC and dielectric measurements give the same value of T_g for pure PB polymer. However, those of pure SBR polymer have a difference of about 4-5°C between DSC/rheology and dielectric measurements. The dielectric α-relaxation time in pure SBR sample is longer than that of rheology: $\tau_\alpha^{dielectric} > \tau_\alpha^{rheology}$, because SBR is a copolymer with different monomers that have different polarizabilities and different dynamics. To take into account this difference, we use $P_{PB}^{dielectric}(T_g) = P_{PB}^{DSC}(T_g)$ and $P_{SBR}^{dielectric}(T_g) \approx P_{SBR}^{DSC}(T_g - 5°C)$ for our fits.

We found that it is possible to describe the PB50% experimental dielectric data applying $\Delta\varepsilon_{PB} \approx 0$ and $\Delta\varepsilon_{PB} << \Delta\varepsilon_{SBR}$. This means that the SBR component dielectric contribution dominates the macroscopic response measured in the glass transition of our polymer blend. The contribution of the PB component and thus the distribution function $P_{PB}^{dielectric}(T_g)$ would not be visible from dielectric data, due to the evolution of $\Delta\varepsilon_{PB}$ with temperature. Shenogin and co-authors [39] also observe a fast decrease of the $\Delta\varepsilon$ of one component PVME in PVME/PS in blends. **Figure 4.12**(b) illustrates the above discussed situation, where $\Delta\varepsilon_{PB}$ is too small to be visible and the total dielectric response is a sum of the α-relaxation of SBR chains contribution $P_{SBR}^{dielectric}(T_g)$ and the β-relaxation of PB chains. As a result, the contribution of $P_{PB}(T_g)$ is too small and is impossible to determine from dielectric data. The T_g distribution, from the Shenogin at al approach [39], and as measured by DSC gives a quantitative prediction for the dielectric signal.
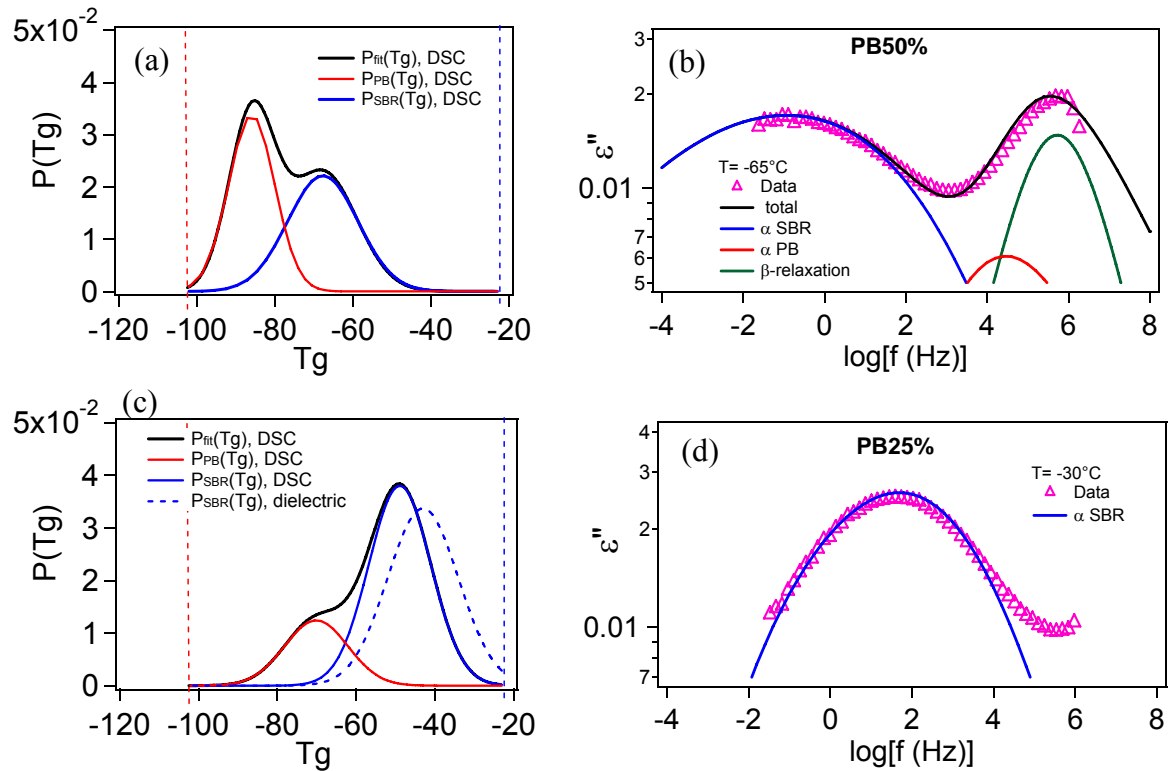
Figure 4.12. $P_{fit}(T_g)$ obtained from DSC fit method for non cross-linked (a) PB50% and (c) PB25% blends (black line), and two sub-distributions: red line is the contribution of PB chains, and blue line is the contribution of SBR chains. Dotted lines are limits of T_g distribution: T_g^{PB} and T_g^{SBR}. Figures (b) and (d) are corresponding dielectric predictions.

Thus when the SBR signal clearly dominates, it allows extracting the contribution of the SBR dynamics only. As a result, it corresponds approximately to the contribution predicted by the self-concentration approach when including statistical fluctuations.

The same procedure can be done for the PB25. The dielectric signal exhibit indeed a 6°C additional shift, as compared to calorimetry as plotted in **Figure 4.12**(c). We do not have any explanation for this 6°C shift – that would requires further studies to be interpreted. However, except this shift, we observe – similar as for PB50% - that the dielectric spectrum is similar to the SBR part of the calorimetric signal as predicted by Shenogin.

Thus to conclude, even if it is difficult to interpret quantitatively the dielectric data, because of the various temperature dependences of each of the components of the blends, we see that at least in the case of PB50% and PB 25%, the dielectric data are in agreement with the local concentration idea.

Indeed, the analysis of our dielectric data shows that the whole T_g distribution can be decomposed into two contributions, each related to one component. This result agrees with the approach developed by Shenogin. In addition, we use $P(T_g)$ which is related to $P(\phi_{eff})$ through the Fox law, validating a posteriori the use of Fox law as a microstructural mixing law.

It is possible to describe the dielectric response from the T_g distribution deduced from DSC data. We will now test if the rheological response is also controlled by the T_g distribution revealed by calorimetry. We will see that contrary to dielectric, the situation is more controlled because the mechanical weight of SBR and PB are similar contrary to the dielectric aces. However, if in the case of the dielectric properties, it is indeed relatively reasonable to sum the signal of each of the component, this is not at all the case for rheology, and we will have to introduce an original method to average correctly the rheological data.

4.4. T_g distribution and linear properties: from DSC to rheology

In this part, we will relate the viscoelastic response of our blends to the T_g distribution obtained by calorimetry. The starting point of our analysis is the following: each domain has its own local T_g and thus behaves as a viscoelastic polymer with a related characteristic time. Contrary to the dielectric response, the amplitude of the viscoelastic response is very similar for each of the pure polymers, PB and SBR at a given T-T_g.

We will not discuss here the relevance of the concentration fluctuation or self concentration. We will simply assume that the blends can be considered as an ensemble of domains as shown in **Figure 4.13**, each of those exhibiting its own glass transition temperature. This idea has been suggested more than ten years ago [67]. In this picture, the elastic modulus of each domain varies with frequency from the rubbery elastic plateau to the glassy one, i.e. from 10^6 Pa to 10^9 Pa typically. At a given temperature, each domain may exhibit very different characteristic relaxation times, fixed by the local value of T-T_g. So at a given frequency (or temperature), some domains may appear as glassy – with a modulus of about 10^9 Pa, and others as rubber-like, with a modulus of 10^6 Pa. Hence, to interpret quantitatively the viscoelastic data, one must be able to derive the macroscopic viscoelastic spectrum from local modulus values of randomly arranged domains varying over 3 orders of magnitude.

It is in general quite difficult to predict from the local mechanical properties of each constituent the macroscopic mechanical behavior of the blend [61]. In the mechanical engineering community, the most efficient way to solve this question appears to be the homogenization technique [68]. This latter is a sophisticated mean field approach predicting the relation between stress and deformation in heterogeneous systems. Homogenization technique consists of dividing the materials in periodic cells and of building a constitutive equation at the scale of a cell. Then the local constitutive equation is extended at the macroscopic level. To do so however, a simple averaging either of the stress or of the strain of the various constituents is performed at one step. This approach fails for very broad distribution of mechanical properties, because neither the stress nor the strain averaging is satisfactory: the stress averaging overestimates the contribution of the rigid domains and the strain averaging overestimates that of the softer domains. Here we propose and test a mechanical approximation that accounts for a 3D average of the viscoelastic modulus. We show that this averaging method of the linear viscoelastic modulus, based on the self-consistent approach of the Olroyd-Palierne model [69,70] gives excellent quantitative results even in the case of a wide distribution of viscoelastic moduli.

In this section we will first estimate the viscoelastic response of a local domain of blends with a local T_g from measurements of the single component systems. We will then explain how we apply self-consistently the Olroyd-Palierne model that has been developed for the prediction of the modulus of a blend of viscoelastic spherical inclusions in a viscoelastic matrix. We will conclude that the self-consistent mechanical model allows predicting without adjustable parameters the viscoelastic response of a blend in the vicinity of the α-relaxation.
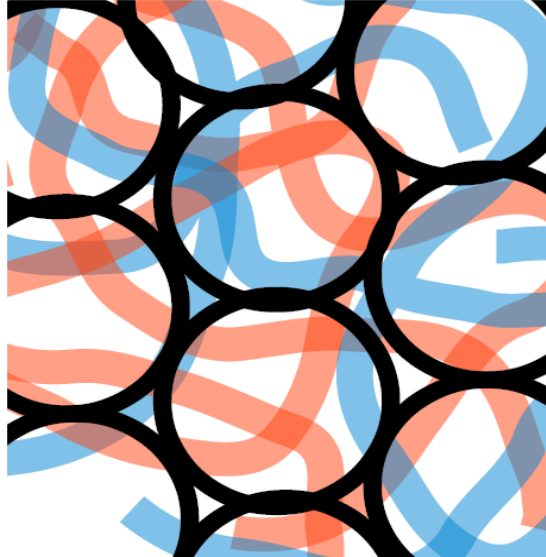
Figure 4.13. Schematic view of nanometric domains relevant for the glass transition. Blue chains and red chains have very different T_g. In the glass transition regime each of the domains has its own dynamic (because of either self-concentration effect or concentration fluctuations). We will assume that, irrespectively to any microscopic model, each domain exhibits - depending on its local glass transition T_g - an elastic modulus between 10^6 and 10^9 Pa.

4.4.1. Estimation of the viscoelastic spectra of a local domain of T_g.

We study solvent mixing and crosslinked PB/SBR blend samples (type B), where T_g^{PB}=-100°C and T_g^{SBR}=-15°C. As we already have precise data of the glass transition temperature distribution $P(T_g)$ from DSC, our next step consists in predicting the viscoelastic spectra from the T_g distribution obtained by DSC measurements.

First, we estimate the local viscoelastic spectrum $G_{loc}^*(T_g)$ corresponding to each local domain of T_g. We can deduce it from the viscoelastic spectrum of both pure PB and pure SBR. In the next section $G_{loc}^*(T_g)$ will be combined with the T_g distribution function $P(T_g)$ extracted from the previous calorimetric methods.

The viscoelastic spectra of the pure polymers can be described using a Havriliak Negami function, see chapter 3.44. The parameters α, β, τ, G_{glass} and G_{rub} were calculated from the fits to the experimental data for pure PB and pure SBR (see **Figure 3.18**(a) and (e)).

Table 4.4. Best chi-square fitting Havriliak-Negami parameters for pure polymers and any local domain of T_g.

	PB	SBR	Local T_g
$\log(\tau_g)$	-0.947	-0.871	$k_{PB} \log(\tau^{PB}_g) + k_{SBR} \log(\tau^{SBR}_g)$
T_g	-100	-15	T_g
α	0.705	0.752	$k_{PB}\alpha_{PB} + k_{SBR}\alpha_{SBR}$
γ	0.284	0.254	$k_{PB}\gamma_{PB} + k_{SBR}\gamma_{SBR}$
G_{glass} (Pa)	9.5×10^8	6.5×10^8	$k_{PB}G^{PB}_{glass} + k_{SBR}G^{SBR}_{glass}$
G_{rub} (Pa)	6.3×10^5	7.4×10^5	$k_{PB}G^{PB}_{rub} + k_{SBR}G^{SBR}_{rub}$

In practice we use the Havriliak-Negami function to describe the viscoelastic modulus $G_{loc}{}^*(T_g)$ of a local domain of T_g:

$$G^*_{loc}(T_g) = G_{glass}(T_g) - \frac{G_{glass}(T_g) - G_{rub}(T_g)}{\left(1 + \left(j\omega\tau_{HN}(T_g)\right)^{\alpha(T_g)}\right)^{\gamma(T_g)}}$$

$$\tau_{HN}(T_g) = \tau(T_g)\left[\tan\left(\frac{\pi}{2(\gamma(T_g)+1)}\right)\right]^{1/\alpha(T_g)} \tag{eq 4.23}$$

All parameters are linearly extrapolated from the one of the two pure polymers. This approach is used for the glassy and rubbery modulus, G_{glass} and G_{rub}, as well as the H-N exponents - all these quantities being in fact hardly different for PB and SBR. Indeed the parameters for pure polymers are shown in **Table 4.4**. They are in practice quite similar, but not exactly equal. Thus we decide to extrapolate linearly each parameter for the local domain of T_g – they are linearly extrapolated from the one of the two pure polymers: $i = i_{PB}k_{PB} + i_{SBR}k_{SBR}$. The coefficient k_{PB} and k_{SBR} are simply given by the relation:

$$k_{PB} = (T_g - T_g^{SBR})/(T_g^{PB} - T_g^{SBR})$$

$$k_{SBR} = (T_g^{PB} - T_g)/(T_g^{PB} - T_g^{SBR}) = 1 - k_{PB} \tag{eq 4.24}$$

The value of $\tau(T_g)$ can be derived from the WLF equation [10].

$$\log_{10}\left(\frac{\tau(T_g)}{\tau_g}\right) = -\frac{C_1^g(T - T_g)}{C_2^g + T - T_g} \tag{eq 4.25}$$

The C_1^g and C_2^g coefficients are determined from WLF fitting of pure polymers. In **Figure 4.14**, we have the WLF plot of the segmental relaxation time $\log\tau$ as a function of temperatures. These two polymers have similar WLF law, and can be approximated by a single fitting: $C_1^g = 11.9$ and $C_2^g = 37.7$.
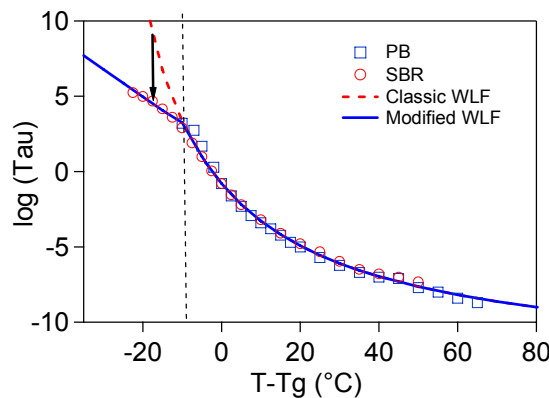
Figure 4.14. Segmental relaxation time of PB (rectangles) and SBR (circles). Classic WLF law (dotted line) and a modified WLF law (solid line): the deviation occurs at $T\text{-}T_g=10°C$.

We note that at $T\text{-}T_g<-10°C$, the data derivate from the WLF behavior and should be replaced by an Arrhenius law because it's in the non equilibrium glass regime [9,71–73]. It appears that this replacement is indeed important for the quality of our prediction.

Hence, in this section we explain how we deduce the local viscoelastic modulus $G_{loc}^*(T_g)$ of a local domain of T_g, from the mechanical property of the pure PB and SBR polymers.

We now have to explain how we can deduce, from the distribution function $P(T_g)$ of local viscoelastic modulus $G_{loc}^*(T_g)$ extracted from the DCS technique, the macroscopic mechanical spectrum of the whole blend.

4.4.2. Description of the macroscopic mechanical response of the blends

First observations on the parallel and series averaging methods. It is interesting to start by analyzing the results that would be obtained from classical – but approximated – mean of averaging. There have been many discussions in the literature on the accuracy of averaging the stress at a given strain, or the strain at a given stress in polymer blends. In **Figure 4.15**, we have plotted for the blends Φ=0.25, 0.5 and 0.75 the results of the stress average - the representative domains being in parallel spring/dashpot representation:

$$G_{//}^* = \int G^*(T_g)P(T_g)dT_g \qquad \text{(eq 4.26)}$$

and the one for a compliance average – the representative domains being in series in a spring/dashpot representation.

$$\frac{1}{G_{ser}^*} = \int \frac{P(T_g)}{G^*(T_g)}dT_g \qquad \text{(eq 4.27)}$$

Clearly neither the parallel nor the series averaging is able to give a correct description, and there are very different. The parallel estimation overestimates the elastic modulus. A glassy domain with a modulus of 10^9 Pa will have a contribution equivalent to the one of 10^3 rubber-like domains, according to (**eq 4.26**). While the same glassy domain, as a single rigid inclusion with a volume fraction of ϕ=10^{-3}, is known to increase the elastic modulus by a factor of $1+(5\varphi/2) \cong 1.0025$.

The series estimation (**eq 4.27**), for symmetrical reasons, underestimated the modulus even for a volume fraction of rubber-like domains of only 10^{-3}. Consequently, in the high frequency domain, the stress averaging (parallel) gives the most efficient approximation of measured ones, while the strain averaging (series) is better at lower frequency. However none of the models are able to give a good prediction of the data in the glass transition domain. For that we need to take into account that there are inclusions of domains in a matrix self-consistently. This can be done thanks to the Olroyd Palierne model.

Application of the Olroyd –Palierne model. The Olroyd-Palierne model [69] is a continuum mechanics calculation of the macroscopic viscoelastic complex modulus G_m^* of a viscoelastic matrix of complex modulus G_{mat}^* embedding various spherical viscoelastic inclusions G_i^* each one with a small volume fraction f_i. Originally the authors of this model have included effects of surface tension that will not be considered in this specific study. The model indeed gives the exact displacement and stress field in and out a spherical viscoelastic inclusion in a viscoelastic matrix. It is extended to the situation where various different – and

more or less diluted – inclusions are present. It gives a rigorous expression for the modulus in the limit of infinitely dilute inclusions, in the absence of interfacial stress that can be written as follows:

$$G_m^* = G_{mat}^* \left(1 + \frac{5}{2} \sum_i f_i H_i \right)$$
(eq 4.28)

where

$$H_i = \frac{2G_i^* - 2G_{mat}^*}{2G_i^* + 3G_{mat}^*}$$
(eq 4.29)

This expression can be seen as a generalization of the Einstein relation for the viscosity of solid suspensions. Indeed, if the inclusions' modulus tends towards infinity, H_i tends toward 1, and (**eq 4.28**) simply becomes $G_m^* = G_{mat}^* \left(1 + \frac{5}{2} \sum_i f_i \right)$, which transforms into the Einstein relation for the complex modulus of a purely viscous system, i.e. $G_{mat}^* = i\omega\eta$.

In our case, the system is entirely constituted of domains, where each of them has a peculiar viscoelastic modulus. However, it can be considered homogeneous at a macroscopic scale with a modulus G_{blend}^* [70,74]. In order to determine this modulus, one can consider the system as a homogenous matrix containing a small fraction of viscoelastic inclusions. Let us choose the inclusions that are representative of the whole domains moduli distribution i.e. that they have the same moduli distribution $P(T_g)$ than the system itself. Thus, as the inclusions are representative of the matrix itself, they must not modify the system modulus. Thanks to (**eq 4.29**), the modulus of the matrix of modulus G_{blend}^* is modified by the presence of the distribution of inclusions, but as the inclusions have the same $P(T_g)$ than the matrix, this modification must vanish. This gives us a self-consistent approximation for the modulus of the blend G_{blend}^*. The assumption used implicitly here is that the matrix can be considered as exhibiting a homogenous viscoelastic modulus around each domain. We will see that this approximation is highly satisfactory in the present case. So we take a distribution of representative inclusions of modulus $G^*(T_g)$ with a volume distribution $\lambda P(T_g)$ and a total volume fraction $\lambda \ll 1$. The fact that the system's modulus is exactly the same with and without the representative inclusions leads to the integral equation that can be deduced from (**eq 4.28**) and (**eq 4.29**) :

$$G_{blend}^* = G_{blend}^* \left(1 + \frac{5}{2} \lambda \int \frac{2G^*(T_g) - 2G_{blend}^*}{2G^*(T_g) + 3G_{blend}^*} P(T_g) dT_g \right)$$
(eq 4.30)

One can see that whatever the value of λ, this relation holds if:

$$\int \frac{2G^*(T_g) - 2G_{blend}^*}{2G^*(T_g) + 3G_{blend}^*} P(T_g) dT_g = 0$$
(eq 4.31)

This gives an integral equation for G_{blend}^* as a function of $P(T_g)$ and $G^*(T_g)$. Indeed this is an integral equation that is not easy to solve, and we choose a recursive method, that appears to be quite efficient. It consists in iterating the following suite – starting from any value of $G_{blend,1}^*$, for instance the value given by (**eq 4.26**) or (**eq 4.27**):

$$G_{blend,n+1}^{*} = \cfrac{1}{\displaystyle\int \cfrac{5P(T_g)dT_g}{2G^{*}(T_g) + 3G_{blendt,n}^{*}}} \qquad \text{(eq 4.32)}$$

In practice, this suite converges in a few tens of steps towards the solution of (**eq 4.31**).
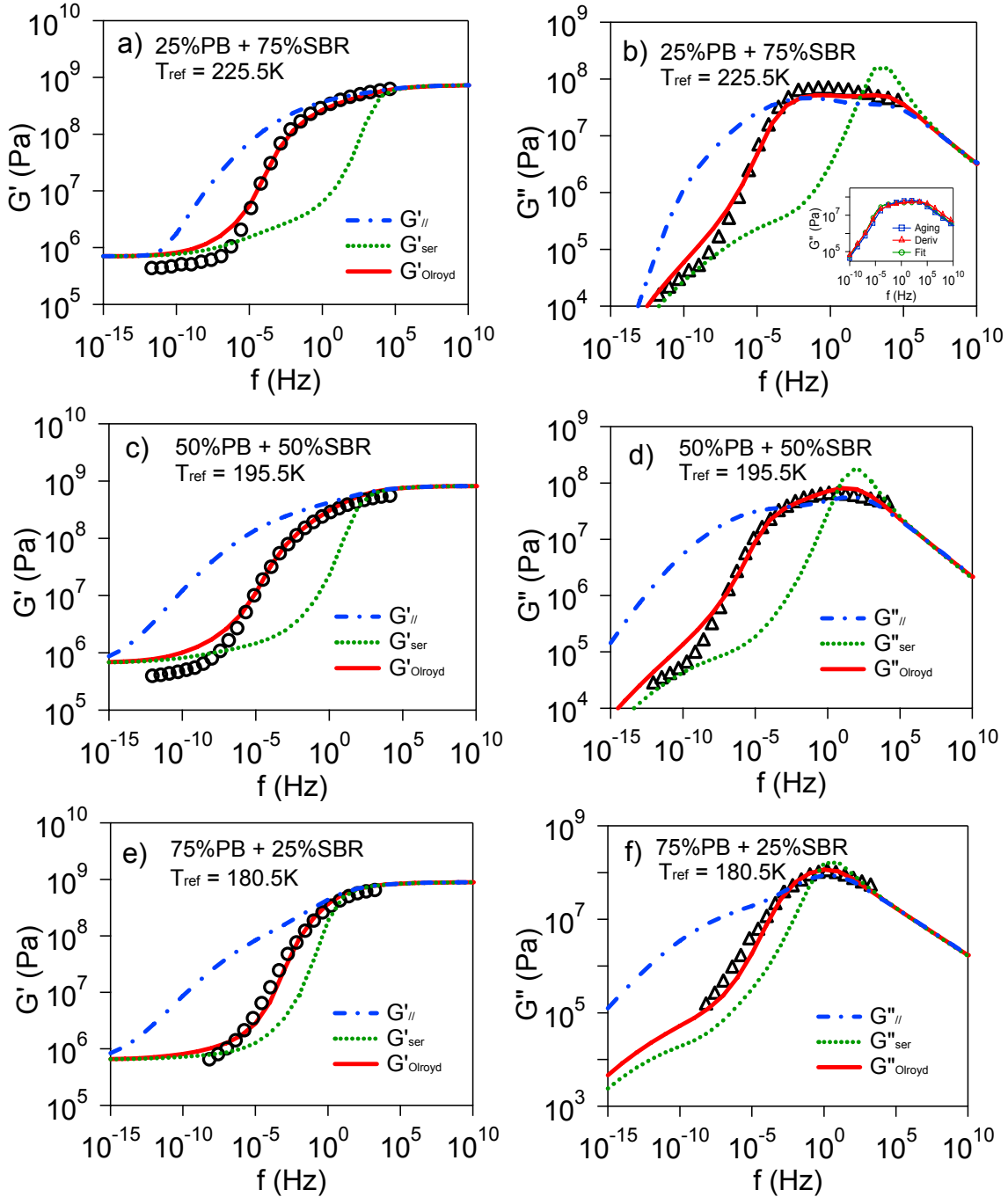
Figure 4.15. Experimental data of master curves for storage modulus (circles) and loss modulus (triangles) as a function of frequency. Comparison between the prediction of the Olroyd Palierne model (solid lines), and the series (dotted lines) and parallel (dashed-dotted lines) averagings for 3 blends, all of them using $P_{fit}(T_g)$. Inset (b): three predictions of G'' corresponding to the use of the $P_{fit}(T_g)$, $P_{deriv}(T_g)$ and $P_{aging}(T_g)$ of Figure 8(a).

As the pure components viscoelasticity are represented by a Dirac distribution of T_g, the more convenient choice for $P(T_g)$ is the fit one. The results are shown in **Figure 4.15**. Clearly the series and parallel approach fail to describe the glass transition domain. The discrepancy between both the series and parallel prediction and the data is indeed of the order of 4 decades in frequency. At opposite the agreement between the data and the self-consistent approach is always good with a discrepancy smaller than a decade in the glass transition regime.

Of course the prediction is not satisfactory at lower frequency. In these domains, Rouse mode becomes predominant, and can not be accounted simply by the self-consistent method, as segment of chain that relaxes in this regime belongs to more than one glassy domain, i.e. distance between crosslinks or entanglements. **Figure 4.16** shows the responses of PB50% blends with 3 types of preparation. They have the same behavior at high frequency which is well described by our self-consistent Olroyd Palierne model. They are different at low frequency Rouse mode domain due to differences in crosslink density. Indeed taking into account the Rouse modes that may extend over various glassy domains is clearly out of the scope of our approach, which is focused on the glass transition.
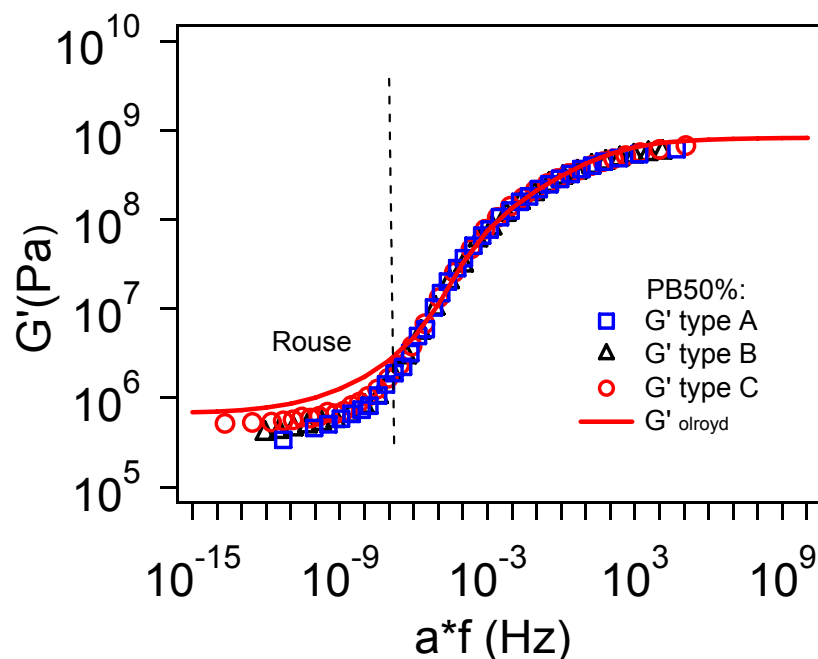
Figure 4.16. Master curves for PB50% storage modulus *G'* as a function of frequency, with 3 types of preparations. References temperatures are the glass transition temperature of each polymer: $T_{ref}=T_g$, the values of which are shown in **Table 3.8**.

Lastly we can compare the various values of $P(T_g)$. In the inset of **Figure 4.15** (b), we have zoomed the three predictions of *G''* corresponding to the $P_{fit}(T_g)$, $P_{deriv}(T_g)$ and $P_{aging}(T_g)$ of **Figure 4.3**(a). We see that the difference is clearly not significant.

To sum up, the use of this method to predict the viscoelastic spectrum of our polymer blends appears to be extremely efficient. In **Figure 4.15**, the viscoelastic data and the prediction from Olroyd-Palierne self-consistent model agrees nearly perfectly. We recall that there is no adjustable parameter in the mechanical prediction, all the data being deduced from the calorimetric measurements and the viscoelastic spectrum of the pure polymers.

There is indeed a huge discrepancy between the estimation from parallel viscoelastic elements and the prediction from Olroyd Palierne self-consistent approach. This originates indeed from the fact that the mechanical averaging decreases the broadness of the viscoelastic spectrum as compare to the one obtained with an additive averaging. As soon as part of the rigid domains – with a glassy modulus 10^3 the one of the rubbery modulus - just consists in independent inclusions with a volume fraction less than 10%, they do not influence significantly the viscoelastic response any longer. At opposite calorimetry measures the sum of the contribution of the relaxations of each domain, and is thus sensitive to the volume fraction of the domains. Thus the apparent broadness of the time relaxation distribution that could be extracted naively from an analysis of the viscoelastic spectrum as the sum of viscoelastic contributions – corresponding to a "parallel" approximation - clearly underestimates the real width of $P(T_g)$ distribution. This is perfectly consistent with discussion in literature about the fact that the product of "translational diffusion coefficient" and "viscosity" increases when decreasing the temperature in the glass transition domain (see the discussion in Chapter 1.2.3). Indeed the two quantities (viscosity and diffusion coefficient) are different averages of the same $P(T_g)$. We show here directly that the mechanical properties originates in the same $P(T_g)$ than calorimetry, but weighted very differently than calorimetry – for which a simple sum gives the correct result. We suggest here that the Olroyd Palierne self-consistent approach allows for the first time to relate the viscoelastic spectrum to precise $P(T_g)$ distribution.

4.4.3. Conclusion on the interpretation of viscoelastic response and its relation to calorimetry

We show that the viscoelastic spectrum of blends in the glass transition domain can be predicted using the T_g distribution measured by DSC applying a self-consistent Olroyd-Palierne model –The model assumes simply that glassy domains are nearly spherical and randomly distributed. This result shows that in the linear regime, a polymer blend can be considered in its glass transition regime as an arrangement of independent viscoelastic domains, each one with a specific glass transition. The length scale of the dynamical heterogeneities that control the viscoelastic mechanical properties of our polymer blends is the same as the one involved in the calorimetry response. This length scale is around 1 nm according to the theoretical approach developed by Shenogin.

4.5. Conclusions on linear properties of PB/SBR blends

This chapter successfully related various linear properties (calorimetry, physical aging, dielectric, rheology) of PB/SBR blends to its glass transition distribution $P(T_g)$.

This $P(T_g)$ can be extracted by different methods from calorimetric measurements with or without physical aging. The length scale associated to α-relaxation can be deduced from the width and position of $P(T_g)$. From calorimetric measurements, the length scale is around a value of ξ=1nm.

From the study of dielectric response, we first remark that β-relaxation is unaffected by the blending. However, the dielectric response of each component exhibits its own temperature variation, leading to a difficulty to extract simply the contribution of each component in the signal. As a result, the α-relaxation observed by dielectric measurements in PB50% blend originates in fact nearly only in the contribution of domains centered on SBR chains. The α-relaxation peak of domains controlled by the dynamics of PB chains is not visible. The contribution of the SBR chain is in agreement with the calorimetric measurement, confirming that the phenomenological Fox law relating local concentration and local T_g is good.

Regarding the viscoelastic spectrum of blends, a polymer blend can be considered in its glass transition regime as an arrangement of independent viscoelastic domains, each one with a specific glass transition and local dynamics. We have proved experimentally for the first time that the assumption of a distribution of glass transition temperature gives quantitative relation between calorimetry and rheology.

To conclude, the heterogeneities of polymer blends as observed in their linear regime are particularly strong at the length scale of segmental movement associated to the α-relaxation (~1nm). However, these heterogeneities are no more relevant at larger length scale involved in rubber elasticity (~10nm).

In the next chapter, we will study the influence of the existence of great dynamic heterogeneities on the nonlinear mechanical properties of polymer blends.

5. Nonlinear properties of PB/SBR blends in the glass transition zone

Most of the mechanical responses of polymers during large deformation are highly nonlinear. In this chapter, the nonlinear mechanical properties of PB, SBR and their blends are studied by simple extension and cyclic shear tests. The objective of this chapter is to answer the following questions:
- Is there a time-temperature superposition for nonlinear mechanical properties in pure polymers and polymer blends?
- How the dynamical heterogeneities influence the plastic deformation of polymers?
- What are the several mechanisms involved in the non linear deformation of a polymer from the rubber state to the glassy state? Can we characterize the transition from rubber non linear elasticity to plastic deformation? Do plastic events occur at the very beginning of the glass transition?

We firstly present some experimental difficulties (i.e. self-heating and non homogeneous deformation) in large deformation tests and some solutions are proposed. Then we give detailed analysis of simple extension test and cyclic shear test respectively, showing that nonlinear time-temperature superposition is valid in our blend system.

We explain the details of the estimation of the non-linear mechanical properties in the glassy domain, as they are intricate with the viscoelastic response of the sample. We then deduce the appearance of plasticity and show that it correlates to the percolation of glassy domains.

5.1. Experimental difficulties

Two difficulties should be taken into consideration: self-heating and non homogeneous deformation.

5.1.1. Adiabatic self-heating

Self-heating is due to low thermal conductivity and relatively high energy dissipation of polymers. For simple extension test, a large portion (~50%) of the mechanical work during deformation is converted to heat [24–26]. For cyclic shear test, the internal heat generation power per unit volume P_v can be calculated as:

$$P_v = E_d f = \pi G'' \gamma_0{}^2 f \qquad \text{(eq 5.1)}$$

At adiabatic condition, the evolution of temperature is

$$\frac{\partial T}{\partial t} = \frac{P_v}{\rho c_p} = \frac{\pi G'' \gamma_0{}^2 f}{\rho c_p} \qquad \text{(eq 5.2)}$$

where
  E_d = Heat generation per unit time per unit volume per cycle ($W \cdot m^{-3} \cdot cycle^{-1}$)

ρ = Density ($\sim$950 $kg \cdot m^{-3}$ for our polymers)

c_p = Heat capacity at constant pressure ($\sim$ 1800 $J \cdot kg^{-1} \cdot K^{-1}$ for our polymers)

This temperature evolution is very important at the glass transition zone where G'' is the maximum, with large deformation amplitude γ_0, and with high frequency. For example, for G''=5×10^7 Pa and γ_0=20%, this corresponds to $\Delta T \approx$ 4K per cycle.
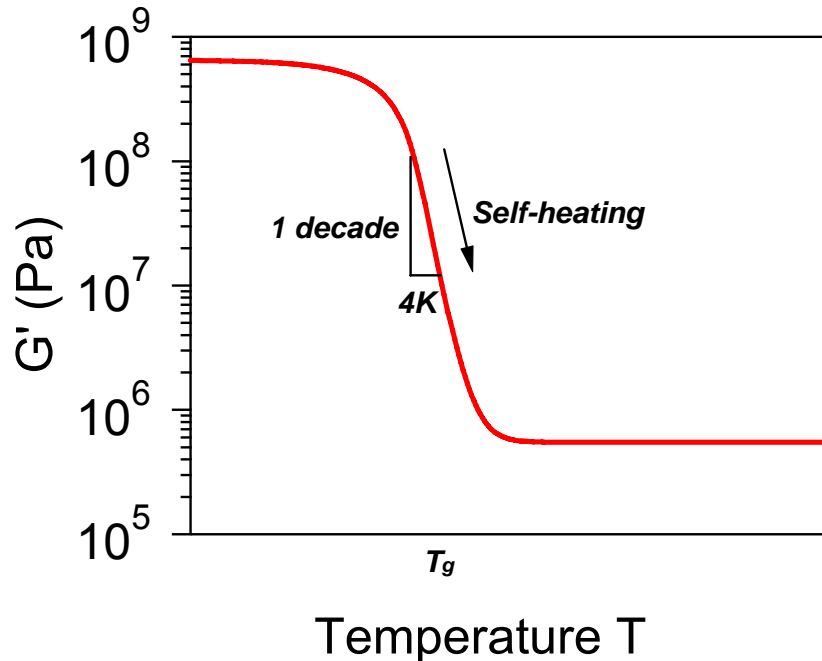
Figure 5.1. A sharp decrease of elastic modulus during self-heating.

Temperature evolution can have an extremely strong influence on the mechanical properties of polymers; since their modulus are strongly temperature dependent (see **Figure 5.1**). Strong self-heating of the material is combined by a sharp decrease of its elastic modulus. For example, a temperature increase of $\Delta T \approx$ 4K at the glass transition zone corresponds to a modulus decrease of about one decade which could be

$$\frac{\Delta G'}{G'} \approx \frac{10^8 - 10^7}{10^8} = 90\% \ .$$

Self-heating is always accompanied by the heat transfer through 3 mechanisms: radiation, conduction and convection. The cooling down of a heated sample by heat transfer is usually fitted by an exponential one:

$$T = T_0 + \Delta T \exp(-t / \tau_{ht}) \tag{eq 5.3}$$

where T_0 is the ambient temperature and τ_{ht} is a characteristic time scale of the heat transfer who depends on the material properties, geometries, and environmental conditions.

We have shown in **Annex C** that the dominant mechanism that controls the heat transfer in shear test sample is conduction towards the metallic holders with the time scale $\tau_{ht} \sim$ 4s, while that in extension test sample is convection with $\tau_{ht} \sim$ 41s.

The real situation is a competition between heat generation and heat transfer, as a function of the frequency or the measurement time t_{mes} (~ 1/frequency). If:

- $t_{mes} \gg \tau_{ht}$, heat transfer is efficient, and the sample is in isothermal condition. With low strain rate in extension test or low frequency in cyclic test, the measurement time t_{mes} is much longer than the heat transfer time scale τ_{ht}. Consequently, there is no self-heating. Most of the measurements in literatures are done under this experimental condition.
- $t_{mes} \approx \tau_{ht}$, there is moderate self-heating and temperature distribution in the sample is not homogeneous due to heat transfer. This situation is to avoid.
- $t_{mes} \ll \tau_{ht}$, heat transfer is not efficient, and the sample is in adiabatic condition. With high strain rate in extension test or high frequency in cyclic test, the measurement time t_{mes} is much shorter than the heat transfer time scale. Consequently, there is strong self-heating but temperature distribution in the sample is homogeneous. Measurements in this situation could be useful, if only the temperature evolution could be precisely measured, by infrared camera, for example.

To sum up, mechanical tests should be performed either at high strain rate (in the adiabatic regime) or at low strain rate (in the isothermal regime). The evolutions of temperature during the deformation of polymers have to be properly measured in both cases by the infrared camera.

5.1.2. Non homogeneous deformation

Another difficulty is that during tensile deformation at glassy state, a stable neck is formed shortly after yield point and it grows until fracture. This phenomenon is associated with the plastic instability in glassy polymers. Therefore, the deformation of glassy polymers under tension is non homogeneous due to the onset of the macroscopic neck in the sample and the true stress is difficult to determine due to the variation of the area of the cross section after the onset of necking. Some techniques [75–77] are developed to record the local deformation by photographic measurements.

Here we limit the analysis of our tensile stress-strain data to strain before necking where the deformation is homogeneous at glassy state and to the whole strain range at rubbery state. The determination of this homogeneous strain domain at glassy state is realized by stress-strain curve and by infrared camera. When necking occurs, the engineering stress shows an anomalous decrease and the neck point shows a stronger local self-heating, as be detected by the infrared camera.

Non homogeneous deformation is however avoided with cyclic shear deformation due to its geometry.

5.2. Simple extension experiments

5.2.1. Measurement procedure

Simple extension experiments are done for pure polymers (PB, SBR) and one polymer blend (PB50/SBR50) from rubbery state to glassy state. The sample geometry and gluing are already described in chapter 2. Temperature is reached by cooling down from above T_g at a rate of 10K/min, and equilibrium at that temperature for 20 minutes.

We do our experiment at constant true strain rate a, which is comparable to the frequency in a cyclic experiment. We will see in the following section that the mechanical response is very sensible to this strain rate. We set in our experiment:

$$\dot{\varepsilon}_{true} = \frac{d\varepsilon_{true}}{dt} = a \qquad \text{(eq 5.4)}$$

so that the true strain goes linearly with time:

$$\varepsilon_{true} = \int_{l_0}^{l} dl/l = \ln(l/l_0) = at \qquad \text{(eq 5.5)}$$

Consequently, the length of the sample as a function of time is an exponential one:

$$l = l_0 \exp(at) \qquad \text{(eq 5.6)}$$

Our simple extension experiments are performed with 4 different strain rates: $a=\dot{\varepsilon}_1=0.0083$/s, $a=\dot{\varepsilon}_2=0.083$/s, $a=\dot{\varepsilon}_3=0.83$/s and $a=\dot{\varepsilon}_4=8.3$/s. The extension ratio $\lambda = l/l_0$ goes from 1 to 2. In practical, the sample is firstly compressed to λ=0.97 with the same strain rate and then stretched to $\lambda = 2$. This pre-compression is needed because it's difficult for the machine to follow the given displacement rate at the very beginning of the test due to inertia of the machine. With pre-compression, the displacement follows the requirements in the elongation regime. It is also worthy noting that in the glassy state, the yield strain at compression is about 5% and our 3% pre-compression is within this limit.

5.2.2. Determination of reliable experimental windows

We will evaluate the self-heating during simple extension test, in order to determine reliable experimental windows.

It is already mentioned above that τ_{ht}=41s. For experiments with strain rates $\dot{\varepsilon} > 1/\tau_{ht}$ (0.025/s), i.e. $\dot{\varepsilon}_2$, $\dot{\varepsilon}_3$ and $\dot{\varepsilon}_4$, the experiment time scale $t_{mes} \approx 1/\dot{\varepsilon} < \tau_{ht}$, so the sample is in adiabatic heating regime with a large self-heating. It is important to follow the temperature evolution during the extension measurements. This is done by the infrared camera, in order to determine a reliable experimental window.
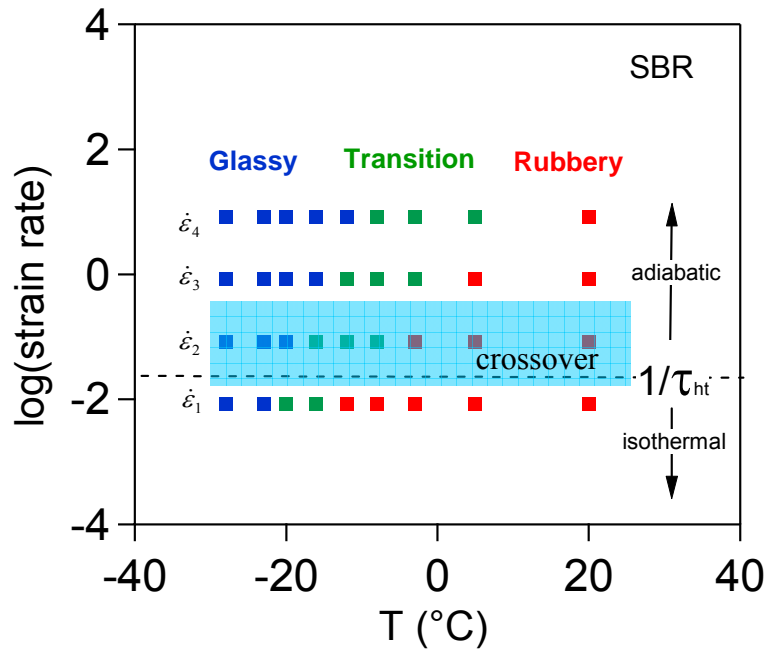
Figure 5.2. Measurement of SBR at different temperatures and strain rates – indicative classification into 3 regimes: glassy (blue), transition (green) and rubbery (red). Shadow zone is a crossover between adiabatic condition and isothermal condition.

Experiments in the glassy state

At low temperature or high strain rate, the polymer is in the glassy state (as is shown by blue points in the **Figure 5.2**).

Figure 5.3 shows the typical glassy state behavior of polymers: an initial (visco) elastic region, followed by yielding at high stress, strain softening at moderate strains. Strain hardening is not observed here because of the necking (localized deformation) and self-heating (decrease of modulus). The initiation of necking can be either identified by the dented form of $\sigma-\lambda$ curve at c point, or by the appearance of cross-form local heating at the same position (c point), illustrated by the infrared image c (see the zoomed cross). It is observed that:

- before yield point (between a and b): homogeneous deformation and very limited self-heating ($\Delta T < 0.5K$).
- after yield point (b, c, d and further): non homogeneous deformation due to necking, leading to a local temperature increase as large as $\Delta T > 20K$.

Thus these data can only be analyzed before the yield point.

Figure 5.3. Sample with glassy state behavior. Nominal stress vs. extension ratio and the evolution of temperature as measured by infrared camera of SBR (T_g=-20°C) at T=-23°C and the highest strain rate $\dot{\varepsilon}_4 = 8.3/s$: i.e. the most "deep" in the glassy regime. Inset temperature evolution is a zoom in the window of λ going from 1 to 1.06 (the yield point).

Figure 5.4. Sample with rubbery state behavior. Nominal stress vs. extension ratio and the evolution of temperature as measured by infrared camera of SBR (T_g=-20°C) at T=20°C and strain rate $\dot{\varepsilon}_4 = 8.3/s$.

Experiments in the rubbery state

At high temperature or low strain rate, the polymer is in the rubbery state. Measurements by infrared camera show very limited self-heating ($\Delta T < 0.3K$), and homogeneous deformation.

In the rubbery state, the data are reliable over the whole observation range and can be considered as isotherm data.

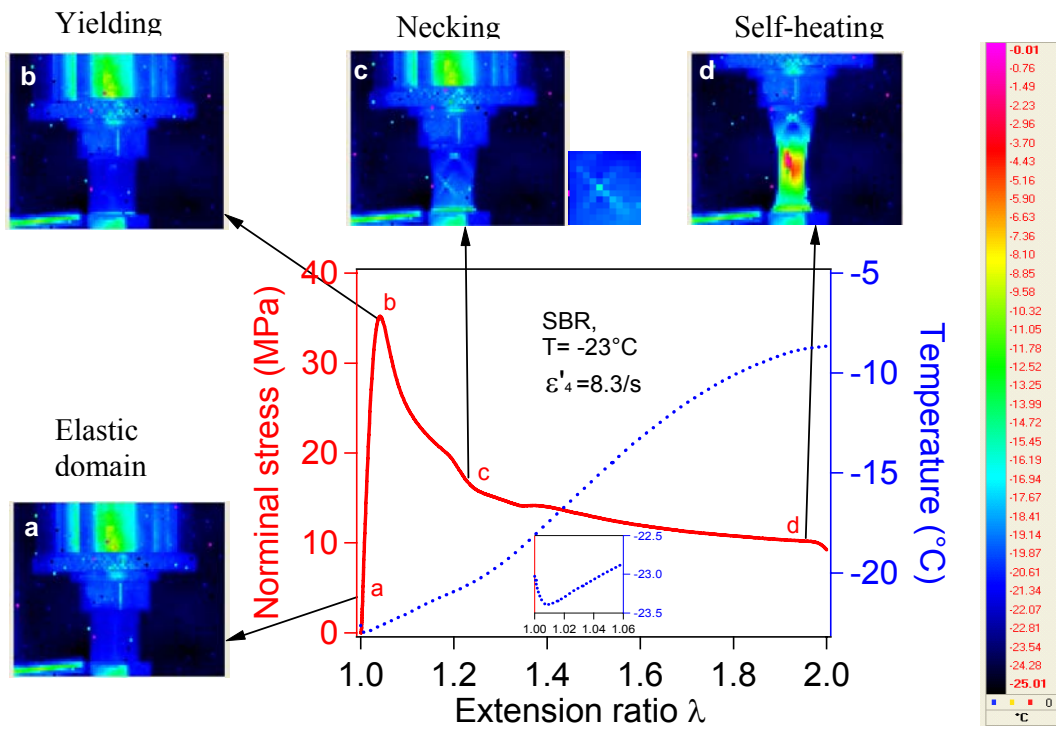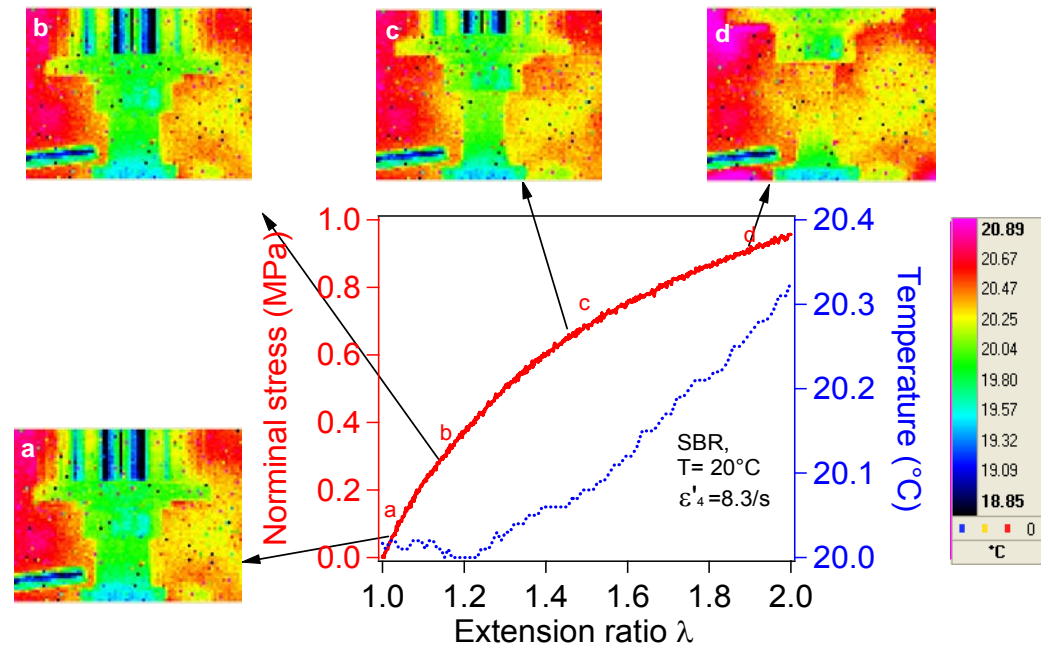## Experiments in the glass transition zone
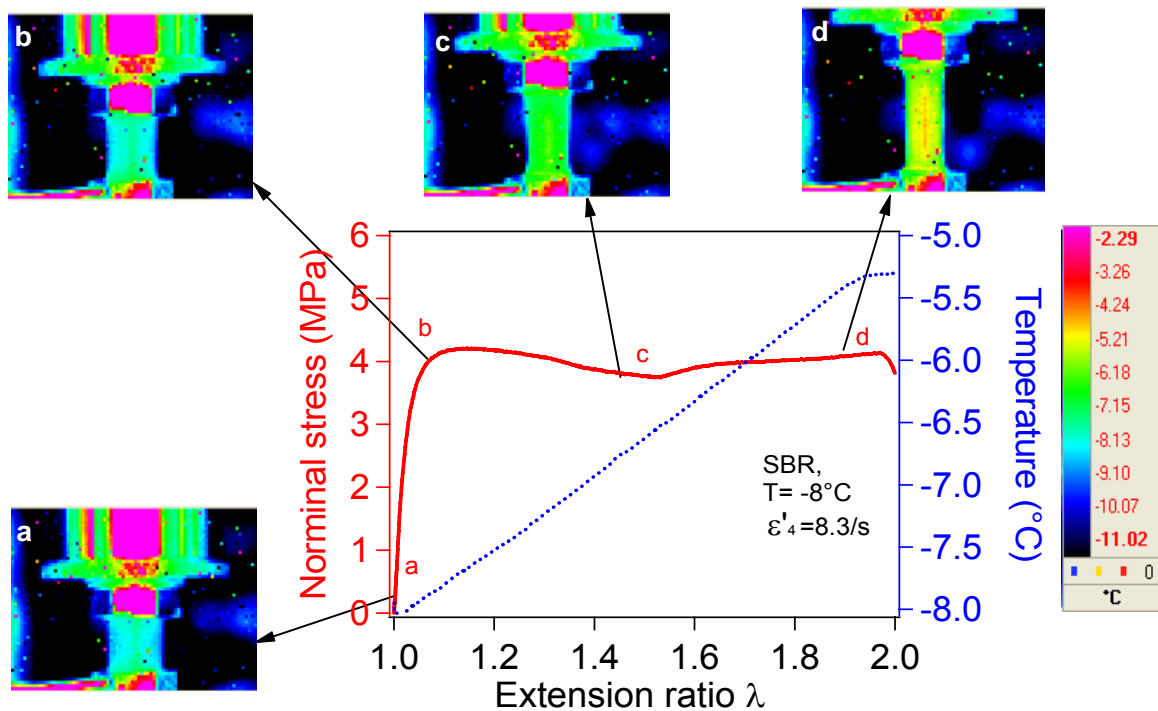
Figure 5.5. Sample at glass transition zone. Nominal stress vs. extension ratio and the evolution of temperature as measured by infrared camera of SBR (T_g=-20°C) at T=-8°C and strain rate $\dot{\varepsilon}_4 = 8.3/s$.

At glass transition zone, the self-heating is moderate between those observed in glassy and rubbery states. The homogeneity of temperature or deformation is also in the intermediate level.

We can define a reliable experimental window where $\Delta T < 0.5K$. For example, in the case of Figure 5.5, strain range from λ=1 to λ=1.2 is considered as reliable since $\Delta T < 0.5K$ and the deformation is homogeneous.

In practical, in the case of measurements at glass transition zone, we can approximately define a reliable strain range from λ=1 to λ=λ_l by calculation of the mechanical work during deformation which corresponds to the energy needed to heat up the sample by 0.5K. This means:

$$\rho c_p \Delta T = \int_{\lambda=1}^{\lambda=\lambda_1} \sigma d\lambda \qquad \text{(eq 5.7)}$$

Let's take the above measurement of **Figure 5.5** as an example, with:

$\rho = 950\,kg \cdot m^{-3}$

$c_p = 1800\,J \cdot kg^{-1} \cdot K^{-1}$

ΔT=0.5K

σ≈4 MPa

We have λ_1≈1.21. This is in good agreement with infrared camera measurement where λ_1=1.2.

The mechanical work calculation method is efficient to determine the reliable strain range for samples in the glass transition zone. We apply this method for pure PB and PB50/SBR50 blend.
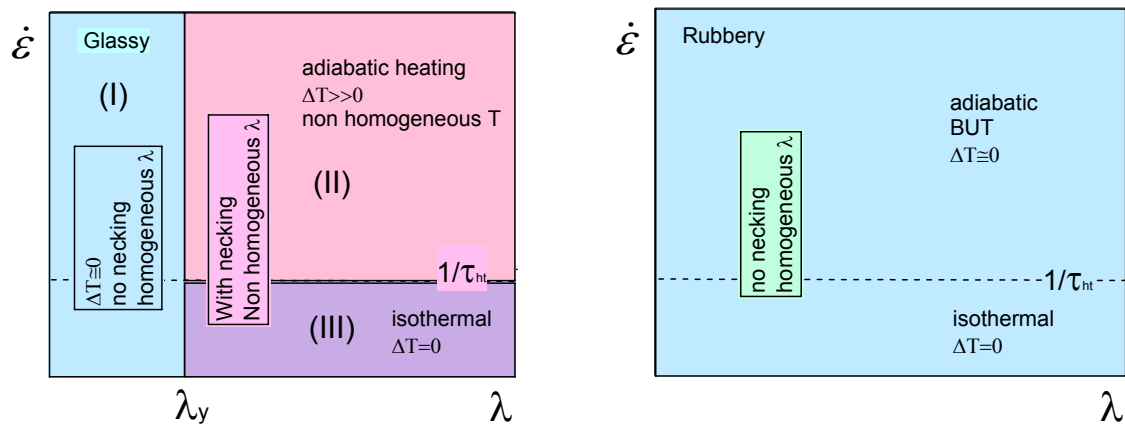
Figure 5.6. Schematics of different measurement windows of (a) glassy state and (b) rubbery state. The reliable experimental window is zone (I) for glassy state and is the whole zone for rubbery state.

All the examples given above are experiments of SBR sample at the highest strain rate $\dot{\varepsilon}_4$, where the adiabatic heating is the most severe. At other strain rates $\dot{\varepsilon}_1$, $\dot{\varepsilon}_2$ and $\dot{\varepsilon}_3$, adiabatic heating is less important, or totally negligible. So the conclusion on the reliable strain range is unaffected (see **Figure 5.6**).

Measurements of pure PB polymer and blend of PB50/SBR50 were also done at various temperatures from glassy state to rubbery state. It was found that the glass transition zone of blend is broadened and need more measurements (as is shown in **Figure 5.7**) but the σ–λ curves are very similar to the pure polymer ones. So we apply the same method to determine reliable strain ranges.

To sum up, we can now define a valid regime for our study where the deformation is homogeneous and the adiabatic self-heating is negligible (ΔT<0.5K). It corresponds to the strain range before yielding for glassy state, the whole strain range for rubbery state, and an intermediate strain range for the glass transition zone.
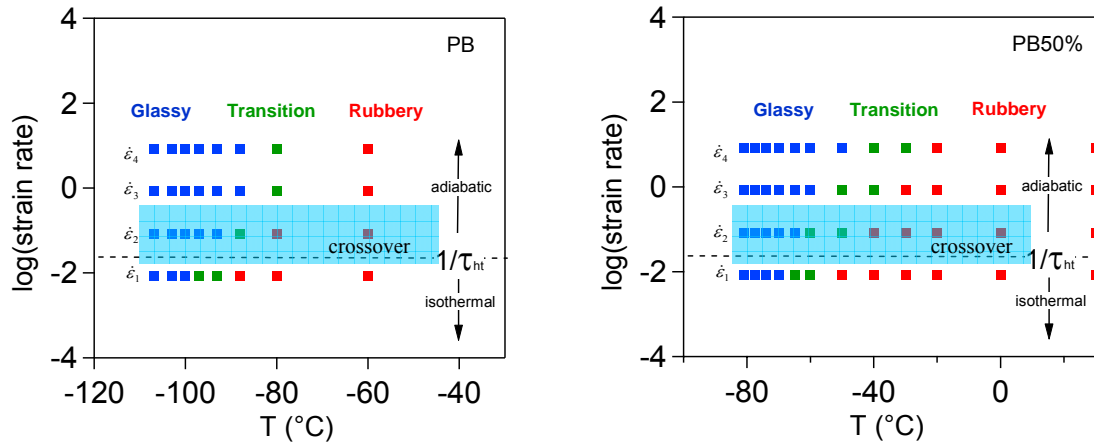
Figure 5.7. Measurement of (a) pure PB and (b) blend of PB50/SBR50 at different temperatures and strain rates – indicative classification into 3 regimes: glassy (blue), transition (green) and rubbery (red). Dashed line is a reference to separate adiabatic condition and isothermal condition.

Influence of the strain rate
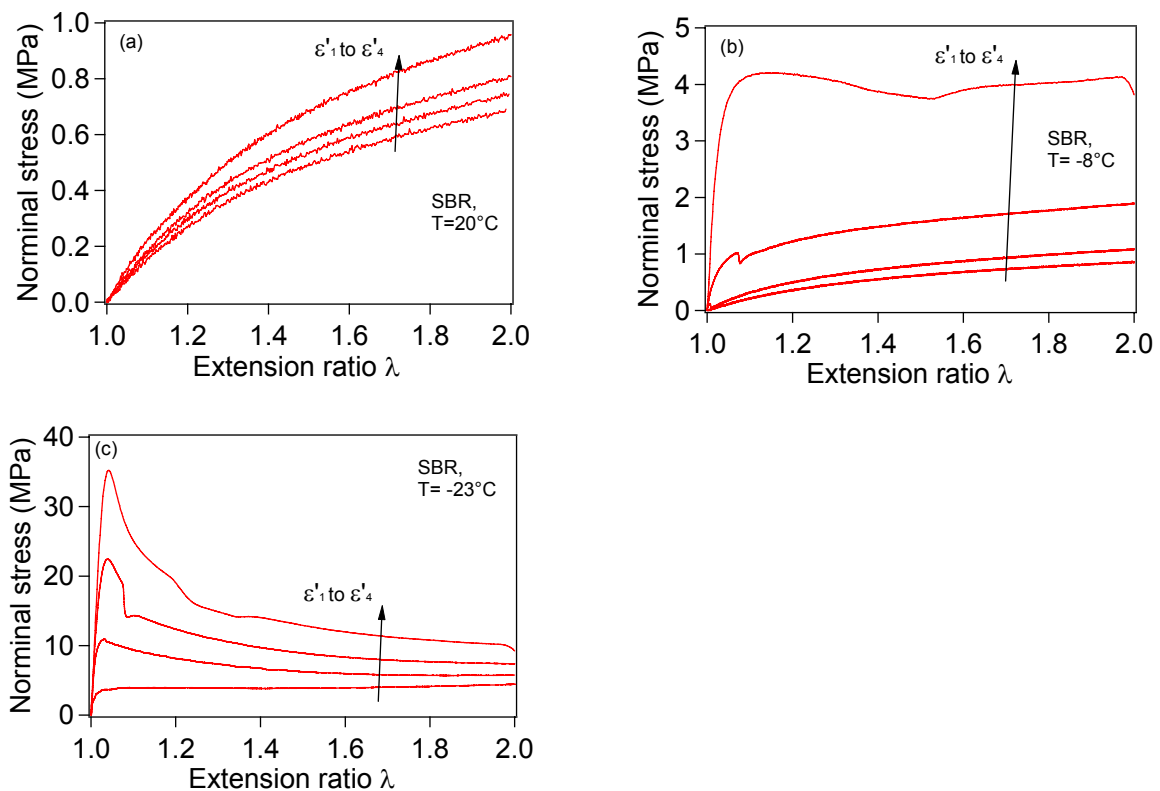
Figure 5.8. Nominal stress vs. extension ratio of SBR at different temperature and strain rate. (a) rubbery behavior (b) glass transition behavior (c) glassy behavior. The sample's glass transition temperature T_g=-20°C, strain rate $\dot{\varepsilon}_1 = 0.0083/s$, $\dot{\varepsilon}_2 = 0.083/s$, $\dot{\varepsilon}_3 = 0.83/s$ and $\dot{\varepsilon}_4 = 8.3/s$.

Some typical σ–λ curves are shown in **Figure 5.8** for pure SBR sample. It can be seen that the mechanical property is very sensible to strain rate. Increasing strain rate is similar as decreasing temperature. In fact, strain rate in extension test is comparable to the frequency in cyclic test.

We will discuss in the following sections the time-temperature superposition in the linear and nonlinear regimes of polymers in extension with some possible physical explanations.

5.2.3. Role of linear viscoelasticity in extension test

We have now overcome the experimental difficulties and can thus analyze our data to extract the nonlinear part of the mechanical response. However this nonlinearity may be superimposed with a pseudo non linearity that originates from linear viscoelasticity.

Indeed, under deformation, rearrangements occur in the system. Some rearrangements are reversible even in the nonlinear regime (e.g. the entanglement slipping). Their typical relaxation time is fast compared to the duration of the experiment. These non-linear but at equilibrium mechanism could be the segmental relaxations – α relaxation – or network relaxations associated to larger length scale corresponding to the distance between entanglements or crosslinks, as long as the segmental relaxation time is smaller than the measurement duration.

There exist also other rearrangements – plastic events - that are irreversible: by that we mean that they last for times longer than the experimental time scale, and that they are thus typical of out equilibrium phenomena, and are likely never observed at thermodynamic equilibrium.

In order to identify different mechanisms which control the nonlinear mechanical properties of polymers in rubbery and glassy states, we have to firstly study the mechanical response in extension that is directly controlled by linear viscoelasticity, which indeed originates in a non-linearity in the stress strain response.

- Firstly we predict the stress-strain curve in extension, in the linear regime, from the rheology measurements and its relaxation time distribution.
- Then we extrapolate the mechanical behavior to large strain, where the slip of entanglement and the Gaussian chain entropic change make additional contributions.

After identifying of all these above contributions, we can quantitatively evaluate the contribution due to plasticity.

Linear viscoelasticity. A general form of the evolution of the stress is written by the Boltzmann superposition principle:

$$\sigma(t) = \int_{-\infty}^{t} E(t-u) \cdot \frac{d\varepsilon(u)}{du} \cdot du \qquad \text{(eq 5.8)}$$

In the above equation, $E(t)$ is the relaxation modulus expressed as $E(t) = \sigma(t)/\varepsilon_0$, and it is well described by the stretched exponential KWW function:

$$E(t) = (E_g - E_r)\exp(-(\frac{t}{\tau_{KWW}})^{\beta}) + E_r \qquad \text{(eq 5.9)}$$

where τ_{KWW} is a characteristic relaxation time and β is a parameter ranging between 0 and 1. E_g is the original modulus at $t=0$ and corresponds to the modulus at the glassy state. E_r is the final modulus at $t=\infty$ and corresponds to the modulus at the rubbery state. We will predict the stress-strain curve in extension, in the linear regime, from the rheology measurements. We have to find all the parameters in **(eq 5.9)**.

The time domain KWW parameters (τ_{KWW} and β) could be directly measured by stress relaxation test. They can also be related to the frequency domain Havriliak-Negami parameters (they are not exactly Fourier transforms of each other), through a method developed by Alvarez et al. [21]:

$$\ln(\frac{\tau_{HN}}{\tau_{KWW}}) = 2.6(1-\beta)^{0.5}\exp(-3\beta)$$ (eq 5.10)

for the characteristic relaxation times and

$$\alpha\gamma = \beta^{1.23}$$ (eq 5.11)

for the β parameter.

The relation between shear modulus G and Young's modulus E is:

$$E = 2G(1+\nu)$$ (eq 5.12)

where ν is the Poisson ratio. Rubbers are incompressible materials and exhibit a Poisson ratio of nearly 0.5, one obtains:

$$E=3G$$ (eq 5.13)

While glassy polymer has a Poisson ration of about 0.3 and $E=2.6G$. In this study, we assume that $E\approx3G$ from the glassy to the rubber state: i.e. $E_g=3G_{glass}$ and $E_r=3G_{rub}$. This assumption is reasonable in this work where we are dealing with mechanical response that vary of orders of magnitudes, and allows for a great simplicity in the presentation of this work.

Table 5.1. Parameters describing KWW functions of pure PB and SBR polymers and blend PB50%, the reference temperature is the T_g of each.

	SBR	PB	PB50
E_g (Pa)	2.0E+09	2.9E+09	4.5E+09
E_r (Pa)	2.1E+06	2.1E+06	1.9E+06
τ_{KWW} (s)	5.0E-03	5.0E-03	5.0E-05
β	0.20	0.20	0.08
τ_{HN}/τ_{KWW}	3.58	3.58	7.11

All the parameters in **(eq 5.9)** can thus be determined (see Table 5.1) from rheology results presented in chapter 3. According to these assumptions, we can determine the time dependent relaxation $E(t)$. We can further calculate the viscoelastic behavior of our polymer samples at constant true strain rate. For simplicity, we suppose that the sample is totally relaxed when the strain rate $\dot{\varepsilon}_{true}$ is applied at time $t=0$ and $\varepsilon=0$, so the Boltzmann equation writes:

$$\sigma(t) = \int_0^t E(t-u) \cdot \frac{d\varepsilon(u)}{du} \cdot du$$ (eq 5.14)

where $\varepsilon(t)=\exp(at)-1$ is the evolution of engineering strain with time. With a change of variable $x=t-u$, this can be calculated as:

$$\sigma(t) = \int_0^t E(t-u) \cdot \frac{d(\exp(au)-1)}{du} \cdot du$$

$$= a\int_0^t E(x)\exp(a(t-x))dx$$

(eq 5.15)

Introducing the KWW function gives:

$$\sigma(t) = a\int_0^t [(E_g - E_r)\exp(-(\frac{x}{\tau_{KWW}})^\beta) + E_r]\exp(a(t-x))dx$$

(eq 5.16)

This can also be written in terms of the strain and strain rate variables:

$$\sigma(\varepsilon, a\tau_{KWW}) = (E_g - E_r)f_1(\varepsilon, a\tau_{KWW}) + E_r\varepsilon$$

(eq 5.17)

where

$$f_1(\varepsilon, a\tau_{KWW}) = (1+\varepsilon)\int_0^\varepsilon \exp(-(\frac{\ln(1+\varepsilon')}{a\tau_{KWW}})^\beta)\frac{1}{(1+\varepsilon')^2}d\varepsilon'$$

(eq 5.18)

In fact, f_1 is an integration of KWW equation (see Annex D for detailed analysis to obtain its analytic form for numerical processing).

In eq 5.17, the first term of the right hand side is the viscoelastic contribution which depends on strain rate and strain, while the second term is the rubber elasticity contribution which is independent of strain rate.

As the value $a\tau_{KWW}$ increases, the value of f_1 goes from 0 to ε, as is shown in **Figure 5.9**. As a consequence, the mechanical behavior changes with strain rate:

- at infinitely small strain rate, $f_1=0$, the behavior is rubber-like and eq 5.17 gives $\sigma = E_r\varepsilon$

- at infinitely large strain rate, $f_1=\varepsilon$, the behavior is glass-like and eq 5.17 gives $\sigma = E_g\varepsilon$
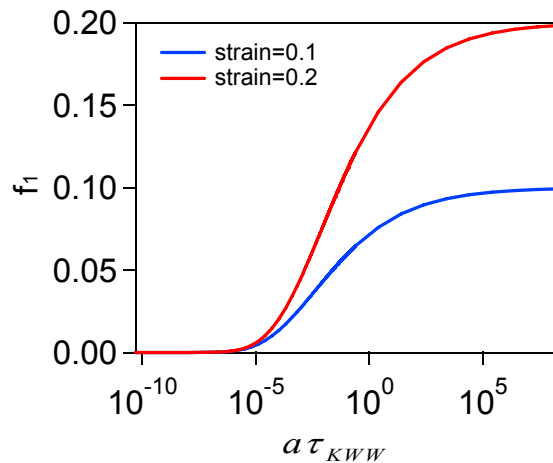

Figure 5.9. Evolution of f_1 as a function of $a\tau_{KWW}$ with strain=0.1 or strain=0.2.

At a given strain rate, the viscoelastic linear stress depends also on strain amplitude. We obtain for our polymer systems the typical $E(t)$ and stress vs. strain curves, as shown in **Figure 5.10**.
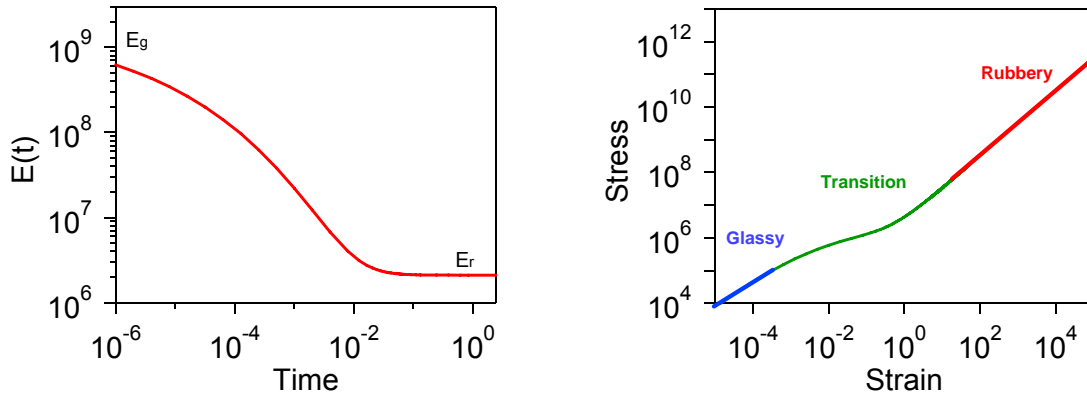
Figure 5.10. (a) The relaxation modulus as a function of time; (b) the modeled log(stress)-log(strain) plot. SBR sample at T_g and strain rate $a=10^{-3}$.

It can be seen from the above figure that:

- at small time scale $t << \tau_{KWW}$, i.e. at small strain $\varepsilon << \dot{\varepsilon}\, \tau_{KWW}$, we have $E(t) \sim E_g$, and $\sigma \sim E_g \varepsilon$, so the mechanical behavior is a glassy one.
- at large time scale $t >> \tau_{KWW}$, i.e. at large strain $\varepsilon >> \dot{\varepsilon}\, \tau_{KWW}$, we have $E(t) \sim E_r$, and $\sigma \sim E_r \varepsilon$, so the mechanical behavior is a rubbery one.
- But in the intermediate regime the stress is not proportional to the stress.

The glass-rubber transition occurs at $t \sim \varepsilon/\dot{\varepsilon} \sim \tau_{KWW}$. That means that at very low strain rate, the glass glass-rubber transition is shifted towards very low strain. This can be seen in **Figure 5.11**.
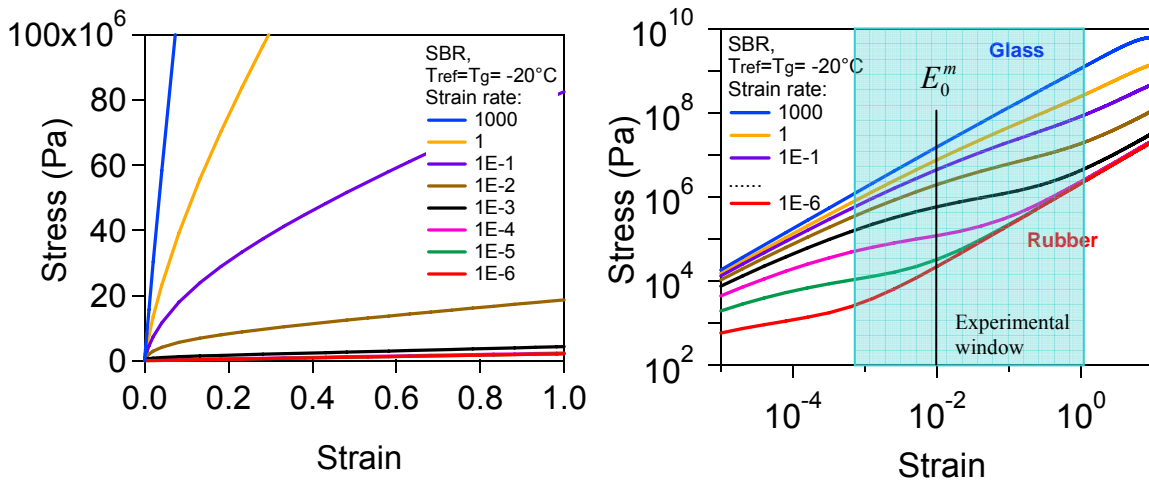
Figure 5.11. The modeled stress-strain curves of SBR at T_g= -20°C at different strain rates from 1000 to 10^{-6} (a) linear vs. linear plot; (b) log vs. log plot. The shadow zone indicates the experimental window. Modulus E_0^m is determined at ε_0=0.01.

Figure 5.11 shows the modeling results for SBR at T_g at different strain rates in the experimental window. At high strain rate, the response is a glassy one, with elastic modulus E_g, and at low strain rate, the response is a rubbery one, with elastic modulus E_r. In the intermediate regime the response is non linear. Practically, the linearity of the response depends thus on the experimental window in time and in strain amplitude.

118

The time window is such that the initial elastic modulus is never measured at infinite small strain, but rather at a certain strain level of typically ε_0=0.01. We calculate the modulus from eq 5.17 at ε_0=0.01 and we call it E_0^m :

$$E_0^m = \frac{\partial \sigma}{\partial \varepsilon}\Big|_{\varepsilon=0.01} \qquad \text{(eq 5.19)}$$

This modulus, corresponding to a measurement at an amplitude of ε_0=0.01 is expected to be the modulus we measure by fitting the stress strain response linearly in the very beginning of stress strain measurement. We will now check whether this assumption is correct or not.

Comparison E_0^m vs. E_0^{exp}. We deduce the value of E_0^m by applying the above model. We compare it to the one of initial slope E_0^{exp} of stress-strain curve. It should be noted that the modeling of E_0^m is done at fixed temperature (i.e. fixed τ_{KWW}) and E_0^m is only a function of strain rate. The evolution of E_0^m and E_0^{exp} with strain rate are shown in **Figure 5.12**, where the value of E_0^m is plotted as a function of strain rate (a) for various samples. They are compared to the master curve of experimental slope E_0^{exp} with shift factors a_T^{WLF} taken from WLF law of rheology measurement in chapter 3, with T_g of each polymer as reference temperature. They are in good agreement and the actual shift factor a_T ($= a/\dot{\varepsilon}$) is very similar to a_T^{WLF} obtained from WLF law.
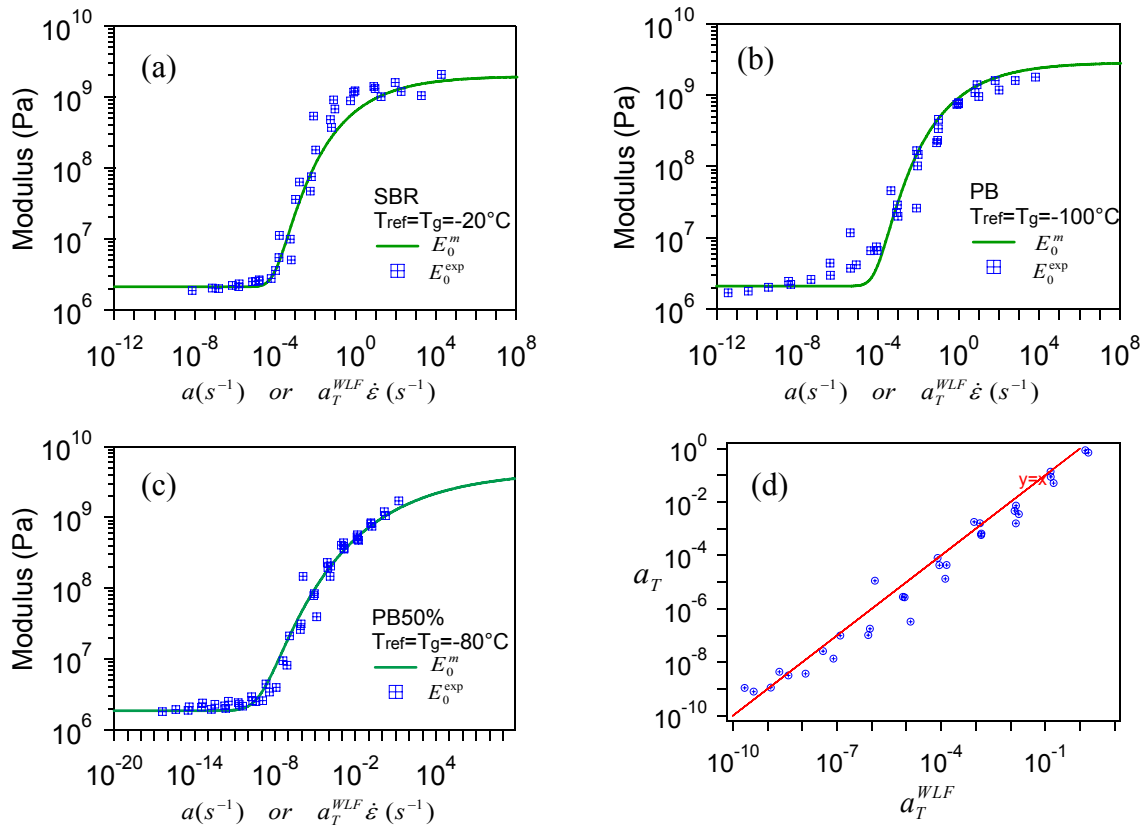

Figure 5.12. Lines are the modellization of E_0^m as a function of strain rate a for (a) SBR, (b) PB and (c) PB50%. Data in squares are experimental E_0^{exp} master curve - shift factor a_T^{WLF} is taken from WLF law of rheology measurement. (d) Actual shift factor a_T ($= a/\dot{\varepsilon}$) vs. a_T^{WLF} .

Lastly, we can compare directly the stress-strain "linear" response to the viscoelastic response. The $E_0^{exp}/3$ master curves are further compared to simple shear rheology results of G' and the absolute value of complex modulus $|G^*|$ as a function of $a_T^{WLF} f$. Since strain rate $\dot{\varepsilon}$ and frequency f are not strictly equivalent, we apply a fixed shift factor k to $a_T^{WLF} f$, which is temperature independent and is only material dependent:

$$\dot{\varepsilon} = kf \qquad\qquad (eq\ 5.20)$$

Figure 5.13 show the master curves obtained from extension and oscillatory shear rheological measurement with:
1. $k = 0.166$, for pure polymers PB and SBR
2. $k = 1$, for polymer blend PB50%
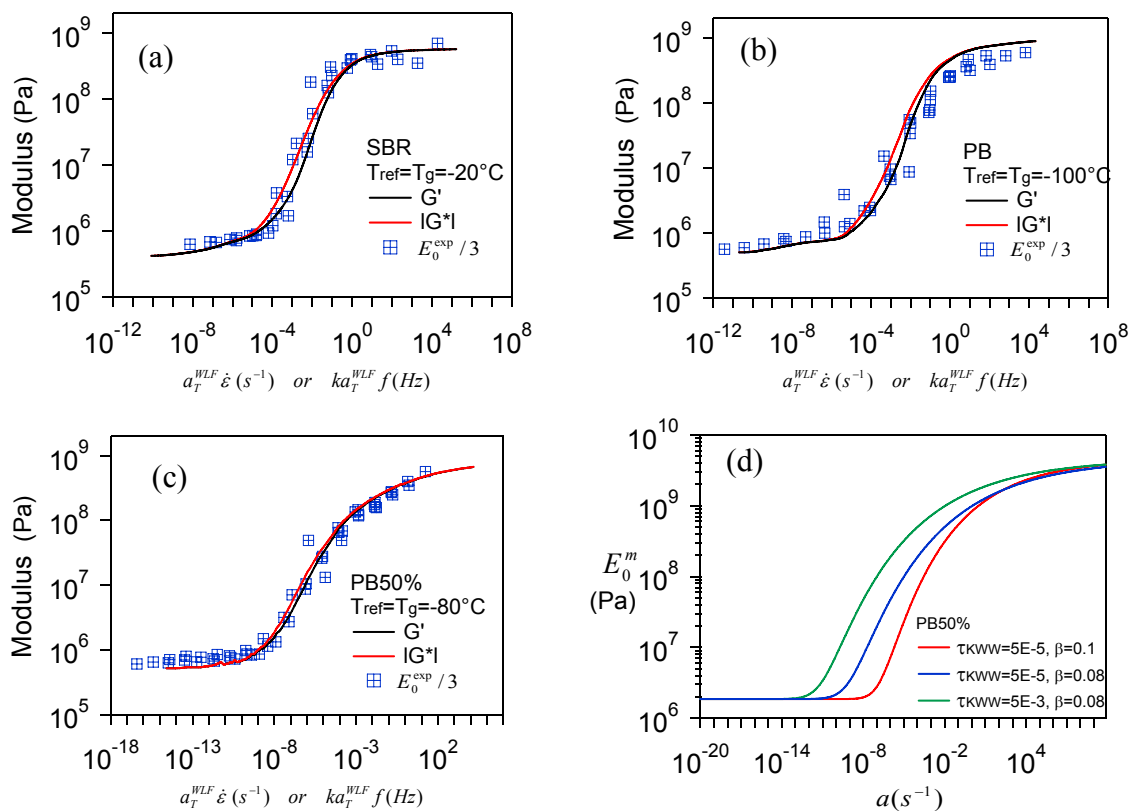
Figure 5.13. Comparison between the master curves of $E_0^{exp}/3$ (squares) as a function of strain rate, rheology measurements G' (black lines) and the absolute value of complex modulus $|G^*|$ (red lines) as a function of frequency of polymer (a) SBR, (b) PB and (c) PB50%. (d) Modellization of E_0^m with different parameters.

It can be seen that:
1. For a given sample, the shift factor k is a fixed one, but we can not find a universal value of k for both pure polymers and blend. This means that even if strain rate and frequency are comparable, we can not establish an exact relation between them. This might be explained by the fact that the position (or t_{KWW}) of the glass transition is dependent on the width of T_g (or parameter β). This can be seen in eq 5.12 and Table

120

5.1 that the ratio of t_{HN}/t_{KWW} is dependent on parameter β and the ratio in blend is **two times** of that in pure polymers. In addition, even at fixed t_{KWW}, the position is also influenced by parameter β (see **Figure 5.13**(d)). This explains, at least to some extent, the **6 times'** difference in factor k.

2. The value of $E_0^{exp}/3$ deduced from the initial slope of the extension stress-strain curves agree with the shear modulus on directly determined by oscillatory shear rheological measurement. We observe the same time-temperature superposition laws (WLF) for extension and shear measurements.

In the following modeling, we will take the shift factor a_T, so we will have $E_0^{exp} = E_0^m$, and we call it simply E_0. We will use **(eq 5.17)** as the apparent non-linearity contribution from linear viscoelasticity in the stress strain measurements.

To conclude, the initial modulus E_0^{exp} in simple extension test is directly related to *G'* and G" in rheology and is well described by our linear stress relaxation model. We will now go further and investigate the nonlinear regime, with the tools that allows extracting from nonlinearities the contribution of linear viscoelasticity.

5.2.4. Nonlinearity in extension test

Definition and classification.

If we define the nonlinearity as the curvature or strain softening in stress-strain curves, this nonlinearity has different origins that should be carefully separated:

1. Apparent nonlinearity from linear viscoelastic relaxation. This contribution is described by **(eq 5.17)**, through the strain dependence of $f_1(\varepsilon, a\tau_{KWW})$:

$$\sigma_{visco} = (E_g - E_r)f_1(\varepsilon, a\tau_{KWW}) + E_r\varepsilon$$

2. The entropic nonlinearity which originates from the Gaussian affine deformation of rubber elasticity, described by the following equation:

$$\sigma_{Gauss} = \frac{E_0}{3}(\lambda - \frac{1}{\lambda^2})$$

3. The structural nonlinearity which comes from structure change and physical events like slipping of entanglements in rubbers, that is classically described by the Mooney-Rivlin expansion :

$$\sigma_{MR} = (2C_1 + \frac{2C_2}{\lambda})(\lambda - \frac{1}{\lambda^2})$$

Where C1 and C2 are structural parameters related to the crosslinking and entanglements densities

4. The structural nonlinearity which comes from structure change and physical events such as local plastic events in glasses. This part is not yet clear in literature and we will give detailed analysis of these phenomena.

Description of nonlinearity in the rubber regime

In the rubber regime, the viscoelastic effect is negligible, and the literature is rich in data modeling. The situation is fairly simple and we describe it here, in order to introduce progressively the difficulties of data analysis.

A typical stress-strain curve of rubber is presented in **Figure 5.14**. The linear elastic behavior is given by $E_0 \varepsilon$. Data fitting by Mooney-Rivlin model and by Rubinstein model both give satisfactory fittings in all the strain range.

In the rubbery state, the linear viscoelastic contribution on the strain softening predicted by (**eq 5.17**) is negligible since

$$f_1(\varepsilon, a\tau_{KWW}) = 0 \qquad \text{(eq 5.21)}$$

and

$$\sigma_{visco} = (E_g - E_r)f_1(\varepsilon, a\tau_{KWW}) + E_r\varepsilon = E_r\varepsilon \qquad \text{(eq 5.22)}$$

so the material is considered as quasi purely elastic at rubbery state and σ_{visco} superpose with εE_0.

The curvature of strain-stress curve is in fact due to entropy changes described by the affine deformation model (Gaussian form) and some physical events like entanglement slipping, which is well described by the Mooney-Rivlin equation or Rubinstein's slip-tube model.

The strain softening from Gaussian statistical entropy change of the chains assumes an affine deformation of the cross-links. Using $\lambda = 1 + \varepsilon$ at small strain regime $\varepsilon \ll 1$ where ε^3 and further terms are negligible, it writes:

$$\sigma_{Gauss} = \frac{E_0}{3}(\lambda - \lambda^{-2}) = E_0\varepsilon - E_0\varepsilon^2 + o(\varepsilon^3) \qquad \text{(eq 5.23)}$$

We compare this equation to a Taylor expansion form: $\sigma = E_0\varepsilon + \dfrac{E_1}{2}\varepsilon^2 + ... + \dfrac{E_{n-1}}{n!}\varepsilon^n$. The first and the second derivatives of the stress are respectively E_0 and $E_1 = \dfrac{\partial^2 \sigma_{Gauss}}{\partial \varepsilon^2}\Big|_{\varepsilon=0} = -2E_0$. The value $E_1 = -2E_0$ corresponds to the affine deformation contribution on the strain softening.

The phenomenological Mooney-Rivlin equation that describes strain softening of rubbers at small strains writes:

$$\sigma_{MR} = (2C_1 + \frac{2C_2}{\lambda})(\lambda - \frac{1}{\lambda^2})$$
$$= (6C_1 + 6C_2)\varepsilon + (-6C_1 - 12C_2)\varepsilon^2 + o(\varepsilon^3) \qquad \text{(eq 5.24)}$$

The first and the second derivatives of the stress are respectively $E_0 = 6C_1 + 6C_2$ and $E_1 = -12C_1 - 24C_2 = -2E_0 - 12C_2$, where the term $-2E_0$ is the Gaussian affine

deformation contribution already described above and the term $-12C_2$ comes from other contributions, e.g. entanglement slipping. This concept is introduced by the slip tube model of Rubinstein and Panyukov [15]. The equation is more complex, and the description of the stress strain response with a simple Taylor expansion is not satisfactory, while the complete response works extremely well. It is why we will not use Taylor expansion of σ_{RP} in this work. Indeed both σ_{MR} and σ_{RP} gives good predictions.
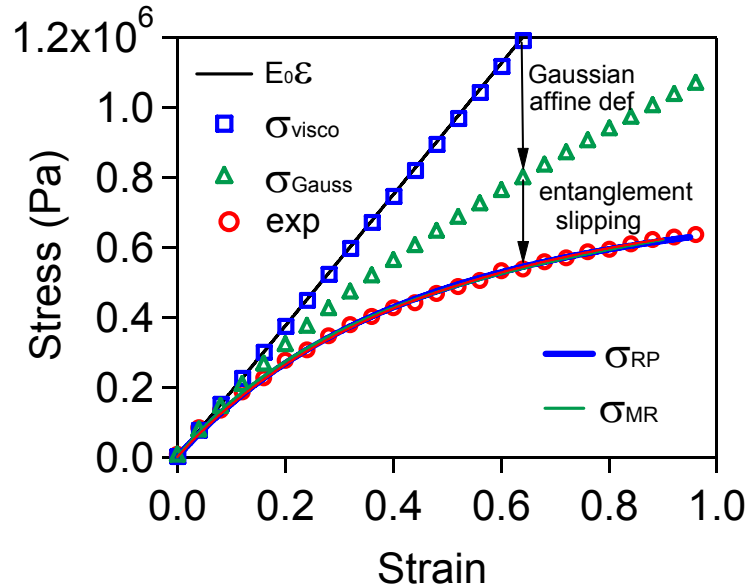

Figure 5.14. Rubbery behavior: PB50% sample (T_g=-80°C), T=30°C, strain rate=0.0083/s. Comparison between pure elastic response with slope E_0 (black), linear viscoelastic model σ_{visco} **(eq 5.17)** (squares), Gaussian affine deformation model σ_{Gauss} **(eq 1.10)** (triangle) and experiments (circles). Experimental results are fitted to Mooney-Rivlin model σ_{MR} **(eq 1.14)** (red line) with $C_1 = 5.7 \times 10^4 \, Pa$ and $C_2 = 2.6 \times 10^5 \, Pa$. Fitting of Rubinstein-Panyukov model σ_{RP} **(eq 1.16)** (blue line) with $G_c = 1 \times 10^4 \, Pa$ and $G_e = 6.2 \times 10^5 \, Pa$.

To conclude, the nonlinearity in rubber is due to Gaussian affine deformation and entanglement slipping. This is well described by Mooney-Rivlin or Rubinstein models. Parameter C_2 is an indicator of the amplitude of structural nonlinearity (entanglement slipping).

Towards plastic structural nonlinearity in glassy state

In the glassy regime, we observe a non linearity that appears at small strain regime (before yield point) as shown in figure 5.15. Let us first remark that in this small strain regime, the effect of Gaussian affine deformation and entanglement slipping are negligible. This can be clearly seen in figure 5.15 where the green triangles indicate the non-linearity that would be predicted by the Gaussian affine assumption.

On another hand, the linear viscoelastic stress relaxation contribution is important. In order to properly evaluate the plastic structural nonlinearity, we quantify the viscoelastic

contribution σ_{visco} **(eq 5.17)** on nonlinearity. This corresponds to the blue squares in figure 5.15. This effect can not explain the mechanical behavior observed – there is thus additional structural nonlinearity which originates in plastic deformation.

It is important to notice that the amplitude of the non linearity is really larger in the glassy regime than in the rubber one. So in order to extract properly the non-linearity amplitude, one will have to adjust the strain window with the mechanical response, especially in the glass transition regime. .
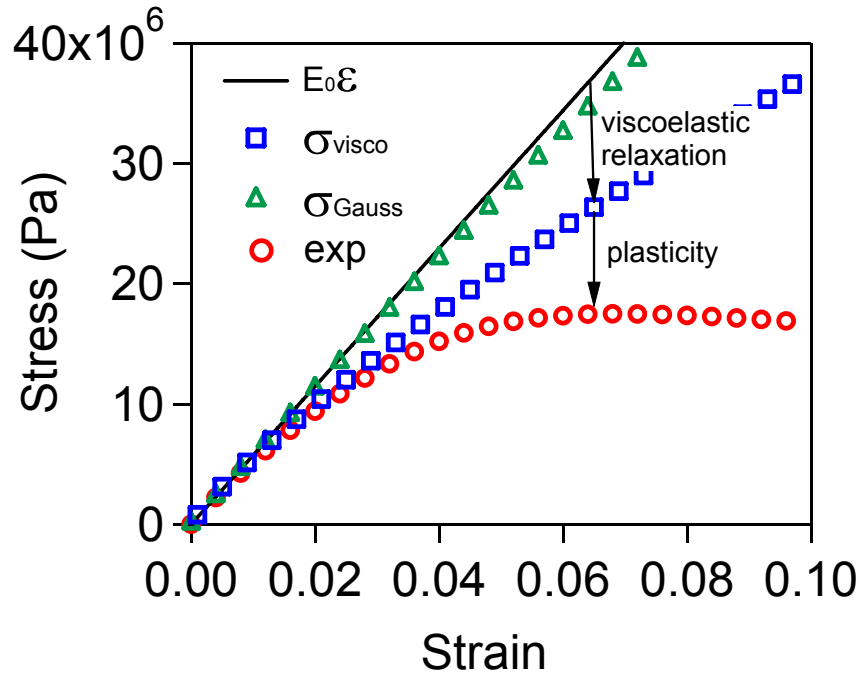
Figure 5.15. Glassy behavior: PB50% sample (T_g=-80°C), T=-74°C, strain rate=8.3/s. Comparison between pure elastic response with slope E_0 (black), linear viscoelastic model σ_{visco} **(eq 5.17)** (squares), Gaussian affine deformation model σ_{Gauss} **(eq 1.10)** (triangle) and experiments (circles).

In the glass transition regime (see **Figure 5.16**), it can be seen that both viscoelastic and Gaussian affine deformation contributions are important. These two contributions should be combined together in order to deduce the contribution of the structural nonlinearity (plasticity or/and entanglement slipping). How do they combine?

Viscoelastic contribution is given by **(eq 5.17)** and Gaussian affine deformation contribution is given by **(eq 1.10)**.
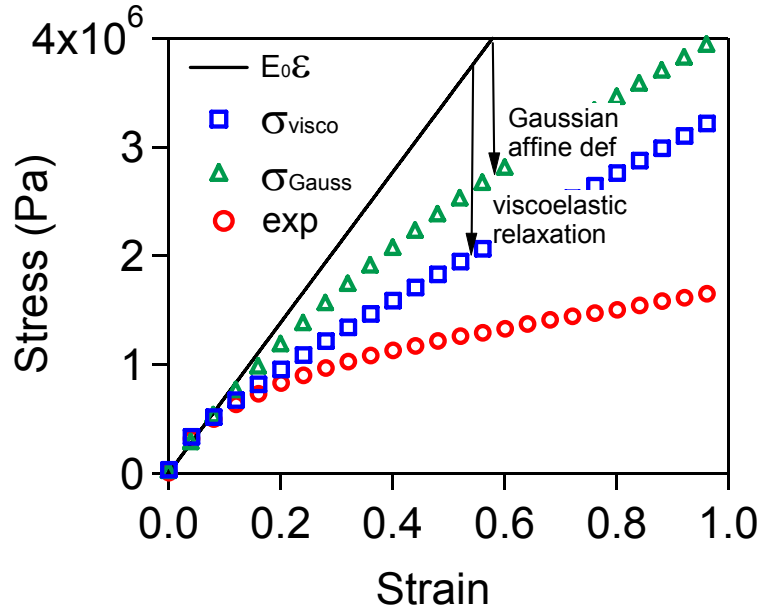
Figure 5.16. Glass transition regime: PB50% sample (T_g=-80°C), T=-60°C, strain rate=8.3/s. Comparison between pure elastic response with slope E_0 (black), linear viscoelastic model σ_{visco} **(eq 5.17)** (squares), Gaussian affine deformation model σ_{Gauss} **(eq 1.10)** (triangle) and experiments (circles).

We must introduce two extremal hypotheses in order to interpret the experiments in the glass transition regime, which lead to two modified viscoelastic models.

<u>Model 1.</u> The Gaussian affine deformation model is applied to all parts of the stress through

the factor $g(\varepsilon) = \dfrac{\sigma_{Gauss}}{\sigma_{lin}} = \dfrac{\dfrac{E_0}{3}(\lambda - \lambda^{-2})}{E_0\varepsilon} = 1 - \varepsilon + o(\varepsilon^2)$. It writes:

$$\sigma_1(\varepsilon, a\tau_{KWW}) = (E_g - E_r)f_1(\varepsilon, a\tau_{KWW})g(\varepsilon) + E_r\varepsilon g(\varepsilon) \qquad \text{(eq 5.25)}$$

<u>Model 2.</u> The Gaussian affine deformation model is applied only to the second term of the stress, i.e. the rubber elasticity one, and it writes:

$$\sigma_2(\varepsilon, a\tau_{KWW}) = (E_g - E_r)f_1(\varepsilon, a\tau_{KWW}) + E_r\varepsilon g(\varepsilon) \qquad \text{(eq 5.26)}$$

From rheological measurements we obtain all parameters involved in the above equations. We can thus predict for each model the evolution of stress-strain curves and compare them to the experimental data.

These two models set two limits of the real situation and results are presented in **Figure 5.17**. By comparing with experimental stress-strain curves at different temperatures and strain rates, it can be seen that for all cases our models fit well with experimental data at small strains. Above a certain strain limit, additional strain softening occurs due to plasticity or/and entanglement slipping, this part corresponds to the structural nonlinearity.
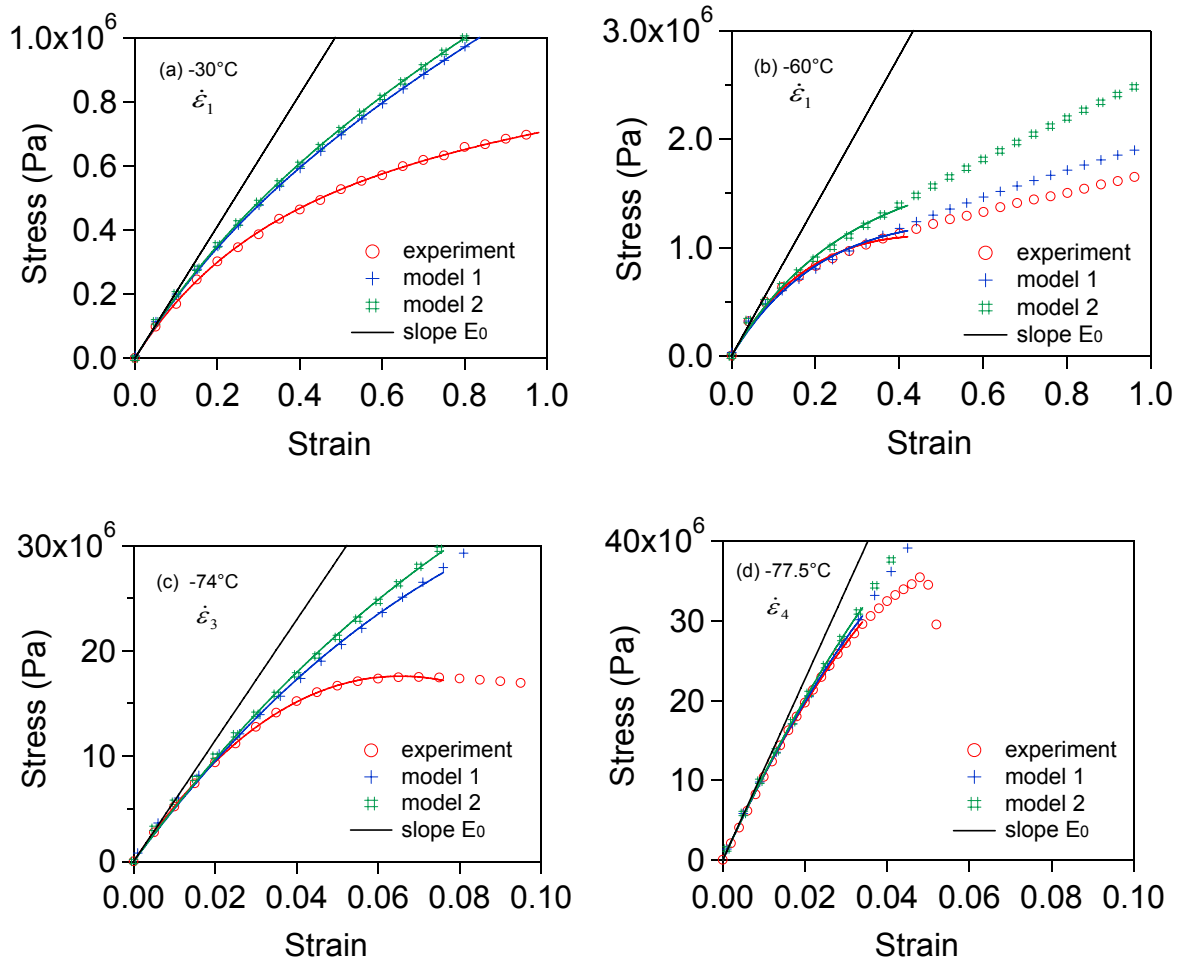
Figure 5.17. Comparison between pure elastic response with slope E_0 (black), viscoelastic model 1 (+), model 2 (#) and experiments (circles). Lines are fits to **(eq 5.27)**. PB50% sample, at different temperatures and strain rates as indicated in the figures.

- Figure 5.17-a: at rubbery state, the response is mainly controlled by Gaussian affine deformation of the polymer chains up to 10% of strain. For higher strains, entanglement slipping occurs.
- Figure 5.17-b: in the glass transition domain, the behavior is mainly viscoelastic. Model 1 (or model 2) gives a good description of the data up to 40% (or 20%) of stain.
- Figure 5.17-c: at glassy state, the behavior is mainly viscoplastic, with a good description of the data up to 2% of stain with model 1 and 2. Same observation by Leterrier and G'Sell of polyurethane resin [78]. Above that limit, local plastic events occur.
- Figure 5.17-d: at deeply glassy state, the behavior is fragile where the material is broken at 5%, and the fit is good up to 3% of strain.

So it seems that two kinds of physical events of structural nonlinearity, i.e. entanglement slipping and local plastic event, occur for polymers from rubbery state to glassy state. And at the glass transition domain, the entanglement slipping is greatly reduced. We will confirm quantitatively these statements in the next part.

To conclude, with two modified viscoelastic models, the strain softening can be well described at small strain i.e. $\varepsilon < 10\%$ in the rubber state and $\varepsilon < 3\%$ in the glassy state. However, they do not account for the observed nonlinearity at larger strain. The additional strain softening at larger strains, i.e. the structural nonlinearity will be estimated in the following part.

How to estimate the structural nonlinearity

To quantitatively evaluate the contribution of these physical events, we will apply an empirical expression to both the experimental data and the predictions of model 1 and 2. This expression is an extrapolation of the Mooney-Rivlin equation with the introduction of a parameter A, that characterize the amplitude of the nonlinearity. It writes:

$$\sigma = \frac{E_0}{3}[1 - \frac{5}{6}A(1 - \lambda^{-1})](\lambda - \lambda^{-2}) \qquad \text{(eq 5.27)}$$

where E_0 is the initial Young modulus measured at linear regime and A is a nonlinearity parameter. Indeed, eq 5.29 is equivalent to a Mooney-Rivlin equation

$$\sigma_{MR} = (2C_1 + 2C_2\lambda^{-1})(\lambda - \lambda^{-2})$$

with

$$E_0 = 6C_1 + 6C_2$$

and

$$A = \frac{6C_2}{5(C_1 + C_2)}$$

The physical meaning of parameter A in our study will be fully discussed in chapter 5.26 and will only be considered at this stage as an indication of the deviation from Gaussian affine deformation equation, since the statistical Gaussian affine deformation elasticity theory corresponds to the particular case of A=0.

We can also fit the modellization data by the same equation and got a parameter A_{visco}. The structural nonlinearity is calculated as the difference between them:

$$A_{\exp} - A_{visco} = A_{ent} + A_{plast} \qquad \text{(eq 5.28)}$$

where
- A_{exp} is the total nonlinearity parameter deduced from experimental data,
- A_{visco} is the nonlinearity parameter deduced from the modified viscoelastic predictions,
- A_{ent} is the structural nonlinearity parameter at rubbery state due to entanglement slipping,
- A_{plst} is the structural nonlinearity at glassy state due to local plastic events.

Indeed it is not possible without any assumption to distinguish in the non linearity $A_{ent}+ A_{plst}$ the respective contribution of entanglements and plasticity, but we will see in the next section that it is quite obvious to separate the two contributions.

Figure 5.18 shows a schematic representation of the meaning of $A_{exp, }A_{visco}$ and their difference $A_{ent} + A_{plast}$ represents the structural nonlinearity, i.e. the deviation of the experimental data from modified viscoelastic behavior predicted by the models we developed .
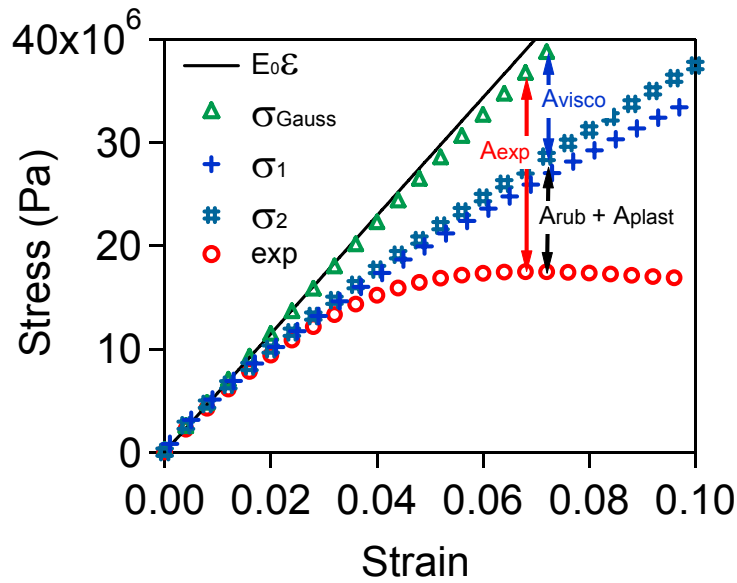
Figure 5.18. Comparison between pure elastic response with slope E_0 (black), Gaussian affine deformation model σ_{Gauss} **(eq 1.10)** (triangle), viscoelastic model 1 σ_1 (+), viscoelastic model 2 σ_2 (#) and experiments (circles). PB50% sample (T_g=-80°C), T=-74°C, strain rate=0.83/s.

The additional strain softening at larger strains, i.e. the structural nonlinearity $A_{ent} + A_{plast}$ can thus be calculated from rubbery state to glassy state. In the next section, we will give results of $A_{ent} + A_{plast}$ obtained by two models and discuss their evolution during the glass transition zone.

5.2.5. Evolution of structural nonlinearity

Now we are ready to evaluate quantitatively the nonlinearities in the glass transition regime. The detailed are presented in **Annex E**, and we just present here the main results.

Experimental data were fitted on a strain range such that the chi-square value χ^2 is equal to a given and constant value. We have estimated the influence of the χ^2 value on the estimation of $A_{ent} + A_{plast}$. We compared the results obtained for two values of χ^2 : $\chi_1{}^2$=5×10^{11} and $\chi_2{}^2$=10^{12}. We observed that the value chosen for χ^2 does not change the main features of the $A_{ent} + A_{plast}$ variation versus linear relaxation time. Details on this comparison are given in the **Annex E.**
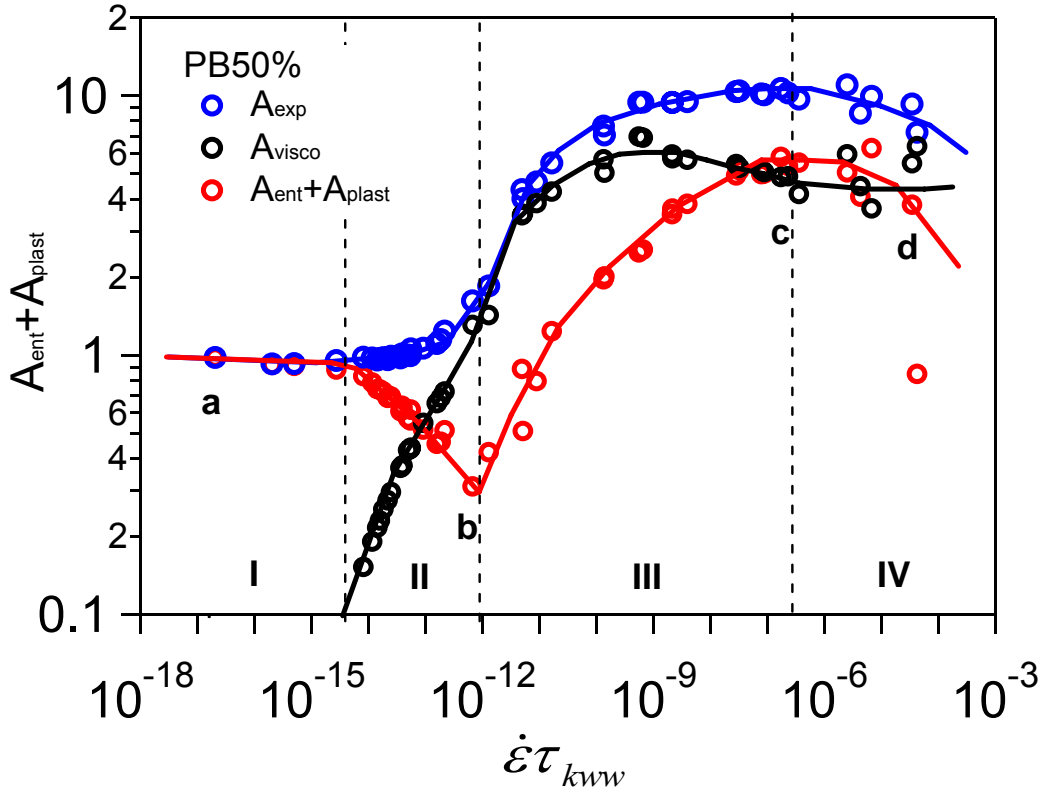
Figure 5.19. Fitting results of A_{exp}, A_{visco} and their difference $A_{ent}+A_{plast}$, with model 1, $\chi_2^2=10^{12}$. Points *a, b, c* and *d* correspond to previous stress-strain curves of **Figure 5.17**.

An example of fitting results is presented in **Figure 5.19**. For clarity, we plot results of A_{exp}, A_{visco} and $A_{ent}+A_{plast}$ only with model 1, $\chi_2^2=10^{12}$. We have shown in **Annex E** that the change of model or χ^2 does not change the conclusion.

It can be seen that the value of A_{exp} goes from 1 (at rubbery state) to 10 (at glassy state) and it has a slight decrease at deeply glassy state. The value of A_{visco} goes from 0 (at rubbery state) to a maximum of 7 (at glass transition zone) and it decreases to a value of about 5 at glassy state. The maximum of A_{visco} in the glass transition domain is reasonable since in this zone, the loss modulus G'', i.e. the viscoelastic contribution on strain softening, is also the maximum. Broadness of the A_{visco} peak should be considered to the broadness of G'' peak

It is interesting to note the significant decrease of the structural nonlinearity ($A_{ent}+A_{plast}$) at zone II, followed by a rapid increase at zone III. This evolution is also observed whatever the model we use (either model 2 or model 1), or whatever the value of χ^2 in the fitting condition (see **Annex E**).

This figure thus summarizes the main result obtained from the non-linearity estimation of stress-strain experiments. Let us just recall that despite the numerous difficulty of extracting the nonlinear data (self-heating, necking, viscoelastic contribution to non linearity, temperature dependence of the amplitude of the nonlinearities and thus of the fit window , we succeed in obtaining robust data, exhibiting clearly two aspects :
-   the entanglement slipping disappears up to a point where the mechanical response is extremely well described by our modified viscoelastic model.

- the plasticity appears progressively already in the middle of glassy domain. We will now discuss these results.

Before discussing the behavior of the nonlinearities with the temperature, we will briefly report the results obtained from cyclic measurements. We will show that these results confirm the results obtained in the simple extension stress strain experiments. We will discuss physically the origin of the nonlinearities lastly.

5.3. Cyclic shear Nonlinearities

We have choose to discuss our data with the Large Amplitude Oscillatory Strain usual tools, and more precisely the one proposed by Cho et al. [79]. For that we first recall the situation of linear regime in order to introduce in the same frame the nonlinearities.

In the linear regime

If a sine wave of strain $\gamma(t) = \gamma_0 \sin(\omega t)$ is applied, the stress response of the material is also a simple sine wave:

$$\begin{aligned}
\sigma(t) &= \sigma_0 \sin(\omega t + \delta) \\
&= \sigma_0 \cos\delta \sin(\omega t) + \sigma_0 \sin\delta \cos(\omega t) \\
&= G'\gamma(t) + G''\dot{\gamma}(t)/\omega \\
&= \sigma'(t) + \sigma''(t)
\end{aligned}$$

(eq 5.29)

where $\sigma'(t)$ is the elastic stress and describes the part of the signal in phase with the strain $\gamma(t)$; $\sigma''(t)$ is the viscous stress and describes the part in phase with $\dot{\gamma}(t)$, i.e. a cosine wave (see **Figure 5.20**).

Figure 5.20. Signal analysis of PB50% sample in the linear case: with *f*=0.01Hz γ_0=0.025 and T_0=-70°C. (a) Stress and strain as a function of time (b) Stress vs. strain curve. (c) Elastic stress (odd part of the total stress signal) vs. time. (d) Viscous stress (even part of the total stress signal) vs. time. (e) Elastic stress vs. strain: the slope is *G'*. (f) Viscous stress vs. $\dot{\gamma}(t)/\omega$: the slope is *G''*.

In the nonlinear regime

When strains are large enough, especially for polymers at glassy state, the strain-stress curves are non-elliptic: the response of the material becomes nonlinear and it cannot be described by simple sinusoidal waves. Our analysis in the nonlinear regime is based on the method developed by Cho et al. [79] to describe Large Amplitude Oscillatory Shear (LAOS).

Large Amplitude Oscillatory Shear (LAOS) analysis

The method Cho et al. [79] consists in the decomposition of a nonlinear stress into an elastic part and a viscous part, similarly to the linear case as described by the third equation of **(eq 5.29)**. However, as the signal is not sinusoidal, it requires taking the odd and the even part of the signal as follows:

$$\sigma'(t) = (\sigma(t) - \sigma(-t))/2 \qquad \text{(eq 5.30)}$$

$$\sigma''(t) = (\sigma(t) + \sigma(-t))/2 \qquad \text{(eq 5.31)}$$

The values of σ' and of σ'' are – in the linear case – the one described by **(eq 5.29)**.

Similarly to the linear case, Cho introduces the generalized moduli Γ' and Γ'' which writes:

$$\sigma'(t) = \Gamma'\gamma(t) \qquad \text{(eq 5.32)}$$

$$\sigma'(t) = \Gamma''\dot{\gamma}(t)/\omega \qquad \text{(eq 5.33)}$$

In the linear case, Γ' and Γ'' correspond to G' and G''. In the nonlinear case, $\sigma'(t)\,\text{vs}\,\gamma(t)$ and $\sigma''(t)$ vs $\dot{\gamma}(t)$ are no longer linear. We use a Taylor expansion of degree 3 of Γ' and Γ'' in fitting $\sigma'(t) = \Gamma'\gamma$ and $\sigma'(t) = \Gamma''\dot{\gamma}/\omega$ respectively:

$$\sigma'(t) = \Gamma_0'\gamma + \Gamma_2'\gamma^3 \qquad \text{(eq 5.34)}$$

$$\Gamma' = \Gamma_0' + \Gamma_2'\gamma^2 \qquad \text{(eq 5.35)}$$

and

$$\sigma''(t) = \Gamma_0''(\dot{\gamma}/\omega) + \Gamma_2''(\dot{\gamma}/\omega)^3 \qquad \text{(eq 5.36)}$$

$$\Gamma_0'' = \Gamma_0'' + \Gamma_2''(\dot{\gamma}/\omega)^2 \qquad \text{(eq 5.37)}$$

Γ_0' and Γ_0'' are the slopes at the origin, Γ_2' and Γ_2'' describe the deviation from the linear behavior of $\sigma'(t)$ and $\sigma''(t)$ respectively. Notice here that Γ_0' and Γ_0'' may depend on the strain amplitude, as well as Γ_2' and Γ_2''.

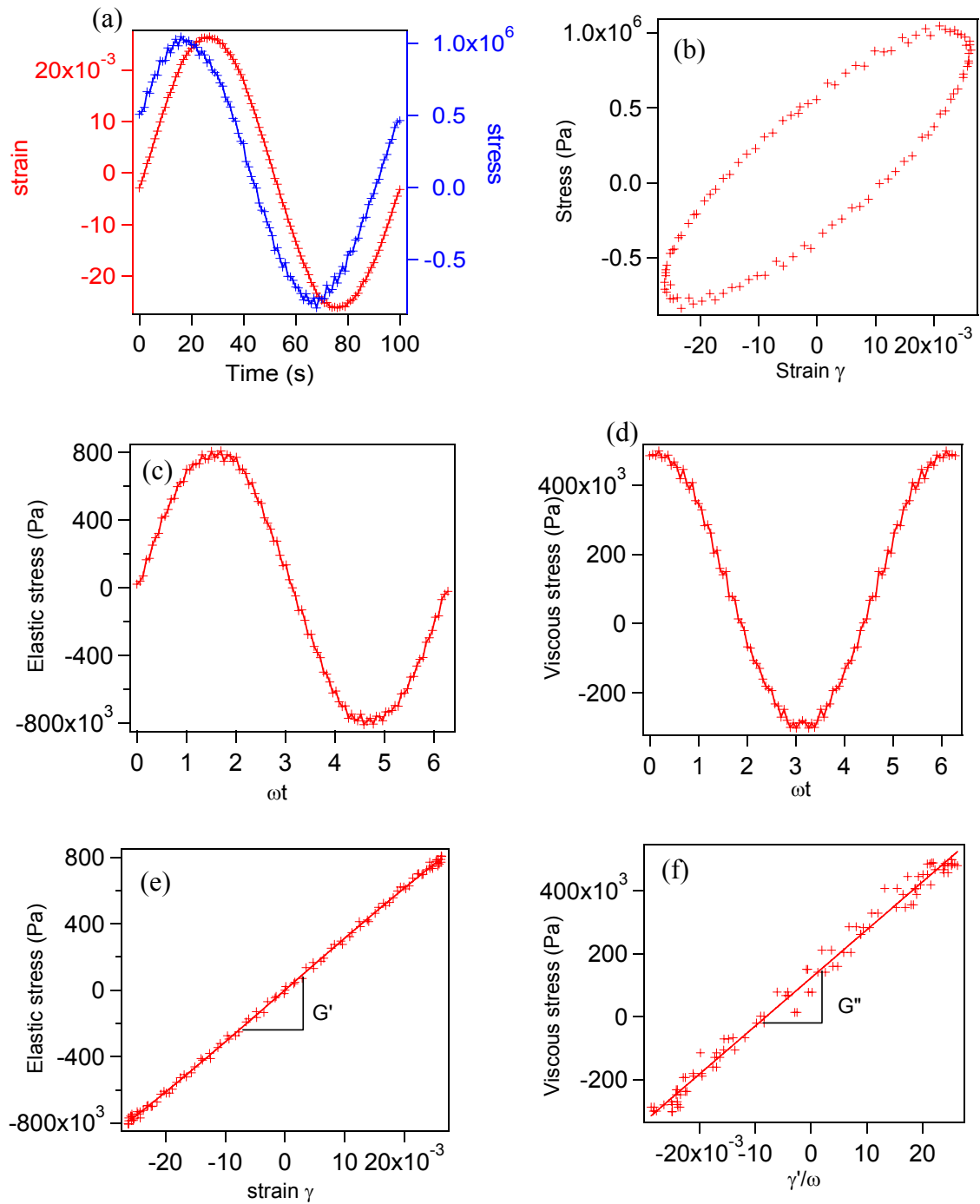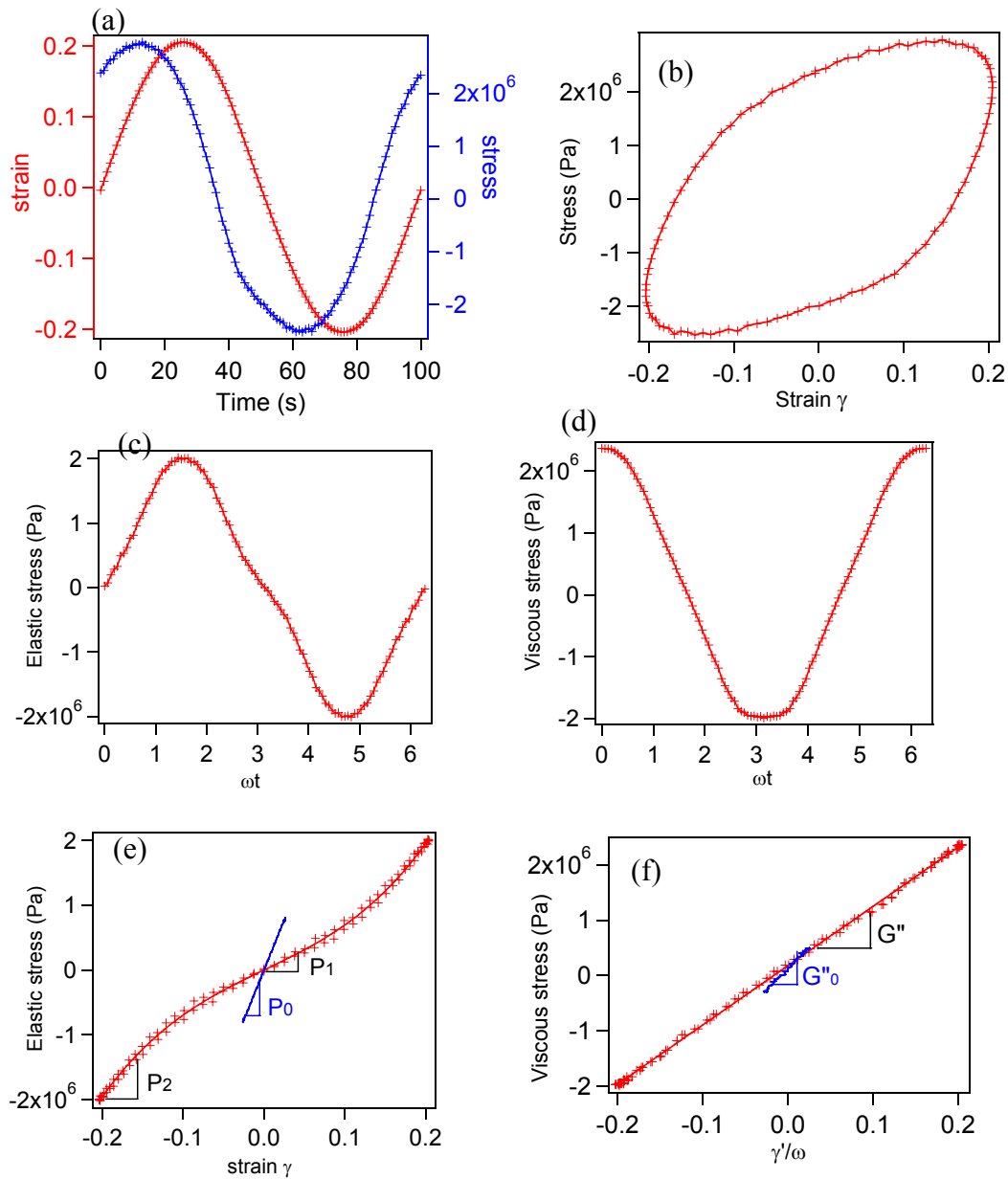**Figure 5.21.** Signal analysis of PB50% sample in the nonlinear case: with f=0.01Hz γ_0=0.2 and T_0=-70°C. (a) Stress and strain as a function of time. (b) Stress vs. strain curve. (c) Elastic stress (odd part of the total stress signal) vs. time. (d) Viscous stress (even part of the total stress signal) vs. time. (e) Elastic stress vs. strain: nonlinear behavior and strain hardening at large strain. (f) Viscous stress vs. $\dot{\gamma}(t)/\omega$: the curve is a straight line.

Figure 5.21 exhibit a typical example of the separation of the stress/strain signal in σ' and of σ''. It can be seen that the viscous stress vs. $\dot{\gamma}(t)/\omega$ curve at large strain is still linear with slope *G''* that is similar to that of small strain in the linear regime G_0''.

At opposite, the elastic stress vs. strain is not linear anymore. We use slopes P_0, P_1 and P_2 in the elastic stress vs. strain curve to describe the nonlinear behavior of the elastic part:

- P_0 is the slope at very low strain amplitude in the linear regime, and $P_0 = \Gamma_0'(\gamma_0 = 0)$

133

- P_1 is the slope at the origin and $P_1 = \Gamma_0{'}(\gamma_0)$
- P_2 is the maximum slope of the "elastic" stress/ strain, observed indeed at large strain, and writes $P_2 = \Gamma_0{'} + 3\Gamma_2{'}\gamma_0{}^2$

We observed that at large strain, P_1 decreases and that $P_2 > P_1$.

To conclude, two kind of nonlinearity are observed for the "elastic" strain:
- The decrease of the elastic modulus at the origin between cycles of different amplitude.
- Strain hardening at large strain amplitude inside each cycle.

One should keep in mind that $\Gamma_0{'}(\gamma_0)$ and $\Gamma_0{''}(\gamma_0)$ are all amplitude dependent parameters.

Evolution of the nonlinearity

We will now describe our result in the situation where f=0.01Hz which corresponds to an isothermal response (see **Annex F**).

Figure 5.22. Evolution of the elastic modulus (a) P1 (b) P2 and (c) loss modulus G" with the strain amplitude and temperature. PB50% sample with f=0.01Hz. Arrows in Figure (a) are data used in the discussion section.

We observe that P_1 (or $\Gamma_0{'}$) deviates significantly at large strain and at low temperature. The comparison between the rheology measurement at 0.02% and cyclic shear MTS measurement at 1% show good agreement at high temperature. While at low temperature, the moduli of cyclic shear measurement are smaller. This is partly because of

machine compliance that is already discussed in annex 4 and also probably because of the temperature calibration. However this discrepancy does not modify the present discussion.

Here, we focus on the deviation of the modulus at large strain from that of small strain at 1%, which is considered to be in the linear regime. We note that the deviation of P_1 appears at $G' > 2 \times 10^6$ Pa – i.e. the beginning of zone III in extension test, indicating that the decrease of the elastic modulus at the origin would be due to plasticity.

G" is weakly affected by large strain, with only slight decrease at large strain amplitude. Indeed these results are similar for f=0.1Hz (isothermal measurements) and for f=10Hz (in the adiabatic measurements)
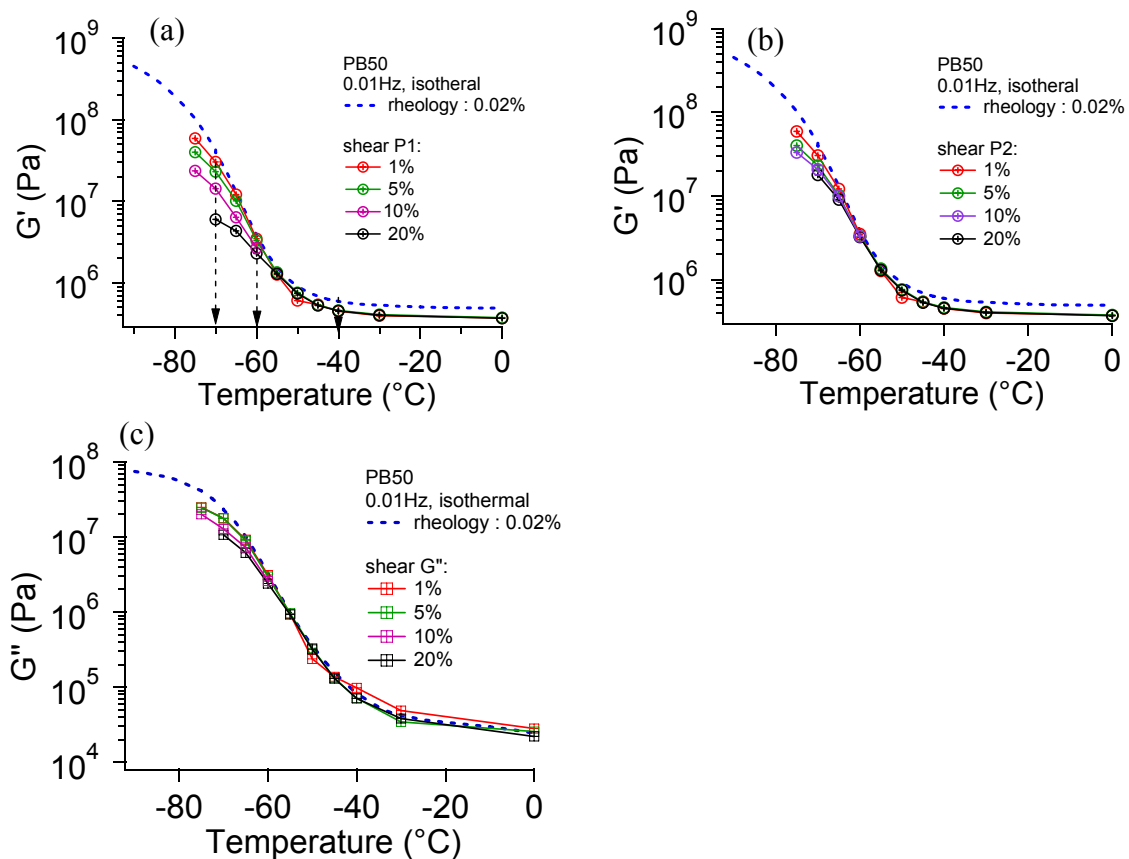
f=0.1Hz

Figure 5.23. Evolution of the elastic modulus (a) P1 (b) P2 and (c) loss modulus G" with the strain amplitude and temperature. PB50% sample with f=0.1Hz.

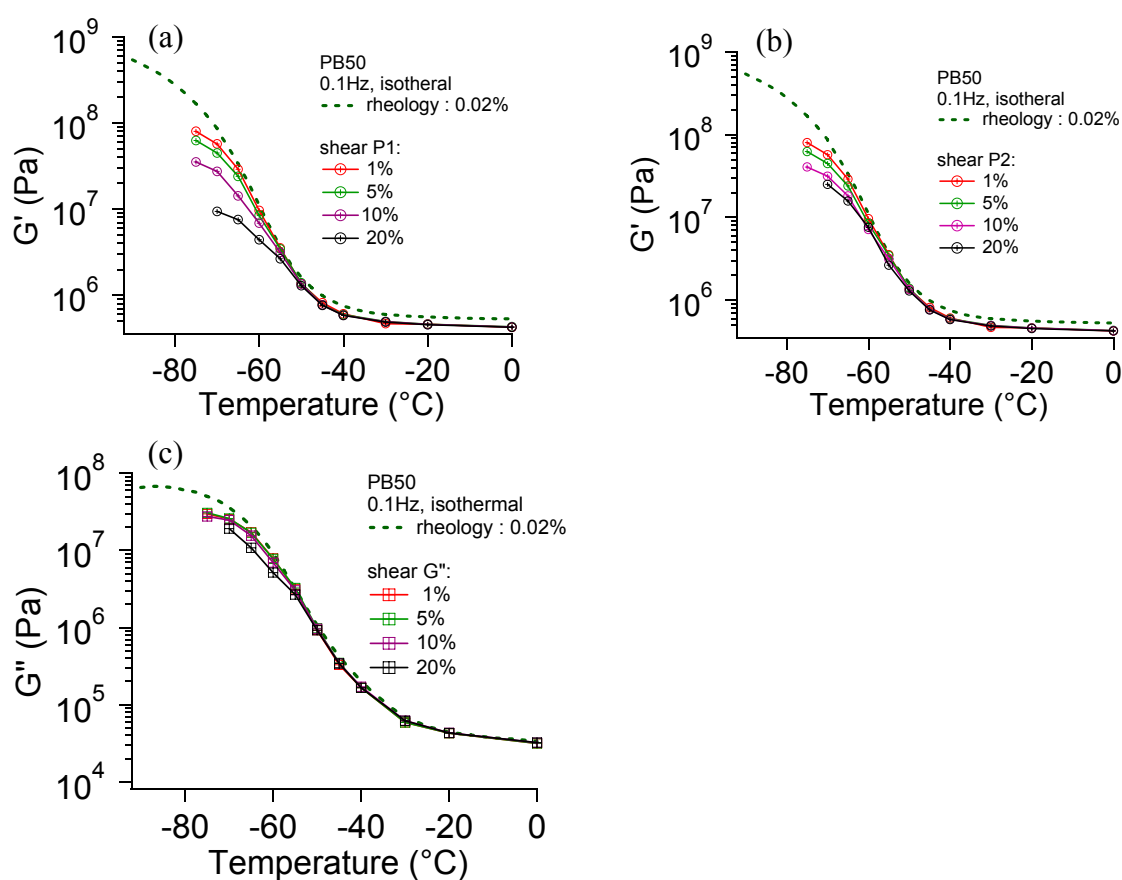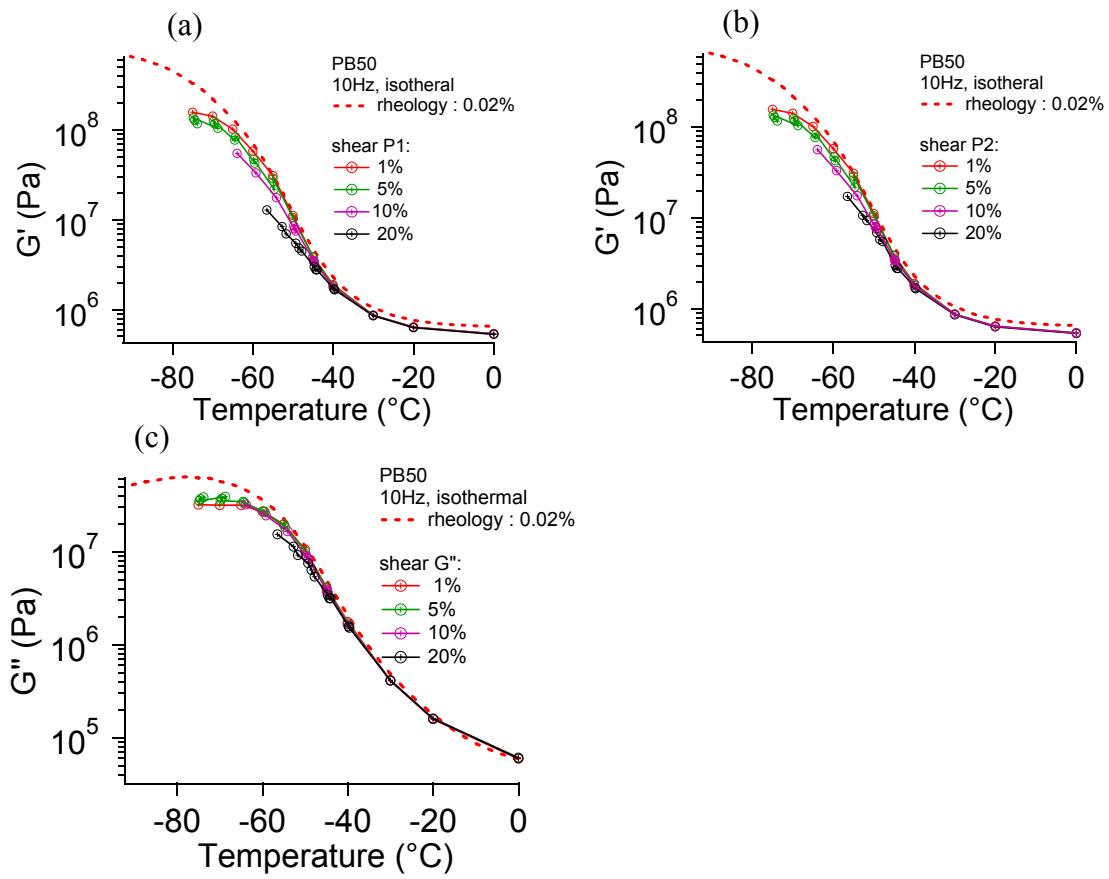The evolution of f=0.1Hz is similar to f=0.01Hz.

Figure 5.24. Evolution of the elastic modulus (a) P_1 (b) P_2 and (c) loss modulus G'' with the strain amplitude and temperature. PB50% sample with *f*=10Hz

The actual amplitude and the actual temperature of each cycle are carefully determined in the reliable experimental window of first 0.5s. The evolution of *f*=10Hz is also similar to others.

Discussions

Cyclic shear measurements of PB50% sample at f=0.01Hz, 0.1Hz and 10Hz show similar results.
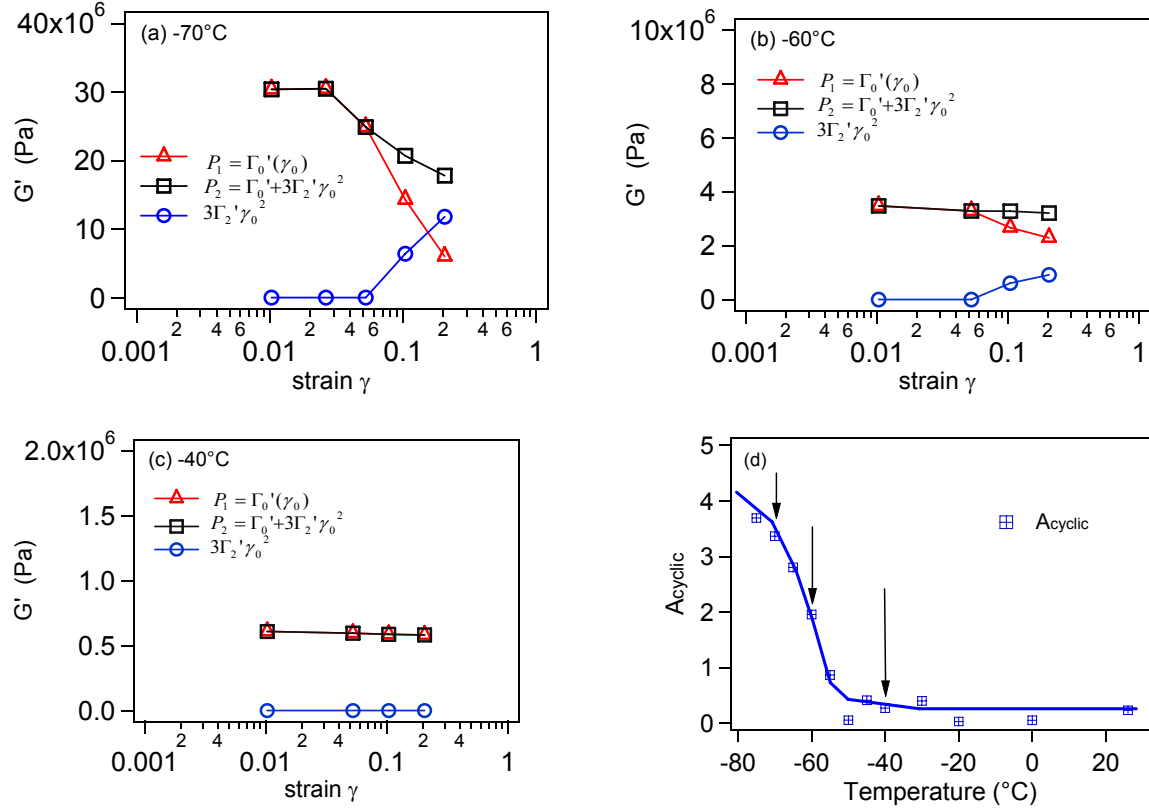
Figure 5.25. Evolution of the linear and nonlinear term of the elastic modulus with the strain amplitude. PB50% sample with f=0.01Hz and (a) T_0=-70°C, (b) T_0=-60°C and (c) T_0=-40°C. (d) The evolution of A_{cyclic} as a function of temperature.

We can study the evolution of P_1, P_2 and their difference with the strain amplitude γ_0. We observed that they are quasi-constant at high temperature (see **Figure 5.25**(a-c)), while at low temperature P_1 and P_2 decreases rapidly. This is also observed as Payne effect in filled elastomer.

With strain hardening inside each cycle, the modulus at large strain P_2 approaches P_0. It is possible that at large strain inside each cycle, the instantaneous strain rate approaches zero and some domains that have gone through local plastic events go back to glassy domains. The modulus at large strain is thus higher than at origin, where the instantaneous strain rate is the maximum.

We can calculate the strain softening parameter A_{cyclic} that is similar to A_{plast} by using **(eq E.3)** and taking the following approximation:

137

$$A_{cyclic} \approx \frac{3}{5} \frac{\left.\dfrac{\partial^2 \sigma'}{\partial \gamma^2}\right|_{\gamma=0.05}}{\left.\dfrac{\partial \sigma'}{\partial \gamma}\right|_{\gamma=0.01}} \approx \frac{3}{5} \frac{\left(\Gamma_0'(\gamma_0 = 0.05) - \Gamma_0'(\gamma_0 = 0.02)\right)/0.03}{\Gamma_0'(\gamma_0 = 0.01)} \qquad \text{(eq 5.38)}$$

Results are presented in **Figure 5.25**(d), it can be seen that the nonlinearity parameter $A_{cyclic} \approx 0$ at high temperature and it grows rapidly to $A_{cyclic} \approx 4$ as temperature approaches the glass transition temperature (T_g=-80°C): the local plastic events appear here.

We can also relate each temperature to $a_T^{WLF} f$, then we plot the evolution of nonlinearity parameter A_{cyclic} and $G' = \Gamma_0'(\gamma_0 = 0.01)$ in a same figure (see **Figure 5.26**).

At rubbery state, $A_{cyclic} \approx 0$, the strain softening is not observed in this regime in cyclic shear test. This is because that the applied strain amplitude (up to 20%) is not large enough be sensitive to the Mooney-Rivlin nonlinearities.

In the glassy transition zone (zone III), the evolution of A_{cyclic} is very similar to that of A_{plast}: both their positions and values.
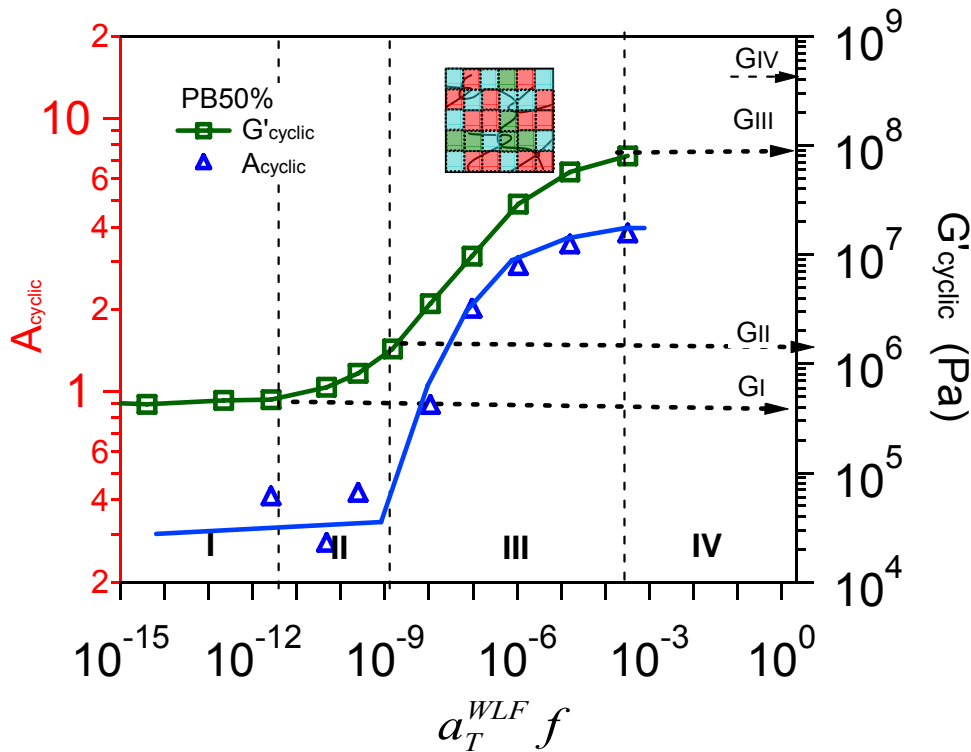
Figure 5.26. Nonlinearity parameter A_{cyclic} in cyclic shear test, and its corresponding value of $G' = \Gamma_0'(\gamma_0 = 0.01)$.

Conclusions

We defined a reliable experimental window for cyclic shear measurement: the first 0.5s of high frequency measurement which is in the adiabatic regime and all the data of low frequencies which is in the isothermal regime. Nonlinear time-temperature superposition of cyclic shear measurement is valid.

The non-elliptic strain-stress curves at large amplitude and low temperature are analyzed by Large Amplitude Oscillatory Shear (LAOS) method that shows a decrease of the elastic modulus at the origin, as well as a strain hardening at large strain amplitude inside each cycle.

This nonlinearity is characterized by a parameter A_{cyclic} are similar to the A_{plast} obtained from simple extension test. We will now discuss the physical origin of these nonlinearities.

5.4. General discussion of nonlinear mechanics

5.4.1. Physical interpretation of $A_{ent}+A_{plast}$
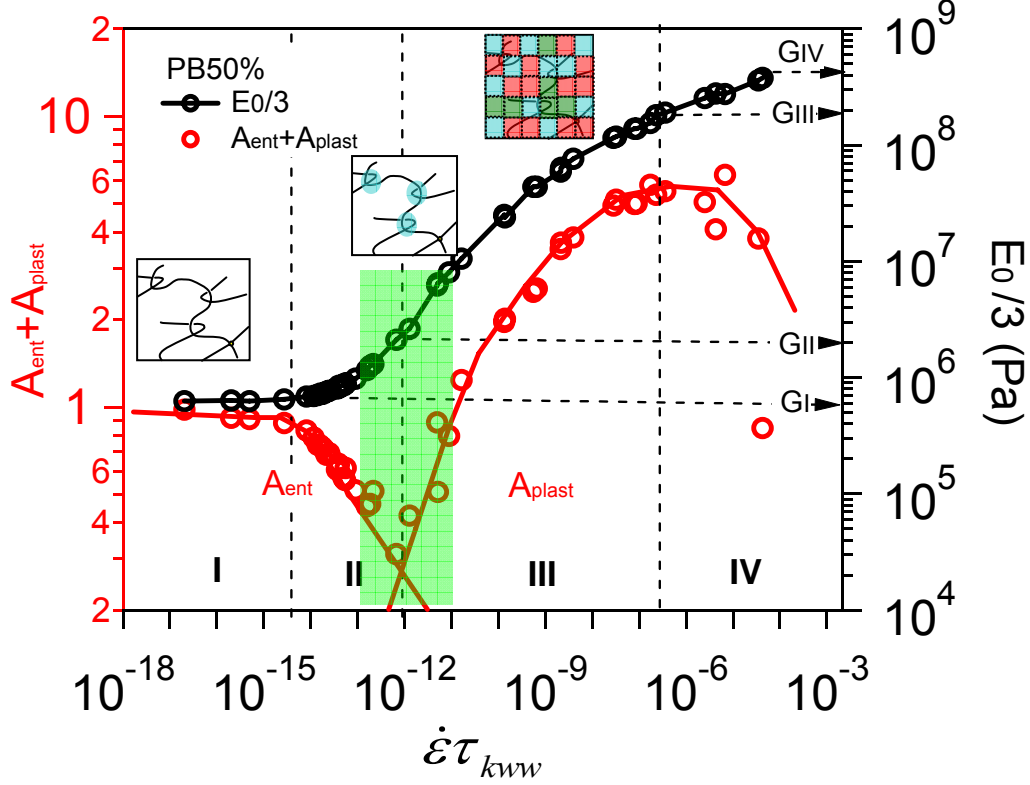
Figure 5.27. Fitting results of $A_{ent}+A_{plast}$ with model 1, $\chi_2^2=10^{12}$, and the corresponding value of $E_0/3$. Separation into 4 zones and their corresponding structures are plotted as inset schematics. Green shadow zone is the crossover zone between entanglement slipping and plasticity.

We compare the evolution of $A_{ent}+A_{plast}$ with the initial shear modulus G_0, and divide the system into 4 zones according to the evolution of $A_{ent}+A_{plast}$

Zone I: rubbery zone. The structural nonlinearity parameter is a constant with $A_{ent}+A_{plast} \approx 1$, and the corresponding modulus is G_{rub} (=6×10^5Pa, represented as G_{II} in the figure). This is the classical rubber elasticity zone where the mechanical behavior is independent on the strain rate. Our fitting model eq 5.29 is indeed equivalent to Mooney-Rivlin model with the relation:

$$A_{MR} = \frac{6C_2}{5(C_1 + C_2)} \qquad \text{(eq 5.39)}$$

Giving $C_1 = 5.7\times10^4\,Pa$ and $C_2 = 2.6\times10^5\,Pa$, we have A_{MR}=0.98. This value represents almost the whole of $A_{ent}+A_{plast}$ and indicates that $A_{ent} \approx A_{MR} \approx 1$ and $A_{plast} \approx 0$ in this regime.

The structural nonlinearity A_{ent} in this zone is due to entanglement slipping (see **Figure 5.28**), which could be described by Rubinstein model (giving $G_c = 1 \times 10^4 \, Pa$ and $G_e = 5.6 \times 10^5 \, Pa$).

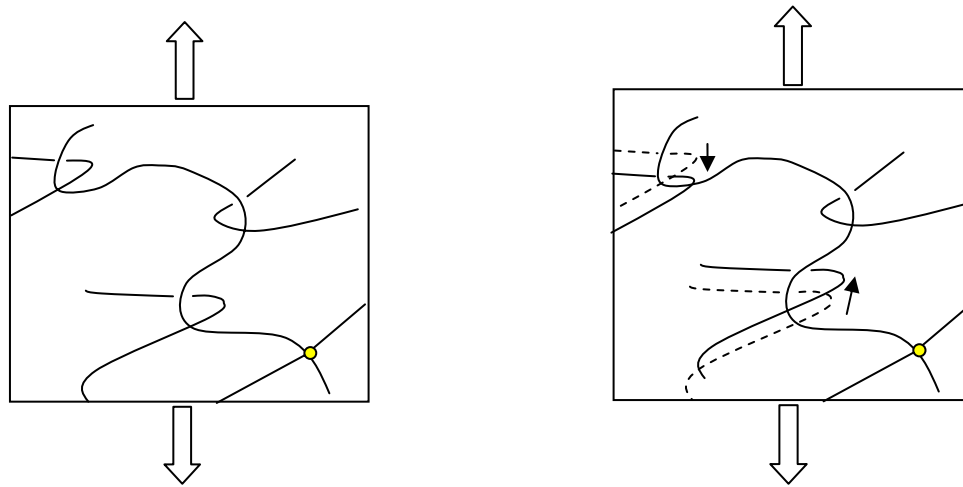**Figure 5.28.** Schematic of slipping of entanglements during deformation at rubbery state. The slipping movement is indicated by arrows. Yellow point is crosslink that doesn't slip.

Zone II: pre-transition zone. The structural nonlinearity decreases towards $A_{ent}+A_{plast}$ =0, and $G_{II} \approx 3G_{rub}$ (=2×10⁶Pa). The value of A_{ent} decreases to its minimum close to zero, where the shear modulus G_{II} is about 3 times G_{rub}. The entanglement slipping events are greatly reduced at this point, probably because chains are less mobile and unable to slip (see **Figure 5.29**). Other physical event like plasticity of glassy domains may be still absent here. We will investigate the concentration of glassy domains in this zone afterwards.

Note that at the crossover zone between zone II and zone III, the response corresponds exactly to our modified viscoelastic model, but that the elastic modulus is larger than the one in the rubber phase. Indeed it would likely correspond to a rubber where all the entanglements have become crosslinks.

Zone III: glass transition zone. The structural nonlinearity parameter increases towards $A_{rub}+A_{plast} \approx 6$, and $G_{III} \approx 300G_{rub}$ (=1.8×10⁸Pa). In fact, in this zone physical event like plastic events begins to dominate and its amplitude grows continually for increasing strain rate or decreasing temperature. Further discussion will be done in the next section (Chapter 5.4.2).

Zone IV: glassy zone. The structural nonlinearity parameter decreases slightly from $A_{rub}+A_{plast} \approx 6$, and $G_{IV} \approx 1000G_{rub}$ (=4×10⁸Pa). As the system goes deeper and deeper into the glassy zone, its behavior becomes more and more fragile. The material could break at very small strains $\varepsilon < 0.05$. Data in this regime are less reliable.
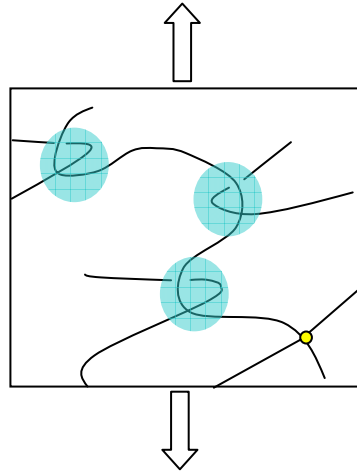
Figure 5.29. Schematic of local glassy domains (blue zones) that prevent entanglements to slip.

We have plotted the experimental time scale $\tau = 1/\dot{\varepsilon}$ as a function of temperature for all the measurements and they are divided into 3 zones: rubber, glass transition and glass (see **Figure 5.30**). The intermediate transition zone corresponds to experiments where the nonlinearity parameter A is near the minima value of $A(\sim 0.5)$ (see the crossover zone in **Figure 5.27**). This crossover zone corresponds to a Young's modulus $2E_{rub} < E_0 < 20E_{rub}$.

The position of the transition zone (T~40°C) corresponds to the high temperature tail of the local glass transition distribution determined in chapter 4 from DSC and rheological measurements
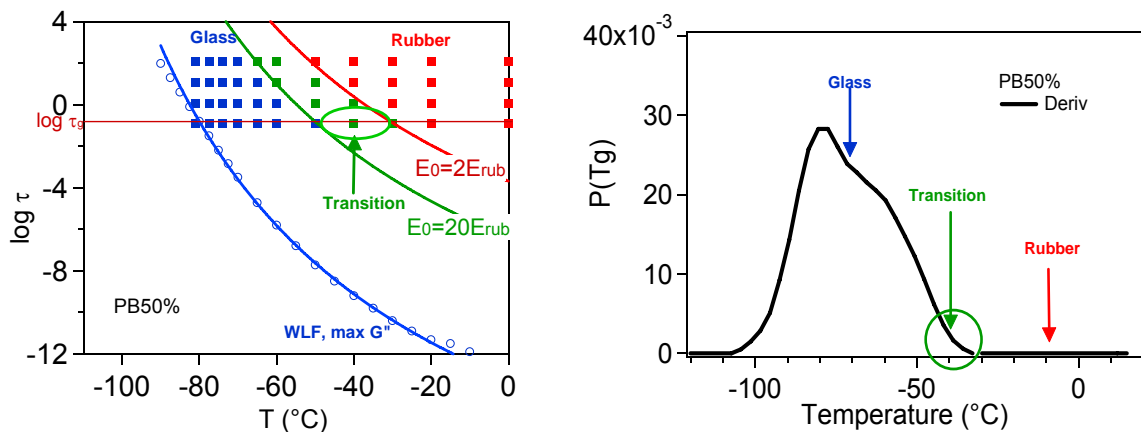
Figure 5.30. (a) Experimental time scale $\tau = 1/\dot{\varepsilon}$ as a function of temperature, and separation to 3 zones: rubber, transition and glass. (b) Position of 3 zones in the local glass transition distribution curve.

This suggests that the structural nonlinearity due to plasticity is related to the local glass transition distribution.

In order to know more precisely in which way the T_g distribution control the onset of plasticity, we should compare these results obtained on the PB to the one deduced from experiments performed on SBR and PB.

5.4.2. What is the relation between structural nonlinearity and plasticity?

This strain softening of glassy polymers can be attributed to local plastic events at small strains below the yield point. In fact, local plastic events can occur at extremely small strains (as small as 10^{-4}) where the material is traditionally described as perfectly elastic [80].

We will try to establish a relation between plasticity and A_{plast} value through Olroyd-Palierne model. Considering that at the beginning of the extension, all the domains of the material are glassy and rigid with a modulus E_0. During the deformation, some domains that have experienced plastic events are more mobile and have lower modulus E_i, with a volume fraction f_i. These domains can be considered as soft inclusions in a rigid matrix, and the macroscopic modulus can be calculated by Olroyd Palierne:

$$E^* = E_{mat}^* \left(1 + \frac{5}{2} \sum_i f_i H_i \right)$$

(eq 5.40)

where

$$H_i = \frac{2E_i^* - 2E_{mat}^*}{2E_i^* + 3E_{mat}^*}$$

(eq 5.41)

The idea is that once relaxed, the plastic domain does not carry any more stress and can thus be assumed to behave as zero-modulus domains. In that approximation the value of H_i for the domains that undergo plastic deformation is :

$$H_i \approx -\frac{2}{3}$$

(eq 5.42)

and the macroscopic modulus is:

$$E \approx E_g \left(1 - \frac{5}{3}\varphi_p \right)$$

(eq 5.43)

where E_g is the matrix modulus and $\varphi_p = \sum_i f_i$ is the total volume fraction of domains that have undergone plastic deformations.

The macroscopic modulus decreases linearly with increasing plastic domains. In order to describe our data, we assume in addition that the number of plastic events (φ_p) increases linearly with strain before yield point with a coefficient K, i.e.:

$$\varphi_p = K\varepsilon,$$

(eq 5.44)

Hence the modulus writes:

$$E = E_g \left(1 - \frac{5}{3}K\varepsilon \right)$$

(eq 5.45)

leading simply for the contribution to non –linearity to be

$$E_1 = -\frac{5}{3}KE_g$$

(eq 5.46)

Applying **(eq E.3)**, the structural nonlinearity caused by plastic events is:

$$A_{ent} + A_{plast} = \frac{3\Delta E_1}{5E_0} = K \qquad \text{(eq 5.47)}$$

Since $A_{ent} \approx 0$ in this zone, we have simply $A_{plast} = K$ and the number of plastic events in the glassy state is evaluated as $\varphi_p = A_{plast}\varepsilon$. For a glassy sample with $A_{plast} \approx 6$ and stretched to yield point $\varepsilon = 0.075$, the volume fraction of plastic domains is:

$$\varphi_p = A_{plast}\varepsilon = 6 * 7.5\% = 45\% \qquad \text{(eq 5.48)}$$

To conclude, the structural nonlinearity in glassy state may be caused by local plastic events. For a naïve model assuming that the plastic events do not carry any stress, we find that the total amount of these events is proportional to strain $\varphi_p = A_{plast}\varepsilon$.

Let us note that in practice, due to the fact that the stress field must be somehow localized. As a consequence, the domains that undergo the larger stresses will thus submit first a plastic event. They will release thus more stress than the average value. As a consequence the value of K is likely overestimated. This can be understood if one try to discuss these effect in the frame of mechanical percolation as we will do now.

<u>Towards percolation ideas</u>

The above plasticity model is based on the system where all the domains are initially glassy with a modulus $E_0 = E_g$. In reality, the macroscopic initial modulus E_0 is a value distributed between the glassy one E_g and rubbery one E_r depending on the domain local glass transition. We assume that each domain of the system can has a modulus that is either E_g or E_r, without intermediate moduli (we will show afterwards that this assumption is reasonable), with a macroscopic E_0. We hypothesize that plasticity events convert the modulus of some domains from E_g to E_r. Since $E_g >> E_r$, the macroscopic initial modulus E_0 is:

$$E_0 = E_g\left(1 - \frac{5}{3}\varphi_r\right) \qquad \text{(eq 5.49)}$$

where φ_r is the total volume fraction of domains with modulus E_r before extension. This equation is in fact correct only if the glassy domains are the majority, i.e. $\varphi_r << 1$. During the extension, a volume fraction of plastic events φ_p increases and the total fraction φ is the sum of these two parts $\varphi = \varphi_r + \varphi_p$. It can be seen that

$$E = E_g\left(1 - \frac{5}{3}\varphi\right) \approx E_0\left(1 - \frac{5}{3}\varphi_p\right) = E_0\left(1 - \frac{5}{3}A\varepsilon\right) \qquad \text{(eq 5.50)}$$

The nonlinearity is again proportional to the volume fraction of plastic domains. This means that at glass transition zone, our plasticity model is still valid.

To verify if the two-modulus assumption is reasonable, we will calculate from experimental results the distribution of storage modulus $P(\log G')$ in the sample, assuming that $E = 3G \approx 3G'$.

The relation between $P(\log G')$ and $P(T_g)$ is:

$$P(\log G') = P(T_g)\left|\frac{dT_g}{d\log G}\right| \qquad \text{(eq 5.51)}$$

The distribution of $P(T_g)$ in PB50% blend is already obtained in chapter 4, and the distribution $P(\log G')$ is presented in **Figure 5.31**(d).
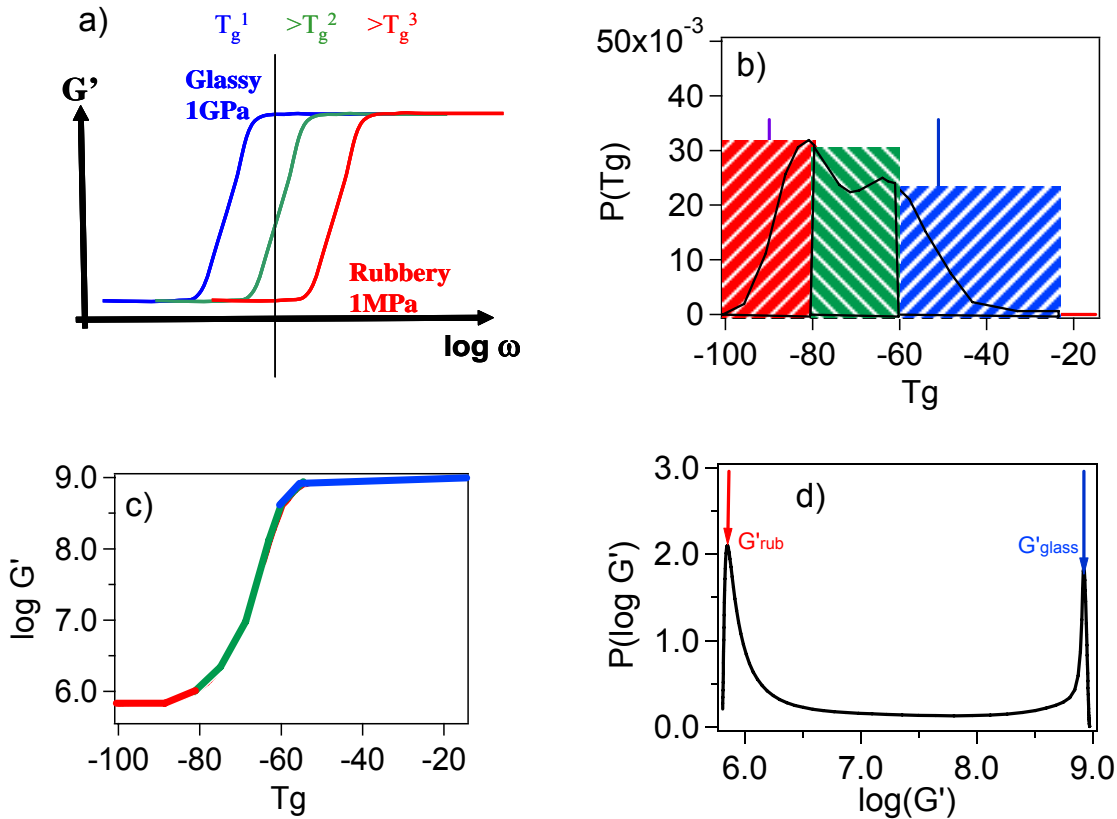
Figure 5.31. (a) schematic of the modulus as a function of local T_g; (b) $P(T_g)$ of PB50% blend; (c) $log(G')$ as a function of local T_g of PB50% blend at f=1Hz; (d) the distribution of $log(G')$ obtained from $P(T_g)$ of PB50% blend at T=-60°C and f=1Hz. Arrows are indicators of the positions of the peaks of $log(G')$.

It shows that the distribution of $log(G')$ has two peaks: one of G'_{rub} at $log(G')$=6 and the other of G'_{glass} at $log(G')$=9. These two peaks (positions indicated by arrows) should no be confused with the bimodal form of $P(T_g)$, and it is in fact due to the broad distribution of $P(T_g)$.

So for polymers or blends with broad distribution of local T_g, it is a good approximation to consider only two components E_g and E_r, without considering the intermediate values.

Percolation of glassy domains

Since the system can be represented by two components, we will go back to the two-component Olroyd-Palierne model to evaluate the concentration of glassy domains φ_g at each zone. We take a system with domains of two moduli: G_{rub}=1MPa and G_{glass}=1000MPa. The volume fractions are respectively φ_r and φ_g, with $\varphi_r + \varphi_g = 1$.
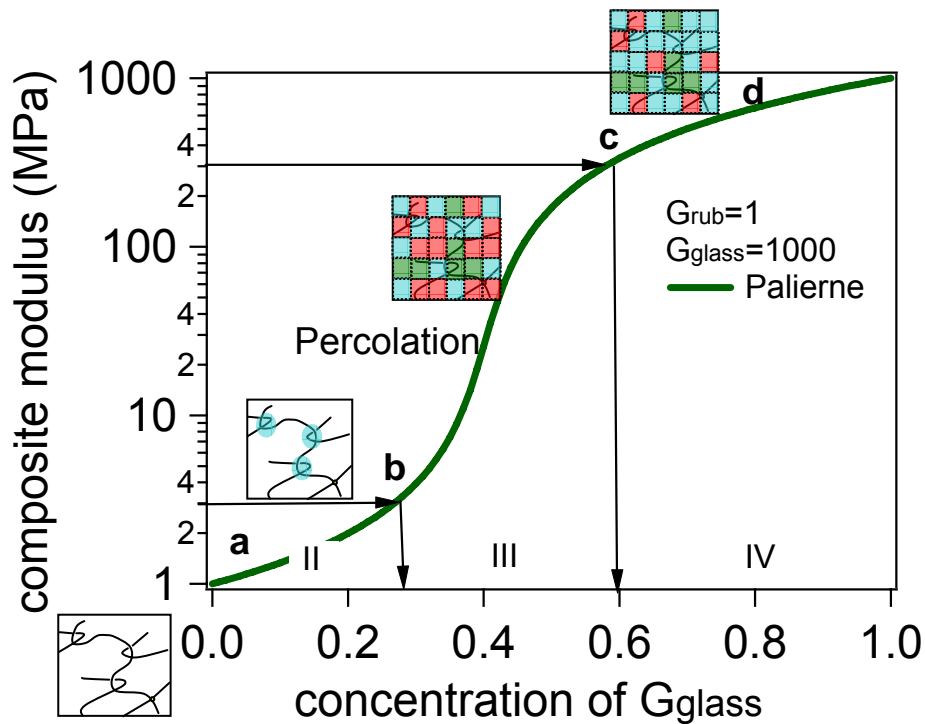
Figure 5.32. Values of the modulus of different zones (at b point, $G_0 \approx 3G_{rub}$, and at c point, $G_0 \approx 300G_{rub}$), and their corresponding concentration of G_{glass} according to Olroyd-Palierne model.

It can be seen from the above **Figure 5.32** that :
- zone I : $\varphi_g \approx 0$
- zone II : φ_g = 0 to 0.3
- zone III : φ_g = 0.3 to 0.6
- zone IV : φ_g > 0.6

The sharp increase of the modulus around φ_g = 0.4 indicates a percolation of the glassy domains in the system. This critical concentration falls in the zone III where the plastic events grow rapidly. We can say that the local plastic events, evidenced by the increase of

structural nonlinearity in zone III, are correlated to the percolation of glassy domains in the system (see **Figure 5.33**).
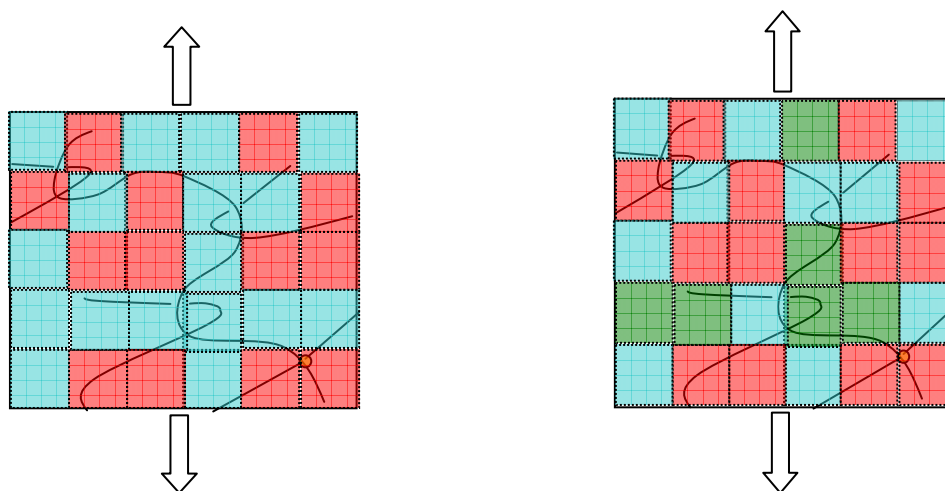
Figure 5.33. Schematics of percolation of glassy domains and plastic events during deformation: (a) before deformation; (b) during deformation. Red =rubbery domains, blue=glassy domains, green=domains with plastic events.

Figure 5.33(a) shows a system where the local glassy domains percolate and the macroscopic modulus is close to the glassy one. During the deformation, some zones experience local plastic events and the local moduli of these zones are decreased. As a consequence, the glassy bridge is broken and the macroscopic modulus becomes close to the rubbery one. This is the physical meaning of the strain softening caused by plasticity in glassy systems.

5.5. Conclusions

We have observed similar nonlinearities in simple extension and cyclic shear measurements.

The nonlinearity at large strain is observed and quantitatively analyzed as a sum of different contributions: linear stress relaxation (*G'* and *G''*), entropic Gaussian affine deformation, and structural nonlinearity by physical events like entanglement slipping and plasticity.

Entanglement slipping in rubbers has a constant level at high temperature or low strain rate. As the system approaches glass transition, the entanglement slipping is greatly reduced due to appearance of glassy domains that immobilize the chains.

Plasticity begins to be dominant as the system goes deeper into the glass transition zone, and glassy domains percolate.

At first analysis, nonlinear time-temperature superposition seems found to be valid either for simple extension and cyclic shear, and either for adiabatic or isothermal measurements (some examples are given in **Annex F** and **Annex G**).

6.   General conclusion

Miscible polymer blend is a highly heterogeneous system, with a very broad glass transition zone. In this study on polybutadiene (PB) and styrene butadiene rubber (SBR) blend system, we have quantitatively related the distribution of relaxation times $P(\tau)$ to the experimental data of calorimetry, rheology, and dielectric measurements, through a distribution of glass transition temperature $P(T_g)$. The length scale ξ of segmental movement associated to the α-relaxation is measured in different techniques. The effect of mechanical couplings of different domains is also studied in the nonlinear mechanical measurements.

First, we study these PB/SBR miscible polymer blends in the linear regime by calorimetry, rheology, and dielectric measurements. In all cases, we observe a broadening of the glass transition zone (or the corresponding α-relaxation peaks), confirming that large dynamic heterogeneities exist in our PB/SBR blend. We observed in general a good time-temperature superposition for pure polymers and polymer blends except for dielectric measurements. The dynamic heterogeneity in the blend system can be characterized by a broad distribution of glass transition temperature $P(T_g)$, extracted by different methods from calorimetric measurements Calorimetric measurement with physical aging at different aging temperature T_a exhibits a peak that reveals the independent contribution of different domain of T_g. The overshoot peaks of polymer blend exhibit thus a broad distribution. There is in addition an aging time-temperature superposition for physical aging.

The $P(T_g)$ obtained by DSC measurements is the origin of viscoelastic properties observed in the glass transition. Using self-consistent averaging method inspired by the Olroyd-Palierne model, we predict quantitatively, with no adjustable parameter, the viscoelastic spectrum of our blends from the T_g distribution obtained by calorimetry. This quantitative prediction confirms thus the assumption that mechanically, a blend can be considered as an ensemble of domains each of which having a different glass transition temperature.

Dielectric measurements show that the T_g distribution existing in our PB/SBR blends can be described assuming two distinct domains, the ones centered on a PB chains and the seconds centered on SBR chains. These results confirm the importance of the self concentration concept proposed by McLeish and Shenogin. The dielectric α-relaxation presents two distinct mean relaxation times. Depending on the intensity of the dielectric response of each component of the blend, the macroscopic dielectric response of the blend can be dominated by the contribution of only one of the two components. In SBR/PB blends, the contribution of the domains rich in SBR chains dominate the macroscopic a relaxation However, contribution of domains centered on PB chains is not visible. This difference gives rise to a huge difference in the α-relaxation peak position (or the macroscopic T_g) observed in calorimetry and in dielectric measurements.

In addition, we evaluate the length scale of the dynamic heterogeneities controlling the physical properties in the glass transition domain. We found a length scale of ξ=1nm for the calorimetric, dielectric and rheological properties. In the glass transition domain, the physical properties are controlled by heterogeneities existing the length scale of the segmental motions

involved in the glass transition (~1nm). In our blend system, we do not observe an effect of blending on at the larger length scales involved in rubber elasticity (~10nm). Moreover, no effect of blending is obvious at smaller length scale associated to the localized motions controlling the β-relaxation (<1nm). The dielectric β-relaxation of polymer blends remains to be that of pure polymer PB and is hardy affected by blending,

Finally, the nonlinear mechanical properties are studied from the rubber state to the glassy state. The nonlinearity at large strain is observed and quantitatively analyzed as a sum of different contributions: We identify four mechanisms occurring in the non linear regime., whose weight varies as the polymer blend goes from rubber to the glassy state linear viscoelastic stress relaxation (related to G' and G'' measured in the linear regime), entropic Gaussian affine deformation, and structural nonlinearity by physical events like entanglement slipping and plasticity. Entanglement slipping in rubbers occurs at high temperature or low strain rate. As the system approaches its glass transition, the entanglement slipping is strongly reduced due to the appearance of few glassy domains that immobilize the chains. Plasticity begins to be dominant as the system goes deeper into the glass transition zone, and the structural nonlinearity is the strongest when there is a percolation of glassy domains.

Annex A. Infrared camera and calibration

The nonlinear mechanical measurements of glassy polymers are always accompanied by a self-heating process, which is due to low thermal conductivity and relatively high energy dissipation of polymers. The temperature evolution of the sample has to be precisely measured by infrared camera during such mechanical measurement in order to be able to analyze the data.

Principle of infrared camera

All objects emit a certain amount of black body radiation as a function of temperatures and this radiation energy output is given by the Stefan-Boltzman law:

$$P = \varepsilon\sigma A T^4 \qquad\qquad (eq\ A.1)$$

where :
P: Heat transfer per unit time
ε : Emissivity, no unit (=1 for a black body, <1 for a non-black body)
σ : Stefan-Boltzmann constant ($=5.67\times10^{-8}W\cdot m^{-2}\cdot K^{-4}$)
A : Area of the object (m^2)
T : Absolute temperature (K)

Generally speaking, the higher an object's temperature, the more infrared radiation is emitted. This radiation has a spectral distribution (described by Planck's law) and the maximum is given by Wien's law:

$$\lambda_{max} = \frac{2898}{T}\mu m \qquad\qquad (eq\ A.2)$$

It describes quantitatively the common observation that the colors vary from red to orange or yellow as the temperature of the thermal radiator increases.

The sun (~6000K) emits yellow light, and the peak of radiation is at about 0.5 μm in the middle of the visible light spectrum. A black body at room temperature (~300K) has a peak of radiation at about 9.7 μm, in the infrared spectrum.

An infrared camera is a device that forms images using infrared radiation, similar to the way an ordinary camera detects visible light. More precisely, the infrared camera measure the radiation power in some given wavelength window, allowing to deduce the temperature distribution of an object.
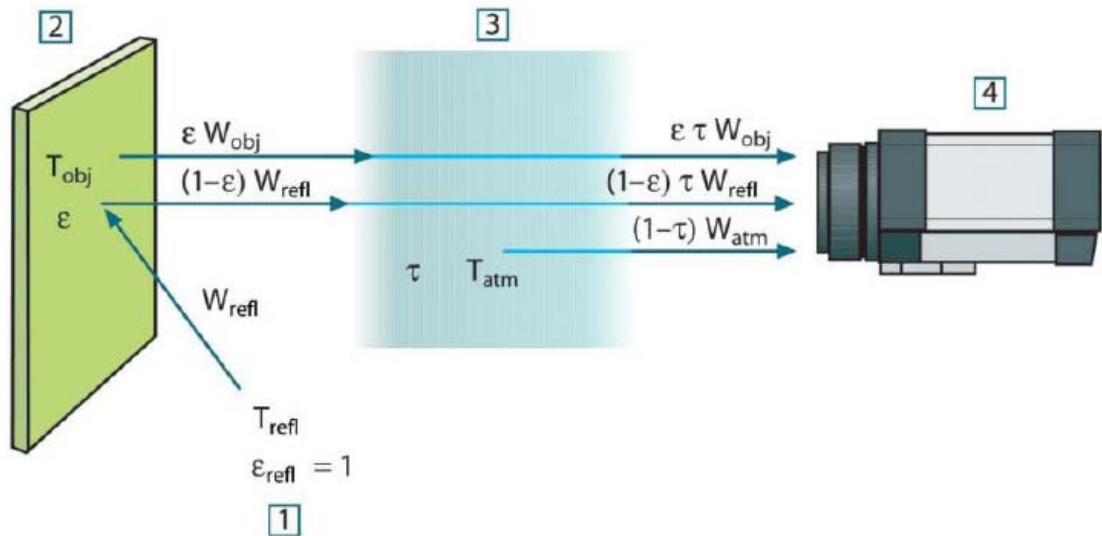
Measurement principles of infrared camera

Figure A.1. Schematic representation of the general thermographic measurement situation with 1: Surroundings; 2: Object; 3: Atmosphere; 4: Camera. In this figure, ε is the emissivity of the object and τ is the transmittance of the atmosphere. Figure from FLIR document *"DG001U-E Photometry Form"*.

When detecting radiations from an object, the camera receives radiation not only from the object itself, but also from the surroundings reflected via the object surface. Both of these contributions become attenuated to some extent by the atmosphere in the measurement path. To this comes a third radiation contribution: the atmosphere it self (see Figure A.1).The total received radiation power can be written as:

$$P_{tot} = \varepsilon\tau P_{obj} + (1-\varepsilon)\tau P_{refl} + (1-\tau)P_{atm} \qquad \text{(eq A.3)}$$

where ε is the emissivity of the object and τ is the transmittance of the atmosphere. P_{tot}, P_{obj}, P_{refl} and P_{amt} are respectively the power from the measurement, the object, the other ambient sources, and the atmosphere.

The camera output voltage signal U is proportional to this power input P: $U \propto P$. To get the temperature of an object, one has to correct the measured voltage of the infrared contribution following the relation:

$$U_{obj} = \frac{1}{\varepsilon\tau}U_{tot} - \frac{(1-\varepsilon)}{\varepsilon}U_{refl} - \frac{(1-\tau)}{\varepsilon\tau}U_{atm} \qquad \text{(eq A.4)}$$

where U_{obj} can be directly converted into object temperature. U_{amt} and U_{refl} correspond respectively to the signal emitted by the atmosphere and the other sources by reflection. The camera operator has to supply a number of parameter value for this calculation: the object emissivity ε, the transmittance of the atmosphere τ, temperature of atmosphere T_{atm}, of object surroundings T_{refl}, object distance, etc. These parameters vary as a function of the measurement conditions and the camera should thus be calibrated.

For our experimental setup for infrared measurement, we have modified our MTS system. Since a classic glassy window is not transparent for infrared waves, we replace it by

a "SOREM FMIR.050" infrared window which is made up of ZnSe material having high transmittance at infrared wavelengths. Indeed, this infrared window has a transmittance of 85% for wavelengths of 7μm-13μm. In addition, our experiments are done at very low temperature, and the condensation in the exterior surface of infrared window and in the chamber should be carefully avoided because water (or ice) shows strong absorption in the infrared region. We keep a continuous dry air flux at the surface of the infrared window, and a nitrogen flux into the chamber to conserve an environment of low humidity, in order to avoid any frost on the window as well as in the neighboring air, and to keep a good repeatable transmittance.

Calibration of infrared camera

The measurement of low object temperature is more critical than measuring high temperature since the "disturbing" radiation sources are relatively much stronger in the first case. In our case of measurement of nonlinear mechanical properties by MTS system, the strongest "disturbing" radiation comes from the window of the chamber in which the temperature is controlled.

We calibrate the infrared camera with our modified experimental setup. The emissivity of rubbers is ε=0.9, atmosphere temperature T_{atm}=23°C, temperature of object surroundings T_{refl} is fixed at the measurement temperature in the chamber. It is found that the transmittance of the atmosphere τ is a parameter of great influence on the measurement results. We thus focus the calibration on the transmittance τ.

We put our calibration sample in a good position in the chamber similar to the one of the sample used for mechanical measurement. We vary the chamber temperature from -80°C to 20°C. Real temperature in the chamber is measured by an integrated thermocouple, as well as two additional thermocouples putting on the surface of the sample. It takes approximately 20 minutes for the sample to achieve temperature equilibrium. Once the temperature is in equilibrium, we measure the power. After the measure on our temperature window, we set the parameters, especially the transmittance, to make sure that the temperature measured by infrared camera is in agreement with thermocouples. Indeed we found that a transmittance of τ=75% is suitable whatever the temperature. This value is reasonable since the intrinsic transmittance of the infrared window is already τ=85%. Taking into account other contributions (atmosphere for example), the real transmittance is expected to be a little smaller than it as observed.
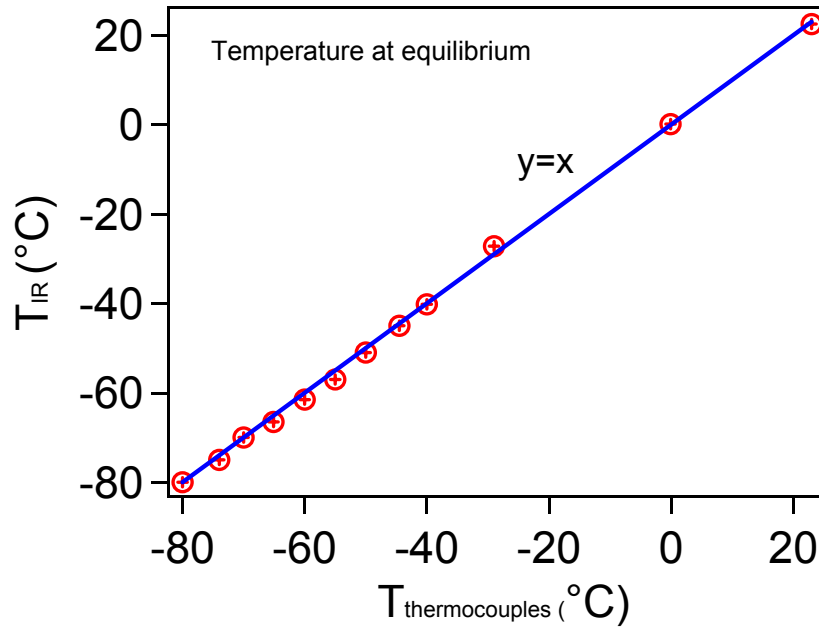
Figure A.2. Calibration of infrared camera with a transmittance of τ=75%. Circles are experimental data of calibration. Line is a reference line of y=x. The quality of calibration is good.

The calibration curve is presented in Figure A.2. It can be seen that with these adjusted parameters, temperature measurement by infrared camera is in good agreement with thermocouples.

It should also be noted that our calibration is done at equilibrium state with an homogenous temperature at least inside the chamber. However, the real situation in our experiment may be more complex as the sample may have a temperature different from the one of the chamber. To fully quantify the withdrawal to this effect, an *in situ* calibration would have to be done by measuring a calibration sample with a different temperature than the one of the chamber, and this for each temperature of the chamber and of the sample. Indeed this calibration is very difficult. So we have assumed in this work that the parameters obtained by a calibration done for the same temperature of the sample and the chamber are also valid with self-heating. This hypothesis is proven to be correct when comparing the infrared camera measurement with the prediction of adiabatic model at the beginning of the test, as is shown in **Figure F.3** of chapter 5.3.

To conclude, we have been able to determine the temperature of the sample with the infrared camera, in our adapted loading machine (infrared window and compressed gases). Indeed using in practice the transmittance of the system of τ=75%, leads to correct measurements of the temperature of the sample during the mechanical test.

Annex B.   Kuhn lengths of PB and SBR

The Kuhn length b and volume v of a Kuhn segment are defined as:

$$b = C_\infty l_0 \qquad \text{(eq B.1)}$$

and

$$v = \frac{C_\infty M_0}{k\rho N_{av}} \qquad \text{(eq B.2)}$$

where :
- b :   the Kuhn segment length (Å)
- C_∞ :   the characteristic ratio of a polymer
- l_0 :   the length of the average backbone bond (Å)
- M_0 : the repeat unit molar mass (g/mol)
- k :   number of backbone bonds per repeat unit
- N_{av} : Avogadro number

        Our homopolymers PB and SBR are composed of different polymer components: 1,4-PB, 1,2-PB and PS. The parameters of these components are found in literatures and are presented in Table B.1. Parameter ρ of 1,2-PB are not found that we use that of 1,4-PB for approximation. Parameter b can be calculated using **(eq B.1)** and supposing a single value of l_0 for all polymers:

$$l_0 = \frac{(9.6+18)}{(5.3+9.5)} = 1.865\text{Å} \qquad \text{(eq B.3)}$$

Table B.1. Parameters C_∞, b, ρ, M_0 and k for different polymer components **[11,81].**

	C_∞	b (Å)	ρ (g/cm3)	M_0 (g/mol)	k
1,4-PB	5.3	9.6	0.826	54	4
1,2-PB	6.8	-	-	54	2
PS	9.5	18	0.969	104	2

        We calculate the parameters of homopolymers PB and SBR as a number average of different components:

$$<C_\infty> = \frac{\sum C_\infty^i n_i}{\sum n_i} = \frac{\sum \dfrac{C_\infty^i w_i k_i}{M_0^i}}{\sum \dfrac{w_i k_i}{M_0^i}} \qquad \text{(eq B.4)}$$

where w_i is the mass fraction of component I (shown in chapter 2.1).

The average value of the Kuhn segment volume is:

$$<v> = \frac{C_\infty}{<\rho> N_{av}} < \frac{M_0}{k} > \qquad \text{(eq B.5)}$$

where

$$< \frac{M_0}{k} > = \frac{1}{\sum \frac{w_i k_i}{M_0^i}} \qquad \text{(eq B.6)}$$

and

$$\rho_{tot} = \frac{1}{\sum \frac{w_i}{\rho_i}} \qquad \text{(eq B.7)}$$

Results are show in Table B.2.

Table B.2. Parameters C_∞, b for pure polymer PB and SBR

	$<C_\infty>$	b (Å)	v (Å^3)
SBR	6.3	11.7	147
PB	5.3	9.9	266

Annex C. Calculation of heat transfer

Let us study how the temperature field sets in the sample and the heat transfer time scale.
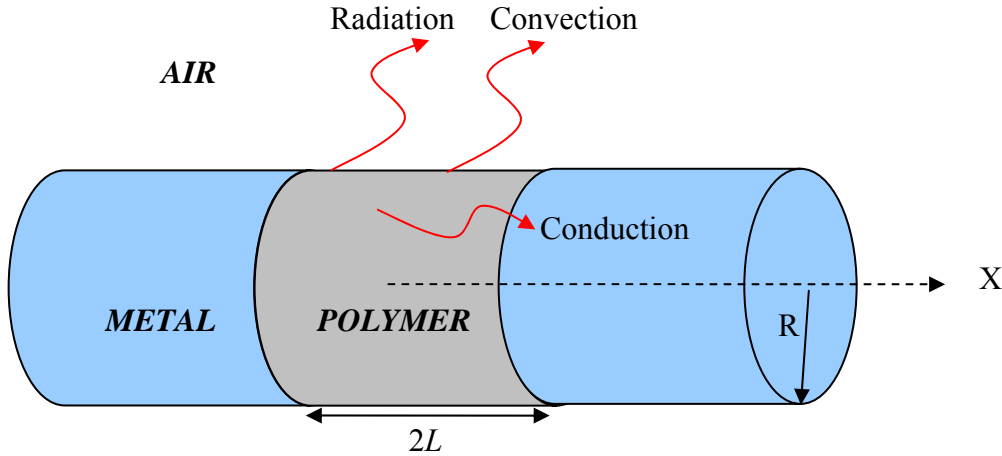

Figure C.1. Schematic of heat transfer by radiation, conduction and convection in our sample.

The heat transfer is mainly by conduction through metal bites in the X direction, and by radiation and convection through air (see **Figure C.1**). The cooling down of a heated sample by heat transfer is usually fitted to an exponential one:

$$T = T_0 + \Delta T \exp(-t / \tau_{ht}) \qquad \text{(eq C.1)}$$

where T_0 is the ambient temperature and τ_{ht} is a certain time scale for the heat transfer who depends on the material properties, geometries, and environmental conditions. Now we will investigate 3 modes of heat transfer separately and evaluate their timescales.

Conduction

The first Fourier's Law states that the heat flux density q through a material is proportional to the negative gradient of temperature:

$$q = -\gamma \frac{\partial T}{\partial x} \qquad \text{(eq C.2)}$$

The second Fourier's law of conduction describes the temporal change:

$$\rho c_p \frac{\partial T}{\partial t} = \gamma \frac{\partial^2 T}{\partial x^2} + P_v \qquad \text{(eq C.3)}$$

where

ρ :   Density ($= 950 \, kg \cdot m^{-3}$ for our polymers)

c_p :   Heat capacity at constant pressure ($= 1800 \, J \cdot kg^{-1} \cdot K^{-1}$)

γ :   Thermal conductivity ($= 0.29 \, W \cdot m^{-1} \cdot K^{-1}$)

P_v :   Internal heat generation per unit volume ($W \cdot m^{-3}$)

The solution for $P_v = 0$ is:

$$T = A\exp(-\frac{t}{\tau_{ht}})\cos(\frac{x\pi}{2L}) + T_{metal}$$ (eq C.4)

and

$$\tau_{ht} = \frac{\rho c_p 4L^2}{\gamma\pi^2}$$ (eq C.5)

with :
    $L = 0.001\,m$ for shear geometry
    $L = 0.005\,m$ for extension geometry

The conductive time scale is:

$$\tau_{cd} = 3\,s \text{ for shear geometry}$$

$$\tau_{cd} = 60\,s \text{ for extension geometry}$$

Radiation

Stefan-Boltzman law gives radiation energy output:

$$P = \varepsilon\sigma AT^4$$ (eq C.6)

where :
    P: Heat transfer per unit time
    ε :   Emissivity, no unit, (=1 for a black body)
    σ :   Stefan-Boltzmann constant ($=5.67\times10^{-8}W\cdot m^{-2}\cdot K^{-4}$)
    A :   Area of the object (m^2)
    T :   Absolute temperature (K)

If a hot object is radiating energy to its cooler surroundings the net radiation energy can be expressed as:

$$\Delta P = \varepsilon\sigma A(T^4 - T_0^4)$$ (eq C.7)

and the temporal evolution is (already integrated in the direction of R) :

$$\rho c_p \frac{\partial T}{\partial t} + \frac{\Delta P}{V} = 0$$ (eq C.8)

For a cylinder with radium R and height h, the area $A = 2\pi Rh$, volume $V = \pi R^2 h$, one obtains:

$$\rho c_p \frac{\partial T}{\partial t} + \frac{2\varepsilon\sigma(T^4 - T_0^4)}{R} = 0$$ (eq C.9)

In the case of $T\approx T_0$, it writes:

$$\rho c_p \frac{\partial T}{\partial t} + \frac{8\varepsilon\sigma}{R} T_0^3 (T - T_0) = 0 \qquad \text{(eq C.10)}$$

Combining the above equation to **(eq C.1)**, the characteristic time is:

$$\tau_r = \frac{\rho c_p R}{8\varepsilon\sigma T_0^3} \qquad \text{(eq C.11)}$$

with :
$R = 0.005 m$
$\varepsilon = 1$
$T_0 = 293 K$

One obtains:

$$\tau_r = 750 \ s$$

Convection

The heat transfer is through movement of the air and is proportional to the difference in temperature between the body surface and its surroundings:

$$P = -hA(T - T_0) \qquad \text{(eq C.12)}$$

wher h is the convective heat transfer coefficient ($W \cdot m^{-2} \cdot K^{-1}$) and at forced convection condition:

$$h = 0.628 \, \text{Re} \, L^{0.5} \, \text{Pr}^{1/3} \qquad \text{(eq C.13)}$$

with :
Re   Reynolds number (~1000)
Pr   Prandtl number (~ 0.7)

Similarly to the radiation calculation, the temporal evolution is:

$$\rho c_p \frac{\partial T}{\partial t} + \frac{2h}{R}(T - T_0) = 0 \qquad \text{(eq C.14)}$$

Combining the above equation to **(eq C.1)**, and the heat transfer time scale by convection is:

$$\tau_{cv} = \frac{\rho c_p R}{2h} \qquad \text{(eq C.15)}$$

t gives :

$$\tau_{cv} = 76 \ s \ \text{ for shear geometry}$$
$$\tau_{cv} = 34 \ s \ \text{ for extension geometry}$$
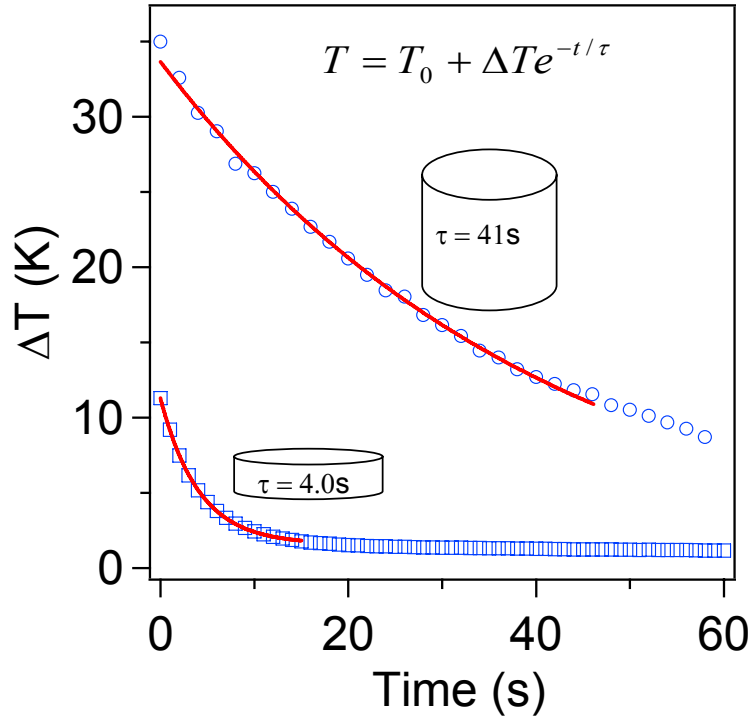
Measurements

Figure C.2. Exponential fits of the cooling of two samples.

Measurements of the temperature change during cooling of two types of samples show that the heat transfer in shear sample has a time scale $\tau_{ht} \sim 4\text{s}$, while that in extension sample is $\tau_{ht} \sim 41\text{s}$ (see **Figure C.2**).

Table C.1. Characteristic heat transfer time scales of two geometries by calculation of different modes and experimental results.

τ (s)	Radiation	Conduction	Convection	Experiment
shear	750	**3**	76	**4**
extension	750	60	**34**	**41**

Conclusion

The temperature evolution in the sample follows this general equation:

$$\rho c_p \frac{\partial T}{\partial t} = -\frac{8\varepsilon\sigma}{R} T_0^3 (T - T_0) - \frac{2h}{R}(T - T_0) + \gamma \frac{\partial^2 T}{\partial x^2} + P_v \qquad \text{(eq C.16)}$$

where the first term in the right hand side is radiation, the second one is convection, the third one is conduction and P_v is heat generation due to self-heating. From the comparison in Table C.1, it can be seen that heat transfer of the sample for shear test is efficient and is controlled by conduction mode while that for extension test is controlled mainly by convection mode. This difference is due to difference in sample geometries.

Annex D. Analytic form of viscoelastic relaxation

In order to decrease the numerical processing time, **analytic form** of the viscoelastic relaxation equation during extension is preferred. As is shown in the main text, at constant true strain rate a, this equation writes:

$$\sigma(t) = a\int_0^t [(E_g - E_r)\exp(-(\frac{x}{\tau_{KWW}})^\beta) + E_r]\exp(a(t-x))dx \qquad \text{(eq D.1)}$$

This can also be written in terms of the strain and strain rate variables:

$$\sigma(\varepsilon, a\tau_{KWW}) = (E_g - E_r)f_1(\varepsilon, a\tau_{KWW}) + E_r\varepsilon \qquad \text{(eq D.2)}$$

where

$$f_1(\varepsilon, a\tau_{KWW}) = (1+\varepsilon)\int_0^\varepsilon \exp(-(\frac{\ln(1+\varepsilon')}{a\tau_{KWW}})^\beta)\frac{1}{(1+\varepsilon')^2}d\varepsilon' \qquad \text{(eq D.3)}$$

In order to obtain the **analytic form**, we change the variables in **(eq D.1)**:

$$y = (\frac{x}{\tau_{KWW}})^\beta \quad \text{and} \quad x = \tau_{KWW}y^{1/\beta} \qquad \text{(eq D.4)}$$

and it becomes:

$$\sigma(t) = a\exp(at)(E_g - E_r)\tau_{KWW}/\beta\int_0^{(t/\tau_{KWW})^\beta}\exp(-y)y^{1/\beta-1}\exp(-ax)dy + E_r(\exp(at)-1) \qquad \text{(eq D.5)}$$

where $\exp(-ax) = \sum_{n=0}^\infty \frac{(-ax)^n}{n!} = \sum_{n=0}^\infty \frac{(-a\tau_{KWW}y^{1/\beta})^n}{n!}$,

so we have :

$$\sigma(t) = a\exp(at)(E_g - E_r)\tau_{KWW}/\beta\int_0^{(t/\tau_{KWW})^\beta}\exp(-y)y^{1/\beta-1}(\sum_{n=0}^\infty \frac{(-a\tau_{KWW}y^{1/\beta})^n}{n!})dy$$

$$+ E_r(\exp(at)-1) \qquad \text{(eq D.6)}$$

The first term of the integration is the incomplete Euler gamma function:

$$\int_0^{(t/\tau_{KWW})^\beta}\exp(-y)y^{1/\beta-1}dy = \gamma\{1/\beta, (t/\tau_{KWW})^\beta\} \qquad \text{(eq D.7)}$$

where $\gamma(s,x)$ is the lower incomplete gamma function: $\gamma(s,x) = \int_0^x y^{s-1}e^{-y}dy$. This function is known by our calculation tool (Igor).

The second term is:

$$-a\tau_{KWW}\int_0^{(t/\tau_{KWW})^\beta}\exp(-y)y^{2/\beta-1}dy = -a\tau_{KWW}\gamma\{2/\beta, (t/\tau_{KWW})^\beta\} \qquad \text{(eq D.8)}$$

Similarly, the rest is:

$$\frac{(a\tau_{KWW})^2\gamma\{3/\beta,(t/\tau_{KWW})^\beta\}}{2}+\cdots+\frac{(-a\tau_{KWW})^n\gamma\{(n+1)/\beta,(t/\tau_{KWW})^\beta\}}{n!} \quad \text{(eq D.9)}$$

The final equation is:

$$\sigma(t)=\exp(at)(E_g-E_r)\frac{a\tau_{KWW}}{\beta}(\sum_{n=0}^{\infty}\frac{(-a\tau_{KWW})^n\gamma\{(n+1)/\beta,(t/\tau_{KWW})^\beta\}}{n!})+E_r(\exp(at)-1)$$

$$\text{(eq D.10)}$$

or

$$\sigma(\varepsilon,a\tau_{KWW})=(\varepsilon+1)(E_g-E_r)\frac{a\tau_{KWW}}{\beta}(\sum_{n=0}^{\infty}\frac{(-a\tau_{KWW})^n\gamma\left\{\frac{(n+1)}{\beta},(\frac{\ln(1+\varepsilon)}{a\tau_{KWW}})^\beta\right\}}{n!})+E_r\varepsilon$$

$$=(E_g-E_r)f_1(\varepsilon,a\tau_{KWW})+E_r\varepsilon$$

$$\text{(eq D.11)}$$

where

$$f_1(\varepsilon,a\tau_{KWW})=(\varepsilon+1)\frac{a\tau_{KWW}}{\beta}(\sum_{n=0}^{\infty}\frac{(-a\tau_{KWW})^n\gamma\left\{\frac{(n+1)}{\beta},(\frac{\ln(1+\varepsilon)}{a\tau_{KWW}})^\beta\right\}}{n!})$$

$$\text{(eq D.12)}$$

This equation converges rapidly for $\varepsilon\in[0,1]$ and could be limited to its first 4 terms.

Annex E. Determination of the evolution of the structural non linearity parameters $A_{ent}+A_{plast}$

Fitting details: experimental results and that of two models are evenly interpolated to 1000 points from 0 to 100% of strain, i.e. 0.1% of strain between two points. The fitting is done to a strain limit where the chi-square is no more than $\chi_1{}^2=5\times10^{11}$. To evaluate the influence of the chi-square value, we do another set of fits with $\chi_2{}^2=10^{12}$.

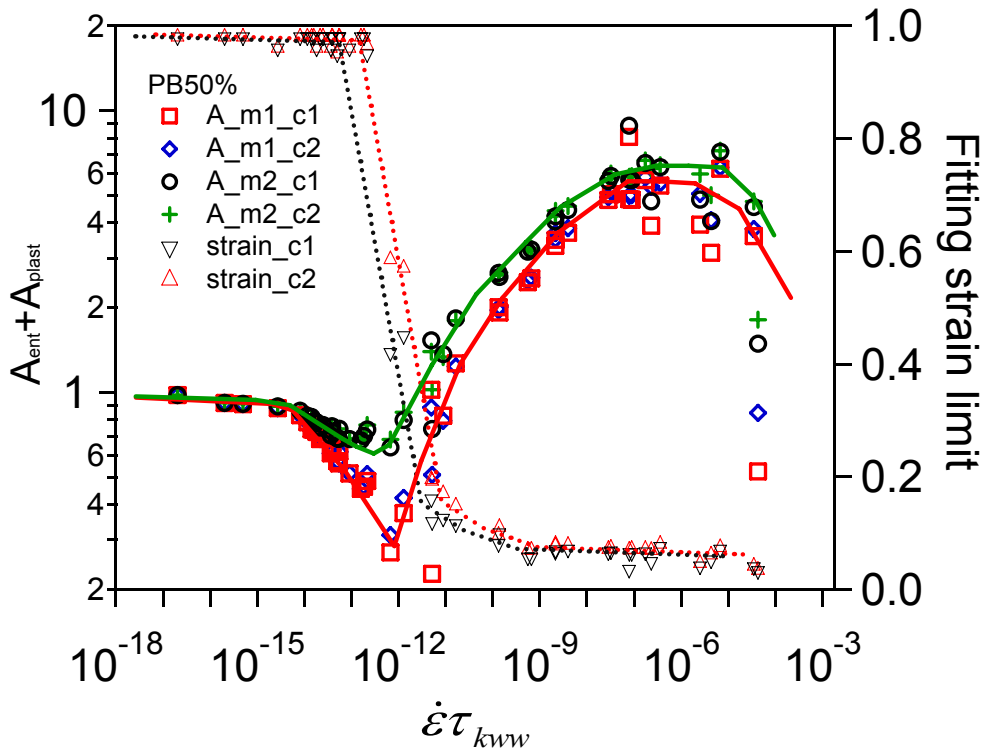**Influence of the choice of model and fitting condition (χ^2)**

Figure E.1. Fitting results of $A_{ent} + A_{plast}$ with two models and two χ^2: $\chi_1{}^2=5\times10^{11}$ with model 1 ($\square$), $\chi_1{}^2=5\times10^{11}$ with model 2 ($\Diamond$), $\chi_2{}^2=10^{12}$ with model 1 (O), $\chi_2{}^2=10^{12}$ with model 2 (+), and the corresponding fitting strain limits. Lines are guide lines for clarity.

For a fixed χ^2 value, the fitting limit is the entire domain up to $\varepsilon = 1$ at rubbery state, and is about $\varepsilon = 0.05$ at glassy state. The transition of this fitting limit is rapid and is about the same position as the minimum of structural nonlinearity. The choice of the value of χ^2 can't be too small otherwise the fitting domain is too small to give reliable results. It can neither be too big otherwise the fitting quality will be compromised. In addition, the fitting domain should be inside the above discussed reliable strain range where the deformation is homogeneous and the adiabatic self-heating is negligible ($\Delta T<0.5K$). It is effectively verified that both $\chi_1{}^2$ and $\chi_2{}^2$ give fitting strain limit in this reliable strain range for all the measurements. From **Figure E.1**, it can be seen that χ^2 has little influence on the values of $A_{rub}+A_{plast}$ and it is the choice of model that has greater influence.

Two models give same results at rubbery state, but at glassy state, the value of $A_{ent} + A_{plast}$ with model 2 (green line) is systematically higher than that of model 1 (red line). This is because in the rubber state, the viscoelastic contribution f_1 is negligible and model 1 is equivalent to model 2. At glassy state, rubbery contribution E_r is negligible compared to viscoelastic contribution, which is not described in the same way by model 1 and 2. Model 1 assumes a Gaussian affine deformation and model 2 not. This gives a difference of about 1 in the values of $A_{ent} + A_{plast}$ at the glassy state. The exact calculation of $A_{ent} + A_{plast}$ in the glassy state will be done in the following paragraphs to verify the discrepancy between model 1 and model 2.

Indeed, using $\lambda = 1 + \varepsilon$ at small strain regime $\varepsilon << 1$ where ε^3 and further terms are negligible, the fitting equation can be written as:

$$\sigma = \frac{E_0}{3}[1 - \frac{5}{6}A(1 - \lambda^{-1})](\lambda - \lambda^{-2})$$

$$= E_0\varepsilon + (-E_0 - \frac{5}{6}AE_0)\varepsilon^2 + o(\varepsilon^3)$$

(eq E.1)

The first and the second derivatives of the stress are respectively E_0 and $E_1 = -2E_0 - \frac{5}{3}AE_0$, where the term $-2E_0$ is the affine deformation contribution already described above and the term $-\frac{5}{3}AE_0$ comes from structural nonlinearity.

A general equation of A value as a function the first and the second derivatives (in the small strain regime) writes:

$$A = A_{exp} = A_{visco} + A_{ent} + A_{plast} = -\frac{3(E_1 + 2E_0)}{5E_0}$$

(eq E.2)

Considering that E_0 is the same for experiment and models, we have:

$$A_{ent} + A_{plast} = -\frac{3(E_1^{exp} - E_1^{visco})}{5E_0} = \frac{3\Delta E_1}{5E_0}$$

(eq E.3)

where $\Delta E_1 = E_1^{visco} - E_1^{exp}$.

The discrepancy of $A_{ent} + A_{plast}$ value between model 1 and model 2 at glassy state is due to the presence (or not) of Gaussian affine deformation in the models. This difference is in practice rather small at glassy state:

$$\Delta(A_{rub} + A_{plast}) \approx 1.2$$

(eq E.4)

and

$$\frac{\Delta(A_{rub} + A_{plast})}{(A_{rub} + A_{plast})} \approx \frac{1.2}{6} = 20\%$$

(eq E.5)

This difference decreases to $\Delta(A_{ent} + A_{plast}) \approx 0.3$ in the glass transition domain and $\Delta(A_{ent} + A_{plast}) \approx 0$ in the rubbery domain. Despite of this discrepancy between model 1 and

model 2, the global decrease-increase dented form of $A_{ent}+A_{plast}$ is always the same with either of the two models.

To conclude, the choice of χ^2 in the fitting procedure should make sure that the fitting limit is always within the reliable strain range. The value of χ^2 has little influence on $A_{ent}+A_{plast}$ value. Model 2 gives higher $A_{ent}+A_{plast}$ value at glassy state than that of model 1. Both models give same evolution of $A_{ent}+A_{plast}$ value. For clarity, we will only use results with model 1, $\chi_2{}^2=10^{12}$ for further discussion.

Annex F.   Details of cyclic shear measurements

Measurement procedure

Cyclic shear experiments are done for one pure polymer (SBR) and one polymer blend (PB50/SBR50). The sample geometry and gluing are already described in chapter 2. Measurements are done at about every 5°C from rubbery to glassy state. Temperature is reached by cooling down at a rate of 10K/min from above T_g, and keeps in equilibrium at that temperature for 20 minutes. We apply a sinusoidal strain $\gamma = \gamma_0 \sin(\omega t)$ of different amplitudes (γ_0=1%, 2%, 5%, 10%, 20%) and different frequencies ($f = \omega / 2\pi$ =0.01Hz, 0.1Hz, 1Hz, 10Hz). The temperature evolution during the test is measured by infrared camera.

Effect of machine compliance

Machine compliance could be a very important source of error when measuring material properties, especially glassy polymers [82,83]. In the measurement of the viscoelastic response of materials, the machine compliance can lead to errors of the dynamic modulus G^*. The dynamic data could be corrected by the following equation:

$$\frac{1}{G^*_{mes}} = \frac{1}{G^*_s} + \frac{1}{G_m}$$

(eq F.1)

where G^*_{mes} is the measured complex shear modulus G^*_s is the actual complex modulus of the sample and G_m is the modulus due to machine compliance, which is assumed to be purely elastic and has only the real component of its complex modulus.
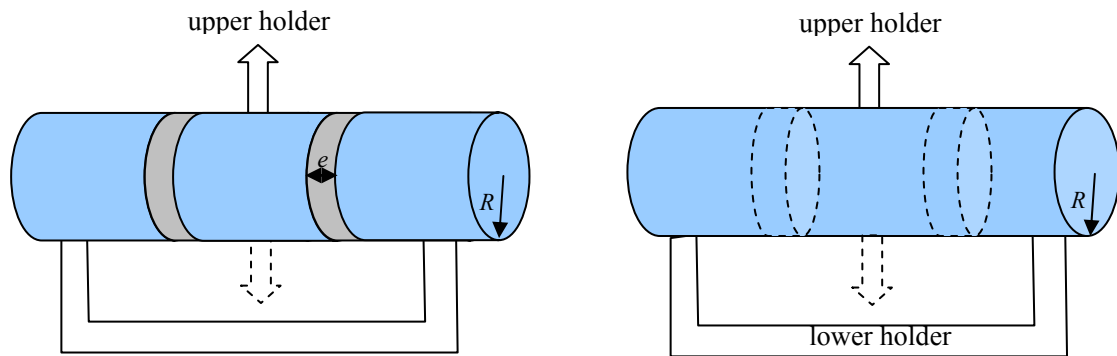

Figure F.1. A simple schematic showing the geometry of cyclic shear of (a) polymer sample for experiments and (b) solid rod for measurement of machine compliance.

The modulus of G_m due to machine compliance is determined by measuring a sample of solid rod (steel) with the same geometry. The equivalent elastic modulus of the system can thus be measured which is $G_m = 4 \times 10^8 \, Pa$ (the loss modulus is negligible: $G''_m = 4 \times 10^6 \, Pa$).

With the machine compliance known, it is possible to correct the results of dynamic complex modulus of the sample with **(eq F.1)**. For example, with $G_{mes}^* \approx G_{mes}^{'} = 2 \times 10^8 \, Pa$, the actual sample shear modulus is $G_s^{'} = 4 \times 10^8 \, Pa$. It could make a factor of 2.

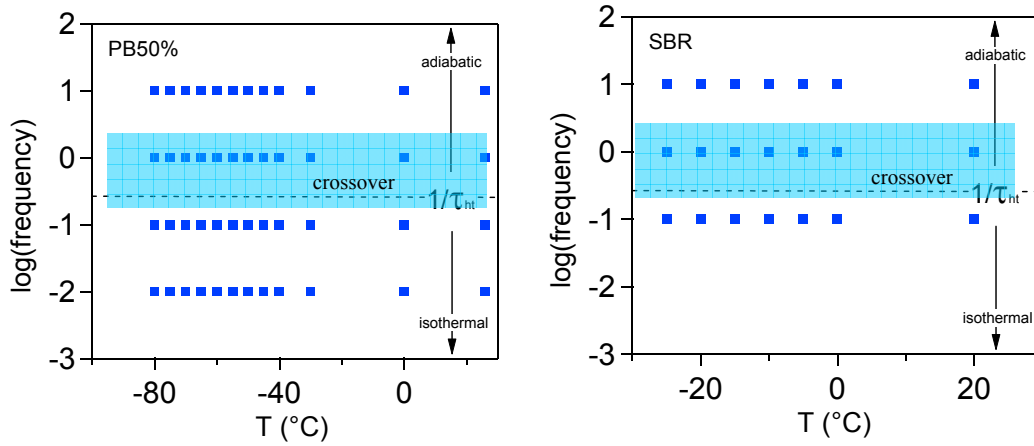**Determination of reliable experimental windows**

Figure F.2. Measurement of (a) PB50/SBR50 samples and (b) SBR samples at different temperatures and frequencies. Dashed line is a reference to separate adiabatic condition and isothermal condition.

Internal energy generation power P_v is proportional to $G''\gamma_0^2 f$, so at large amplitude and high frequency, adiabatic self-heating is important. With this sample geometry, the characteristic heat transfer time scale τ_{ht} equals 4s (see Annex 1).
-   If the frequency is low and $1/f >> \tau_{ht}$, the sample is isothermal.
-   If the frequency is high, $1/f << \tau_{ht}$ and $t << \tau_{ht}$, the first several cycles are in the adiabatic regime, there is self-heating and temperature in the sample is homogeneous. If $1/f << \tau_{ht}$ and $t >> \tau_{ht}$, the temperature in the sample is not homogeneous and is in a new equilibrium state.

We will give some examples of strain stress curves and temperature evolutions, in order to determine reliable experimental windows.

High frequency

Adiabatic self-heating is important for experiments at large amplitude and high frequency (see **Figure F.3**). Temperature increases rapidly. The stress strain curves seem to be elliptic but the declination becomes more and more horizontal: i.e. the modulus decreases.

The temperature evolution is measured by infrared camera, which is compared to the prediction in adiabatic condition giving:

$$\Delta T = \frac{\int^1 \sigma d\gamma}{\rho c_p} \qquad \text{(eq F.2)}$$
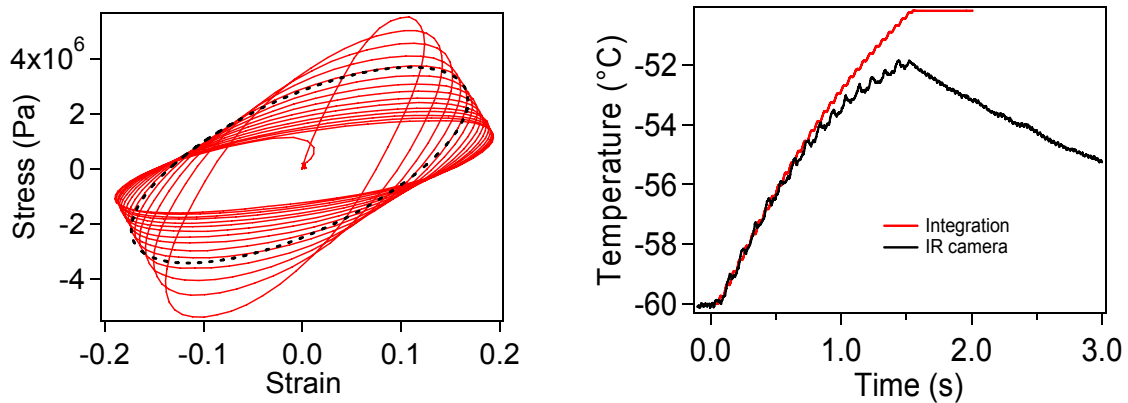
168

Figure F.3. (a) stress strain curves and (b) temperature evolution of experiment of PB50% with T_0=-60°C, f=10Hz, γ_0=0.2. Dotted line is an elliptic fit to the fifth cycle.

From **Figure F.3**(b), two temperature evolutions measured by infrared camera and calculated by the integration in the adiabatic regime superpose very well at the beginning, and they deviate after about 0.5 second. This means that the first 0.5 second is really in the adiabatic regime and the temperature distribution is homogeneous. Data in the first 0.5s, i.e. the first 5 cycles, are reliable and beyond this regime should not be considered.

It is also noted that the actual strain amplitude grows during this reliable experimental window. So during this window, the actual amplitude and the actual temperature of each cycle should be carefully determined.

In addition, we have checked that under adiabatic condition, two samples with the same actual temperature have the same mechanical behavior, regardless of their initial temperatures at equilibrium (see **Figure F.4**).
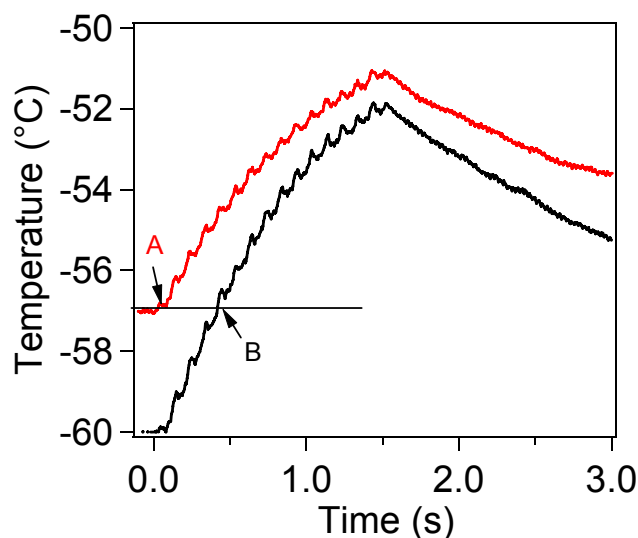

Figure F.4. Temperature evolutions of two measurements where A point and B point have the same mechanical behavior.

Conclusion: reliable experimental window at high frequency is the first 0.5s, i.e. the first 5 cycles for f=10Hz. It is in the adiabatic regime and self heating is homogeneous. The actual amplitude and the actual temperature of each cycle should be carefully determined.

Low frequency

For experiments with f=1Hz, self-heating is also observed but from the first cycle (after 0.5s), the temperature distribution is already non homogeneous in the sample, so this frequency is the crossover of isothermal and adiabatic conditions and these data should not be considered as reliable.

For experiments with f=0.1Hz and f=0.01Hz, no self-heating is observed, and all the samples are in the isothermal condition.

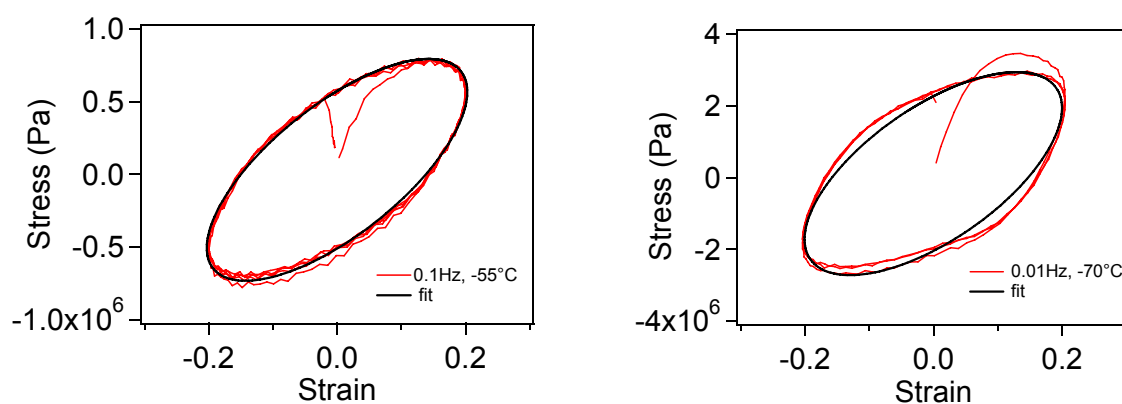**Figure F.5.** Stress-strain curves of experiment of PB50% with f=0.01Hz, γ_0=0.2. (a) T_0=-55°C, (b) T_0=-70°C. Black lines are elliptic fits.

It can be seen from **Figure F.5** that some cures have an elliptic form, others do not. We will show that the non-elliptic form is an intrinsic property and is not related to thermo-elasticity (i.e. the small cyclic temperature variations due to entropic variations).

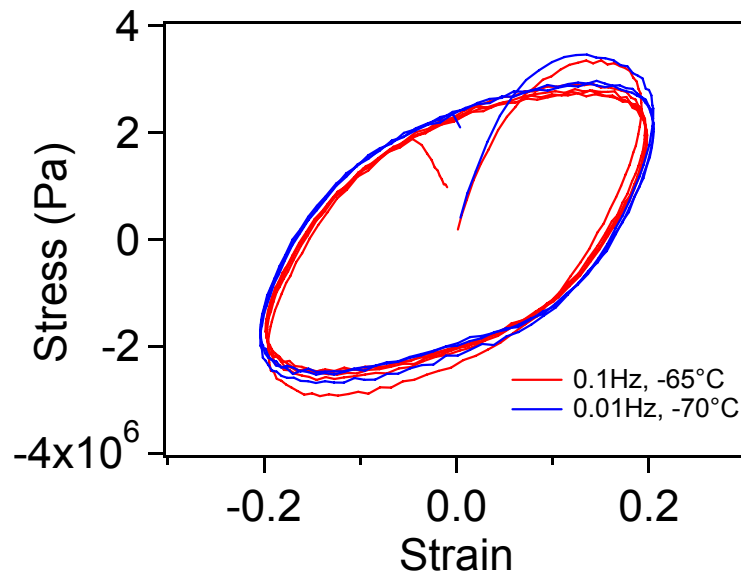**Time-temperature superposition: non-elliptic form is not thermo-elasticity**

Figure F.6. Stress-strain curves of experiment of PB50% with f=0.01Hz or 0.1Hz, γ_0=0.2, T_0= - 65°C or -70°C.

Thermo-elasticity is the cyclic temperature variation during each cycle due to entropy change of the structure and its frequency should be two times of the solicitation, i.e. 2ω. We were not able to detect significantly thermo-elasticity effect during our measurements. In addition, it should not appear on isothermal condition. This is also confirmed by the well superposed curves of 0.1Hz and 0.01Hz, indicating that both frequencies are in the isothermal condition, there is no thermo-elasticity, and time-temperature superposition is valid.

Conclusion: All data of f=0.01Hz and f=0.1Hz are reliable, they are in the isothermal regime. Time-temperature superposition is valid in the isothermal regime. Non-elliptic form stress-strain curves should be carefully analyzed.

Annex G. Nonlinear time-temperature superposition in extension

It is already discussed that in the linear regime, the initial modulus of extension has a time-temperature superposition that is close to the WLF one in small amplitude oscillatory shear test in rheology. We plot some combinations of temperature and strain rate (inverse of the time scale), to see the time-temperature superposition in nonlinear regimes.
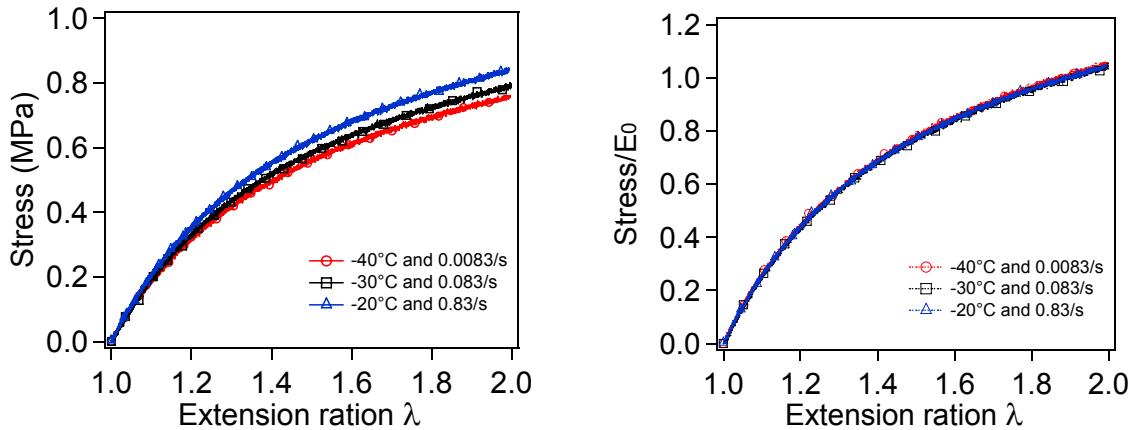

Figure G.1. (a) Nominal stress vs. extension ratio of PB50/SBR50 blend at different temperature and strain rate: T=-40°C and $\dot{\varepsilon}_1 = 0.0083/s$ ($\circ$); T=-30°C and $\dot{\varepsilon}_2 = 0.083/s$ ($\square$); T=-20°C and $\dot{\varepsilon}_3 = 0.83/s$ (Δ). (b) Nominal stress normalized by initial modulus vs. extension ratio with same conditions.

At rubbery state, the nonlinear time-temperature superposition is valid: different curves superpose in all the strain range – the only differences at large strain (**Figure G.1**(a)) is due to the slight differences in initial modulus, and can be totally erased if we plot the stress normalized by initial shear modulus (**Figure G.1**(b)). It should be noted that at rubbery state, data in all the strain range is valid.

At glassy state (see **Figure G.2**), even if data beyond yield point is less reliable due to great self-heating and non homogeneous deformation, it still seems that we observe a time-temperature superposition.

In fact, the lowest strain rates $\dot{\varepsilon}_1$ is in the isothermal regime, so the temperature in the sample is lower than that with other strain rates. Strain rate $\dot{\varepsilon}_2$ is in the crossover regime between isothermal and adiabatic ones. Strain rates $\dot{\varepsilon}_3$ and $\dot{\varepsilon}_4$ are in the adiabatic regime, temperature evolutions of two of them should be the same.

We plot again the stress normalized by initial shear modulus (**Figure G.2**(b)) of two experiments at adiabatic regime with strain rates $\dot{\varepsilon}_3$ and $\dot{\varepsilon}_4$. It was found that before yield point, the curves before yield point are well superposed. As necking appears, the dented form due to necking is more obvious in the highest strain rate $\dot{\varepsilon}_4$. At larger strains, they superpose again very well.
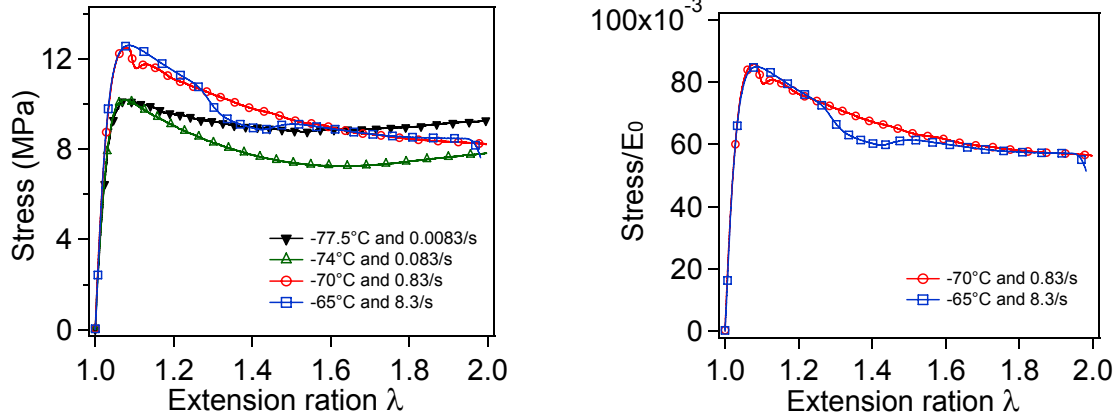
Figure G.2. (a) Nominal stress vs. extension ratio of PB50/SBR50 blend at different temperature and strain rate: T=-77.5°C and $\dot{\varepsilon}_1 = 0.0083/s$ (▼); T=-74°C and $\dot{\varepsilon}_2 = 0.083/s$ (Δ); T=-70°C and $\dot{\varepsilon}_3 = 0.83/s$ (○); T=-60°C and $\dot{\varepsilon}_4 = 8.3/s$ (□). (b) Nominal stress normalized by initial modulus vs. extension ratio with same conditions.

To conclude, the nonlinear time-temperature superposition seems to be valid for polymers at rubbery state (isothermal) or for polymers in the deeply adiabatic self-heating regime at glassy state.

References

[1]   M. D. Ediger, Annu. Rev. Phys. Chem. **51**, 99 (2000).

[2]   P. G. Debenedetti and F. H. Stillinger, Nature **410**, 259 (2001).

[3]   M. D. Ediger, C. A. Angell, and S. R. Nagel, J. Phys. Chem. **100**, 13200 (1996).

[4]   J. M. Hutchinson, Prog. Polym. Sci. **20**, 703 (1995).

[5]   P. Combette and I. Ernoult, *Physique Des Polymères: Structure, Fabrication, Emploi* (Presse internationales Polytechnique, 2005).

[6]   J. Zhao, S. L. Simon, and G. B. McKenna, Nat. Commun. **4**, 1783 (2013).

[7]   L. Berthier and G. Biroli, Rev. Mod. Phys. **83**, 587 (2011).

[8]   L. C. Pardo, P. Lunkenheimer, and A. Loidl, Phys. Rev. E **76**, 030502 (2007).

[9]   G. B. McKenna, Nat. Phys. **4**, 673 (2008).

[10] J. D. Ferry, *Viscoelastic Properties of Polymers*, 3rd Revised edition (John Wiley & Sons Inc, 1980).

[11] M. Rubinstein and R. H. Colby, *Polymer Physics* (Oxford University Press, 2003).

[12] L. R. G. Treloar, *The Physics of Rubber Elasticity* (Oxford University Press, 2005).

[13] S. K. Kumar, S. Shenogin, and R. H. Colby, Macromolecules **40**, 5759 (2007).

[14] A. Dequidt, D. R. Long, P. Sotta, and O. Sanséau, Eur. Phys. J. E **35**, 1 (2012).

[15] M. Rubinstein and S. Panyukov, Macromolecules **35**, 6670 (2002).

[16] I. Chang, F. Fujara, B. Geil, G. Heuberger, T. Mangel, and H. Sillescu, J. Non-Cryst. Solids **172–174, Part 1**, 248 (1994).

[17] H. Sillescu, R. Böhmer, G. Diezemann, and G. Hinze, J. Non-Cryst. Solids **307–310**, 16 (2002).

[18] H. Sillescu, J. Non-Cryst. Solids **243**, 81 (1999).

[19] M. T. Cicerone, F. R. Blackburn, and M. D. Ediger, Macromolecules **28**, 8224 (1995).

[20] S. Havriliak and S. Negami, J. Polym. Sci. Part C Polym. Symp. **14**, 99 (1966).

[21] F. Alvarez, A. Alegra, and J. Colmenero, Phys. Rev. B **44**, 7306 (1991).

[22] R. Quinson, J. Perez, M. Rink, and A. Pavan, J. Mater. Sci. **31**, 4387 (1996).

[23] O. A. Hasan and M. C. Boyce, Polymer **34**, 5085 (1993).

[24] S. N. Rudnev, O. B. Salamatina, V. V. Voenniy, and E. F. Oleynik, Colloid Polym. Sci. **269**, 460 (1991).

[25] O. B. Salamatina, S. N. Rudnev, V. V. Voenniy, and E. F. Oleynik, J. Therm. Anal. **38**, 1271 (1992).

[26] S. V. Shenogin, G. W. H. Höhne, and E. F. Oleinik, Thermochim. Acta **391**, 13 (2002).

[27] R. S. Hoy and M. O. Robbins, J. Polym. Sci. Part B Polym. Phys. **44**, 3487 (2006).

[28] R. S. Hoy and M. O. Robbins, Phys. Rev. E **77**, 031801 (2008).

[29] R. S. Hoy and M. O. Robbins, *Strain Hardening of Polymer Glasses: Entanglements, Energetics, and Plasticity* (2007).

[30] van Melick H.G.H., Govaert L.E., and Meijer H.E.H., Polymer **44**, 2493 (2003).

[31] E. J. Kramer, J. Polym. Sci. Part B Polym. Phys. **43**, 3369 (2005).

[32] R. S. Hoy, J. Polym. Sci. Part B Polym. Phys. **49**, 979 (2011).

[33] H.-N. Lee, K. Paeng, S. F. Swallen, and M. D. Ediger, Science **323**, 231 (2009).

[34] P. Sollich, F. Lequeux, P. Hébraud, and M. E. Cates, Phys. Rev. Lett. **78**, 2020 (1997).

[35] O. A. Hasan and M. C. Boyce, Polym. Eng. Sci. **35**, 331 (1995).

[36] E. Oleinik, O. Salamatina, S. Rudnev, and S. Shenogin, Vysokomol. Soedin. Seriya Seriya B **35**, 1819 (1993).

[37] S. Arrese-Igor, A. Alegría, and J. Colmenero, Macromolecules **43**, 6406 (2010).

[38] T. Lodge and T. McLeish, Macromolecules **33**, 5278 (2000).

[39] S. Shenogin, R. Kant, R. H. Colby, and S. K. Kumar, Macromolecules **40**, 5767 (2007).

[40] R. Colby and J. Lipson, Macromolecules **38**, 4919 (2005).

[41] R. Kant, S. Kumar, and R. Colby, Macromolecules **36**, 10087 (2003).

[42] J. Colmenero and A. Arbe, Soft Matter **3**, 1474 (2007).

[43] J. Pathak, R. Colby, S. Kamath, S. Kumar, and R. Stadler, Macromolecules **31**, 8988 (1998).

[44] S. Kamath, R. Colby, S. Kumar, K. Karatasos, G. Floudas, G. Fytas, and J. Roovers, J. Chem. Phys. **111**, 6121 (1999).

[45] E. Leroy, A. Alegria, and J. Colmenero, Macromolecules **36**, 7280 (2003).

[46] A. Alegria, J. Colmenero, K. L. Ngai, and C. M. Roland, Macromolecules **27**, 4486 (1994).

[47] H. Watanabe and O. Urakawa, Korea-Aust. Rheol. J. **21**, 235 (2009).

[48] Y. Hirose, O. Urakawa, and K. Adachi, Macromolecules **36**, 3699 (2003).

[49] A. Arbe, A. Alegria, J. Colmenero, S. Hoffmann, L. Willner, and D. Richter, Macromolecules **32**, 7572 (1999).

[50] T. Sakaguchi, N. Taniguchi, O. Urakawa, and K. Adachi, Macromolecules **38**, 422 (2005).

[51] G. C. Chung, J. A. Kornfield, and S. D. Smith, Macromolecules **27**, 964 (1994).

[52] C. Roland and K. Ngai, Macromolecules **24**, 2261 (1991).

[53] S. Hoffmann, L. Willner, D. Richter, A. Arbe, J. Colmenero, and B. Farago, Phys. Rev. Lett. **85**, 772 (2000).

[54] J. Zhao, M. D. Ediger, Y. Sun, and L. Yu, Macromolecules **42**, 6777 (2009).

[55] I. Cendoya, A. Alegría, J. M. Alberdi, J. Colmenero, H. Grimm, D. Richter, and B. Frick, Macromolecules **32**, 4065 (1999).

[56] S. Koizumi, Soft Matter **7**, 3984 (2011).

[57] S. K. Kumar, R. H. Colby, S. H. Anastasiadis, and G. Fytas, J. Chem. Phys. **105**, 3777 (1996).

[58] E. Kim, E. J. Kramer, W. C. Wu, and P. D. Garrett, Polymer **35**, 5706 (1994).

[59] C. Creton, J.-L. Halary, and L. Monnerie, Polymer **40**, 199 (1999).

[60] S.-H. Chough and D.-H. Chang, J. Appl. Polym. Sci. **61**, 449 (1996).

[61] M. R. Piggott, *Load Bearing Fibre Composites* (Springer, 2002).

[62] K. Schröter, R. Unger, S. Reissig, F. Garwe, S. Kahle, M. Beiner, and E. Donth, Macromolecules **31**, 8966 (n.d.).

[63] P. Shi, R. Schach, E. Munch, H. Montes, and F. Lequeux, Macromolecules (2013).

[64] L. Bellon, S. Ciliberto, and C. Laroche, Europhys. Lett. EPL **51**, 551 (2000).

[65] L. Bellon, S. Ciliberto, and C. Laroche, Eur. Phys. J. B **25**, 223 (2002).

[66] H. Bodiguel, F. Lequeux, and H. Montes, J. Stat. Mech. Theory Exp. **2008**, P01020 (2008).

[67] G. Katana, E. W. Fischer, T. Hack, V. Abetz, and F. Kremer, Macromolecules **28**, 2714 (1995).

[68] N. Charalambakis, Appl. Mech. Rev. **63**, 030803 (2010).

[69] J. F. Palierne, Rheol. Acta **29**, 204 (1990).

[70] F. Lequeux and A. Ajdari, Phys. Rev. E Stat. Nonlin. Soft Matter Phys. **63**, 030502 (2001).

[71] S. L. Simon, J. W. Sobieski, and D. J. Plazek, Polymer **42**, 2555 (2001).

[72] J. Colmenero, A. Alegra, J. M. Alberdi, F. Alvarez, and B. Frick, Phys. Rev. B **44**, 7321 (1991).

[73] A. Arbe, J. Colmenero, M. Monkenbusch, and D. Richter, Phys. Rev. Lett. **81**, 590 (1998).

[74] Y. Hemar, R. Hocquart, and F. Lequeux, JPhys II **5**, 1567 (1995).

[75] C. G'Sell, J. M. Hiver, A. Dahoun, and A. Souahi, J. Mater. Sci. **27**, 5031 (1992).

[76] C. G'Sell, J. M. Hiver, and A. Dahoun, Int. J. Solids Struct. **39**, 3857 (2002).

[77] E. Parsons, M. C. Boyce, and D. M. Parks, Polymer **45**, 2665 (2004).

[78] Y. Leterrier and C. G'sell, J. Mater. Sci. **23**, 4209 (1988).

[79] K. S. Cho, K. Hyun, K. H. Ahn, and S. J. Lee, J. Rheol. **49**, 747 (2005).

[80] G. J. Papakonstantopoulos, R. A. Riggleman, J.-L. Barrat, and J. J. de Pablo, Phys. Rev. E Stat. Nonlin. Soft Matter Phys. **77**, 041502 (2008).

[81] S. Wu, J. Polym. Sci. Part B Polym. Phys. **27**, 723 (1989).

[82] K. Schröter, S. A. Hutcheson, X. Shi, A. Mandanici, and G. B. McKenna, J. Chem. Phys. **125**, 214507 (2006).

[83] S. A. Hutcheson and G. B. McKenna, J. Chem. Phys. **129**, 074502 (2008).

Titre : Mécanique linéaire et non linéaire des mélanges de polymères miscibles autour de la transition vitreuse.

Des mélanges de polymères miscibles de Polybutadiène (PB) et Polystyrène Butadiène (SBR) sont étudiés afin de mettre en relation leur structure microscopique avec leur comportement mécanique macroscopique dans les domaines linéaire et non linéaire.

Les hétérogénéités dynamiques existent dans ces mélanges. Elles sont particulièrement visibles aux échelles de longueur associées aux modes de relaxation α (~1nm). Mais elles ne sont observées ni sur des échelles plus grandes associées à l'élasticité caoutchoutique (~10nm), ni sur des échelles plus petites associées aux modes de relaxation β (<1nm).

On suppose qu'un mélange peut être considéré comme un ensemble de domaines avec des températures de transition vitreuse différentes. La distribution de la température de transition vitreuse $P(T_g)$ est déterminé via des mesures calorimétrique avec ou sans vieillissement physique. Avec le modèle de champs moyen auto cohérent d'Olroyd-Palierne, on peut prévoir quantitativement les spectres viscoélastiques linéaires des mélanges à partir de ceux des homopolymères et des données calorimétriques, sans paramètre ajustable. Cela confirme l'hypothèse qu'un mélange peut être considéré comme un ensemble de domaines avec des températures de transition vitreuse différentes.

Les propriétés mécaniques non linéaires sont aussi étudiées. Les glissements d'enchevêtrement sont immobilisés par des zones vitreuses quand la transition vitreuse s'approche. La plasticité commence et les non linéarités structurales deviennent les plus importantes quand il y a la percolation des zones vitreuses.

Mots-clés: mélanges des polymères miscibles, transition vitreuse, hétérogénéité dynamique, plasticité

Title: Linear and non linear mechanical properties of miscible polymer blends near glass transition

Miscible polymer blends of Polybutadiene (PB) and Styrene Butadiene Rubber (SBR) are studied in order to relate their microscopic structure to their macroscopic linear and nonlinear mechanical properties.

The dynamic heterogeneities of polymer blends are particularly strong at the length scale of segmental movement associated to the α-relaxation (~1nm). It is neither obvious in our blend system in larger length scale involved in rubber elasticity (~10nm), nor in smaller length scale of localized motions controlling the β-relaxation (<1nm).

We assume that a blend can be considered as an ensemble of domains of various local glass transition temperatures. Using calorimetric data, with or without aging, we probe the distribution of glass transition temperature $P(T_g)$ of miscible polymer blends. Using self-consistent averaging method inspired by the Olroyd-Palierne model, we predict quantitatively, with no adjustable parameter, the linear viscoelastic spectrum of our blends from that of pure polymers and the T_g distribution obtained by calorimetry. This quantitative prediction confirms thus the assumption that mechanically, a blend can be considered as an ensemble of domains each of which having a different glass transition temperature.

The nonlinear mechanical properties are studied. As the system approaches glass transition, the entanglement slipping is greatly reduced due to appearance of glassy domains that immobilize the chains. Plasticity begins to be dominant as the system goes deeper into the glass transition zone, and the structural nonlinearity is the most strong when there is a percolation of glassy domains.

Keywords: miscible polymer blends, glass transition, dynamic heterogeneity, plasticity.